Universitat Autònoma de Barcelona

Solution Processable Oxides for Inverted and Carbon-based Perovskite Solar Cells

Alba Mingorance Ferrer

Solution Processable Oxides for Inverted and Carbon-based Perovskite Solar Cells

DEFENDED BY:

Alba Mingorance Ferrer

THESIS DIRECTORS:

Dra. Mónica Lira-Cantú

Dr. Jordi Fraxedas Calduch

TUTOR:

Dr. Jordi García-Antón Aviñó

PROGRAMA DE DOCTORAT EN CIÈNCIA DE MATERIALS

UNIVERSITAT AUTÒNOMA DE BARCELONA

FACULTAT DE CIÈNCIES

A thesis submitted for the degree of

Doctor of Philosophy

September 2019

ICN2 Institut Català de Nanociència i Nanotecnologia

EXCELÈNCIA SEVERO OCHOA

CSIC

Institut Català de Nanociència i Nanotecnologia
Edifici ICN2 Campus de la UAB,
08193 Bellaterra, Barcelona

Universitat Autònoma de Barcelona
Departament de Química
08193 Bellaterra, Barcelona

Memòria presentada per aspirar al Grau de Doctor per Alba Mingorance Ferrer:

Alba Mingorance Ferrer

Dra. Mónica Lira-Cantú, responsable del grup Laboratory of Nanostrcutured Materials for Photovoltaic Energy, i el Dr. Jordi Fraxedas Calduch, responsable del grup ForceProbe Microscopy and Surface Nanoengineering, en el centre d'investigació Institut Català de Nanociència i Nanotecnologia (ICN2).

Certifiquen que el treball descrit en aquesta Tesis titulada: "Solution Processable Oxides for Inverted and Carbon-based Perovskite Solar Cells", presentada per Alba Mingorance Ferrer per optar al grau de Doctor, ha estat realitzada sota la seva direcció.

_____ _____

Dra. Mónica Lira-Cantú Dr. Jordi Fraxedas Calduch

Vist i plau del Tutor de la Tesis:

_____

Dr. Jordi García-Antón Aviñó

Bellaterra, September 2019

To my family.

“You’re the first, you’re the last, my everything.”

Contents

Abstract

This thesis is dedicated to the improvement of photovoltaic performance and stability of Perovskite Solar Cells (PSCs). Halide perovskites have recently emerged as promising harvester materials for photovoltaic devices, achieving record efficiencies over 25 %.However, theircurrent drawback is lifetime stability, which is the key factor that impedes the commercialization of the technology.

In this thesis work, the application of transition metal oxides (TMOs) have been developed as transport layers in PSC, as a result, we observed an improvement in the device stability. TMOs thin filmsshow excellent compatibility with halide perovskites due to their good transparency and excellent charge transfer properties. To achieve longer lifetimes in PSCs, the understanding of the degradation processes, mainly occuring at the oxide/perovskite interfaces, hasbeen deeply investigated. Thesehalide perovskite absorbers and semiconductor oxide layers have be applied to two PSC architectures: inverted PSC and C-based perovskite solar cell.The processable semiconductor oxide are also characterized by their low cost, can be fabricated as water-based solutions and are capable of being synthesized at low temperatures, thereby enabling the production of flexible substrates with printable possibilities at large scale fabrication. C-based PSCs are fully printable and provide an easy fabrication. We have also found that the use of NiO_x as a hole transport material (HTM) can improve the photovoltaic parameters of PSC devices. Finally, the functionalization of metal-oxide interlayers (TiO_2/ZrO_2) in C-based PSCs with the use of organic molecules, such as 5 aminovaleric acid iodide (5-AVAI), can increase the performance of this kind of solar cells.

This work addresses the technological issues stated above and proposes suitable concepts for the improvement in terms of efficiency and stability employing transition metal oxides (TMOs) in PSCs. We have used several

experimentaltechniques such as X-Ray Diffraction (XRD) and Photoelectron Spectroscopies (XPS-UPS) in order to better understand the degree of crystallinity and the electronic properties of the materials. Microscopy techniques, such as Scanning Electron Spectroscopy (SEM), Atomic Force Microscopy (AFM), Focused Ion Beam (FIB) were also employed to determine the morphology of the layers and to understand the degradation mechanisms that occur at the interface level with the final aim of enhancing the photovoltaic performance and stability of solar cell devices.

Abbreviations & Symbols

5-AVA	5-aminovaleric acid
AcAc	acetylacetonate
AFM	atomic force microscopy
APMS	3-Aminopropyltrimethoxysilane
AZO	aluminium-doped zinc oxide (Al:ZnO)
BHJ	bulk heterojunction
Bl-TiO_2	blocking layer TiO_2
CB	conduction band
CBM	conduction band minimum
CIGS	copper indium gallium selenide
CN-PPV	poly (p-phenylenevinylene)
CPSC	carbon-based Perovskite Solar Cell
c-TiO_2	compact TiO_2
CVD	chemical vapor deposition
DMF	dimethylformamide
DMSO	dimethyl sulfoxide
DSSC	dye sensitized solar cell
EDX	energy dispersive X-ray
Eg	band gap
Ef	Fermi energy level
ETL	electron transport layer
FA	formamidinium
FAI	formamidinium iodide
FAPI	formamidinium lead triiodide

FF	fill factor
FTO	fluorinated doped tin oxide
GBL	ɣ-butyrolactone
GO	graphene oxide
H3pp	3-phosphonopropionic acid
HCl	Chlorhydric acid
HTL	hole transport layer
HTM	hole transport material
HOMO	highest occupied molecular orbital
IP	Ionization Potential
IPA	isopropanol
IPCE	incident photon-to-current efficiency
ITO	indium-tin oxide
IV	current-voltage
J	current density
J_{sc}	short-circuit current density
LUMO	lowest unoccupied molecular orbital
MA	methylammonium
MAI	methylammonium iodide
MAPI	methylammonium lead iodide
MEEA	2-[2-(2-methoxyethoxy)ethoxy]acetic acid
MEH-PPV	poly(2-methoxy-5-(2-ethylhexyloxy)-1-4-phenylenevinylene)
MeOH	methanol
Mp-TiO_2	mesoporous TiO_2
Mp-ZrO_2	mesoporous ZrO_2

MPP	maximum power point
NMP	N-methyl-2-pyrrolidone
OPV	organic photovoltaic cell
OSC	organic solar cell
PA	4-pyridinecarboxylic acid
PABA	4-aminobenzoic acid
PVSK	perovskite
QDSC	quantum dot solar cell
P3HT	poly(3-hexylthiophene)
PBZT	poly(p-phenylenebenzobisthiazole)
$PC_{60}BM$	[6,6]-phenyl-C61-butyric acid methyl ester
$PC_{70}BM$	[6,6]-phenyl-C71-butyric acid methyl ester
PCE	power conversion efficiency
PEI	polyethylenimine
PES	photoelectron spectroscopy
PET	polyethylene terephthalate
PSC	perovskite solar cell
PEDOT:PSS	(poly(3,4-ethylenedioxythiophene) poly (styrenesulfonate))
P_{max}	maximum power density
PPV	poly(p-phenylenevinylene
rGO	reduced graphene oxide
R.H.	relative humidity
Rs	series resistance
Rsh	shunt resistance
RT	room temperature

R2R	roll-to-roll
SAM	self-assembled monolayer
SCO	secondary cut off
SEM	scanning electron microscopy
SF-PPV	poly[2-aloxy-5-alkanesulfonyl-1-4-phenylene vinylene]
Spiro-OMeTAD	2,2',7,7'-tetrakis(N,N-dimethoxyphenylamine)-9,9'-spirobifluorene
ssDSSC	solid state dye sensitized solar cell
TCO	transparent conductive oxide
TiAcAc	titanium diisopropoxide bis(acetylacetonate)
TMO	transition metal oxide
UPS	ultraviolet photoelectron spectroscopy
UV	ultraviolet
UV-Vis	ultraviolet visible
VB	valence band
VBM	valence band maximum
V_{oc}	open circuit voltage
WF	work function
XPS	x-ray photoelectron spectroscopy
XRD	x-ray diffraction
UPS	UV photoelectron spectroscopy
α	optical absorption coefficient
ε	extinction coefficient
η	efficiency
μ	mobility
λ	wavelength

σ	conductivity
ϕ/φ	work funtion

List of Figures

List of Tables

Chapter 1

Introduction

1.1 Energy

The ever increasing world population, which reached 7.6 billion people in 2017 and it is expected to reach 8.6 billion by 2030, has a direct strong effect on natural resources like water, food and energy. Thus, the demand of energy has become one of the most challenging matters that we have to face in the 21st century [1]. The current energy supply based on natural fossil fuels is no longer sustainable. In addition, environmental issues such as the greenhouse gas effect, one of the main responsible for the climate change, call for the urgent development of new technologies based on clean and sustainable energy sources. Renewable energy is intensively studied since it comes from inexhaustible natural resources such as sunlight, wind, rain, biomass or waves. **Figure 1.1** shows the estimated proportion of renewable energy sources in 2016, which supplies about 23.7 % of the total world energy demand [2].

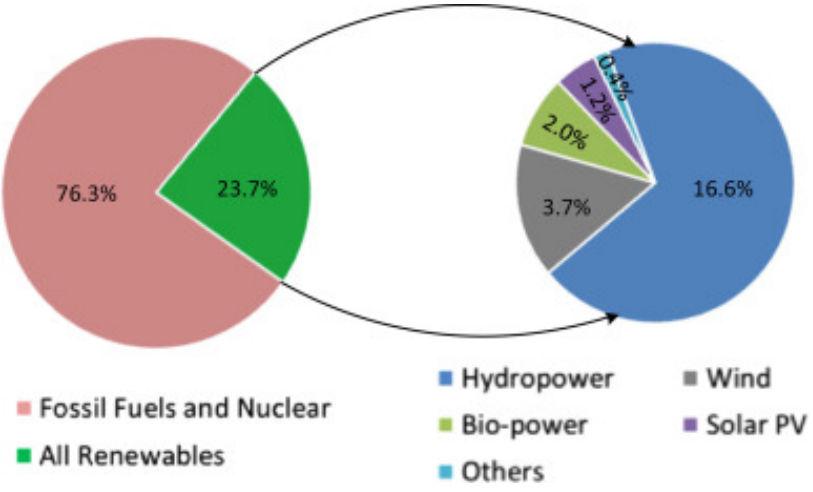

Figure 1.1 Estimated renewable energy sources of Global Energy for 2016. *Extracted from* [2].

As a conclusion of the United Nation Climate Change Conference held in Paris (COP21) in 2015, the world nations prepared and adopted The Paris Agreement which central aim is to reinforce the response of all nations to combat climate change. The governments should achieve the goal of keeping the global average temperatures

below the 2 degree Celsius (°C) increase. For instance, by 2020 EU aims to reach a reduction of 20 % of greenhouse gas emissions [3]. If stronger action is not implemented after 2030, the average temperature is expected to increase ~2.6 ˚C by the year 2100 [4].

One of the main sources of clean energy comes from the sun. Solar energy is sustainable, inexhaustible and CO_2-free. Solar light can be converted to generate electricity, heat (solar thermal energy) and chemical energy (solar fuels). The devices based on semiconductor materials that convert solar energy into electricity are termed as photovoltaics. The term photovoltaic comes from the Greek word *phos*, which means light, and *volt*, which refers to Alessandro Volta, the Italian physicist who invented the battery [5].

1.2 Solar cells

The photovoltaic effect was first discovered by the scientist Edmond Becquerel in 1839, who observed this effect in an electrolytic cell made of two platinum electrodes in an electrolyte solution. Becquerel used silver chloride dissolved in an acidic media. Then, the current of the cell was enhanced when his setup was irradiated with sunlight [6].

Photovoltaic solar technology can be classified into three generations, depending on the used materials and device architectures. The first generation of photovoltaics is based on silicon and was developed by scientists at Bell laboratories in the early 1950s, where the original solar cell had power conversion efficiency (PCE), [defined in next Chapter see **Eq 2.3**], of 6 % [7]. Since then, the cell efficiency has significantly improved. In April 2014, Panasonic's HIT-IBC solar cells based on n-type crystalline-Si wafers hold the world record with a conversion efficiency of 25.6 % [8].

This cell minimizes the optical, recombination and resistance loss which directly enhance the conversion efficiency. This first generation includes monocrystalline (c-Si) and polycrystalline silicon solar cells and the associated technology dominates the

current photovoltaic market [9]. However, alternative technologies have also been developed, called second generation solar cells, and known as thin films solar cells. In this category we can find amorphous silicon (a-Si) and semiconductor materials such as cadmium-telluride (CdTe) or copper indium gallium selenide (CIGS). In contrast to c-Si, these materials are simpler and less expensive to produce, applied in a solar cell they can achieve efficiencies as high as 22.9 % for CIGS and 21.0 % for CdTe [10]. Nevertheless, the toxicity and availability of several elements such as indium (In), tellurium (Te) and selenium (Se) limit their potential for large-scale application [11]. The third generation solar cells encompasses the most recent technologies, such as Organic Solar Cells (OSCs), Quantum Dot Solar Cells (QDSCs), Dye Sensitized Solar Cells (DSSCs), all-oxide solar cells and Halide Perovskite Solar Cells (PSCs). These are characterized by the possibility to be fabricated on light weight and flexible substrates applying low-cost and scalable solution processing techniques.

These 3rd generation solar cells will be described in the following section, giving special emphasis to PSCs during this entire thesis. **Figure 1.2** shows the evolution of the best achieved conversion efficiencies of all kinds of solar cells since 1976 by the corresponding research groups or companies.

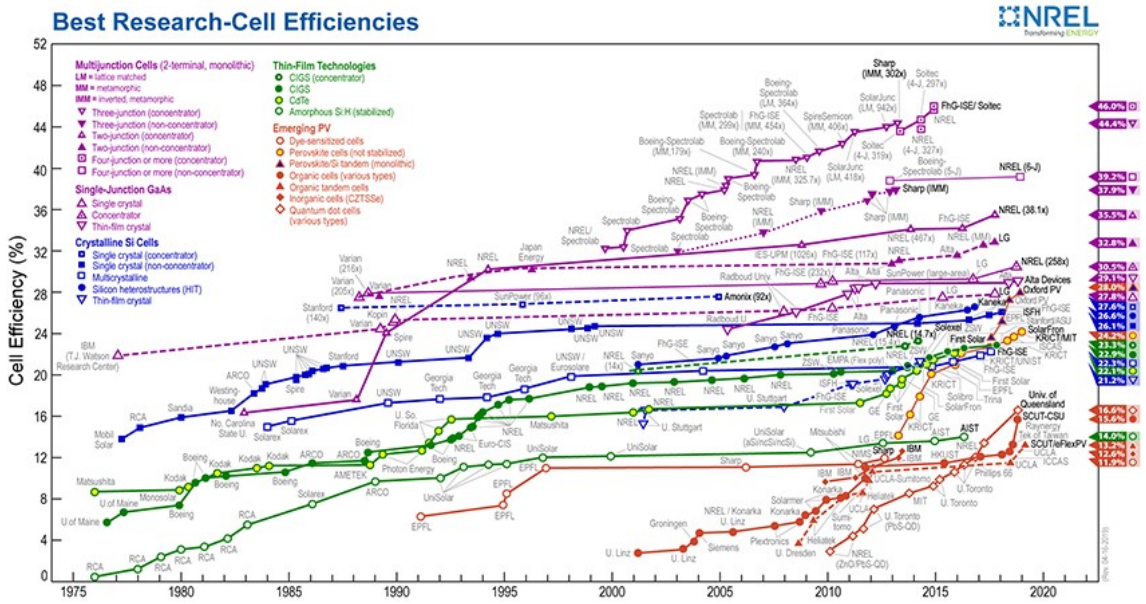

Figure 1.2 Reported timeline of the evolution of solar cell PCEs since 1976. *Extracted from*[12].

1.2.1 Organic Solar Cells (OSCs)

In 2000, the Nobel Prize in Chemistry was awarded to the scientists Alan Heeger, Alan MacDiarmid and Hideki Shirakawa for the discovery and development of organic conductive polymers [13]. Several years later, these polymers were employed as absorbers in OSCs. **Figure 1.3 (a)** shows the layered architecture of an OSC. The main layer, the active layer, which is in charge of the absorption of photons, is composed by the donor and acceptor materials (represented in blue and red colors, respectively). A transparent conductive electrode (TCO) is necessary in order to let the light pass through and reach the absorber material. The back electrode is usually a metal such as Ag, Au or Al (among others). Transporting layers such as hole transport layer (HTL) and electron transport layer (ETL) are included between the active layer and electrodes in order to enhance the charge transport.

An organic semiconductor polymer serves as an electron donor and another polymer, a fullerene compound, or small organic semiconductor molecule can serve as an electron acceptor. Both, the ETL and the HTL, are blended together to form what is called a bulk heterojunction. The most used organic donors include: poly(p-phenylenevinylene) (PPV), poly(2-methoxy-5-(2-ethylhexyloxy)-1-4-phenylenevinylene) (MEH-PPV), poly(p-phenylenebenzobisthiazole) (PBZT) and poly(3-hexylthiophene) (P3HT)[14]. Some examples of organic acceptors include: poly(p-phenylenevinylene) (CN-PPV), [6,6]-phenyl-C61-butyric acid methyl ester ($PC_{60}BM$) or poly[2-aloxy-5-alkanesulfonyl-1-4-phenylene vinylene] (SF-PPV). Most improvements have been found with materials such as fullerenes $PC_{60}BM$ and $PC_{70}BM$, which represents the state-of-the-art [15]. **Figure 1.3 (b)** shows the functional mechanism of an OSC. When light reaches the active layer, a photon excites an electron from the HOMO to the lowest unocopied molecular orbital (LUMO) in the donor material generating an exciton. The charged species diffuse through the donor material to the donor-acceptor interface. Finally, at this interface, the exciton dissociates and the electron moves to the LUMO of the acceptor and to the electrode while the hole migrates to the other electrode.

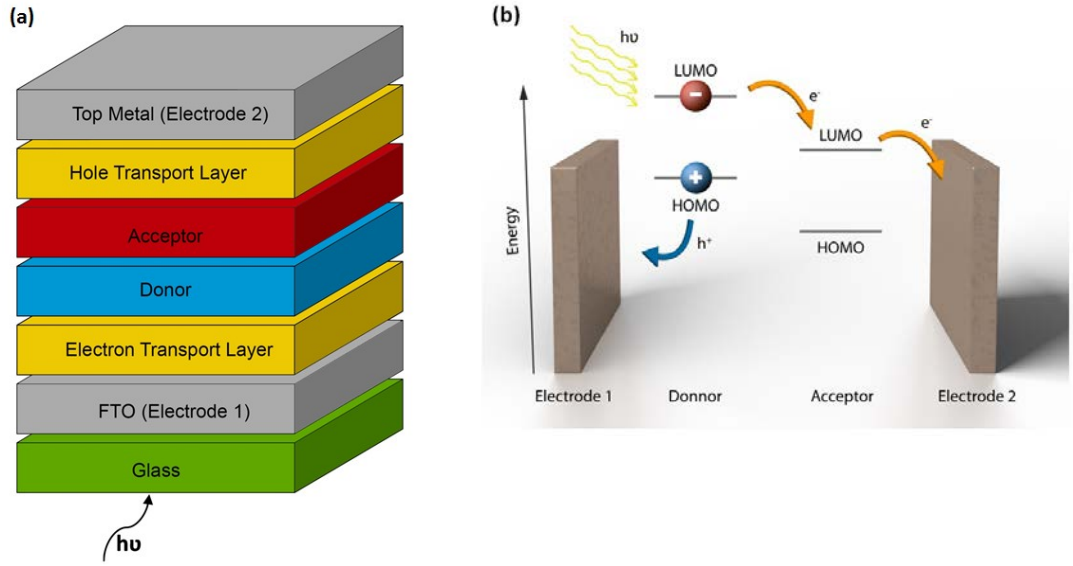

Figure 1.3 (a) Scheme of different layers of an OSC. *Adapted from* [16]**(b)** Functional mechanism of an OSC. *Adapted from*[17] .

The transport layers (in yellow color in **Figure 1.3 (a)**) play an important role in order to promote ohmic contact formation and minimize series resistance (Rs) and charge recombination [18]. From the PCE point of view, due to the used materials, an impressive 12 % was achieved in 2012 [19].The record efficiency reached by OSC is 15 % for single junction solar cell [20](~11 % certified [21]) and 17.3 % for a 2-terminal monolithic solution processed tandem OPV [22] (~12 % certified [21]).

The relatively simple fabrication and molecular versatility is one of the most attractive facts of the OSC technology. Different techniques such as simple roll-to-roll (R2R), spin coating, spraying and vaporization were applied for mass production of OSCs [19]. However, further work is needed in order to find organic molecules with good extinction coefficients for proper exciton dissociation process and also, an enhancement of their PCE and stability for commercialization requirements.

1.2.2 Quantum Dot Solar Cells (QDSCs)

QDSCs have attracted considerable interest in the last 20 years, due to their optoelectronic properties. Quantum dots have the potential to increase the PCE and even surpass the Shockley-Quiessler limit [23]. The tunability of Quantum Dots bandgap is possible through the control of the Quantum Dots size. This allows

obtaining a broad light absorption spectrum. Several semiconductors have been used in the QDSCs such as: PbS, CdS, CdSe, $CuInS_2$ and Ag_2S [24]. Surface engineering is one of the key issues of the QDSCs [25].

Baek and co-workers achieved a PCE of 11.7 % using a PbS based QDSCs which was able to retain over 90 % of its initial performance after 1 year of storage under ambient conditions [25]. QDSCs applying TMOs as transport layers have been studied by Gao and co-workers. In their work they used molybdenum oxide (MoO_x) and vanadium oxide (V_2O_x) as efficient HTLs in a ZnO/PbS QDSCs heterojunction exhibiting a certified 4.4 % PCE [26]. Currently, the record certified efficiency of QDSCs is 13.4 % based on $CsPbI_3$ QDs [27].

Despite of their advantages, one of the limitations in QDSCs is the fast electron-hole recombination because of the defect states at the surface which provides many recombination centres [28].

1.2.3 Dye-sensitized Solar Cells (DSSCs)

DSSCs are characterized by the application of a dye, responsible for light harvesting, absorbed on a mesoporous semiconducting oxide layer. The DSSC field received worldwide recognition after the appearance in a *Nature* publication by O'Regan and Grätzel, exhibiting an exceeding 7 % PCE [29]. The DSSC consisted in a I^-/I^-_3 redox couple in the electrolyte solution, a ruthenium coordination complex as light absorber and a mesoporous oxide electrode (TiO_2), as an ETL. The scheme of the DSSC working mechanism is shown in **Figure 1.4**.The photon is absorbed by the dye, and then the photo-excitation of the dye takes place, after that, the electron is injected into the conduction band of the mesoporous TiO_2 (mp-TiO_2), leaving the dye in the oxidized state. The injected electron flows to the back contact and then through the external load to the counter electrode. The dye molecule is regenerated by the redox system, such as iodide/triiodide couple, and the redox system, at the same time, is reduced at the counter electrode, by electrons passed through the load. The difference between the Fermi level of the solid and the redox potential of the electrolyte corresponds to the voltage generated under illumination [30].

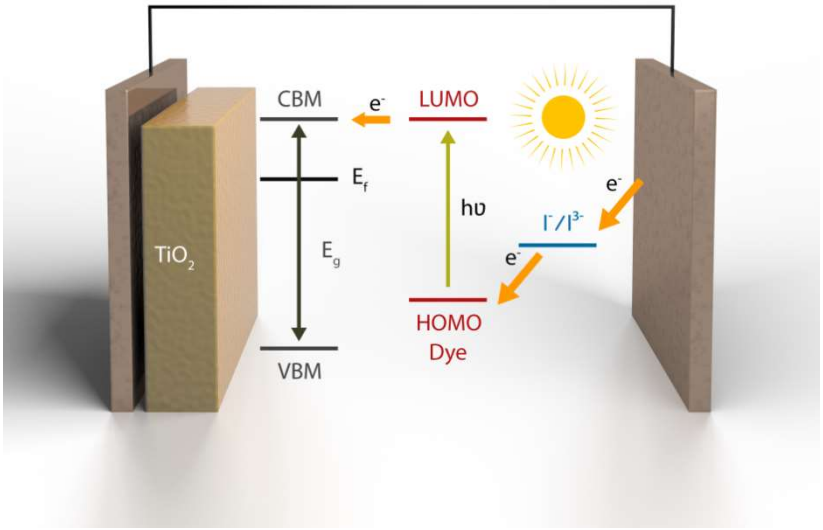

Figure 1.4 Scheme of the functional mechanism of a DSSC witha I^-/I^-_3 redox couple. *Adapted from* [31].

The PCE of the DSSCs depends on the different photovoltaic parameters. The open circuit voltage (V_{oc}), is determined by the difference of the electrons of the TiO_2 semiconductor in the Fermi-level and the energy level of redox potential in the electrolyte solution. The short circuit current (J_{sc}), which is the current through the solar cell when the voltage across the solar cell is zero, is affected by the light-harvesting capacity of the dye molecules.

The use of other dyes based on Co^{2+}/Co^{3+}, Fe^{2+}/Fe^{3+} and Cu^{+}/Cu^{2+} have also been investigated in order to enhance the working efficiency and reduce the voltage loss [32]. Despite the great achievements in DSSC, the concern about long-term stability is still a challenge. Many factors could induce to the degradation, such as the use of volatile solvents (acetonitrile), the dye desorption in electrolyte solution, the degradation of cobalt-based complexes [33], the electrode corrosion and the visible light absorption by I^-/I_3^-[32].

To eliminate leakage and solvent evaporation from the electrolyte, in 1998, Grätzel and co-workers developed the solid-state (ssDSSCs) by using 2,2',7,7'-tetrakis(N,N-dimetoxyphenylamine)-9,9'-spirobifluorene (Spiro-OMeTAD) [34]. However, this kind of technology revealed low PCE as compared to the liquid-based DSSCs. Hagen *et al.* were the first to report on a solid-state device based on a molecular semiconductor [35]. O'Regan *et al.* reported a system based on electrodeposited layers of ZnO with a

PCE of 1.5 % [36]. Currently, the highest PCE for a DSSCs is 14.3 % with a Co(II/III) tris(phenanthroline) based redox electrolyte [37] and for ss-DSSCs the record is 11 % PCE, using a solid HTL composed of a blend of $[Cu(tmby)_2]$ $(TFSI)_2$ and $[Cu(tmby)_2]$ (TFSI) [38].

1.2.4 Halide Perovskite Solar Cells (PSCs)

Organic-inorganic hybrid PSCs have become the most attractive emerging photovoltaic technology due to the high efficiency achieved in just a few years: certified records of 24.2 % [12]and 27.3% [39] for single junction PSCs and perovskite/silicon tandem solar cells have been reported, respectively.

Back in 2009 Miyasaka *et al.* reported a successful replacement of the dye in a liquid electrolyte DSSCs by a perovskite absorber, leading to an unexpected 3.8 % PCE [40]. In 2012, Park *et al.* reported a higher PCE of 9.7 % using perovskite nanocrystals as the light absorber, and a thick mp-TiO_2 film and spiro-MeOTAD as the ETL and HTL, respectively [41-42].

Since then, significant improvement in PCE has been observed in only a few years which are attributed to the enormous efforts in the optimization of the device architecture, the fabrication methods, the interface engineering, the replacement of the unstable materials that induce a fast degradation, the study of the solvents and the deeper understanding of the physicalproperties of the device. For instance, Saliba *et al.*, has recently reported a stabilized efficiency of 21.1 % achieved with a triple cation halide PSC using a mixture of cesium, methylammonium and formamidinium (Cs/MA/FA) [43]. Another example is given by Seok and co-workers who were able to reduce defects in materials and consequently reduce the energy loss in the device towards manufacturing high performance solar cells of 22.1 % [44].

In a PSC photovoltaic device, the light-to-electron conversion initiates with the light (or photon) adsorption by the halide perovskite, followed by the generation and transport of the generated charges and finally the collection of the charges by the electrodes. The study and the further understanding of the main operational processes in PSCs have become a key point to reveal the properties of the perovskite material and the

pursuit for optimal interfaces and electrodes in order to enhance the working device. **Figure 1.5** shows the working mechanism of PSCs.

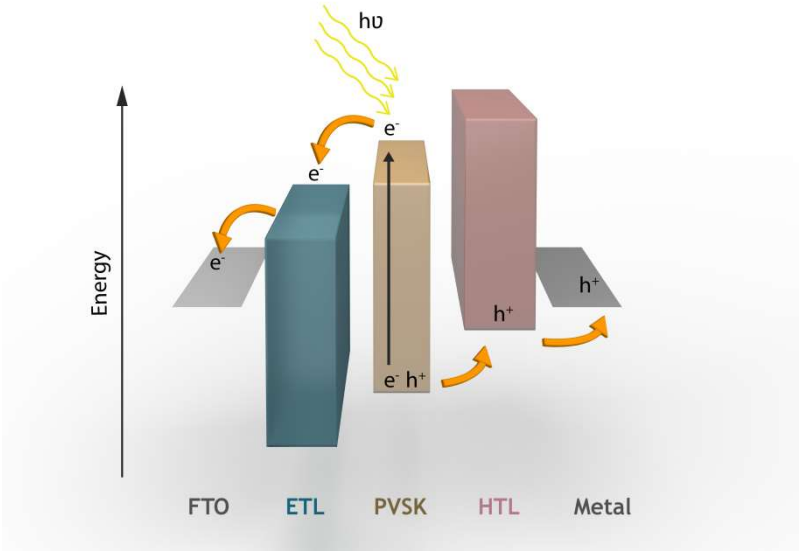

Figure 1.5 Schematic band diagram and working principle of PSCs. *Adapted from* [45]

The optical properties of the perovskites can be modified through the combination of monovalent cations (MA, FA) or halogen components (Cl^-, Br^-, I^-). The $MAPbI_3$ absorber has a direct bandgap of 1.6 eV while $MAPbBr_3$ has a larger bandgap of around 2.3 eV suitable for tandem solar cells applications [46]. $FAPbI_3$ shows a narrower bandgap of 1.5 eV, thus allowing theoretically larger currents when employed as an absorber [47]. The well-known $MAPbI_3$ perovskite presents an absorption onset of about 800 nm and large absorption coefficient in the visible range ($\approx 10^5 cm^{-1}$), thus it can guarantee an efficient light-harvesting by creating a high density of photoexcited charges [48]. Also, the hole mobility of the perovskite lies within 2-10 $cm^2\ V^{-1}\ s^{-1}$ and the range of the electron mobility is between 5-12 $cm^2\ V^{-1}\ s^{-1}$ [49]. **Figure 1.6** shows the band alignment for different compositions of perovskite such as $MAPbI_3$, $FAPbI_3$, $FAPbBr_3$ and $MAPbBr_3$ with different band gap (E_g) values and the different halide perovskites are sandwiched between the ETL and the HTL [50].

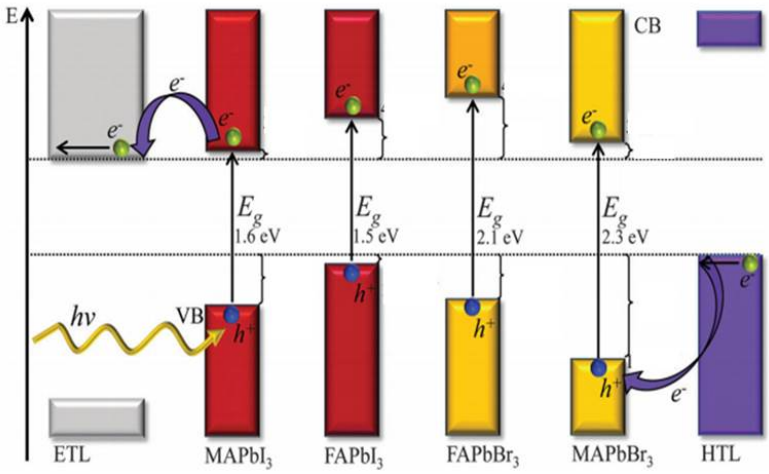

Figure 1.6 Schematic band matching for electron injection between perovskite, ETL and HTL for different perovskite absorbers. *Adapted from* [50].

The aim towards excellent photovoltaic performance is the passivation of the surfaces which can reduce radiative recombination and promote the acceleration of electron transfer at the interfaces. The application of metal oxides as transport layers has proved to be a successful strategy to avoid non-radiative recombinationin PSCs. For instance, Jung and co-workers employed an MgO coating layer for delaying charge recombination and consequently increasing the efficiency of the solar cell [51]. Palomares *et al.* applied an Al_2O_3 overlayer on nanocrystalline TiO_2 films, which hindered charge recombination [52].

Regarding the fabrication of the perovskite film, several preparation methods have been reported, such as the dual source evaporation [53], sequential (two-step) solution deposition [54] with an "anti-solvent" approach where the insoluble solvent causes a supersaturation inducing a rapid crystallization of the perovskite, one-step spin coating [55], vapour-assisted solution process [56] and screen printing process [57].

1.2.5 Device Architecture

Although there is a variety of possible device architectures and materials, the majority of photovoltaic energy conversions use semiconductor materials in the form of p-n junctions. Basically, a PSC can be divided in five different layers (**Figure 1.7**): two current collectors, two transport layers and the main absorber layer. The most important layer of the solar cell is the main absorber (active layer), made of the halide

perovskite. This layer is sandwiched between the two transport layers, which are characterized by their electron and hole transport (or blocking) properties and thus are known as HTL or ETL, respectively. These transport layers are employed to enhance the separation of charges and improve charge extraction reducing recombination. These three layers (ETL/halide perovskite/HTL) are at the same time sandwiched between the two current collectors (or top and bottom electrodes in **Figure 1.7**). The electrodes are responsible for the collection of charges obtained from the main absorber and transport layers, and are characterized by their high conductivity. At least one these top/bottom electrodes must be transparent (e.g. transparent conductive oxide (TCO), aluminium doped zinc oxide (AZO), etc.) so the light can arrive to the interior of the solar cell or the main absorber (active layer). The other current collector is usually made of a metallic electrode (Au, Ag, Cu, C, etc). The TCO is coated on an insulating substrate (e.g. glass, plastic, etc) as the bottom electrode. Due to their high transparency and low sheet resistance, the most used TCOs are ITO, FTO or AZO. Although the HTL and ETL can be made of organic or inorganic semiconductors, in this thesis work we limit these materials to semiconductor oxides. The most applied semiconductor oxides used as ETL are TiO_2, SnO_2 or ZnO, among others. For the HTL, the most applied oxides are bare or doped NiO, MoO_3, V_2O_5, among others.

The device configuration of perovskite based photovoltaics can be classified as either normal-type or inverted-type structures [58] and the configuration depends on the transport layer placed next to the TCO (bottom electrode). If an ETL is deposited next to the TCO, the solar cell has the normal configuration but if the layer next to the TCO is a HTL then we have the inverted configuration. **Figure 1.7** shows the different layers that form the normal **(a)** and the inverted **(b)** configuration PSC. In any of these two configurations, if the layers are made as dense thin films, the configuration is called “planar configuration”, but if any of the layers (especially the ETL) is made of mesoporous oxide nanostructures (nanoparticles), the PSC configuration is known as the “mesoporous configuration”.

The operational system widely accepted for both structures consists of a perovskite absorber layer, which absorbs light and generates electron-hole pairs. The electrons and holes diffuse and get separated through ETL and HTL and are finally collected by

the corresponding electrode, also described in Chapter 1 on the physics in solar cell [59].

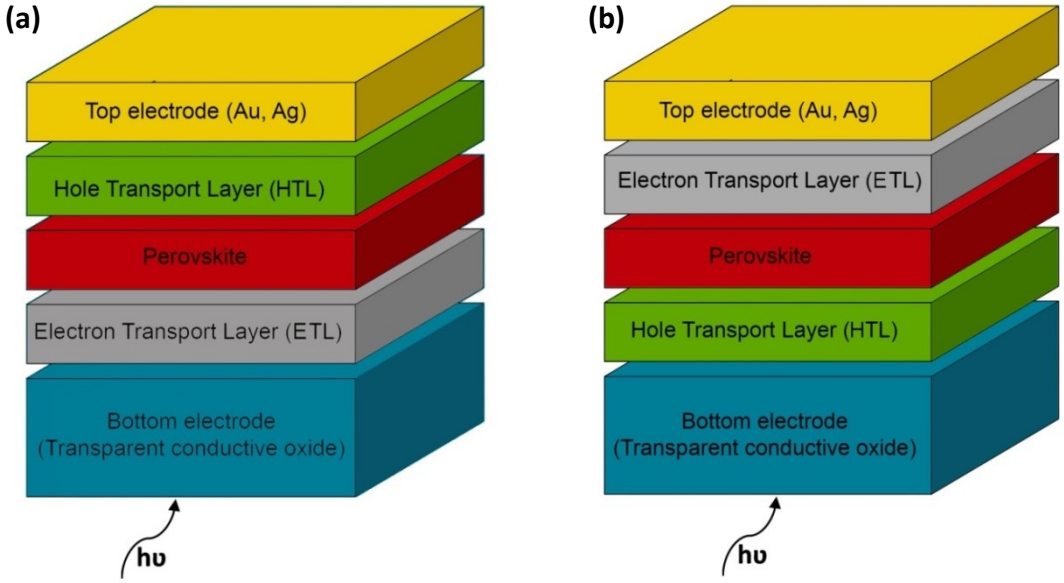

Figure 1.7 PSC stack in normal **(a)** and inverted **(b)** configurations. In both cases the configuration is planar.

The photovoltaic performance of a PSC is highly dependent on the quality of the perovskite crystals, the interface layer and the contacts. The most common device configuration is the normal mesoporous configuration composed of several layers: an FTO acting as the TCO; a blocking layer TiO_2 (bl-TiO_2)/mp-TiO_2) acting as the ETL; $CH_3NH_3PbI_3$ ($MAPbI_3$) as the main absorber layer; Spiro-OMeTAD acting as the HTL; and finally, a Ag or Au, acting as the top electrode. Previous studies have shown that the highest reported PCE presently exceeds 24 % [12] achieved with normal configuration shown in **Figure 1.7 (a)**.

The fabrication of the normal configuration PSC employs TiO_2 as an ETL, which needs high temperature sintering process for its fabrication. In the contrary, the inverted configuration can be fabricated via a low-temperature and solution-processing methods, which are compatible with large-scale fabrication, such as roll to roll (R2R), printing/coating process [23-24] allowing for the fabrication of these solar cells on flexible substrates.

The carbon-based configuration consisted in a mesoporous $TiO_2/ZrO_2/C$ configuration. This configuration led to an effective alternative as a low cost and abundant source in order to replace the cost effective back electrodes in usual PSCs, such as gold or silver. Also, the simple fabrication using printing methods made this configuration a promising configuration towards the future commercialization.

In this thesis we focus on the development of inverted (Chapter 4) and carbon-based PSCs (Chapter 5), the application of oxide interfaces, their efficiency improvement and device stability (Chapter 6).

1.3 Perovskite solar cells stability

Although PSCs is a very promising technology, main challenges prevent their development and commercialization. The two most important are related to the toxicity of heavy metals such as Pb and Sn, and the stability of complete devices and modules. In this section, the different parameters which directly affect the degradation process and some possible solutions to avoid the degradation paths are discussed.

We can separate the main stability issues in three categories (**Figure 1.8**): light, atmosphere, moisture and temperature, LAMT (a), extrinsic (b) and intrinsic (c) factors [62]. The LAMT factors are those that have been extensively studied by the research community and thus, many are the strategies already known and followed to overcome them. The intrinsic and extrinsic factors relates to issues observed in materials (chemical and physical properties) and devices respectively, as will be described in the following section.

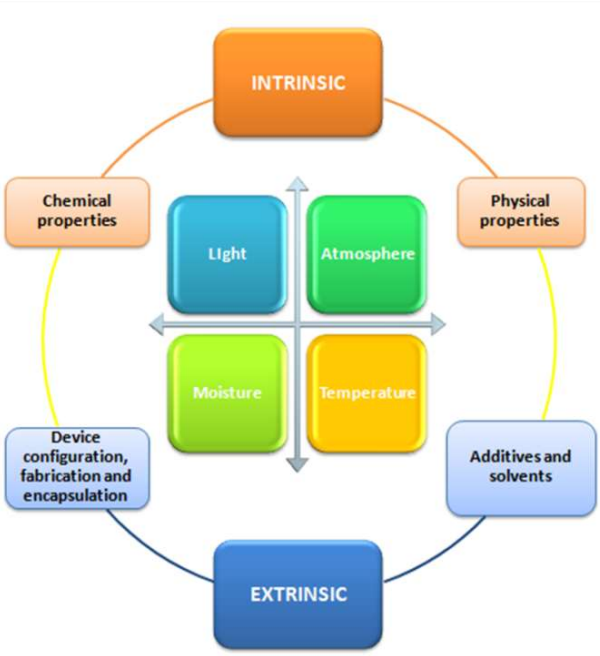

Figure 1.8 Different parameters which could affect the long-term stability of the PSCs: Light, Atmosphere, Moisture and Temperature (LAMT), extrinsic and intrinsic factors. *Adapted from* [63].

1.3.1 Light, atmosphere, moisture and temperature (LAMT)

Light is an important external factor to take into account for the PSCs lifetime. Snaith *et al.* studied the photoinduced instability of PSCs and they found that performance of the encapsulated device could degrade slower than for the unpacked device. For the outdoor measurements it is necessary to use a UV filter to improve the photostability [64]. Li *et al.* studied the light degradation of $CH_3NH_3PbI_3$ thin films, and they observed that after 480 min of irradiation the ratio of metallic Pb with respect to the total Pb amount was about 33 %. Their research exhibited an accelerated decomposition of perovskite films by light [65]. Also, Farooq and co-workers investigated the impact of a $CH_3NH_3PbI_3$ absorber exposed to different UV bands of the range between 310-317 nm. At 311 nm UV radiation directly decreases the J_{sc} of all PSCs samples after 500 h [66]. In this sense, Lee *et al.* investigated the effects of perovskite degradation under UV light. A set of PSCs were exposed to 365 nm of UV light for 1000 h and an important degradation was detected even in a glovebox conditions (absence of oxygen or moisture) [67].

The second factor is the atmosphere. Degradation with oxygen may cause superoxide species and the photo-oxidized $CH_3NH_3PbI_3$ decomposition into PbI_2. Crystalline

perovskite films show a superoxide formation and consequently low stability. One way to improve the stability is the passivation by iodide salts which reduce the superoxide formation [68]. In addition, Yang and co-workers also found that oxygen induces the transformation from $CH_3NH_3PbI_3$ to PbI_2, which could be due to absorbed oxygen at the grain boundaries [69].

The components in ambient conditions, such as moisture, H_2O and O_2, directly influence the chemical stability of PSCs, leading to a degradation of the perovskite layer with the colour changing from dark brown to yellow. Wang *et al.* reported the hydrolysis reaction when the perovskite material is under exposure to moisture. First, $CH_3NH_3PbI_3$ degrades into PbI_2 and CH_3NH_3I in presence of water, where methylammonium iodide (MAI) further decomposes into CH_3NH_2 (aq) and HI (aq). Simultaneously, HI (aq) with O_2 could produce H_2 (g) and I_2 (s), which can easily induce a faster degradation process for non-encapsulated devices [70]. Liu *et al.* reported the use of oxides such as Mn_3O_4, ZnO and TiO_2, obtained by a simple and scalable fabrication method to achieve better humidity tolerance [71]. Given the sensitivity of the perovskites to moisture, a controlled humidity environment is mandatory for perovskite preparation and film growth [72]. In addition, Snaith *et al.* reported perovskite thin films fabricated under controlled humidity conditions where the quality of films exhibited an improvement in photoluminescence, resulting in a reduction of trap density in the film [73].

The last LAMT factor which directly affects the stability of PSCs is temperature, which plays a crucial role in the degradation pathways. The crystal structure of the perovskite material is affected by temperature since $CH_3NH_3PbI_3$ has three different structural phases, a cubic phase (Pm-3m) above 56.8 °C, a tetragonal phase (I4/mcm) from -113.1 °C to 56.8 °C, and an orthorhombic phase (Pnma) below -113.1 °C[74]. The thermal stability of the methyl ammonium halide perovskite is already proved above 300 °C.

However, Rensmo *et al.* demonstrated by in situ analysis (under UHV environment) with PES that the degradation of $CH_3NH_3PbI_3$ can occur at low temperatures, closer to 100 °C, where the halide perovskite decomposes by sublimation into CH_3NH_2 and HI, resulting in the formation of the PbI_2 residue [75].

1.3.2 Extrinsic and intrinsic factors affecting device stability

The extrinsic factors are more related to device configuration, device fabrication and device encapsulation. In terms of device stability, the inverted planar architecture ofITO/PEDOT:PSS/VO_x/$MAPbI_{3-x}Br_x$/$PC_{60}BM$/Ag could maintain nearly 90 % of their initial PCE after 4000 h under storage under N_2 conditions [76]. An alternative solution to avoid degradation was found by Han and co-workers with the implementation of the hole-transport free PSCs with carbon stack configuration (HPSC), also called C-based PSCs (CPSC) [57]. The group developed a triple-layer perovskite junction: a layer of mp-TiO_2 which acts as an ETL, a mesoporous layer of insulating ZrO_2 (mp-ZrO_2) used as a scaffold and finally a porous carbon layer used as back electrode. The perovskite solution is infiltrated by drop-casting through the carbon layer which, thanks to its hydrophobic nature, prevents the degradation of the solar cell by moisture. Stability over 1000h has been demonstrated in ambient air for printable carbon-based hole-conductor-free mesoscopic PSCs without any encapsulation under continuous irradiation [77]. And very recently, Nazeeruddin *et al.* reported a remarkable long-term stability over 10,000 h by fully printable industrial-scale process [78]. This triple junction CPSC could be the closest architecture to commercialization. The reasons behind are in the elimination of expensive HTL and electrodes, such as spiro-MeOTAD and gold for instance. The record efficiency in carbon-based PSC was achieved by Zhang and co-workers. They inserted $SrCl_2$ as a precursor solution, in the perovskite crystal structure which lead to better pore filling and consequently better PSC performance of 15.9 % [79].

Device encapsulation is another important extrinsic factor to take into account in the degradation studies. For instance, Dong and co-workers used the UV-curable epoxy for the encapsulation and better results in terms of performance compared to thermally curable epoxy were achieved. Using UV-curable epoxy 90 % of their initial efficiency was maintained after 48 h of light soaking at 85 °C and 65 % R.H.

Intrinsic factors affecting the degradation process of PSC refer to the physical and chemical properties of materials in any part of device (absorber layer, interlayers or electrodes), as well at the interfaces (perovskite/transport layer or transport layer/electrode). For example, the partial substitution of the caesium cation for

$HC(NH_2)^{2+}$ in a $FAPbI_3$ perovskite has been proposed. The combination of different cations in the halide perovskite is a new strategy to enhance device efficiency and stability. Saliba *et al.* reported a mixture of a triple cation Cs/MA/FA, achieving a PCE of 21.1 % under operational conditions after 250 h. Adding Cs to MA/FA mixture provides better crystal growth and robustness to the device [43].

Another strategy is the use of additives to grow large-size grains of the halide perovskite. The resulting PSCs show an improvement in defect passivation and stability in comparison with PSCs with smaller grain-size. In addition, the application of TMOs and their functionalization can reduce the intrinsic degradation. TMOs are being employed as a replacement of organic semiconductors, such as spiro-MeOTAD. As will be described in detail in the following section, TMOs can be found as simple binary oxides or as doped oxides, as bilayers with another oxide layer, as complex oxide or functionalized with organic modifiers. For instance, Kim *et al.* applied a Cu-doped NiO_x as a HTL in the inverted architecture ITO/Cu:NiO/perovskite/PCBM/C_{60}-bis surfactant/Ag.

They exhibited a remarkably enhancement of the electrical conductivity and the perovskite film quality, resulting in the improvement of PCE up to 15.4 % [80]. In addition, Yao *et al.* studied the insertion of polyethylenimine (PEI) cations within the layers of 2D perovskite. An improvement of resistance to moisture and an enhancement in charge transport has been proved [81]. Wang *et al.* introduced a thin Al_2O_3 layer which protected $MAPbI_3$ from moisture and at the same time, reduced charge recombination [70]. In this sense, employing highly stable and water-resistant additives can guarantee an enhancement of the long-term stability of PSCs. Also the use of mixed-ion perovskite such as $MAPb(I_{1-x}Br_x)_3$ can improve stability due to the smaller size of Br anion [46].

This thesis work is based on two of the strategies mentioned above: (a) the application of TMOs as replacement of the transport and the scaffold layers in PSCs and (b) the application of organic modifiers which can functionalize the oxide and the halide perovskite surface. This is accomplished by the application of two different architectures for PSC: inverted structure PSCs and the Carbon-based PSCs respectively.

The aim of this work is the fabrication of devices which can stand long operational stability. The following sections will describe the reasons behind the selection of the materials and the PSC architecture applied in this thesis work.

1.4 Improving PSC stability through Transition Metal Oxides (TMOs)

The application of TMOs as transport layers in PSCs can guarantee low cost, versatility, large scale fabrication and the most important, the enhancement of the stability and moisture resistance. You *et al.* reported a solution-processed lead halide PSC with p-type NiO_x as HTL and n-type ZnO as ETL. This structure was ITO/NiO_x/perovskite/ZnO/Al, where ZnO isolates the perovskite layer from the Al electrode, preventing device degradation. After 60 days of storage in air at RT, the PCE still retained the 90 % of their initial PCE [82]. In this context, Najafi *et al.* also applied NiO as HTL and ZnO as ETL in flexible substrates where PSCs exhibited excellent stability, retaining more than 85 % of the initial efficiency after 1000 h soaking [83]. Zheng and co-workers used a CrO_x as an interfacial layer between the ETL and the electrode. After 20 days the cells with CrO_x exhibited much less degradation as compared to the cells without CrO_x. This metal oxide provides a favourable energy-band matching and a protection against water and oxygen [84]. Yoon *et al.* applied In_2O_3 by a solution process as an ETL in PSCs resulting in an enhancement of the photo-stability due to the wide E_g of the metal oxide, which leads to a 14.6 % PCE [85].
Also, Hongwei Han and co-workers applied the mesoporous double oxide layer of TiO_2/ZrO_2, which provides more than 1000 h in ambient air under full sunlight [86].

Figure 1.9 shows the efficiency response (performance loss) after stability analysis observed in PSCs applying oxides as transport layers. We can demonstrate that performance loss in the PSCs is reduced in six different scenarios: (1) After the replacement of organic semiconductors (e.g., poly (3,4-ethylenedioxythiophene) polystyrenesulfonate, PEDOT) by oxides as in (a) and (p). (2) with the application of doped oxides as in (f), (h), (n) and (q). (3) with the application of ternary or complex oxides as in (m). (4) after the replacement with double oxide layers as in (b), (c), (d), (j)

and (k). (5) with the application of oxides as both the ETL and the HTL as in (e), (r) and (s). (6) by the functionalization of the oxide interface with organic molecules as in (c), (g), (i), (o) or (t). In all cases, the application of metal oxide layers results in an enhanced stability of the PSCs.

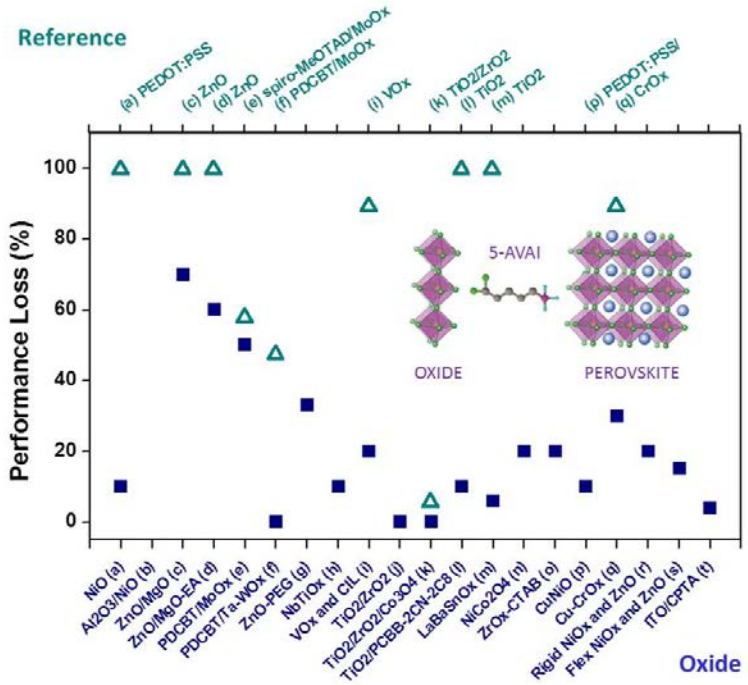

Figure 1.9 Performance loss (%) using metal oxides or interface engineering in stability analysis of PSCs. Different stability test were applied for each study.(a)ITO/NiO_x/perovskite/ZnO/Al and ITO/PEDOT:PSS/perovskite/PCBM/Al [87];(p) ITO/PEDOT:PSS/perovskite/PCBM/C_{60}/Ag and ITO/CuNiO/perovskite/PCBM/C_{60}/Ag)[88]. (f) ITO/C_{60}-SAM; (h) FTO/$NiMgLiO_x$/perovskite/PCBM/$NbTiO_x$/Ag [89], 1.8n with the configuration of ITO/$NiCo_2O_4$/perovskite/PC_{61}BM:C_{60}/ZrAcac/Ag [90], 1.8q with the configuration of FTO/ CrO_x/perovskite/PCBM/Ag and FTO/Cu-CrO_x/perovskite/PCBM/Ag [91].(Figure 1.8b with the configuration of FTO/TiO_2/mp-TiO_2/Al_2O_3/NiO/$MAPbI_{3-x}Cl_x$-NiO/Spiro-OMeTAD/Au [92], 1.8c using the configuration FTO/ZnO/perovskite/Spiro-OMeTAD/Au and FTO/ZnO/MgO/perovskite/Spiro-OMeTAD/Au [93], 1.8d with the architecture of FTO/ZnO/perovskite/Spiro-OMeTAD/Au and FTO/ZnO/MgO-EA/perovskite/Spiro-OMeTAD/Au [93], 1.8j employing the architecture of FTO/TiO_2/ZrO_2/carbon with infiltrated 2D:3D perovskite [78] and 1.8k using the configuration of FTO/TiO_2/ZrO_2/carbon and FTO/TiO_2/ZrO_2/Co_3O_4/carbon with infiltrated perovskite [94].(Figure 1.8e ITO/C_{60}-SAM/SnO_x/PC_{60}BM/perovskite/dopedSpiro-MeOTAD/MoO_x/Au and ITO/C_{60}-SAM/SnO_x/PC_{60}BM/perovskite/PDCBT/MoO_x/Au[95], 1.8r with rigid glass/ITO/NiO_x-np/perovskite/PCBM/ZnO-np/Al, 1.8s using flexible PEN/ITO/NiOx-np/perovskite /PCBM/ZnO-np/Al. *Extracted from* [96].

1.4.1 Transition metal oxides as hole transport layers (HTL)

Basically, the HTL materials are in charge of the extraction of holes from the absorber material (perovskite) to the electrode. An ideal HTL for PSCs has to fulfil the following requirements: (a) matching the CB and VB energy level with the absorber material, (b) high mobility, (c) low-temperature solution processablility, (d) suitable surface energy

and (e) chemical inertness [97]. TMOs semiconductors such as NiO_x, CuO_x, CrO_x, MoO_x, V_2O_5have been widely used as HTL.

NiO is a p-type semiconductor, where the valence band maximum (VBM) and the conduction band minimum (CBM) contain contributions from the Ni 3d states [98]. NiO is an excellent electron blocker due to the small electron affinity (2.1 eV). NiO is also an attractive functional gas-sensing material for application both in thermoelectric and chemiresistive gas sensors. NiO films can be formed by UVO treatment or oxygen plasma treatment of metallic nickel, or solution processed nickel containing precursors.

MoO_3 was firstly applied in organic light-emmiting diode (OLEDs) for the good efficiency as a hole injection material acting as a p-type semiconductor. The 4d band of molybdenum oxide is unoccupied and contributes to the conduction band of the oxide. MoO_3 became an attractive HTL for improving device performance and stability in OSCs [99]. MoO_3 can be synthesized at low temperatures and cost-effective processing methods [100]. Also, MoO_3 is more stable as compared to widely used organic PEDOT:PSS. Furthermore, MoO_3 is highly transparent and easy to process [101]. Several preparation methods can be applied such as: sputtering, thermal evaporation and solution processing [102]. Very important for environmental issues is that MoO_3 is a non-toxic material [103].

CuO has been widely investigated for practical applications such as high temperature superconductivity, magnetic storage, gas sensing, photoelectrochemical catalysis and photovoltaics. CuO is an intrinsic p-type semiconductor [104]. Cupric oxide present the advantage of being abundant, low-cost, easy to prepare and exhibits good matching with VBM levels of perovskite absorber layer in inverted PSCs [105].

V_2O_5 can be deposited by low temperature solution processing methods such as sol-gel precursors. The most widely used fabrication method is the application of sol-gel such as vanadium (V) oxytriisopropoxide (ViPr), however, this precursor exhibits high cost, high toxicity and high reactivity. In this thesis, a water-based solution processable V_2O_5 was used [106].

Al_2O_3 is an oxide usually used as an insulating layer in order to reduce the degradation rate of the perovskite. Wang *et al.* fabricated PSCs employing a bilayer of Al_2O_3/NiO to

avoid interface recombination and they achieved PCE of 10.1 %. Also, the PSCs without encapsulation exhibited stability over 270 days under ambient conditions [92].
Another example is $NiCo_2O_4$ which is a p-type semiconductor where Ni occupies octahedral sites and Co occupies both octahedral and tetrahedral sites [107]. It has been found in several applications such as oxygen reduction, Li-ion batteries and electrocatalysis [90]. For instance, Ouyang and co-workers inserted this ternary oxide as a HTL and reached a PCE of 18.2 % due to a better growth crystallization [90].

1.4.2 Transition metal oxides as electron transport layers (ETL)

In ETL, electrons are injected and transported through the electrode. Also, some requirements must be satisfied for a good ETL: (a) high transmittance inthe UV-Vis region, (b) band alignment matching with perovskite and (c) chemically inertness [108]. TMOs semiconductors such as TiO_2, ZnO, SnO_2, ZrO_2, In_2O_3 andNb_2O_5 have been widely used as ETL. TiO_2 is also an attractive candidate for many applications (paints, coatings, plastics, fibers, cosmetics, etc.). Fujishima and Honda firstly reported the possibility of use TiO_2 as a photoelectrode to decompose water [109]. TiO_2 can be deposited by magnetron sputtering, evaporation, sol-gel processing and chemical vapour deposition (CVD).

ZnO is currently used as ETL in PSCs. The ionization potential (IP) of ZnO is large enough to act as a good hole blocking layer. ZnO can be preparedwith sol-gel [110], solvothermal [111]or hydrothermal processes [112]. Another metal oxide used in PSCs is the well-known SnO_2. This metal oxide is suitable for various applications such as solar cells, catalytic support materials, transparent electrodes and solid state chemical sensors [113]. The interest of $SnO_2$is based on its high IP, its good thermal stability and good mechanical durability, excellent optical transparency, high mobility and easy preparation procedure at low temperatures. In addition, SnO_2 shows good band alignment with the perovskite [114].

WO_x is another attractive metal oxide which exhibits high chemical stability, high electron mobility, and excellent light transmittance [115]. WO_3 is highly stable, with the capability of survive in a harsh and corrosive strong acidic media. Also, this oxide

has a E_g in the range of 2.6-3.1eV depending on its crystal structure, which makes it very attractive for their optical and electronic properties and their application in the aerospace and aeronautic fields [116]. In order to prepare WO_x several synthesis methods can be applied: thermal evaporation, CVD and hydrothermal procedures [117].

Lanthanum doped-$BaSnO_3$ exhibits a high carrier mobility of 0.69 cm^2/Vs and its wide E_g of 4.0 eV makes this material promising as a transparent insulator oxide [118]. Shin *et al.* developed a new strategy to obtain $LaBaSnO_x$ below 300 ˚C and they achieved a champion PCE of 21.2 % [119].

ZnO/MgO is another example of bilayer semiconductor oxide. MgO is a semiconductor oxide with a E_g of 7.6 eV, also it can be used for gas sensors, superconductivity, solar cells, electronics and catalysis [120]. ZnO-MgO thin films can be fabricated by several techniques such as pulsed laser deposition, CVD or magnetron sputtering [120].

1.5 Defect passivation through the functionalization of oxide surfaces

Together with the application of oxides as transport layers, the functionalization of oxide surfaces by organic molecules (organic modifiers or organic additives) is a promising alternative to enhance the stability of PSCs. The main issue resides in the evaluation of PSCs under more realistic operational conditions like continuous light illumination or outdoor testing. Studies under such conditions are very scarce [118-119]. Reported stability studies made to PSCs showing no more than ~10 % performance loss after ≥ 1000 h stability analysis under continuous 1 sun AM 1.5G illumination are summarized in **Figure 1.10**.

The graph indicates that long operational stability can be achieved (i) in any of the three PSCs configurations: normal (green area), inverted (yellow area) and C-based (purple area); (ii) applying 3D, 3D/2D [78] and 2D [123] halide perovskites (HPs) structures containing Cs, Rb, MA and/or FA cations, as in $MAPbI_3$ [86-116], double cation MAFA [95] or CsFA [121-122] triple cation RbCsFA [126] or CsMAFA [124-125] and quadruple cation RbCsMAFA (this work) (iii) by replacing the unstable spiro-OMeTAD with novel organic hole transporting materials (HTMs) like EH44,BDPSO

[129], and PDCBT [95]; (iv) if metal oxides are applied as transporting layers in the form of doped [86-127], complex oxides [119] as oxide multilayers [75-128] or as metal oxide layers functionalized with organic molecules [127], polymers [92-123] or C_{60} derivatives; or (v) by the application of additives for the passivation of defects. In all these examples, a recipe to achieve these exceptional PV stabilities resides in the engineering and passivation of defects found in any material of the device, the absorber, the transport layers or the interfaces [93-129]. The normal configuration which shows a small performance lost is:1) ITO/SnO_2/PCBM:PMMA/CsMAFA/PMMA/Spiro-OMeTAD/Au[134]2) ITO/SnO_2/CsFAMABrI/EH44/MoO_x/Al [127], 3) ITO/C_{60}-SAM/FAMABrI/ PDCBT/Ta-WO_x/ Au [95], 4) FTO/c-TiO_2/mp-TiO_2/ CsFAMABrI/ CuSCN/ r-GO/Au[128], 5) FTO/La-$BaSnO_3$/$MAPbI_3$/NiO/FTO/glass [119], 6) FTO/c-TiO_2/mp-TiO_2:OM/CsFAMABrI/Spiro-OMeTAD/Au[96]. For inverted configuration 1)ITO/NiO/CsFABrI/LiF/PC60BM/SnO2/ZnSnO2/ITO/LiF/Ag [124], 2) FTO/PEDOT:PSS/BAMAI/PCBM/Al[123],3)FTO/NiMg(Li)O/$MAPbI_3$/PCBM/Ti(Nb)O_x/Ag [89], 4) ITO/BDPSO/$MAPbI_3$/C_{60}/BCP/Ag [129], 5) FTO/LiNiO/CsFAMAI/C_{60}/Al[135], and finally the carbon-based PSC: 1)FTO/c-TiO_2/mp-TiO_2/ZrO_2/$MAPbI_3$-5AVA/carbon[131],2)FTO/c-TiO_2/mp-TiO_2/ZrO_2/$(HOOC(CH_2)_4NH_3)_2PbI_4$/carbon[78], 3)PET/Gr/$TiO_2$/PCBM/$MAPbI_3$/ Spiro:OMETAD/CSCNT[136]. The reduction of defect density mitigates recombination and prolongs the lifetime of charges leading to efficient and stable PSCs.

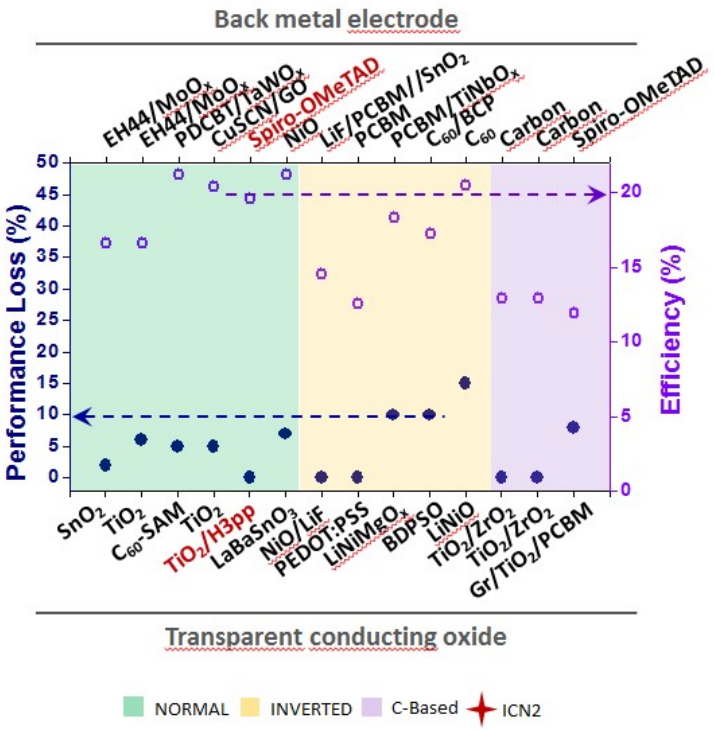

Figure 1.10 Operational PSCs stability studies reported in the literature with less than 10% performance loss after analysis of more than 1000h under continuous 1 sun illumination [96].

In all these cases, engineering and passivation of defects has been the key component to enhance device stability. The reduction of defect density mitigates recombination and prolongs charge carrier lifetimes leading to efficient and stable PSCs. Defects can be found in the oxide or perovskite materials in the bulk or interfacial layer and are the responsible for detrimental processes in the PSCs such as charge recombination or ion migration, among others. Defects can also facilitate oxygen migration through the perovskite material, which could accelerate the degradation processes in operational devices [137].

Several studies about the functionalization of the interfaces have been reported in order to passivate the defects and consequently enhance PSCs device performance by the use of SAMs, also called organic modifiers. Different functional groups, such as silanes, phosphonates, carboxylates, catechols, alkynes, alkenes and amines, can be applied for interfacial modification. Silanes and carboxylates are the mostly studied ones due to the environment-friendliness of carboxylic acid and the high reactivity of silanes [138]. Han *et al.* inserted an organic silane SAM between TiO_2 and $CH_3NH_3PbI_3$

in hole-conductor free PSCs based on carbon. Optimized interface band alignment and enhancement of the charge lifetime were achieved. As a result, a PCE of 12.7 % was obtained. Also, it was proved that the silane SAM helps to reduce the charge recombination through defects [139]. Wang *et al.* reported the study of a SAM with a carboxylic acid group that was added to the inverted perovskite architecture of FTO/NiO_x/SAM/$MAPbI_3$/PCBM/bis-C_{60}/Ag. The selected SAM was 4-bromobenzoic acid and the PCE showed a value exceeding 18 % [140]. De Marco and co-workers introduced Guanidinium additive in order to passivate the defects thorough the suppression of iodide vacancies. Eventually, the V_{oc} was improved and better efficiencies exceeding 17 % were obtained [141]. These different SAMs applications in PSCs will be discussed more in detail in Chapter 5 and Annex. Another passivation approach is the use of 3D-2D perovskites. Grancini *et al.* used the 2D-3D perovskite blend and a solar cell of 11.2 % efficiency with a long-term stability for more than 10,000 h were obtained [78].

Taking all the information described above on the effect of TMOs and their surface functionalization to enhance PSC efficiency and stabilityinto account, in this thesis we have focused on (a) the fabrication of inverted PSCs applying metal oxides as transport layers and (b) the application of the C-based PSC configuration fabricated by screen printing, where two different TMOs are applied as mesoscopic films and organic modifiers passivate defects at interfaces.

1.6 Objectives of the thesis

1.6.1 General objective

The main objective of this work is the development of synthesis and processing methods for the fabrication of halide PSCs with high efficiency and stability applying TMOs as transport layers.

TMOs have been selected due to the high thermal and moisture resistance that confer to PSCs. These were synthesized by sol-gel methods and used as transport and as scaffold layers in PSCs. When possible, the TMOs were obtained by low temperature synthesis methods.

Organic modifiers have been selected in order to functionalize oxide (and halide perovskite) surfaces in order to passivate defects. The latter should decrease charge recombination and reduce device degradation. As a result highly efficient PSCs are obtained.

PSCs with two different configurations have been chosen: (a) inverted PSC fabricated by spin coating, and (b) C-based PSCs fabricated by screen printing. These two configurations have been selected due to their characteristic enhanced efficiency and stability.

1.6.2 Specific objectives

1.6.2.1 Synthesis of solution processing TMOs

Synthesis of solution processing HTL and ETL made from TMOs, including NiO, ZnO, TiO_2, MoO_3, CuO and V_2O_5. Their syntheses are low cost atlow-temperature with the possibility to carry out under water or alcohol solvents.

1.6.2.2 Characterization of TMOs thin films

Another specific objective is the study of TMOs thin films properties such as optical, electronic, morphological, and crystallographic properties to further understand the functionalities of these oxides applied in the PSCs.These studies were carried out usingdifferent techniques such as X-Ray and Ultraviolet Photoelectron Spectroscopy (XPS-UPS) to understand the electronic properties of the material and XRD to better

understand the crystallinity properties of the TMOs. Also, Ultraviolet-visible spectroscopy was employed to determine the transparency and E_g of the TMOs.

1.6.2.3 Surface functionalization and characterization

Another specific objective is the application of surface functionalization through the application of organic molecules in order to reduce charge recombination and enhance the crystallization of the perovskite. The organic molecules were selected and introduced during the fabrication process of the PSCsand further characterized in order to know the interaction between them and the perovskite material inside the photovoltaic device. In-depth study of the interaction between the organic molecules and the selected surface was made through the fabrication of SAMs on oxides. The characterization was then carried out with AFM, Kelvin probe, XPS/UPS and microscopy analysis.

1.6.2.4 Fabrication of Perovskite Solar Cells

Fabrication of complete PSCs devices, employing TMOs in inverted configuration PSC and in hole transport-free carbon based PSC, was carried out by low-cost techniques such as spin coating or screen printing. Additionally, thescreen printing technique permits the fabrication of PSCs on almost any substrate and at large scale.

1.6.2.5 Complete solar cell characterization

Finally, the complete PSCs under investigation were measured by a sun simulator setup under ambient air conditions. Microscopy techniques such as Scanning Electron Microscopy (SEM), AFM and Focused Ion Beam (FIB) were employed to determine the morphology of the layers.

1.6.2.6 Stability analysis of complete PSCs

In order to control the degradation process of the complete PSCs studies of lifetime following the ISOS-protocols were carried out, in the dark or under continuous illuminationin ambient conditions.

1.7 Scope of the work

The different TMOs and PSCs are presented in different chapters. At the beginning of each of these chapters have a short introduction and a literature review of the reported solar cells. Then, it follows a description of the results and finally the conclusions and references.

This thesis is organized in the following way:

Chapter 1: A complete introduction is presented in this chapter which provides a brief overview of photovoltaic technologies and the requirements to use renewable energy sources such as solar energy.

Chapter 2: Describes the experimental methodologies and characterization instruments employed in this research and their application in PSCs.

Chapter 3: The optical, electronic and crystallographic properties of TMOs are discussed in this chapter. A characterization study between different temperatures and their properties is presented. Techniques such as, XRD, Ellipsometry, UV-Vis and XPS/UPS are used.

Chapter 4: Is focused on the study and optimization in terms of photovoltaic response of inverted PSCs using TMOs as transport layers and SAMs for the interface engineering experiments.

Chapter 5: The results of the optimization of C-based PSCsin terms of photovoltaic response using TMOs as HTL and ETL are presented. In this chapter, two different infiltration methods are described (one step and two step) also the results of the insertion of SAMs in PSCsis exhibited.

Chapter 6: The stability results regarding the lifetime of C-based PCSs are exhibited. Two ISOS protocols are employed such as, ISOS-D and ISOS-L.

Annex: preliminary results on the electronic study of SAMsand their surface funtionalization are presented.

And finally, at the end of this thesis work, the main conclusions are discussed.

1.8 References

[1] UN, “United Nations. World population prospects. The 2017 Revision,” 2017.

[2] A. Hussain, S. M. Arif, and M. Aslam, “Emerging renewable and sustainable energy technologies: State of the art,” *Renew. Sustain. Energy Rev.*, vol. 71, pp. 12–28, 2017.

[3] “Paris Agreement, 21st conference of the parties, European Comission 2015.”

[4] “International Energy Agency (IEA). Energy and climate change.,” 2015.

[5] K. Jäger, “Solar Energy. Fundamentals, technology and systems,” 2014.

[6] D. Lincot, “The new paradigm of photovoltaics: From powering satellites to powering humanity,” *Comptes Rendus Phys.*, vol. 18, no. 7, pp. 381–390, 2017.

[7] C. S. F. D. M. Chapin G. L. Pearson, “A New Silicon p-n Junction Photocell for Converting Solar Radiation into Electrical Power,” *J. Appl. Phys.*, vol. 25, no. 5, pp. 676–677, 1954.

[8] C. Yu, S. Xu, J. Yao, and S. Han, “Recent Advances in and New Perspectives on Crystalline Silicon Solar Cells with Carrier-Selective Passivation Contacts,” *Crystals* , vol. 8, no. 11. 2018.

[9] Y. Lee, C. Park, N. Balaji, Y.-J. Lee, and V. A. Dao, “High-efficiency Silicon Solar Cells: A Review,” *Isr. J. Chem.*, vol. 55, no. 10, pp. 1050–1063, 2015.

[10] M. A. Green, Y. Hishikawa, E. D. Dunlop, D. H. Levi, J. Hohl-Ebinger, and A. W. Y. Ho-Baillie, “Solar cell efficiency tables (version 51),” *Prog. Photovoltaics Res. Appl.*, vol. 26, no. 1, pp. 3–12, 2018.

[11] J. M. Ball, M. M. Lee, A. Hey, and H. J. Snaith, “Low-temperature processed meso-superstructured to thin-film perovskite solar cells,” *Energy Environ. Sci.*, vol. 6, no. 6, pp. 1739–1743, 2013.

[12] F. Alta and E. S. Asu, “NREL Efficiency Chart,” *Www.Nrel.Gov*, p. 2020, 2019.

[13] “Nobel Prize in Chemistry,” 2000.

[14] Y.-L. L. Michael L. Chabinyc, “Semiconducting polymers for thin-films electronics,” *J. Macromol. Sci. Part C Polym. Rev.*, 2006.

[15] F. C. Krebs, “Fabrication and processing of polymer solar cells: A review of printing and coating techniques,” *Sol. Energy Mater. Sol. Cells*, vol. 93, no. 4, pp. 394–412, 2009.

[16] P. P. Kumavat, P. Sonar, and D. S. Dalal, “An overview on basics of organic and dye sensitized solar cells, their mechanism and recent improvements,” *Renew. Sustain. Energy Rev.*, vol. 78, pp. 1262–1287, 2017.

[17] H. Zeng, X. Zhu, Y. Liang, and X. Guo, “Interfacial Layer Engineering for

Performance Enhancement in Polymer Solar Cells," *Polymers* , vol. 7, no. 2. 2015.

[18] R. Po, C. Carbonera, A. Bernardi, and N. Camaioni, "The role of buffer layers in polymer solar cells," *Energy Environ. Sci.*, vol. 4, no. 2, pp. 285–310, 2011.

[19] E. R. Rwenyagila, "A Review of Organic Photovoltaic Energy Source and Its Technological Designs," *Int. J. Photoenergy*, vol. 2017, p. 12, 2017.

[20] X. Che, Y. Li, Y. Qu, and S. R. Forrest, "High fabrication yield organic tandem photovoltaics combining vacuum- and solution-processed subcells with 15% efficiency," *Nat. Energy*, vol. 3, no. 5, pp. 422–427, 2018.

[21] M. A. Green, Y. Hishikawa, E. D. Dunlop, D. H. Levi, J. Hohl-Ebinger, and A. W. Y. Ho-Baillie, "Solar cell efficiency tables (version 52)," *Prog. Photovoltaics Res. Appl.*, vol. 26, no. 1, pp. 3–12, 2018.

[22] L. Meng *et al.*, "Organic and solution-processed tandem solar cells with 17.3% efficiency," *Science (80-.).*, vol. 361, no. 6407, pp. 1094–1098, 2018.

[23] O. E. Semonin, J. M. Luther, and M. C. Beard, "Quantum dots for next-generation photovoltaics," *Mater. Today*, vol. 15, no. 11, pp. 508–515, 2012.

[24] M. R. Kim and D. Ma, "Quantum-Dot-Based Solar Cells: Recent Advances, Strategies, and Challenges," *J. Phys. Chem. Lett.*, vol. 6, no. 1, pp. 85–99, Jan. 2015.

[25] S.-W. Baek *et al.*, "A hydro/oxo-phobic top hole-selective layer for efficient and stable colloidal quantum dot solar cells," *Energy Environ. Sci.*, vol. 11, no. 8, pp. 2078–2084, 2018.

[26] J. Gao *et al.*, "n-Type Transition Metal Oxide as a Hole Extraction Layer in PbS Quantum Dot Solar Cells," *Nano Lett.*, vol. 11, no. 8, pp. 3263–3266, 2011.

[27] E. M. Sanehira *et al.*, "Enhanced mobility $CsPbI_3$ quantum dot arrays for record-efficiency, high-voltage photovoltaic cells," *Sci. Adv.*, vol. 3, no. 10, 2017.

[28] Z. Ahmad, M. A. Najeeb, R. A. Shakoor, S. A. Al-Muhtaseb, and F. Touati, "Limits and possible solutions in quantum dot organic solar cells," *Renew. Sustain. Energy Rev.*, vol. 82, pp. 1551–1564, 2018.

[29] B. O'Regan and M. Grätzel, "A low-cost, high-efficiency solar cell based on dye-sensitized colloidal TiO2 films," *Nature*, vol. 353, pp. 737–740, 1991.

[30] M. Grätzel, "Dye-sensitized solar cells," *J. Photochem. Photobiol. C Photochem. Rev.*, vol. 4, no. 2, pp. 145–153, 2003.

[31] B. Tripathi, P. Yadav, and M. Kumar, "Theoretical upper limit of short-circuit current density of TiO2 nanorod based dye-sensitized solar cell," *Results Phys.*, vol. 3, pp. 182–186, 2013.

[32] M. Wang *et al.*, "An organic redox electrolyte to rival triiodide/iodide in dye-

sensitized solar cells," *Nat. Chem.*, vol. 2, p. 385, 2010.

[33] H. Ellis, V. Leandri, A. Hagfeldt, G. Boschloo, J. Bergquist, and D. Shevchenko, "Laser desorption/ionization mass spectrometry of dye-sensitized solar cells: identification of the dye-electrolyte interaction," *J. Mass Spectrom.*, vol. 50, no. 5, pp. 734–739, 2015.

[34] U. Bach *et al.*, "Solid-state dye-sensitized mesoporous TiO2 solar cells with high photon-to-electron conversion efficiencies," *Nature*, vol. 395, pp. 583–585, 1998.

[35] J. Hagen *et al.*, "Novel hybrid solar cells consisting of inorganic nanoparticles and an organic hole transport material," *Synth. Met.*, vol. 89, no. 3, pp. 215–220, 1997.

[36] B. O'Regan, D. T. Schwartz, S. M. Zakeeruddin, and M. Grätzel, "Electrodeposited Nanocomposite n–p Heterojunctions for Solid-State Dye-Sensitized Photovoltaics," *Adv. Mater.*, vol. 12, no. 17, pp. 1263–1267, Sep. 2000.

[37] K. Kakiage, Y. Aoyama, T. Yano, K. Oya, J. Fujisawa, and M. Hanaya, "Highly-efficient dye-sensitized solar cells with collaborative sensitization by silyl-anchor and carboxy-anchor dyes," *Chem. Commun.*, vol. 51, no. 88, pp. 15894–15897, 2015.

[38] Y. Cao *et al.*, "11% efficiency solid-state dye-sensitized solar cells with copper(II/I) hole transport materials," *Nat. Commun.*, vol. 8, p. 15390, 2017.

[39] www.oxfordpv.com/news/oxford-pv-setsworld-record-perovskite-solar-cell, "No Title."

[40] A. Kojima, K. Teshima, Y. Shirai, and T. Miyasaka, "Organometal Halide Perovskites as Visible-Light Sensitizers for Photovoltaic Cells," *J. Am. Chem. Soc.*, vol. 131, no. 17, pp. 6050–6051, 2009.

[41] H.-S. Kim *et al.*, "Lead Iodide Perovskite Sensitized All-Solid-State Submicron Thin Film Mesoscopic Solar Cell with Efficiency Exceeding 9%," *Sci. Rep.*, vol. 2, p. 591, 2012.

[42] M. M. Lee, J. Teuscher, T. Miyasaka, T. N. Murakami, and H. J. Snaith, "Efficient Hybrid Solar Cells Based on Meso-Superstructured Organometal Halide Perovskites," *Science (80-.).*, vol. 338, no. 6107, pp. 643–647, 2012.

[43] M. Saliba *et al.*, "Cesium-containing triple cation perovskite solar cells: improved stability, reproducibility and high efficiency," *Energy Environ. Sci.*, vol. 9, no. 6, pp. 1989–1997, 2016.

[44] W. S. Yang *et al.*, "Iodide management in formamidinium-lead-halide–based perovskite layers for efficient solar cells," *Science (80-.).*, vol. 356, no. 6345, pp. 1376–1379, 2017.

[45] N. Marinova, S. Valero, and J. L. Delgado, "Organic and perovskite solar cells:

Working principles, materials and interfaces," *J. Colloid Interface Sci.*, vol. 488, pp. 373–389, 2017.

[46] J. H. Noh, S. H. Im, J. H. Heo, T. N. Mandal, and S. Il Seok, "Chemical Management for Colorful, Efficient, and Stable Inorganic–Organic Hybrid Nanostructured Solar Cells," *Nano Lett.*, vol. 13, no. 4, pp. 1764–1769, 2013.

[47] G. E. Eperon, S. D. Stranks, C. Menelaou, M. B. Johnston, L. M. Herz, and H. J. Snaith, "Formamidinium lead trihalide: a broadly tunable perovskite for efficient planar heterojunction solar cells," *Energy Environ. Sci.*, vol. 7, no. 3, pp. 982–988, 2014.

[48] S. De Wolf *et al.*, "Organometallic Halide Perovskites: Sharp Optical Absorption Edge and Its Relation to Photovoltaic Performance," *J. Phys. Chem. Lett.*, vol. 5, no. 6, pp. 1035–1039, 2014.

[49] C. Motta, F. El-Mellouhi, and S. Sanvito, "Charge carrier mobility in hybrid halide perovskites," *Sci. Rep.*, vol. 5, p. 12746, 2015.

[50] T. Jesper Jacobsson *et al.*, "Exploration of the compositional space for mixed lead halogen perovskites for high efficiency solar cells," *Energy Environ. Sci.*, vol. 9, no. 5, pp. 1706–1724, 2016.

[51] T. S. Sherkar *et al.*, "Recombination in Perovskite Solar Cells: Significance of Grain Boundaries, Interface Traps, and Defect Ions," *ACS Energy Lett.*, vol. 2, no. 5, pp. 1214–1222, 2017.

[52] E. Palomares, J. N. Clifford, S. A. Haque, T. Lutz, and J. R. Durrant, "Slow charge recombination in dye-sensitised solar cells (DSSC) using Al2O3 coated nanoporous TiO2 films," *Chem. Commun.*, no. 14, pp. 1464–1465, 2002.

[53] M. Liu, M. B. Johnston, and H. J. Snaith, "Efficient planar heterojunction perovskite solar cells by vapour deposition," *Nature*, vol. 501, p. 395, 2013.

[54] J. Burschka *et al.*, "Sequential deposition as a route to high-performance perovskite-sensitized solar cells," *Nature*, vol. 499, pp. 316–319, 2013.

[55] N. J. Jeon, J. H. Noh, Y. C. Kim, W. S. Yang, S. Ryu, and S. Il Seok, "Solvent engineering for high-performance inorganic–organic hybrid perovskite solar cells," *Nat. Mater.*, vol. 13, p. 897, 2014.

[56] Q. Chen *et al.*, "Planar Heterojunction Perovskite Solar Cells via Vapor-Assisted Solution Process," *J. Am. Chem. Soc.*, vol. 136, no. 2, pp. 622–625, 2014.

[57] Z. Ku, Y. Rong, M. Xu, T. Liu, and H. Han, "Full Printable Processed Mesoscopic CH3NH3PbI3/TiO2 Heterojunction Solar Cells with Carbon Counter Electrode," *Sci. Rep.*, vol. 3, p. 3132, 2013.

[58] H. Zhou *et al.*, "Interface engineering of highly efficient perovskite solar cells," *Science (80-.).*, vol. 345, no. 6196, pp. 542–546, 2014.

[59] M. I. Asghar, J. Zhang, H. Wang, and P. D. Lund, "Device stability of perovskite

solar cells – A review," *Renew. Sustain. Energy Rev.*, vol. 77, pp. 131–146, 2017.

[60] Y. Galagan, "Perovskite Solar Cells: Toward Industrial-Scale Methods," *J. Phys. Chem. Lett.*, vol. 9, no. 15, pp. 4326–4335, 2018.

[61] Q. Hu, H. Wu, J. Sun, D. Yan, Y. Gao, and J. Yang, "Large-area perovskite nanowire arrays fabricated by large-scale roll-to-roll micro-gravure printing and doctor blading," *Nanoscale*, vol. 8, no. 9, pp. 5350–5357, 2016.

[62] M. Lira-Cantu, "The future of semiconductor oxides in next-generation solar cells," *Met. Oxides Ser.*, 2018.

[63] Y. Reyna, A. Pérez-Tomás, A. Mingorance, and M. Lira-Cantú, "Stability of Molecular Devices: Halide Perovskite Solar Cells BT - Molecular Devices for Solar Energy Conversion and Storage," H. Tian, G. Boschloo, and A. Hagfeldt, Eds. Singapore: Springer Singapore, 2018, pp. 477–531.

[64] T. Leijtens, G. E. Eperon, S. Pathak, A. Abate, M. M. Lee, and H. J. Snaith, "Overcoming ultraviolet light instability of sensitized TiO2 with meso-superstructured organometal tri-halide perovskite solar cells," *Nat. Commun.*, vol. 4, p. 2885, 2013.

[65] Y. Li *et al.*, "Light-Induced Degradation of CH3NH3PbI3 Hybrid Perovskite Thin Film," *J. Phys. Chem. C*, vol. 121, no. 7, pp. 3904–3910, 2017.

[66] A. Farooq *et al.*, "Spectral Dependence of Degradation under Ultraviolet Light in Perovskite Solar Cells," *ACS Appl. Mater. Interfaces*, vol. 10, no. 26, pp. 21985–21990, 2018.

[67] S.-W. Lee *et al.*, "UV Degradation and Recovery of Perovskite Solar Cells," *Sci. Rep.*, vol. 6, p. 38150, 2016.

[68] N. Aristidou *et al.*, "Fast oxygen diffusion and iodide defects mediate oxygen-induced degradation of perovskite solar cells," *Nat. Commun.*, vol. 8, p. 15218, 2017.

[69] J. Yang *et al.*, "Oxygen- and Water-Induced Energetics Degradation in Organometal Halide Perovskites," *ACS Appl. Mater. Interfaces*, vol. 10, no. 18, pp. 16225–16230, 2018.

[70] G. Niu, W. Li, F. Meng, L. Wang, H. Dong, and Y. Qiu, "Study on the stability of CH3NH3PbI3 films and the effect of post-modification by aluminum oxide in all-solid-state hybrid solar cells," *J. Mater. Chem. A*, vol. 2, no. 3, pp. 705–710, 2014.

[71] G. Liu, W. S. Y. Wong, N. Nasiri, and A. Tricoli, "Ultraporous superhydrophobic gas-permeable nano-layers by scalable solvent-free one-step self-assembly," *Nanoscale*, vol. 8, no. 11, pp. 6085–6093, 2016.

[72] T. Leijtens *et al.*, "Hydrophobic Organic Hole Transporters for Improved Moisture Resistance in Metal Halide Perovskite Solar Cells," *ACS Appl. Mater.*

Interfaces, vol. 8, no. 9, pp. 5981–5989, 2016.

[73] G. E. Eperon *et al.*, "The Importance of Moisture in Hybrid Lead Halide Perovskite Thin Film Fabrication," *ACS Nano*, vol. 9, no. 9, pp. 9380–9393, 2015.

[74] P. S. Whitfield *et al.*, "Structures, Phase Transitions and Tricritical Behavior of the Hybrid Perovskite Methyl Ammonium Lead Iodide," *Sci. Rep.*, vol. 6, p. 35685, 2016.

[75] B. Philippe *et al.*, "Chemical and Electronic Structure Characterization of Lead Halide Perovskites and Stability Behavior under Different Exposures—A Photoelectron Spectroscopy Investigation," *Chem. Mater.*, vol. 27, no. 5, pp. 1720–1731, 2015.

[76] H. Back *et al.*, "Achieving long-term stable perovskite solar cells via ion neutralization," *Energy Environ. Sci.*, vol. 9, no. 4, pp. 1258–1263, 2016.

[77] M. Duan, Y. Hu, A. Mei, Y. Rong, and H. Han, "Printable carbon-based hole-conductor-free mesoscopic perovskite solar cells: From lab to market," *Mater. Today Energy*, vol. 7, pp. 221–231, 2018.

[78] G. Grancini *et al.*, "One-Year stable perovskite solar cells by 2D/3D interface engineering," *Nat. Commun.*, vol. 8, p. 15684, 2017.

[79] H. Zhang *et al.*, "SrCl2 Derived Perovskite Facilitating a High Efficiency of 16% in Hole-Conductor-Free Fully Printable Mesoscopic Perovskite Solar Cells," *Adv. Mater.*, vol. 29, no. 15, p. 1606608, 2017.

[80] J. H. Kim *et al.*, "High-Performance and Environmentally Stable Planar Heterojunction Perovskite Solar Cells Based on a Solution-Processed Copper-Doped Nickel Oxide Hole-Transporting Layer," *Adv. Mater.*, vol. 27, no. 4, pp. 695–701, 2015.

[81] K. Yao, X. Wang, Y. Xu, F. Li, and L. Zhou, "Multilayered Perovskite Materials Based on Polymeric-Ammonium Cations for Stable Large-Area Solar Cell," *Chem. Mater.*, vol. 28, no. 9, pp. 3131–3138, 2016.

[82] J. You *et al.*, "Improved air stability of perovskite solar cells via solution-processed metal oxide transport layers," *Nat. Nanotechnol.*, vol. 11, p. 75, 2015.

[83] M. Najafi *et al.*, "Highly Efficient and Stable Flexible Perovskite Solar Cells with Metal Oxides Nanoparticle Charge Extraction Layers," *Small*, vol. 14, no. 12, p. 1702775, 2018.

[84] S. Zheng *et al.*, "Metal Oxide CrOx as a Promising Bilayer Electron Transport Material for Enhancing the Performance Stability of Planar Perovskite Solar Cells," *Sol. RRL*, vol. 2, no. 6, p. 1700245, 2018.

[85] S. Yoon *et al.*, "Solution-processed indium oxide electron transporting layers for high-performance and photo-stable perovskite and organic solar cells," *Nanoscale*, vol. 9, no. 42, pp. 16305–16312, 2017.

[86] A. Mei *et al.*, "A hole-conductor–free, fully printable mesoscopic perovskite solar cell with high stability," *Science (80-.).*, vol. 345, no. 6194, pp. 295–298, 2014.

[87] J. You *et al.*, "Improved air stability of perovskite solar cells via solution-processed metal oxide transport layers," *Nat. Nanotechnol.*, vol. 11, p. 75, 2015.

[88] W. S. Yang *et al.*, "High-performance photovoltaic perovskite layers fabricated through intramolecular exchange," *Science (80-.).*, vol. 348, no. 6240, pp. 1234–1237, 2015.

[89] W. Chen *et al.*, "Efficient and stable large-area perovskite solar cells with inorganic charge extraction layers," *Science (80-.).*, vol. 350, no. 6263, pp. 944–948, 2015.

[90] D. Ouyang *et al.*, "Strategic Synthesis of Ultrasmall NiCo2O4 NPs as Hole Transport Layer for Highly Efficient Perovskite Solar Cells," *Adv. Energy Mater.*, vol. 8, no. 16, p. 1702722, 2018.

[91] P.-L. Qin *et al.*, "Copper-Doped Chromium Oxide Hole-Transporting Layer for Perovskite Solar Cells: Interface Engineering and Performance Improvement," *Adv. Mater. Interfaces*, vol. 3, no. 14, p. 1500799, 2016.

[92] Y. Wang, T. Mahmoudi, H.-Y. Yang, K. S. Bhat, J.-Y. Yoo, and Y.-B. Hahn, "Fully-ambient-processed mesoscopic semitransparent perovskite solar cells by islands-structure-MAPbI3-xClx-NiO composite and Al2O3/NiO interface engineering," *Nano Energy*, vol. 49, pp. 59–66, 2018.

[93] J. Cao *et al.*, "Efficient, Hysteresis-Free, and Stable Perovskite Solar Cells with ZnO as Electron-Transport Layer: Effect of Surface Passivation," *Adv. Mater.*, vol. 30, no. 11, p. 1705596, 2018.

[94] A. Bashir *et al.*, "Spinel Co3O4 nanomaterials for efficient and stable large area carbon-based printed perovskite solar cells," *Nanoscale*, vol. 10, no. 5, pp. 2341–2350, 2018.

[95] Y. Hou *et al.*, "A generic interface to reduce the efficiency-stability-cost gap of perovskite solar cells," *Science (80-.).*, vol. 358, no. 6367, pp. 1192–1197, 2017.

[96] Haibing Xie et al., "No Title," *Submitted*, 2018.

[97] P. Qin, Q. He, D. Ouyang, G. Fang, W. C. H. Choy, and G. Li, "Transition metal oxides as hole-transporting materials in organic semiconductor and hybrid perovskite based solar cells," *Sci. China Chem.*, vol. 60, no. 4, pp. 472–489, 2017.

[98] E. L. Ratcliff *et al.*, "Evidence for near-Surface NiOOH Species in Solution-Processed NiOx Selective Interlayer Materials: Impact on Energetics and the Performance of Polymer Bulk Heterojunction Photovoltaics," *Chem. Mater.*, vol. 23, no. 22, pp. 4988–5000, 2011.

[99] N. K. Elumalai, A. Saha, C. Vijila, R. Jose, Z. Jie, and S. Ramakrishna, "Enhancing

the stability of polymer solar cells by improving the conductivity of the nanostructured MoO3 hole-transport layer," *Phys. Chem. Chem. Phys.*, vol. 15, no. 18, pp. 6831–6841, 2013.

[100] X. Li, F. Xie, S. Zhang, J. Hou, and W. C. H. Choy, "MoOx and V2Ox as hole and electron transport layers through functionalized intercalation in normal and inverted organic optoelectronic devices," *Light Sci. &Amp; Appl.*, vol. 4, p. e273, 2015.

[101] K. E. Lee, L. Liu, and T. L. Kelly, "Effect of Molybdenum Oxide Electronic Structure on Organic Photovoltaic Device Performance: An X-ray Absorption Spectroscopy Study," *J. Phys. Chem. C*, vol. 118, no. 48, pp. 27735–27741, 2014.

[102] X. Li, W. C. H. Choy, F. Xie, S. Zhang, and J. Hou, "Room-temperature solution-processed molybdenum oxide as a hole transport layer with Ag nanoparticles for highly efficient inverted organic solar cells," *J. Mater. Chem. A*, vol. 1, no. 22, pp. 6614–6621, 2013.

[103] F. Cheng, Y. Wu, Y. Shen, X. Cai, and L. Li, "Enhancing the performance and stability of organic solar cells using solution processed MoO3 as hole transport layer," *RSC Adv.*, vol. 7, no. 60, pp. 37952–37958, 2017.

[104] D. Wu, Q. Zhang, and M. Tao, "LSDA+ U study of cupric oxide: Electronic structure and native point defects," *Phys. Rev. B*, vol. 73, no. 23, p. 235206, 2006.

[105] W.-F. F. Zhi-Kai Yu Wen-Qing Liu, Zhong-Qiang Zhang, Yu-Jing Liu, Jie-Lin Yan, Tao Ye, and H.-Y. L. Wei-Tao Yang Hong-Zheng Chen, "Solution processed CuOx as an efficient hole-extraction layer for inverted planar heterojunction perovskite solar cells," *Chinese Chem. Lett.*, vol. 28, pp. 13–18, 2017.

[106] G. Terán-Escobar, J. Pampel, J. M. Caicedo, and M. Lira-Cantú, "Low-temperature, solution-processed, layered V2O5 hydrate as the hole-transport layer for stable organic solar cells," *Energy Environ. Sci.*, vol. 6, no. 10, pp. 3088–3098, 2013.

[107] R. Alcántara, M. Jaraba, P. Lavela, and J. L. Tirado, "NiCo2O4 Spinel: First Report on a Transition Metal Oxide for the Negative Electrode of Sodium-Ion Batteries," *Chem. Mater.*, vol. 14, no. 7, pp. 2847–2848, 2002.

[108] K. Mahmood, S. Sarwar, and M. T. Mehran, "Current status of electron transport layers in perovskite solar cells: materials and properties," *RSC Adv.*, vol. 7, no. 28, pp. 17044–17062, 2017.

[109] A. Fujishima and K. Honda, "Electrochemical Photolysis of Water at a Semiconductor Electrode," *Nature*, vol. 238, p. 37, 1972.

[110] L. Qian *et al.*, "Hybrid polymer-CdSe solar cells with a ZnO nanoparticle buffer layer for improved efficiency and lifetime," *J. Mater. Chem.*, vol. 21, no. 11, pp. 3814–3817, 2011.

[111] J. Zhang, Sun, Yin, Su, Liao, and Yan, “Control of ZnO Morphology via a Simple Solution Route,” *Chem. Mater.*, vol. 14, no. 10, pp. 4172–4177, 2002.

[112] C. Pacholski, A. Kornowski, and H. Weller, “Self-Assembly of ZnO: From Nanodots to Nanorods,” *Angew. Chemie Int. Ed.*, vol. 41, no. 7, pp. 1188–1191, 2002.

[113] M. Aziz, S. Saber Abbas, and W. R. Wan Baharom, “Size-controlled synthesis of SnO2 nanoparticles by sol–gel method,” *Mater. Lett.*, vol. 91, pp. 31–34, 2013.

[114] L. Xiong *et al.*, “Review on the Application of SnO2 in Perovskite Solar Cells,” *Adv. Funct. Mater.*, vol. 28, no. 35, p. 1802757, 2018.

[115] K. Wang *et al.*, “Low-Temperature and Solution-Processed Amorphous WOX as Electron-Selective Layer for Perovskite Solar Cells,” *J. Phys. Chem. Lett.*, vol. 6, no. 5, pp. 755–759, 2015.

[116] K. Mahmood, B. S. Swain, A. R. Kirmani, and A. Amassian, “Highly efficient perovskite solar cells based on a nanostructured WO3–TiO2 core–shell electron transporting material,” *J. Mater. Chem. A*, vol. 3, no. 17, pp. 9051–9057, 2015.

[117] N. Mukherjee, M. Paulose, O. K. Varghese, G. K. Mor, and C. A. Grimes, “Fabrication of nanoporous tungsten oxide by galvanostatic anodization,” *J. Mater. Res.*, vol. 18, no. 10, pp. 2296–2299, 2003.

[118] K. K. James, P. S. Krishnaprasad, K. Hasna, and M. K. Jayaraj, “Structural and optical properties of La-doped BaSnO3 thin films grown by PLD,” *J. Phys. Chem. Solids*, vol. 76, pp. 64–69, 2015.

[119] S. S. Shin *et al.*, “Colloidally prepared La-doped $BaSnO_3$ electrodes for efficient, photostable perovskite solar cells,” *Science (80-.).*, vol. 356, no. 6334, pp. 167–171, 2017.

[120] Ö. E. Ayşe Kaya Balta Nail Eker, İbrahim Okur, “MgO and ZnO composite thin films using the spin coating method on microscope glasses,” *Mater. Sci. Appl.*, vol. 6, pp. 40–47, 2015.

[121] L. K. Ono, Y. Qi, and S. Liu, “Progress toward Stable Lead Halide Perovskite Solar Cells,” *Joule*, vol. 2, no. 10, pp. 1961–1990, 2018.

[122] P. Gao, A. R. Bin Mohd Yusoff, and M. K. Nazeeruddin, “Dimensionality engineering of hybrid halide perovskite light absorbers,” *Nat. Commun.*, vol. 9, no. 1, p. 5028, 2018.

[123] H. Tsai *et al.*, “High-efficiency two-dimensional Ruddlesden–Popper perovskite solar cells,” *Nature*, vol. 536, p. 312, 2016.

[124] K. A. Bush *et al.*, “23.6%-efficient monolithic perovskite/silicon tandem solar cells with improved stability,” *Nat. Energy*, vol. 2, p. 17009, 2017.

[125] D. Bi *et al.*, “Multifunctional molecular modulators for perovskite solar cells with over 20% efficiency and high operational stability,” *Nat. Commun.*, vol. 9, no. 1,

p. 4482, 2018.

[126] S.-H. Turren-Cruz, A. Hagfeldt, and M. Saliba, “Methylammonium-free, high-performance, and stable perovskite solar cells on a planar architecture,” *Science (80-.).*, vol. 362, no. 6413, pp. 449–453, 2018.

[127] J. A. Christians *et al.*, “Tailored interfaces of unencapsulated perovskite solar cells for >1,000 hour operational stability,” *Nat. Energy*, vol. 3, no. 1, pp. 68–74, 2018.

[128] N. Arora *et al.*, “Perovskite solar cells with CuSCN hole extraction layers yield stabilized efficiencies greater than 20%,” *Science (80-.).*, vol. 358, no. 6364, pp. 768–771, 2017.

[129] R. Shang *et al.*, “Disodium Benzodipyrrole Sulfonate as Neutral Hole-Transporting Materials for Perovskite Solar Cells,” *J. Am. Chem. Soc.*, vol. 140, no. 15, pp. 5018–5022, 2018.

[130] Y. Hou *et al.*, “A generic interface to reduce the efficiency-stability-cost gap of perovskite solar cells,” *Science (80-.).*, 2017.

[131] X. Li *et al.*, “Outdoor Performance and Stability under Elevated Temperatures and Long-Term Light Soaking of Triple-Layer Mesoporous Perovskite Photovoltaics,” *Energy Technol.*, vol. 3, no. 6, pp. 551–555, 2015.

[132] A. Mingorance *et al.*, “Interfacial Engineering of Metal Oxides for Highly Stable Halide Perovskite Solar Cells,” *Adv. Mater. Interfaces*, vol. 5, p. 1800367, 2018.

[133] M. Lira-Cantú, “Perovskite solar cells: Stability lies at interfaces,” *Nat. Energy*, vol. 2, p. 17115, 2017.

[134] S.-H. Turren-Cruz, A. Hagfeldt, and M. Saliba, “Methylammonium-free, high-performance and stable perovskite solar cells on a planar architecture,” *Science (80-.).*, p. eaat3583, 2018.

[135] H. Tsai *et al.*, “Light-induced lattice expansion leads to high-efficiency perovskite solar cells,” *Science (80-.).*, vol. 360, no. 6384, pp. 67–70, 2018.

[136] Q. Luo *et al.*, “All-Carbon-Electrode-Based Endurable Flexible Perovskite Solar Cells,” *Adv. Funct. Mater.*, vol. 28, no. 11, p. 1706777, Mar. 2018.

[137] B. Li, V. Ferguson, S. R. P. Silva, and W. Zhang, “Defect Engineering toward Highly Efficient and Stable Perovskite Solar Cells,” *Adv. Mater. Interfaces*, vol. 5, p. 1800326, 2018.

[138] S. P. Pujari, L. Scheres, A. T. M. Marcelis, and H. Zuilhof, “Covalent Surface Modification of Oxide Surfaces,” *Angew. Chemie Int. Ed.*, vol. 53, no. 25, pp. 6322–6356, 2014.

[139] L. Liu *et al.*, “Fully Printable Mesoscopic Perovskite Solar Cells with Organic Silane Self-Assembled Monolayer,” *J. Am. Chem. Soc.*, vol. 137, no. 5, pp. 1790–1793, 2015.

[140] Q. Wang *et al.*, “Effects of Self-Assembled Monolayer Modification of Nickel Oxide Nanoparticles Layer on the Performance and Application of Inverted Perovskite Solar Cells,” *ChemSusChem*, vol. 10, no. 19, pp. 3794–3803, 2017.

[141] N. De Marco *et al.*, “Guanidinium: A Route to Enhanced Carrier Lifetime and Open-Circuit Voltage in Hybrid Perovskite Solar Cells,” *Nano Lett.*, vol. 16, no. 2, pp. 1009–1016, 2016.

Chapter 2

Methodology and Materials

The understanding of the properties of the material, thin films and devices used in this present work requires systematic characterization and optimization. In this chapter, the different materials employed, as well as the synthesis and fabrication processes developed, including a brief description of the used equipment for characterization, are described.

2.1 Materials

This section summarizes the different materials used in this thesis both commercially available or prepared and synthesized in our laboratory.

2.1.1 Commercial materials

All chemicals and reactants are commercially available and used as-received without further purification.

2.1.1.1 Chemical reactants

- Oxide precursors: titanium isopropoxide [$Ti(OiPr)_4$] (97%, Sigma Aldrich); zinc acetate dihydrate $Zn(OAc)_2.2H_2O$ (99.99 %, Sigma Aldrich); potassium hydroxide KOH (85%, Sigma Aldrich); nickel acetatetetrahydrate$Ni(CH_3COO)_2.4H_2O$ (98%, Sigma Aldrich); copper (II) acetatemonohydrate $Cu(CO_2CH_3)_2.H_2O$ (98 %, Sigma Aldrich); sodium metavanadate $NaVO_3$ (99.9 %, Sigma Aldrich), Titanium diisopropoxide bis(acetylacetonate) (TiAcAc) (75 %, Sigma Aldrich).
- Etching reagents: Zn powder (Fluka Analytical); hydrochloric acid HCl (37 %, Panreac).
- Perovskite precursors: lead iodide PbI_2 (99 %, TCI); MAI CH_3NH_3I (98 %, Dyesol).

- Polymers: poly(3-hexylthiophene-2,5-diyl) P3HT (98 %, Merck); [6,6]-phenyl-C61-butyric acid methyl ester PCBM (99.5 %, Solenne).
- Solvents: dimethylformamide anhydrous DMF (99.8 % Sigma-Aldrich); dimethylsulfoxide anhydrous DMSO (99.9 % Sigma Aldrich); gamma-butyrolactone (GBL) (99 % Sigma Aldrich);2-propanol anhydrous IPA (99.5 % Sigma Aldrich); methanol (MeOH) (99.8 %, Sigma Aldrich); ethanol (99.5 % Panreac); 2-[2-(2-Methoxyethoxy)ethoxy]acetic acid MEEA (Sigma Aldrich); terpineol (95.0 % Sigma Aldrich).
- Screen printing pastes: TiO_2 paste DSL 30NR-D (Dyesol); ZrO_2 paste Zr-Nanoxide ZT/SP (~18wt %, Solaronix) carbon paste C2150317D3 (Gwent Group); conductive silver paste C2081126P2 (Gwent Group).
- Organic molecules as additives or SAMs: 5-AVAI (Greatcellsolar); C_6H_4-1,4-$(CO_2H)_2$(TPA) (98 % Sigma-Adrich); $H_2NC_6H_4CO_2H$ (PABA) (99 % Sigma-Aldrich); 3-(H3pp) $(HO)_2P(O)CH_2CH_2COOH$ (94 % Sigma-Aldrich).

2.1.1.2 Transparent conductive oxide (TCO) substrates

Two different TCO substrates have been employed: Transparent conducting substrates consist of fluorine doped tin oxide (10 % F), F:SnO_2 (FTO) on glass obtained from SOLEMS (FTO TEC 7/2.2). The glass thickness is about of 2.2mm and the FTO layer thickness is about 250 nm, made by CVD deposition and with a 6-8 ohm resistance. For screen printing, the FTO substrates were obtained from GreatCell Solar (former Dyesol). These are about 300 mm x 300 mm substrates with FTO deposition by CVD on TEC8 glass and with a glass thickness about 2.2 mm and a sheet resistance of 8Ω/square.

2.1.1.3 Mesh for screen printing

For the preparation of thin films and solar cells by the screen printing method, a screen with the desirable electrode design is made on synthetic cloth stretched over a frame under tension. The design for the different layers were: for the mesotitania layer squares of 6 mm x 6mm on a total area of 15x10 cm^2, for the meso zirconia 10 mm x 15mm rectangles on a total area of 15x10 cm^2 and for the carbon layer 6 mm x 15 mm rectangles on a total area of 15x10 cm^2 were used. In this study, the mesh was chosen

taking into account the viscosity and the size of the nanoparticles of the ink required for high resolution print and the compatibility of the mesh with the inks. It is also important that the mesh has a strong chemical and mechanical resistance. The characteristics of the mesh used for each paste are as follows: for printing the meso TiO_2 and ZrO_2 layers, the mesh was 130/34 (threads/cm), 55 µm thick with an aperture of 40 µm, a thread diameter of 34 µm, and an open area of 27 %. The mesh for printing the carbon layer was 61/64 (threads/cm), 101 µm thick with an aperture of 90 µm, a thread diameter of 64 µm and an open area of 31 %.

The screen printing equipment was a SA111576 Uniprint PM model. The 58 cm x 58 cm x 5 cm aluminium frames were obtained from EntelatsPremia SL. **Figure 2.1** shows the different screens used for screen printing corresponding to the different solar cell layer: TiO_2, ZrO_2 and carbon, respectively. The inks were selected as a function of the viscosity and thickness required to infiltrate the perovskite solution. The carbon ink had a solid content between 38.0-42.0 % and a viscosity between 7.0 and 10.0 Pa.s. The silver conductive ink had a solid content between 64.5-65.5 % and a viscosity between 1.1 and 0.9 Pa.

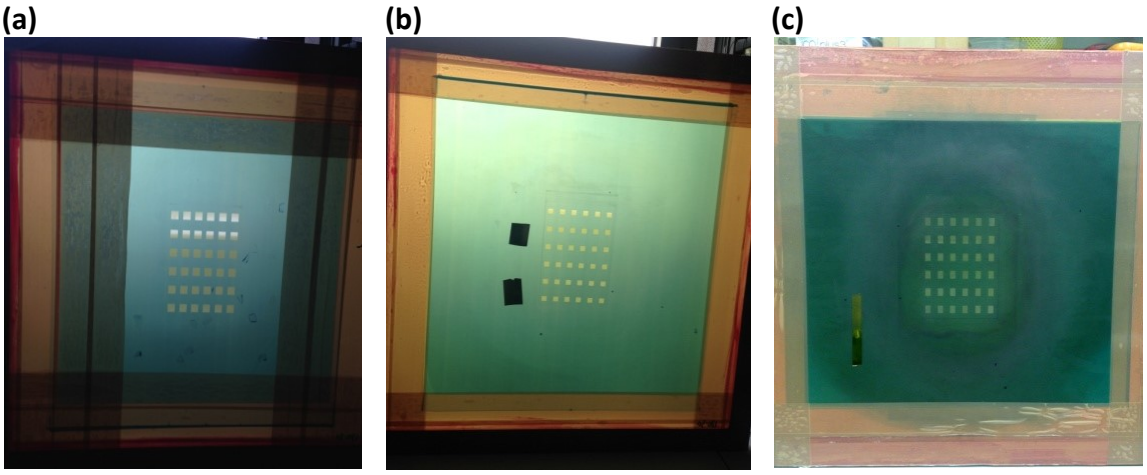

Figure 2.1 Image of **(a)** TiO_2, **(b)** ZrO_2 and **(c)** carbon screens for screen printing.

2.1.2 Materials preparation and synthesis

2.1.2.1 Semiconductor Oxides

This section describes the synthesis of the metal oxides by different methods applying different additives and solvents.

Semiconductor Oxides as HTL:

Synthesis of NiO_x

We have followed the method described by Nalage *et al.*[1]. The precursor of the NiO sol-gel was prepared with 3.75 g of nickel (II) acetate tetrahydrate in 50 ml of (MeOH) solution. The solution was then stirred for 3 hours at 60˚C.

Synthesis of MoO_3

For the synthesis of MoO_3 by sol-gel, 1.37 g of sodium molybdate (Na_2MoO_4) was dissolved in 37 ml of water. Then the solution was passed through a cationic exchange resin DOWEX50 WX2 50-100 and 70 ml were collected. The initial colourless solution did not change, but the initial pH was 7.5 and the final was 2. The final sol-gel was concentrated to 9-10 mg/ml and could be kept at RT for several months [2].

Synthesis of CuO_x

The CuO_x synthesis was prepared following the Armelao *et al.* method [3]. The precursor of the CuO_x sol-gel was prepared by adding 0.5 g of copper (II) acetate monohydrate in 50 ml of absolute ethanol which was stirred continuously for 1h at RT.

Synthesis of V_2O_5

Synthesis of $V_2O_5.0.5H_2O$ xerogel was carried out by the cationic ion-exchange method described by Livage *et al.* [4]. Briefly, 4.5 g of sodium metavanadate were dissolved in water at 80 °C. After cooling down to RT, the solution was passed through a cationic exchange resin DOWEX50 WX2 50-100. The solution changed from transparent to yellow-orange corresponding to the formation of metavanadic acid. The final sol-gel was concentrated to 9-10 mg/ml. The V_2O_5 gel can be stored in ambient atmosphere at RT for several months (up to one year) in a closed glass baker.

Semiconductor Oxides as ETL:

Synthesis of TiO_2

For the preparation of the TiO_2 sol-gel solution, 0.7 ml of acetyl acetone were added slowly, dropwise, with constant stirring to a 1 ml of titanium iso-propoxide [$Ti(OiPr)_4$]. After mixing, 5.1 ml of ethanol (99.5 %) were added and the solution was stabilized for 24 h. The final [$Ti(OiPr)_4$] concentration is 0.51 M. The colour of the solution was orange-yellow, being stable for several weeks at RT [5].

Synthesis of ZnO nanoparticles

The ZnO precursor was prepared following the methods reported in the literature [6], [7]. Typically, 2.97 g of $Zn(OAc)_2.2H_2O$ were dissolved in 125 ml of MeOH and heated to 60 °C. At this temperature, 1.51 g KOH were added and the solution was refluxed for 3 h at 65 °C. The precipitated particles were then allowed to settle for 12 h. The mixture was carefully decanted and the precipitate was then dissolved in 50 ml of MeOH. The particles were then suspended and allowed to settle for another 12 h. After the final stage of the synthesis of the ZnO nanoparticles, the MeOH was removed by decantation and the particles were suspended in chlorobenzene to a final concentration of 40 mg/ml. Finally 2-[2-(2-methoxyethoxy)ethoxy]acetic acid (MEEA) at 4 % w/w with respect to the weight of ZnO was added as a stabilizer.

2.1.2.2 Halide Perovskite solutions

The preparation of all perovskite precursor solutions were made under N_2 atmosphere in glovebox conditions (<5ppm of H_2O and <1ppm of O_2).

$CH_3NH_3PbI_3$ (MAPI) perovskite solution

All of these solutions were prepared for the fabrication of C-based PSC by screen printing.

Two-step process:

$CH_3NH_3PbI_3$ solution: the perovskite precursor solution was prepared following Hongwei Han's method [8]. The solution was prepared by dissolving 0.46 g lead iodide

(PbI_2) in 1 ml of anhydrous DMF and stirred at 70 °C. MAI solution was obtained by dissolving 0.5 g of MAI into 30 ml of IPA.

One-step process:

$CH_3NH_3PbI_3$ solution with 5AVAI: the perovskite precursor solution was prepared following Hongwei Han's method, at 35 % weight solids in solution [9]. The solution was prepared by dissolving 0.922 g PbI_2, 0.014 g 5AVAI and 0.314 g MAI in 2 ml of GBL and stirred at 60 °C overnight for 14 h approximately under N_2 glovebox conditions.

$CH_3NH_3PbI_3$ solution with PABA: The perovskite solution was infiltrated using a precursor solution containing 0.922 g PbI_2, 0.014 g 5AVAI and 0.314 g MAI with different amount of PABA in 2 ml of GBL and stirred at 60 °C for 14 hours overnight.

$CH_3NH_3PbI_3$ solution with TPA: the perovskite solution was infiltrated using a precursor solution containing 0.922 g PbI_2, 0.014 g 5AVAI and 0.314 g MAI and the different amount of TPA in 2 ml of anhydrous DMF and stirred at 60 °C overnight for 14 hours under N_2 glovebox conditions.

$CH_3NH_3PbI_3$ solution with H3pp: the perovskite solution was infiltrated using a precursor solution containing 0.922 g PbI_2, 0.014 g 5AVAI and 0.314 g MAI and the different amount of H3pp in 2 ml of GBL and stirred at 60 °C overnight for 14 hours under N_2 glovebox conditions.

Mixed-Ion perovskite solution,$[HC(NH_2)_2]_{0.85}(CH_3NH_3)_{0.15}Pb(I_{0.85}Br_{0.15})_3$

This solution was prepared for the fabrication of the inverted PSC by spin coating. **Figure 2.2** shows the different perovskite solution preparation, for the conventional MAPI and the mixed-ion perovskite solution.

The perovskite films were deposited using a precursor solution containing formamidiniumiodide FAI (1 M), PbI_2 (1.1 M), methylammonium bromide MABr (0.2 M) and lead bromide $PbBr_2$ (0.2 M) in anhydrous DMF:DMSO, 4:1 (v/v) under N_2 glovebox conditions.

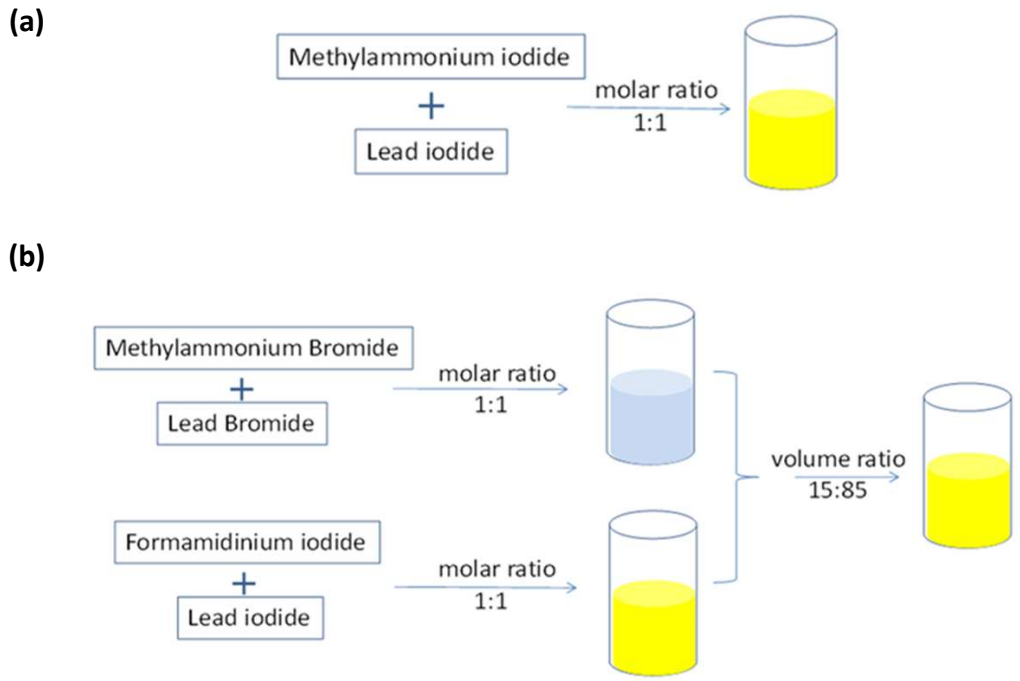

Figure 2.2 Scheme of the preparation procedures for **(a)** MAPI solution and **(b)** mixed-ion perovskite solution.

2.2 Fabrication processes

In this section, the preparation processes to obtain the PSC by spin coating and screen printing methods are described.

2.2.1 Spin coating technique

The spin coating technique is a procedure used to deposit uniform thin films on flat substrates. Usually, a small amount of coating solution is deposited on the centre of a substrate, either while the substrate is spinning or stationary. The substrate is then rotated at desirable speed in order to spread the coating solution by centrifugal force. **Figure 2.3** shows the spin coater equipment from Laurell Technologies model WS-650MZ-23NPP/LITE used in this thesis and the scheme of the spin coating process.

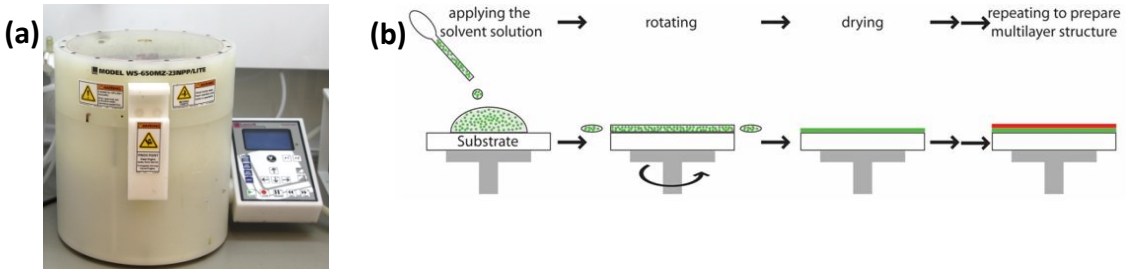

Figure 2.3 (a) Image of a spin coater used in this thesis and **(b)** schematic process of the spin-coating technique. *Extracted from*[10].

All type of solvents can be applied, in the case of volatile solvents the evaporation of the solvent and thin film fabrication is easier than with water-based solutions. The thickness of the films depends on the speed of deposition, evaporation of the solvent and the concentration of the solution. Spin coating is commonly used to deposit layers in photolithography, in semiconductor industry and in magnetic disk coatings, among others.

In this thesis, spin coating was used to deposit sol-gel semiconductor oxides, perovskite solutions and polymer solutions to create thin films with a nanoscale thickness in inverted PSCs configuration.

2.2.2 Screen printing technique

The screen printing technique is used to transfer ink onto a substrate. A squeegee is moved across the screen to fill the open mesh apertures with ink. It is very important to control the parameters of squeegee pressure, print speed, print gap and the angle from squeegee to the screen to obtain the optimum print of the ink. The key advantage of screen-printing is the relative simplicity and low cost of the process. **Figure 2.4** shows a picture of the screen printer used and a scheme of the screen-printing process.

In solar cell research, it is necessary the replacement of the evaporated metal (Au/Ag) as a back electrode with low cost materials to reduce the cost of solar cell fabrication.

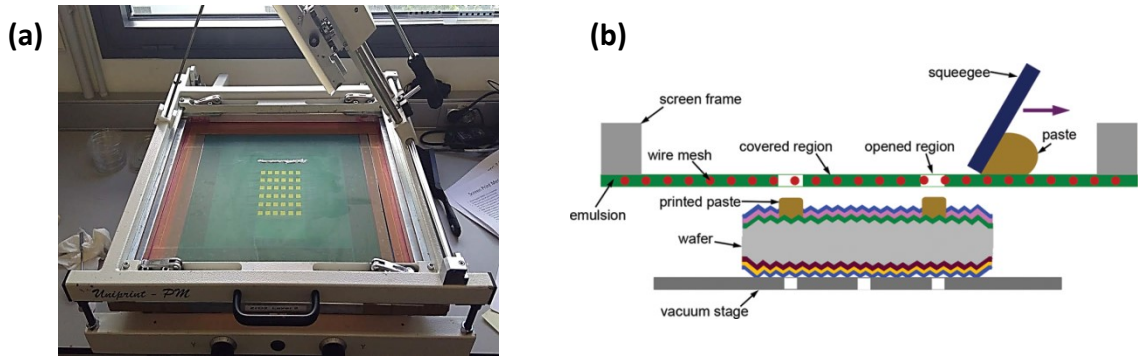

Figure 2.4 (a) Image of the screen printer used in this thesis and **(b)** schematic of the screen-printing process. *Extracted from*[11].

Therefore, carbon-based electrodes have been widely investigated as alternative materials due to their low cost, easy preparation and large-scale fabrication. In this thesis, PSCs with hole-conductor-free based on triple mesoscopic layer (mesoscopic TiO_2, mesoscopic ZrO_2 and carbon electrode) and a TiO_2 compact layer were obtained using the screen printing technique.

2.2.3 Fabrication of PSCs

Before the fabrication of the devices the FTO substrates were cut into desired dimensions (1 cm x 2.5 cm) applying a glass-cutting machine. The FTO was partially removed from the glass via etching by Zn powder and HCl (2 M) using cotton sticks, exposing a glass line to avoid short circuiting the cell. Afterwards, the FTO substrates were rinsed with water and cleaned by standard sequential procedures: sonication with soapy water for 10 min, distilled water for 10 min twice, and ethanol (99.5 %) for 10 min sequentially. The substrates were then dried under N_2 flux and finally cleaned for 20 min in a UV-surface decontamination system (Novascan, PSD-UV) connected to an O_2 gas source.

2.2.3.1 Fabrication of inverted PSCs by spin coating

PSCs with the inverted configuration FTO/NiO_2/halide perovskite/ PCBM:ZnO/Au, were fabricated as follows: The NiO films were deposited on the FTO substrates by spin-coating applying three different concentrations of the NiO_x-precursor solution in MeOH: 0.06 M, 0.15 M and 0.21 M, respectively. The substrates were spin-coated at

80 ˚C (70 µl, 8000 rpm, during 20 s) and annealed at 450 ˚C for 2 h in air. The prepared $FA_{0.85}MA_{0.15}Pb(I_{0.85}Br_{0.15})_3$ perovskite solution was deposited onto the NiO film substrate by spin-coating in a two-step process; first at 2000 rpm for 10 s and then at 5000 rpm for 30 s. During the second step, 110 µL of chlorobenzene were poured onto the spinning substrate for 15 s prior to the end of the program. The substrates were then annealed at 100 ˚C for 1 h in a nitrogen filled glove box. The mixed-ion perovskite film was then cooled down to RT. For the $PC_{70}BM$ ETL, a polymer based on a fullerene structure was applied, using only a 0.01 g/ml solution of $PC_{70}BM$ in chlorobenzene. This solution was applied by spin-coating at 7000 rpm for 30 s under a N_2 glovebox. In the case of the ZnO ETL, a ZnO solution in chlorobenzene was applied by spin-coating on top of the mixed-ion perovskite solution at 7000 rpm for 30 sec in N_2 glovebox atmosphere. To fabricate the bilayer of $PC_{70}BM$/ZnO as an ETL, $PC_{70}BM$ in chlorobenzene solution was first applied and after drying at 40 °C for 10 min, a ZnO solution was then spin coated on top of the $PC_{70}BM$ layer. In the last option a mix solution of $PC_{70}BM$ (0.01 g/ml) with ZnO in molar ratio 1:1 in chlorobenzene solvent was used. In all cases, an 80 nm of gold top electrode was thermally evaporated under high vacuum on top of each ETL layer.

2.2.3.2 Fabrication of C-based PSCs by screen printing

The fabrication of the C-based PSCs by screen printing was carried out applying the one-step or the two-step perovskite infiltration method. The main difference between these two methods is the way that the halide perovskite solution is infiltrated into what we call the “Shell”, which is the FTO/c-TiO_2/mp-TiO_2/mp-ZrO_2/C triple layer. Here c-TiO_2 refers to the compact layer of TiO_2 while mp-TiO_2 and mp-ZrO_2 to the mesoporous layers of the TiO_2 (about 500 nm thickness) and ZrO_2 (about 2.0 µm thickness), respectively. The carbon layer electrode is denoted by C (with approximately 10 µm thickness). The as-prepared “Shell” can be stored in the dark in air until utilization. The preparation of each of the layers that makes the “Shell”, as well as the two methods used to infiltrate the halide perovskite are described as follows:

"Shell" preparation:

A thin c-TiO_2 was deposited by spray pyrolysis (**Figure 2.5 (a)**) onto the already etched FTO substrate at 300 ˚C using a prepared solution of TiAcAc 10 % in IPA. The spraying consisted of 25 alternating horizontal and vertical stokes, with no visible droplets on the substrate in order to make a homogeneous layer. The c-TiO_2 layer (**Figure 2.5 (b)**) was then cooled down to RT.

Afterwards, a layer of mp-TiO_2 was deposited by the screen printing technique (**Figure 2.5 (c)**) on top of the c-TiO_2 thin film, then sintered in the oven with a sequence of 10 min ramps to 100 ˚C, 200 ˚C, 300 ˚C and 550 ˚C for 30 min, respectively. The mp-TiO_2 thin film was prepared by a dilute suspension of TiO_2 paste in terpineol with 2:3 volume ratio and printed on top of the c-TiO_2 (**Figure 2.5 (d)**).

Subsequently, the mp-TiO_2 layer was cooled down and a meso zirconia (mp-ZrO_2) layer was deposited by screen printing (**Figure 2.5 (c)**) using a ZrO_2 paste, ensuring uniformity of the coating with no bubbles. Afterwards, the mp-ZrO_2 layer was sintered in the oven with a sequence of 10 min ramps at 100 ˚C, 200 ˚C, 300 ˚C, and 400 ˚C for 30 min, respectively (**Figure 2.5 (e)**).

The last printed layer is the porous carbon (C) electrode; in this case we also have to ensure coating uniformity and the absence of any bubbles in order to achieve a well formed "Shell". The carbon paste is screen printed (**Figure 2.5 (c)**) on top of the ZrO_2 layer and baked at 150 ˚C in the oven for 10 min and then at 400 ˚C for 30 min to remove the binder and to enable infiltration of the perovskite. The printed FTO/c-TiO_2/mp-TiO_2/mp-ZrO_2/carbon layer (**Figure 2.5 (f)**) is referred here to as the "Shell". Once the "Shell" has cooled down, it was maintained on a hot plate at 70 °C before perovskite infiltration.

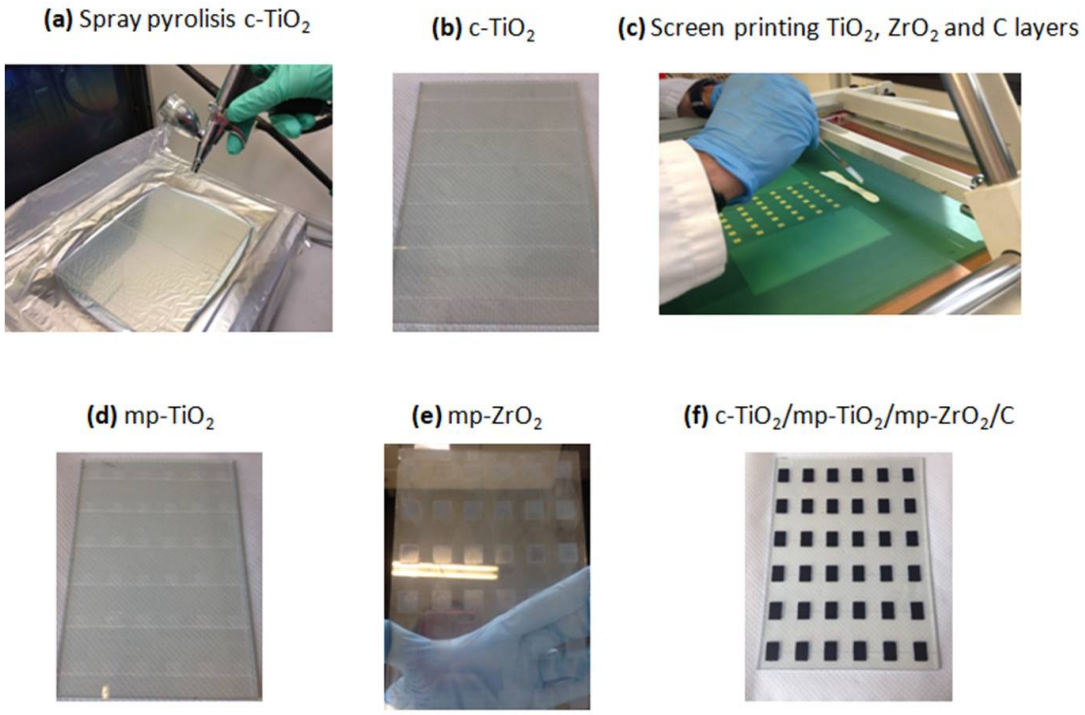

Figure 2.5 Images of the fabrication steps of the "Shell". **(a)** spray pyrolysis of the c-TiO2 layer; **(b)** c-TiO_2 after sintering; **(c)** Screen printing of the mp-TiO_2, ZrO_2 and Carbon layers, **(d)** mp-TiO_2 after sintering, **(e)** mp-ZrO_2 after sintering and **(f)** the "Shell": c-TiO_2/mp-TiO_2/mp-ZrO_2/C.

Infiltration of the halide perovskite in the "Shell":

For the one-step method, the perovskite solution was infiltrated into the "Shell" by drop-casting. The infiltration of the perovskite solution was carried out following the Han *et al.* method [9] as described in Section 2.1.2.2. When the perovskite solution was well dissolved and exhibiting an homogeneous yellow transparent colour, 4 µl of the solution were drop casted onto the active area of the shell. The shells were then left on a hot plate inside a fume hood at 50 °C for 4 h.

For a two-step process (see also Section 2.1.2.2), 4 µl of lead Iodide solution was dropped casted through the carbon layer of the shell. The solution was prepared by dissolving 0.46 g lead iodide (PbI_2) in 1 ml of anhydrous DMF and stirred at 70 °C. Then, in the second step, a solution of the MAI was provided for the subsequent formation of the perovskite. The MAI solution was prepared with 0.5 g of MAI dissolved in 50 ml of anhydrous IPA inside an N_2 glovebox. Then the devices are then immersed in this solution for 30 min and then rinsed in anhydrous IPA in order to remove the excess material. Finally the devices are sintered in an oven at 70 °C for 10 minutes in order to evaporate the solvent. **Figure 2.6** shows images of the infiltration process.

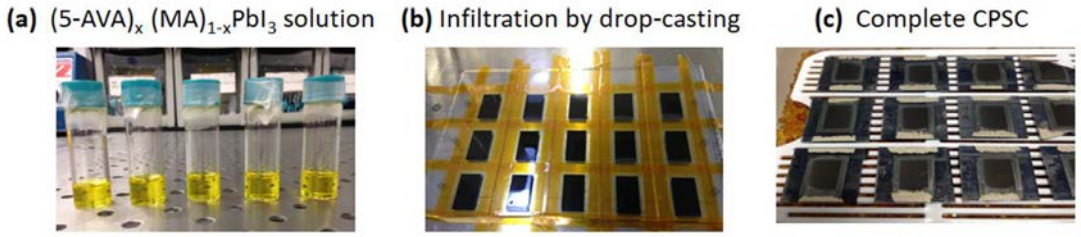

Figure 2.6 Images of the infiltration steps of the halide perovskite in the "Shell". **(a)** $(5\text{-AVA})_x(MA)_{1-x}PbI_3$ **(b)** infiltration by drop-casting and **(c)** complete CPSC.

Final device preparation:

After the "Shell" was infiltrated with the halide perovskite solution by either of the two methods, silver paint was applied to improve the device contacts. The silver contacts were then cured on a hot plate at 40 °C for 2 h. Finally, the devices were kept in a sealed box in a vacuum in the dark overnight before the measurements under a solar simulator.

Device post-humidity treatment:

After the first control measurement, a post-humidity treatment was carried out in order to reduce or eliminate hysteresis in the final device. The C-based PSC were kept in a humidity oven (Memmert) at 25 °C and 70 % R.H. overnight for 12 hours approximately. The C-based PSCs were then measured again using a solar simulator.

2.3 Characterization techniques

In this section the different characterization techniques that have been used in this thesis are described.

2.3.1 Materials Characterization

2.3.1.1 UV-Visible (UV-Vis)

Ultraviolet-visible absorption spectroscopy measures the absorption of light across the ultraviolet and visible spectral range through a sample. The most commonly employed method to determine the molar concentration of an absorbing species in a solution is

to use the Beer-Lambert law $A = \mathcal{E}.b.c$, where A is absorbance (unitless), Ɛ is the wavelength-dependent molar absorptivity coefficient with units of $M^{-1}cm^{-1}$; b is the path length of the sample usually expressed in cm; and c is the concentration of the sample expressed in $molL^{-1}$.

In this thesis, ultraviolet-visible absorption spectroscopy was used on different TMOs in thin films. The aim was to determine in which wavelength range the TMOs applied as HTLs and ETLs were able to absorb a maximum intensity and to evaluate their transparency. **Figure 2.7** shows the UV-visible absorption equipment used in this work.

Description of the equipment: Ultraviolet-visible absorption spectra were recorded by using a Cary Scan 4000 spectrophotometer in the 300-600 nm wavelength range.

Figure 2.7 Image of the UV-Visible spectrophotometer used in this thesis.

2.3.1.2 X-Ray Diffraction (XRD)

XRD is an analytical technique used for the determination of the atomic and molecular structure of materials providing information on unit cell parameters and crystalline phase identification in powder and thin films samples. Crystallinity causes a beam of incident X-rays to diffract into many specific directions. By measuring the angles and intensities of these diffracted beams, the electron density within the crystal can be obtained. From this electron density, it is possible to determine the position of the atoms, their chemical structure and additional information. The X-rays are generated when electrons are thermally emitted from a cathode (usually a tungsten filament)

towards the anode inside an X-ray tube. The electrons striking the anode cause the emission of radiation toward the sample. The interaction of the incident X-rays with the sample produces constructive interference when Bragg's Law is satisfied, i.e. nλ=2d sinΘ, where n is a positive integer (1, 2, 3, etc.), λ is the wavelength of the incident X-rays, d is the spacing between the lattice planes *(hkl)* and θ is the angle of the diffracted wave with respect to the incoming one. This is a powerful technique for the interesting applications which include; identification of crystalline phases, quantitative analysis, particle size and crystal structure determination. **Figure 2.8** shows the XRD equipment used for the samples of this present work.

In this thesis, X-Ray diffraction was used for the following purposes: 1) to identify the characteristic peaks of the TMOs used as both HTL and ETL; 2) to confirm if the desired oxide had been synthesized in the correct phase; 3) to determine the presence of any unreacted precursor and 4) to ascertain the relationship between perovskite formation and impurities.

Figure 2.8 Image of the X-Ray diffraction equipment used in this thesis.

Description of the X-ray powder diffraction equipment: The X-ray Powder Diffraction measurements were performed with a Malvern PANalyticalX'pert Pro MPD diffractometer (Multipurpose Diffractometer) at RT using Cu K_α radiation (λ=1.540 Å). The MPD is suitable for the analysis of polycrystalline samples at RT. This

diffractometer has a vertical θ-θ goniometer (240 mm radius), where the sample stages are fixed and do not rotate around the omega axis, as in ω-2θ diffractometers. The detector used was an X'Celerator, which is an ultra-fast X-ray detector based on Real Time Multiple Strip (RTMS) technology.

Description of the thin film X-ray diffractometer: The thin films XRD measurements were performed with a Malvern PANAlyticalX'pert Pro MRD (Materials Research Diffractometer) Diffractomter. The MRD is suitable for the structural characterization in thin-films materials at room and high temperatures. This diffractometer has a horizontal ω-2θ goniometer (320 mm radius) in a four-circle geometry and it works with a ceramic X-ray tube with CuKα anode (λ=1.540 Å). This diffractometer is equipped with different incident and diffracted optics which can be interchanged depending on the application required. The detector used is a Pixcel which is a fast X-ray detector based on Medipix2 technology.

2.3.1.3 Focused Ion Beam (FIB)

FIB is a technique commonly used in materials science. A FIB setup uses a focused beam of ions, usually from gallium, to image a sample in a chamber operated at low beam currents or at high beam currents for site specific sputtering or milling. FIB columns can be incorporated into other analytical instruments such as scanning electron microscopes, and in this regard, FIB is commonly used in conjunction with SEM in a dual platform instrument. In addition, FIB can be used in conjunction with energy-dispersive X-Ray spectroscopy (EDX) to explore the chemical characterization and the elemental analysis of the sample. The basic FIB instrument consists of a vacuum system and chamber, a liquid metal ion source, an ion column, a sample stage, detectors and a gas delivery system. **Figure 2.9** shows the image of the FIB-SEM equipment used in this present work.

In this thesis, a FIB/SEM dual cross-section platform instrument was used for perovskite samples. A trench was first made in the surface of the PSC to expose a cross section image of the film. The aim was to examine the degree of degradation and the

thickness of the different layers of PSC. Finally EDX was used to determine the elemental composition of the sample.

Figure 2.9 The used FIB/SEM equipment.

Description of the equipment: the FIB-SEM equipment was a Crossbeam 1560XB, which is a high resolution field emission (FE-SEM) combined with a FIB Ga^+ column with a multi-channel gas injection system. It was equipped with two detectors: Everhart-Thornley SE and a high efficiency In-lens SE detector. The Auriga 40 (Carl Zeiss) Workstation is a high resolution FE-SEM with GEMINI column technology combined with an N_2 injection system, a X-Ray Detector, an Everhart-ThornleySE and a high efficiency In-lens SE detector, and a EsB Backscattered Electrons Detector. The control software used was SmartSEM^{TM} with graphical user interface (GUI), auto level system, and chamber scope.

2.3.1.4 X-Ray Photoelectron Spectroscopy (XPS) and Ultraviolet Photoelectron Spectroscopy (UPS)

Photoelectron spectroscopy is a technique used to study the surface of a material using X-rays or UV light as an excitation source to promote electronic emission. This technique is based on the photoelectric effect, which can determine the binding energies of electrons in a material. The photoelectric effect derives from the fact that solids emit electrons, called photoelectrons, when light is directed onto them. This effect is attributed to the transfer of energy from the light to an electron in the

material. The photoemission technique can be used to study roughly the first 2 nm of a surface. This technique provides information on the oxidation state, the elemental composition of the material, and surface contamination. **Figure 2.10** shows an image of the XPS/UPS equipment used in this present work.

In this thesis, XPS/UPS was used to measure the oxidation and reduction states of the species related to changes in temperature; the thickness homogeneity of the oxide deposited on FTO substrates; and the energy levels of the oxides. In the case of UPS, this technique was used to determine the Valence Band (VB) and IP of the different materials.

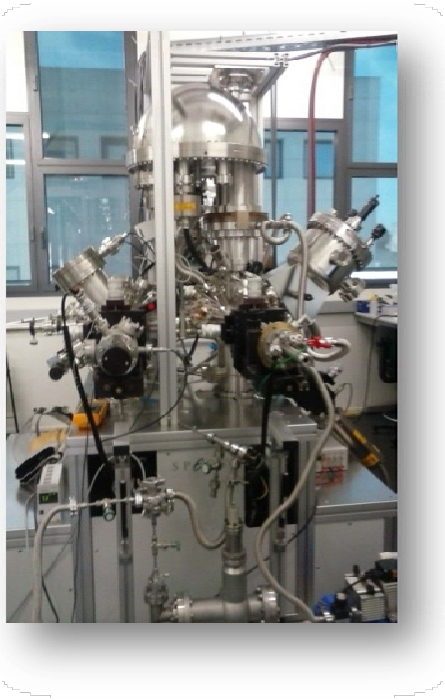

Figure 2.10 Image of XPS-UPS equipment at ICN2.

Description of the equipment: XPS and UPS measurements were performed with a Phoibos 150 analyzer (SPECS GmbH, Berlin, Germany) in ultra-high vacuum conditions (base pressure 10^{-10}mbar). XPS measurements were performed with a monochromatic Kα X-ray source (1486.6 eV) and UPS measurements with monochromatic HeI UV source (21.2 eV). The determination of the IPs was done by aapplying bias of -10 V to the sample.

2.3.1.5 Atomic Force Microscopy (AFM) / Kelvin Probe Force Microscopy (KPFM)

AFM is a high resolution type of scanning probe microscopy technique used to characterize surfaces, most notably the surface topography. The main parts of the equipment are a cantilever with a small tip (probe) at the free end, a laser, a 4-quadrant photodiode and a scanner. AFM can optically measure the vertical and lateral deflections of the cantilever, and acquire high resolution images. This technique can produce a topographical image of the sample surface, based on the interactions between the tip and the sample. For imaging, the reaction of the probe to the forces that the sample imposes on it can be used to form an image of the three-dimensional shape of a sample surface at high resolution. There are different operational modes: contact mode, dynamic (tapping mode), and non-contact mode.

In this thesis, AFM was used to determine the topography of the HTM used in inverted PSCs made by the spin coating technique.

Kelvin Probe Force Microscopy (KPFM) is a non-contact variant of AFM, capable of measuring the surface potential of the samples. It carries out a mapping of the work function (WF) of the surface which is related to many surface phenomena; including catalytic activity, doping of semiconductors, charge trapping in dielectrics and corrosion. The map of the WF produced by KPFM gives information about surface electronic states. **Figure 2.11** shows an image of the AFM-KPFM equipment used in this present work.

In this thesis, KPFM was used to determine the change of surface potential related to the interaction of the materials.

Figure 2.11 Image of AFM-KPFM equipment used in this thesis.

Description of the equipment: the analysis were carried out with an Ayslum Research MFP-3D, model MFP-3D Classic that can measure from -20 ˚C to 300 ˚C. The instrument has also a high voltage option of 220 V ac and a frequency range between 0-2 MHz.

2.3.1.6 Scanning Electron Microscopy (SEM)

SEM is a technique that images the sample surface by scanning it with a high-energy beam of electrons in a raster scan pattern. SEM can achieve a resolution above 1 nanometer in lateral and topographic dimensions. The electrons interact with atoms in the sample, producing various signals that contain information about the sample's surface topography and chemical composition. The main parts of the equipment are the electron gun, electron lenses, the column, sample stage and the detectors. **Figure 2.12** shows the SEM equipment used in this present work.

In this thesis, SEM was used to determine the topography and confirm the thickness of the different layers of C-based PSCs made by the screen printing technique.

Figure 2.12 Image of the SEM equipment used in this thesis.

Description of the equipment: the measurements were carried out using a Quanta 650 FEG SEM with high resolution, from Thermo Fisher (formerly FEI Company). The imaging detector used was a backscatter electron detector (BSED) working in Low Vacuum mode (for insulating samples). The SEM parameters used for image acquisition were: a spot size of 4 nm (approximately 100 pA beam current) and HV of 20.00 kV. The EDS detector was an Inca 250 SSD XMax20.

2.3.1.7 Ellipsometry

Ellipsomtery is an optical measurement technique which determines the transmission and reflection properties of light impacting on a material. Ellipsometry can be used to characterize composition, roughness, thickness, crystalline nature and electrical conductivity. The advantages of this technique are: high precision in wavelength, non-destructive and fast acquisition. However, the interpretation of the data is not straight-forward.

The state of polarization is defined by the phase and amplitude relationships between the two components, p and s. Ellipsometry is interesting because it shows how p- and s- components change upon reflection or transmission in relation to each other. A

known polarization is reflected or transmitted from the sample and the output polarization can be measured. The change in polarization is the ellipsometry measurement. Ellipsometry is used in many different fields from semiconductor physics to microelectronics and biology. **Figure 2.13** shows a picture of the ellipsometer used in this present work. In this thesis, ellipsometry was used to evaluate film thickness of oxides.

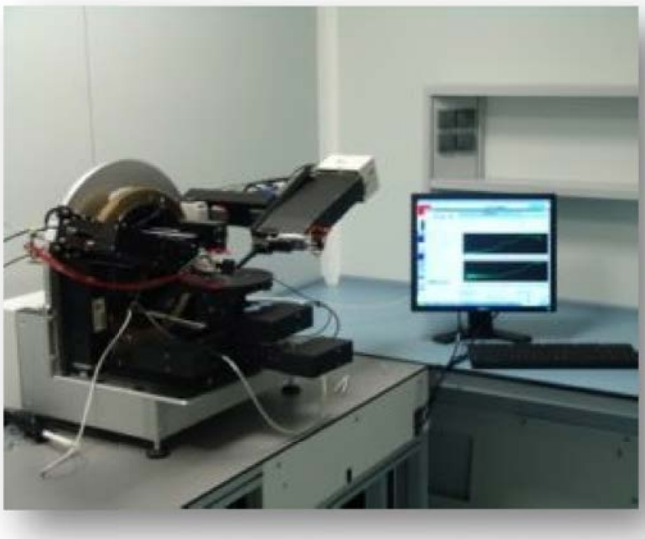

Figure 2.13 Image of the ellipsometry setup.

Description of the equipment: Variable angle spectroscopic ellipsometry was performed using a SEMILAB GES5 rotating polarizer ellipsometry coupled to a Peltier cooled CCD detector. Four angles of incidence were collected for each sample around their Brewster angle. Typical values were 55, 60, 65, and 70 degrees. Fitting of the experimental data was performed using the Cauchy law for the transparency region, as well as the Tauc-Lorentz model for the extended spectral region, including both transparency and absorption. The analysis was carried out using the Winelli II software.

2.3.1.8 Profilometry

The profilometer is an instrument used to measure the surface profile of a sample. There are two operational modes: contact and non-contact. In the case of the contact profilometer, the most important part is the tip, which is moved in contact with the

sample over a given distance at constant force. A non-contact profilometer uses white-light optical profiling and is also used to measure the sample surface but without any physical contact. The contact profilometer does not require any modelling. **Figure 2.14** shows the profilometer used in this present work.

In this thesis, a contact profilometer was used to determine the thickness of the layers of shells composed of TiO_2, ZrO_2 and carbon, made for the fabrication of PSCs using the screen printing technique.

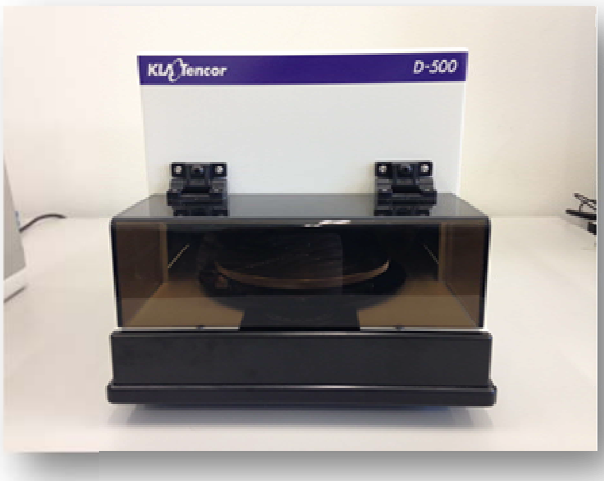

Figure 2.14 Image of the profilometer used in this thesis.

Description of the equipment: the measurements were carried out using a KLA Tencor Inc. Alphastep D500 model with a 2 µm diamond tip stylus, a vertical resolution of 1 nm, a vertical measurement range up to 1.2 mm, a scan size up to 30 mm, a force range between 0.03 mg to 15 mg, and a microscope camera for positioning the sample.

2.3.2 Device Characterization

2.3.2.1 Current-Voltage measurement

The current density vs. voltage measurement is the basic characterization of a solar cell used to obtain photovoltaic parameters, such as short circuit current density (J_{sc}),

V_{oc}, fill factor (FF), and light-to-electricity PCE. The $J_{sc}$is controlled by the light harvesting efficiency of the light absorber and the charge transfer yield at the interfaces between the active layer and the transport layers. The $J_{sc}$is due to the generation and collection of light-generated carriers and depends on a number of factors: the area of the cell, the number of photons, the spectrum of incident light, and the optical properties. Furthermore, the optimization of the matching energy levels between different materials is critical for enhancing J_{sc}. **Figure 2.15** shows the representation of the IV curves of a device under illumination.

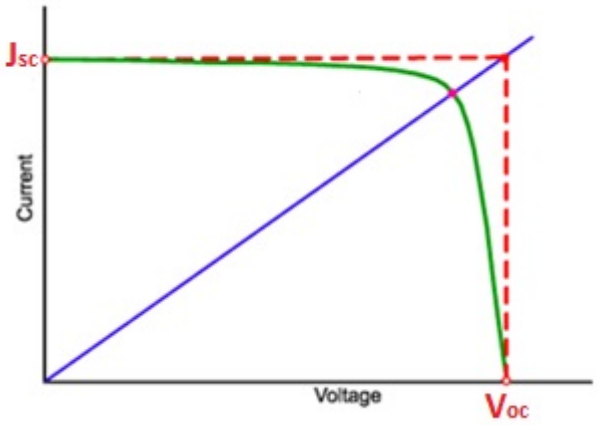

Figure 2.15 I-V curves of a device under illumination.

The open-circuit voltage is the maximum possible voltage across a solar cell when no current is flowing. The FF is a parameter that determines the maximum power area from a solar cell. Graphically, the FF is a measure of the "squareness" of the curve and is also the area which will fit in the IV curve. Thus,

$$FF = \frac{V_{mp}J_{mp}}{J_{sc}V_{oc}}, \tag{2.1}$$

where V_{mp} is the value of voltage at maximum power point (MPP) and J_{mp} is the value of current density at MPP.

The FF of the device can be influenced by the Rs (resistance of the components) and the shunt resistance (Rsh) (resistance resulting from recombination of the photo-generated charges).

The light-to-electricity PCE is determined by the ratio of maximum power density (power per unit area, P_{max}) of the device and the power of incident light (P_{in}), with a value of 100 mW/cm^2. The maximum power density of the device is expressed in terms of J_{sc}, V_{oc} and FF, according to the equation:

$$P_{max} = J_{sc}V_{oc}FF \tag{2.2}$$

so that,

$$PCE = \frac{P_{max}}{P_{in}} = \frac{J_{sc}V_{oc}FF}{P_{in}}. \tag{2.3}$$

Thus, for an efficient solar cell the FF, J_{sc} and V_{oc} all should be as high as possible. In PSCs, the I-V curves are often dependent on the scan direction, leading to hysteresis.

The illumination conditions commonly used is the Air Mass 1.5 (AM 1.5) solar spectrum [12]. The AM 1.5 global spectrum corresponds to sunlight attenuated by passing through the atmosphere at an angle of 48° from zenith. For convenience, the intensity of the AM1.5 spectrum is normalized so that the integrated irradiance is 1000 W/m^2.

Description of the equipment:

These photovoltaic parameters are typically measured using controlled light intensity provided by a solar simulator lamp of 1000W/m^2, similar to the output of the sun, under AM 1.5G illumination. The solar simulator used in this study was a SteuernagelSolarkonstant KHS1200 with a light intensity adjusted to 1000 W/m^2 with a bolometric Zipp&Konen CM-4pyranometer. Calibration of the sun simulator was made with a calibrated reference Silicon Cell code RR-97-0 from 2-11-2010. The AM 1.5G reference spectrum was according to an ASTM G173 standard[13].

Solar decay and I-V curves were measured using a Keithley 2601 multimeterwith the Labwindows acquisition software.

2.3.2.2 Incident Photon-to-Current Conversion Efficiency (IPCE)

The IPCE is a parameter that can determine how efficiently a solar cell converts incident light into electrical energy, flowing in the external circuit, at a certain wavelength. The IPCE measurement is based on illuminating the sample by a monochromatic light and recording the generated short-circuit photocurrent. The IPCE value depends on different parameters including light harvesting efficiency (LHE), electron injection efficiency ($\emptyset_{inj}$), and charge collection efficiency ($\emptyset_{coll}$), as shown in the following equation:

$$IPCE = LHE\emptyset_{inj}\emptyset_{coll} \quad (2.4)$$

Figure 2.16 shows the IPCE setup used in this work. The calculated integrated short-circuit solar cell AM1.5 current should be very close to the current measured by exposing the cell to the output of a solar simulator.

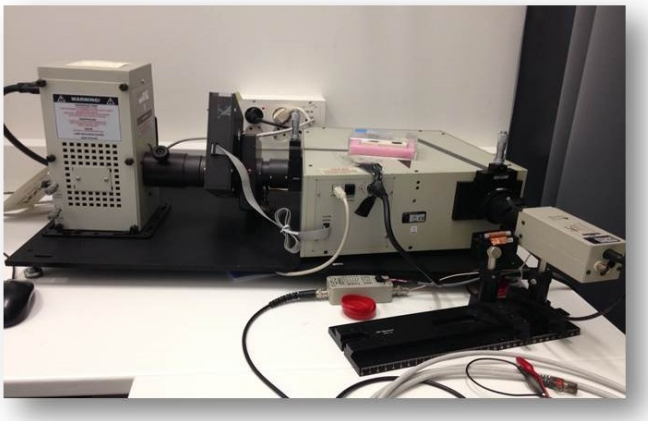

Figure 2.16 The IPCE setup used in this thesis.

Description of the equipment:

IPCE analyses were carried out with a QE/IPCE measurement system from Oriel at 10 nm intervals between 300 and 700 nm. The instrument uses a xenon arc lamp source, monochromator, filters and reflective optics to provide stable monochromatic light to a photovoltaic test device.

2.3.3 Stability

The stability measurements were carried out in accordance with the ISOS protocols [14]. For indoor measurements, the ISOS-D-1 shelflife test was used to analyse the stability of the PSCs at ambient temperature of approximately 23 ˚C and ambient R.H. of approximately 50 % stored in the dark.

The solar cells were kept under the desired conditions and analysed under the sun simulator at defined periods of time. The system works in an open circuit. In this study, the PSC devices were not encapsulated and were kept in the dark under a dry atmosphere (R.H 10 % and RT, 25 °C). The inverted PSCs were measured with a 0.125 cm^2 mask and the C-based PSCs were measured with a 0.079 cm^2 mask, under 1 sun with a full sunlight intensity of 1000 W/m^2.

The indoor long-term stability measurements made for 1000h were carried out in the laboratory of Prof. Antonio Urbina at the University of Cartagena. The samples were placed under an ABET AM1.5 Class AAA solar simulator with a 7.1 mm^2 mask. A Keithley Model 230 was used as a voltage source and a Keithley Model 6514 for a current source.

2.4 References

[1] S. R. Nalage, A. T. Mane, R. C. Pawar, C. S. Lee, and V. B. Patil, “Polypyrrole–NiO hybrid nanocomposite films: highly selective, sensitive, and reproducible NO2 sensors,” *Ionics (Kiel).*, vol. 20, no. 11, pp. 1607–1616, 2014.

[2] Y.-I. Lee, J.-H. Youn, M.-S. Ryu, J. Kim, H.-T. Moon, and J. Jang, “Highly efficient inverted poly(3-hexylthiophene): Methano-fullerene [6,6]-phenyl C71-butyric acid methyl ester bulk heterojunction solar cell with Cs2CO3 and MoO3,” *Org. Electron.*, vol. 12, no. 2, pp. 353–357, 2011.

[3] L. Armelao, D. Barreca, M. Bertapelle, G. Bottaro, C. Sada, and E. Tondello, “A sol–gel approach to nanophasic copper oxide thin films,” *Thin Solid Films*, vol. 442, no. 1, pp. 48–52, 2003.

[4] J. Livage, “Sol-gel chemistry and electrochemical properties of vanadium oxide gels,” *Solid State Ionics*, vol. 86–88, pp. 935–942, 1996.

[5] M. Lira-Cantu, A. Chafiq, J. Faissat, I. Gonzalez-Valls, and Y. Yu, “Oxide/polymer interfaces for hybrid and organic solar cells: Anatase vs. Rutile TiO2,” *Sol. Energy Mater. Sol. Cells*, vol. 95, no. 5, pp. 1362–1374, May 2011.

[6] W. H. H. Womelsdorf et al. 2004, “Nanoparticulate, redispersible zinc oxide gels, Leverkussen, US patent.”

[7] C. K. Frederik, T. Yi, T. Ralf, and W. A. Jens, “A simple nanostructured polymer/ZnO hybrid solar cell—preparation and operation in air,” *Nanotechnology*, vol. 19, no. 42, p. 424013, 2008.

[8] T. Liu *et al.*, “Critical parameters in TiO2/ZrO2/Carbon-based mesoscopic perovskite solar cell,” *J. Power Sources*, vol. 293, pp. 533–538, 2015.

[9] A. Mei *et al.*, “A hole-conductor–free, fully printable mesoscopic perovskite solar cell with high stability,” *Science*, vol. 345, no. 6194, pp. 295–298, 2014.

[10] S. M. Kandjaniet al. , “Inorganic–Organic Perovskite Solar Cells,” *Sol. Cells - New Approaches and Reviews.*, Intech Open, 2015.

[11] Y. Tao, “Screen-Printed Front Junction n-Type Silicon Solar Cells,” *Printed Electronics Current Trends and Applications.*, Intech Open, 2016.

[12] J. Nelson, “The Physics of Solar Cells,” *Imp. Coll. Press*, 2004.

[13] R. S. S. I. A. G-173, “https://rredc.nrel.gov/solar//spectra/am1.5/.”

[14] M. O. Reese *et al.*, “Consensus stability testing protocols for organic photovoltaic materials and devices,” *Sol. Energy Mater. Sol. Cells*, vol. 95, no. 5, pp. 1253–1267, 2011.

Chapter 3

Transition Metal Oxides

3.1 Introduction

Transition Metal Oxides (TMOs) are materials having partially filled d subshells in the oxidation state, from groups 3-12 in the periodic table [1]. TMOs are present in many fields such as chemistry, geology, and condensed matter physics or engineering.

In recent years, the interest in TMOs, including ZnO, TiO_2, V_2O_5, MoO_3, and NiO, among many others, has rapidly grown due to their interesting properties such variable work function (WF), semiconducting properties with a p- or n-type character, favourable energy level alignment with many organic and inorganic materials, and good optical properties like transparency to specific photon ranges. All of these factors are important requirements for photovoltaic applications [2]. These oxides are extensively used in photovoltaics because they are ideally suited to complement the halide perovskite absorber in solar cells: they possess good compatibility with perovskite material, optical transparency, simple and low cost processing and can confer additional moisture resistance [3-4].

Semiconductor oxides have recently become the focus of extensive research due to the high stability properties that provide to PSCs. The presence of dopants or the functionalization of their surfaces can modify the electrical, physical and chemical properties of these TMOs in order to achieve enhanced photovoltaic performance and stability. For instance, the improvement can appear in terms of moisture tolerance [5], hysteresis free behaviour [6] and the enhancement of PCE lifetime stability [7].

Figure 3.1 shows the band energy alignment diagram of different TMOs with respect to $CH_3NH_3PbI_3$ perovskite.

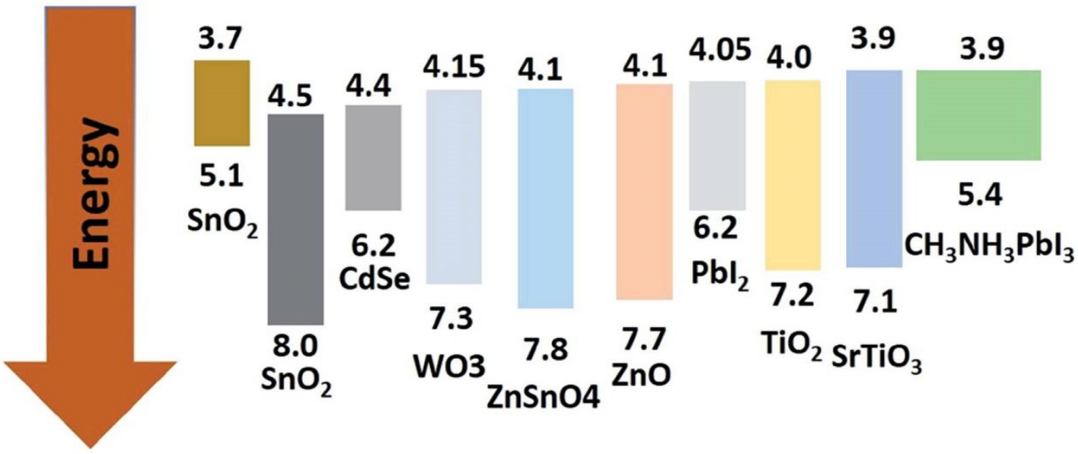

Figure 3.1 Band energy diagram of different TMOs with respect to $CH_3NH_3PbI_3$ perovskite. *Extracted from* [8].

In this thesis we applied TMOs as transport layers for PSCs due to their high charge transfer, uniformity and homogeneity of the layers, reduction of charge accumulation at the interfaces and low temperature synthesis[8]. HTL materials such as NiO, CuO_x, CrO_x, MoO_3, V_2O_5 and WO_3 have been used for PSCs due to their wide E_g, good chemical stability, the high performance results on flexible devices which is a key point for the future commercialization of the technologies [9].

High PCE devices have been reported a using the TMOs mentioned above. For instance, You *et al.* applied NiO as HTL and ZnO as ETL in an inverted planar architecture. They achieve an uncertified 16.1 % PCE, also they demonstrate an improvement in stability in ambient air as compared to devices made with organic transport layers [4]. Regarding TiO_2, Snaith and co-workers used TiO_2 prepared by a solution processed spin-coating method, with a 15.2 % efficiency [10]. For this reason, we have selected the following oxides: NiO, ZnO and TiO_2.

In this chapter, we discuss about the synthesis of TMOs by the solution processing method and the fabrication of dense thin films on top of the transparent conducting substrates such as FTO. The as- prepared thin films of NiO, TiO_2,ZnO, MoO_3, CuO and V_2O_5 were characterized and their properties compared in order to select the most suitable oxides to

apply in PSCs. We have used XRD, Ellipsometry, UV-Vis and XPS/UPS to characterize these materials.

3.2 Effect of sintering temperature on the crystalline structure of TMOs

In this section we investigate the effect of the sintering temperature of TMOs and their crystalline structure. The samples were analyzed as powderfollowing the synthesis procedure detailed in Chapter 2. A 15 ml of oxide solution was added in a duroplan petri dish, and then, introduced in the oven at the desired temperature. The temperature was maintained for 2 h using a 3 °C/min heating ramp. **Figure 3.2** shows the XRD patterns of the TMOs after annealing process at different temperatures for **(a)** NiO, **(b)** TiO_2, **(c)** ZnO, **(d)** MoO_3, **(e)** CuO and **(f)** V_2O_5.

The XRD studies of the powder samples were carried out using a Malvern PANalyticalX'pert Pro MPD diffractometer, as already described in Chapter 2. The XRD patterns were analysed by identifying the observed peaks with the standard pattern provided by Highscore software library files.

Nickel Oxide (NiO)

NiO is one of the most popular HTM used in PSCs. It can replace PEDOT:PSS and Spiro-OMeTAD. PEDOT:PSS is a poor electron blocker, shows acidic pH and is highly hygroscopic [11], while Spiro-OMeTAD is highly unstable, especially at high temperatures [12]. NiO and its doped analogues have provided long term stability and carrier mobility, in fact, the most stables PSCs under continuous illumination use NiO. In this thesis work, we use NiO as HTL in inverted planar PSCs and the NiO thin films were prepared by the spin coating deposition method.

Figure 3.2 (a) shows the XRD patterns of the NiO powder samples prepared at 150 °C, 250 °C and 350 °C sintering temperatures, respectively. Characteristic diffraction peaks belonging to the space group Fm3m, corresponding to a cubic crystal system (a=b=c=4.1678 Å) can be observed for NiO at 250 °C (reference code 00-047-1049 from Highscore library).

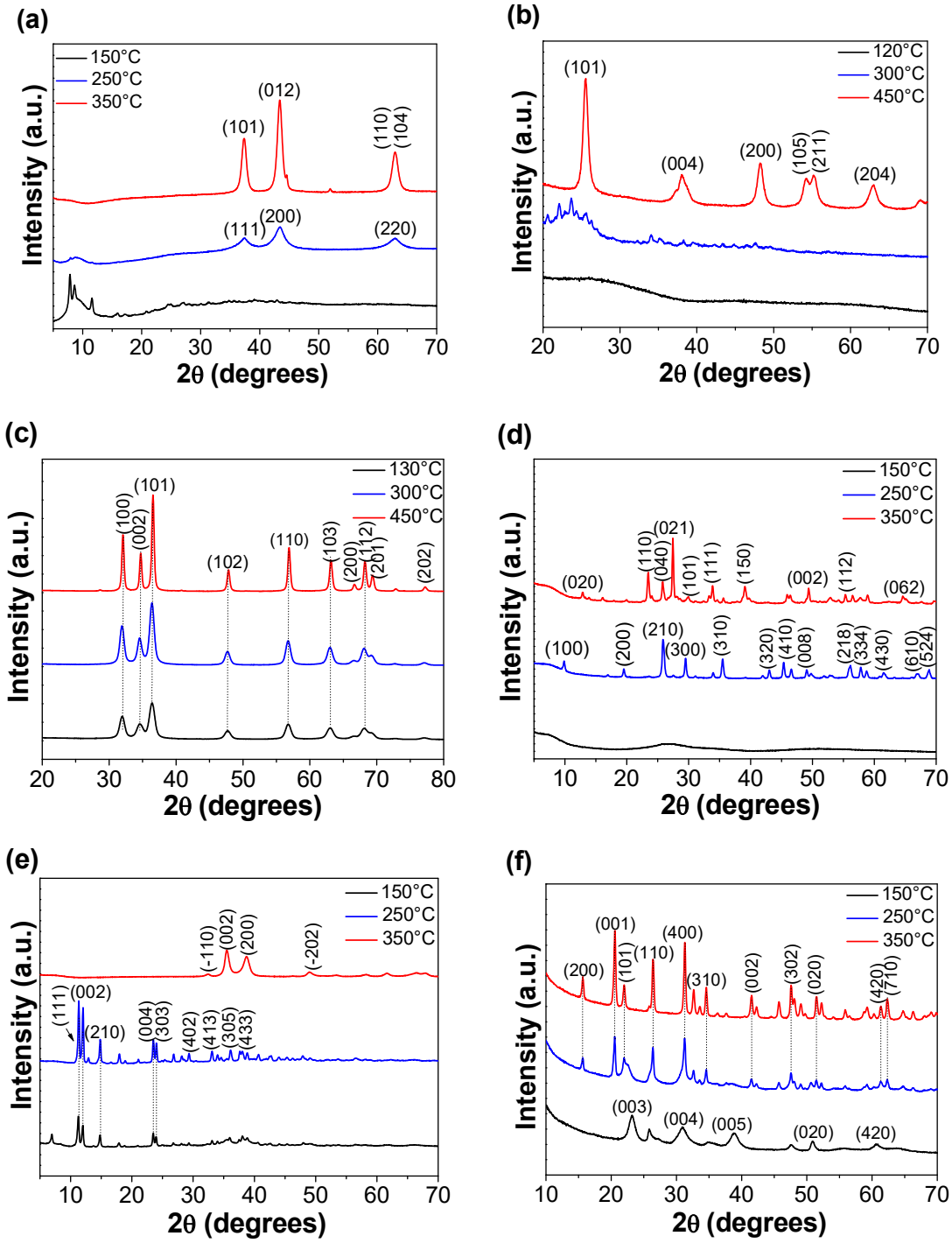

Figure 3.2 Indexed X-ray diffraction patterns of **(a)** NiO, **(b)** TiO_2, **(c)** ZnO, **(d)** MoO_3, **(e)** CuO and **(f)** V_2O_5 in powder after annealing at various preparation temperatures.

Meanwhile, for 350 °C, the diffraction peaks were in accordance with the R-3m space group in the rhombohedral crystalline structure (reference code 00-044-1159). For the lowest temperature, 150 °C, there is a broad amorphous diffraction peak at approximately 2θ=10

degrees, which is also significant at 250 °C.Therefore, the best sintering temperature in this study is the highest one, 350 ˚C.

Titanium Oxide (TiO_2)

TiO_2 is an n-type semiconductor and has been extensively used as ETL due to its excellent properties for the injection of charges after the absorption of light by the absorber (perovskite). It is employed as a dense thin layer in normal and planar configuration PSCs and also as mp-TiO_2 layer. Up to date, TiO_2 is present in the most efficient and most stable PSCs. **Figure 3.2 (b)** shows the X-Ray diffractograms of the TiO_2 samples sintered at 120 °C, 250 °C and 450 °C, respectively.

From the structural analysis, the TiO_2 powder at 450 °C exhibits a crystalline structure with an anatase phase, with tetragonal crystal symmetry of (I41/amdspace group, reference code 00-004-0477). As observed in **Figure 3.2 (b)**, an amorphous crystalline structure dominates at and below 250 ˚C.

Zinc Oxide (ZnO)

ZnO is a promising ETL due to its high conductivity, transparency and versatility. The most important feature is that it can be easily prepared at low temperatures and thus, is an important oxide for the fabrication of flexible devices [13]. ZnO was applied in this work as an ETL in inverted PSCs configuration.

Figure 3.2 (c) shows the diffraction patterns of ZnO at three different temperatures: 130 °C, 300 °C and 450 °C, respectively. We observe that the crystallinity increases with temperature. Moreover, a good matching between the experimental diffractograms and the patterns from database was obtained for all temperatures and showed a hexagonal crystal system (reference code 01-080-0075) with P63mc space group. These data show that ZnO is an attractive oxide which can be annealed at temperatures as low as 130 °C showing good crystallinity. Reported results from our group have also found that the quality of the ZnO surface improve with temperature (less surface defects are found at higher temperature) [14]. This ZnO is one of the best oxides candidates to be applied for low temperature fabrication of PSCs, especially for solar cells on flexible (plastic) substrates.

Molybdenum Oxide (MoO_3)

We also studied the crystallographic characteristics of MoO_3, generally used as a HTL in PSC devices. MoO_3 is a n-type semiconductor with promising applications for its non-toxicity and ambient condition stability [15]. Using a MoO_3/PEDOT:PSS bilayer structure, Hou *et. al.* obtained 14.8 % PCE with an enhancement of the stability as compared to the cells employing only PEDOT:PSS [15].

The XRD patterns of the samples sintered at different temperatures are shown in **Figure 3.2 (d)**. For the sample annealed at 250 °C, all the diffraction peaks can be indexed to the standard hexagonal MoO_3 structure (reference code 00-021-0569), with lattice constants a=10.531 Å, b=10.531 Å and c=14.876 Å. This phase builds zigzag chains of MoO_6 octahedra along the c-axis linked to each other by corner sharing, giving an hexagonal crystalline structure with large 1D tunnels [16].

In contrast, a phase change was observed in the sample annealed at 350 °C, leading to a formation of a single orthorhombic α-MoO_3 phase. The experimental reflections are in good agreement with the corresponding references from the database (reference code 00-005-0508), with cell parameters a=3.962 Å, b=13.858 Å and c=3.697 Å, which correspond to the Pbnm space group. We observed that by increasing temperature, the crystallinity enhanced [17] and finally, at 150 °C it can be observed that MoO_3 presents an amorphous structure.

Copper Oxide (CuO)

We also studied the crystalline structure of the CuO used as a p-type semiconductor in PSCs. CuO is an ideal HTL for PSCs with a good matching to the perovskite energy levels. For instance, Sun *et al.* applied CuO into inverted architecture (ITO/PEDOT:PSS/Perovskite/PCBM/BPHEN/Ag) achieving a PCE of 16.9 % [18].

The XRD spectra of the copper oxide powder at different temperatures are shown in **Figure 3.2 (e)**. At low temperatures, between 150 °C and 250 °C, a copper acetate form can be observed due to the synthesis precursors, such as copper (II) acetate monohydrate. This is a significant sign that a higher temperature is required for a good crystallization, in order to obtain CuO. The crystal structure of this copper acetate is tetragonal (a=13.36 Å, b=13.36 Å

and c=15.08 Å), in good agreement with patterns from literature (reference code 00-027-1126). We also observed a change from copper acetate to CuO when the temperature was increased up to 350 °C. At 350 °C, a CuO phase in a monoclinic system was formed, with C2/c symmetry [19], matching the corresponding patterns from the literature (reference code-00-045-0937).

Vanadium Pentoxide (V_2O_5)

V_2O_5 is a good candidate as a HTL in PSCs and an alternative replacement to PEDOT:PSS or Spiro-OMeTAD.V_2O_5 is demonstrated to form an efficient hole injection/collection junction with the perovskite absorber material [20]. For instance, Peng *et al.* incorporated solution processed V_2O_x into PEDOT:PSS and obtained 17.5 % PCE [21].

The XRD spectra corresponding to this oxide are shown in **Figure 3.2 (f)**. The V_2O_5 phase is clearly present at 250 °C. At 350 °C, the crystallinity of the peak increases. An orthorhombic crystal structure, with Pmmn space group, is common for both temperatures with the following lattice parameters; a=11.510 Å, b=3.559 Å and c=4.371 Å, in good agreement with the pattern from the database (reference code 00-009-0387). At the lower temperature of 150 °C, these peaks can be mainly indexed as the $V_2O_5.1.6H_2O$ orthorhombic phase, in good agreement with pattern from database (reference code 00-040-1296). And some peaks from the orthorhombic phase $V_2O_5$are also present (blue peaks)[22].
The V_2O_5 developed in our group hasa 2D layered van der Waals (vdW) structure. The material isobtained as sol-gel in water and shows good crystallinity even at RT. For this reason, this solvent-free water-based 2D oxide is, together with ZnO, another oxide suitable for the fabrication of PSCs on flexible (plastic) substrates.

3.3 Analysis of thin film thickness by Ellipsometry

The analysis of the thickness of the TMOs films was carried out by applying the ellipsometry technique. The variation of the oxide thin film thickness was carried out by the optimization of the spin speed of the spin coater during thin film fabrication. Once prepared and annealed on FTO substrates, the TMOs films were analysed and the data acquired with the

ellipsometry technique. In order to build a proper model, the optical properties of both the oxide films and the FTO substrate must be first determined, by UV-Visible technique. Results are shown in **Figure 3.3.** The refractive index (n) describes how fast light propagates through the material and the extinction coefficient is a measurement of how strongly a molecular species absorbs light at a given wavelength. The higher the complex refractive index, the denser and more compact the oxide thin film layer is. However, it has been demonstrated that a decrease of the refractive index with a decrease of thickness layer not always occur[23].

In the case of inverted architecture PSCs, the thickness of the p-type semiconductor oxide NiO and n-type semiconductor ZnO were determined. Meanwhile, TiO_2 thickness used in C-based PSCs were studied by profilometry technique. As shown in **Figure 3.3 (a)**, the thicknesses of the oxides determined by Ellipsometry can be easily varied withinthe 30 – 110nmrange.

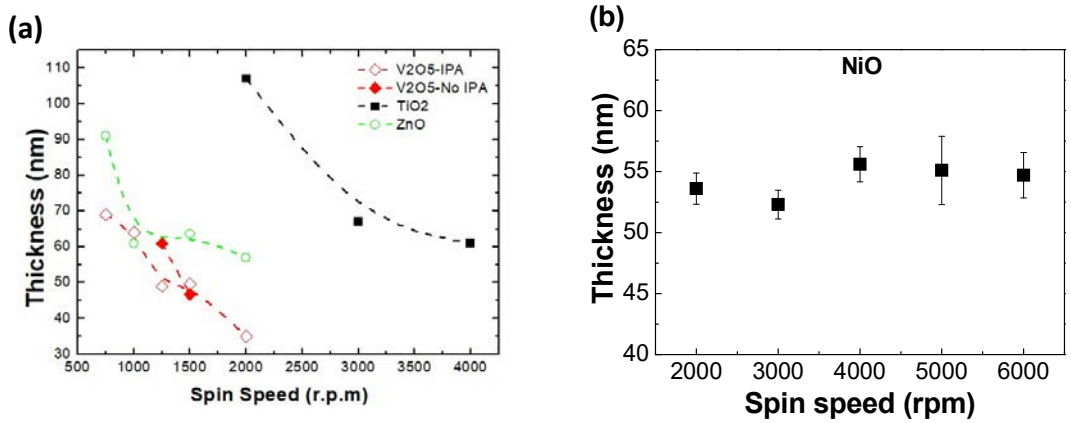

Figure 3.3 (a) Thickness of the TMOs thin films vs. the spin speed during fabrication as determined by ellipsometry. **(b)** Thicknesses of the NiO thin film obtained from ellipsometry.

In the case of NiO, there was no significant effect of the spin speed on the oxide thickness as observed in **Figure 3.3 (b).** In the analysed spin speed range, between 2000 and 6000 rpm, the film thickness was obtained in the 50-60 nm range. In all cases, the thickness values obtained are in good agreement with those required in PSCs. As compared to recent studies, You *et al.* employed approximately 80 nm thick NiO_x film while for the ETL they used 70 nm thick ZnO on an ITO substrate, which effectively worked as a good HTL and ETL, respectively, leading to excellent photovoltaic performance of up to 16 % PCE [4].

3.4 Optical properties of thin films: Band Gap analysis by UV-Vis

UV-Vis spectroscopy was used to analyse the optical properties of these oxides as thin films, at different sintering preparation temperatures and the results are shown in **Figure 3.4**. In order to minimize optical losses in the thin film photovoltaic device it is essential that the TMOs layer exhibit low absorption.

The thin films were prepared on FTO substrates using the same volume of sol-gel solution and coated at the same spin speed. UV-Vis absorbance of the samples was measured using a FTO slide as the reference. In the case of NiO, the films show an absorption band at ≈326 nm (**Figure 3.4 (a)**). At 150 °C, an additional band is found around 500 nm, which can be attributed to the presence of the corresponding hydroxide, as will be proved by XPS analysis (**Figure 3.7**). For TiO_2(**Figure 3.4 (b)**), a broad band absorption is observed at around 490 nm. This band shifts towards lower wavelengths when the sintering temperature is increased up to 450 °C, at which the absorption band stabilises at about 400 nm: This shift has been attributed to the gradual transformation of Titanium hydroxides into oxides, as found in XPS spectra (**Figure 3.15**)[22].

The ZnO films showan absorption band around 357 nm, with no significant differences between sintering temperatures (**Figure 3.4 (c)**). At 130°C, a shoulder around 400nm can be observed, which is related to a lower crystallinity of the oxide as demonstrated by XRD. Regarding MoO_3, thespectra are very similar at lower temperatures, whereas at 350°C a clear change in the trend of the spectrum can be observed [see **Figure 3.4 (d)**]. This effect could be due to the different oxidation states (observed by XPS) of the MoO_3as the temperature increases: at 150°C, a Mo^{5+} species is present, whereas at higher temperatures the majority species is Mo^{6+} (**Figure 3.10**). One has to take into account that XPS is a surface technique while UV-Vis is not,thus the comparison between both techniques is not straightforward. CuO (**Figure 3.4 (e)**) shows very similar absorption profiles for the 250°C-350 °C temperature range,in the region below 700nm. At 150°C, the profile was slightly different, which can be attributed to the presence of copperacetate, whose presence are confirmed by XPS and XRD analyses (**Figure 3.12** and **Figure 3.1 (e)**, respectively)[19].

And finally, for the V_2O_5(**Figure 3.4 (f)**) no significant differences between temperatures can be observed. All the samples show a band around 400nm, with almost no absorption above 500 nm. A slightly different trend for the sample obtained at 120 °C could be related to the reduction to V^{4+}, which is demonstrated by XPS analysis (**Figure 3.14**).

UV-Vis analyses are also used to calculate the E_g of the thin films taking into account the fundamental absorption edge of the films. This optical E_g is estimated using Tauc's equation:

$$(\alpha h\upsilon)^2 = A(h\upsilon - Eg), \tag{3.1}$$

Where, hυ is the photon energy and A is a proportionality constant. The variations of $(\alpha h\upsilon)^2$ versus the photon energy (hυ) for each oxide are plotted in **Figure 3.5** and summarized in **Table 3.1**. The extrapolation to α=0 gives the E_g value [24]. **Table 3.1** shows the E_g values of TMOs depending on the temperature and **Figure 3.5** shows the estimation of E_g for NiO, TiO_2, ZnO, MoO_3, CuO and V_2O_5.

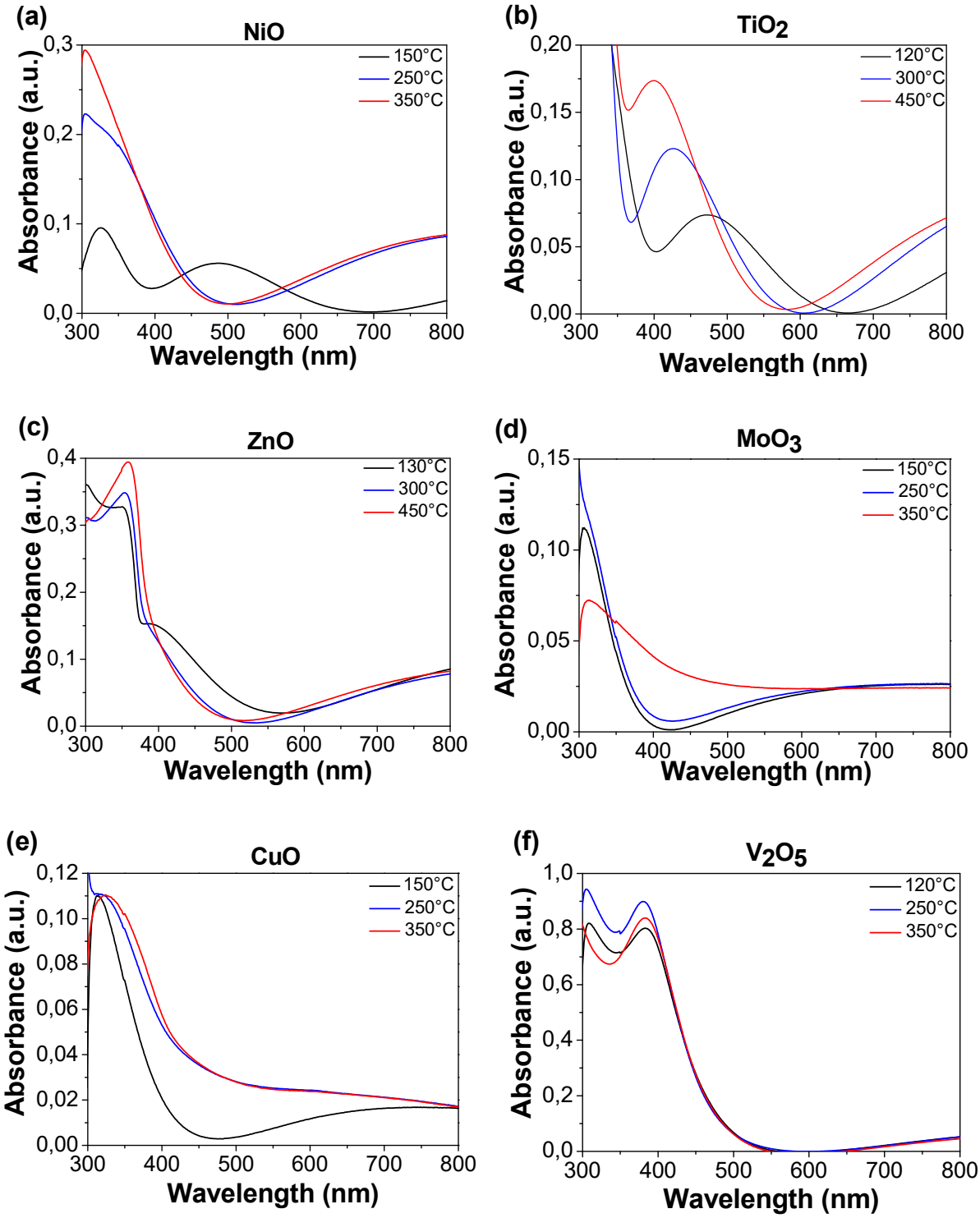

Figure 3.4 UV-Vis absorption spectra of studied TMOs employed as an HTL and ETL with different annealing temperatures. **(a)** NiO, **(b)** TiO_2, **(c)** ZnO, **(d)** MoO_3, **(e)** CuO and **(f)** V_2O_5.

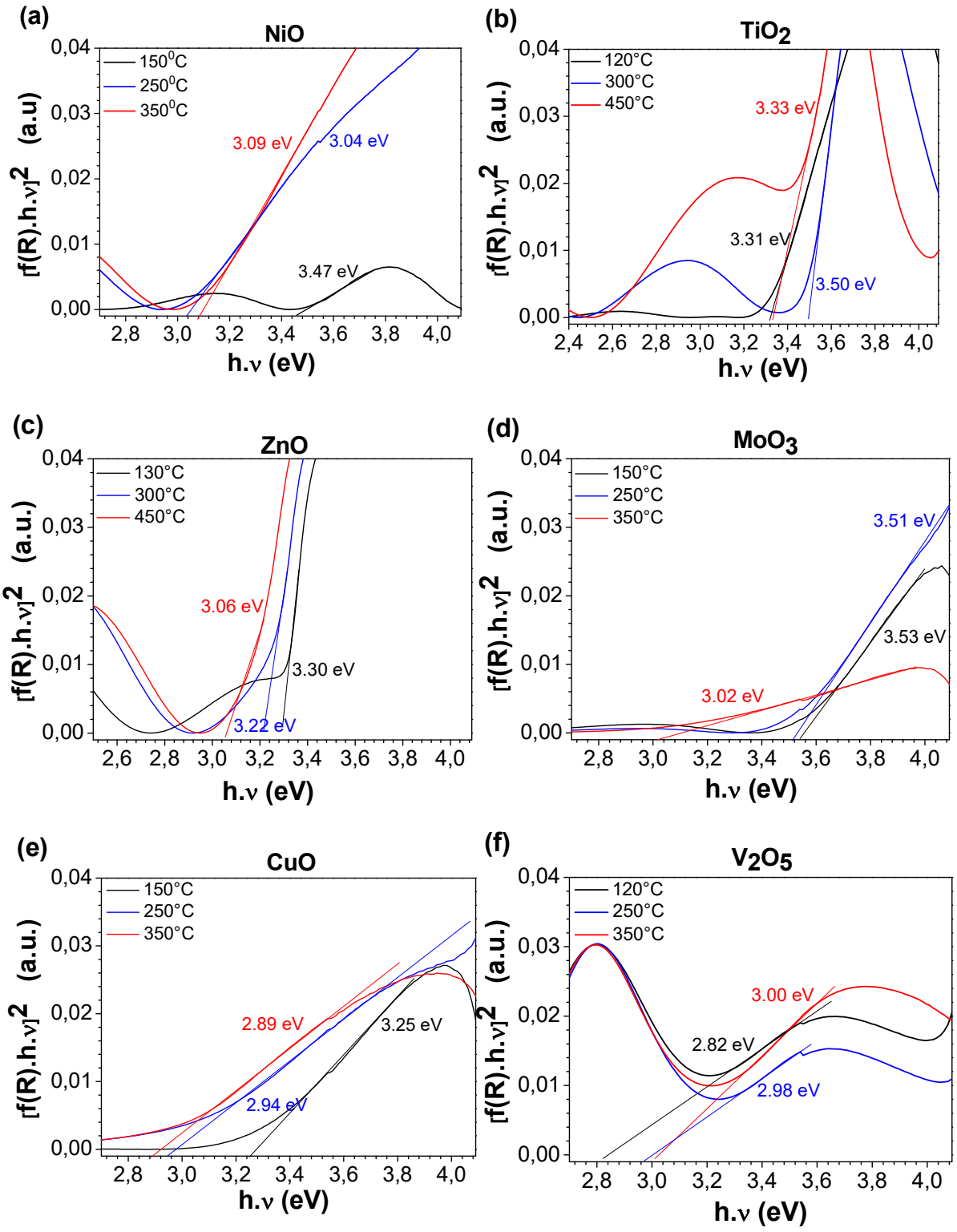

Figure 3.5 Estimation of Eg by plots of $(\alpha h\upsilon)^2$ against hυ for TMOs at different sintering temperatures. **(a)** NiO, **(b)** TiO_2, **(c)** ZnO, **(d)** MoO_3, **(e)** CuO and **(f)** V_2O_5.

Table 3.1 Experimental Eg values of the TMOs depending on the temperature.

Oxide	Temperature (°C)	Eg(eV)
NiO	150	3.5
	250	3.0
	350	3.1
TiO_2	120	3.3
	300	3.5
	450	3.3
ZnO	130	3.3
	300	3.2
	450	3.1
MoO_3	150	3.5
	250	3.5
	350	3.0
CuO	150	3.3
	250	2.9
	350	2.9
V_2O_5	120	2.8
	250	2.9
	350	3.0

These experimental values are in good agreement with those found in the literature. For example, Bouzidi *et al*., reported the E_g for MoO_3 located between 3.1 and 3.3 eV depending on the substrate temperature by the spray pyrolisis technique [25]. For the CuO_x, a direct bandgap of 2.4 eV was determined[26]. Teran-Escobar *et al.* calculated an optical E_g for fresh samples of V_2O_5 for the value of 2.7 eV [27]. In the case of the well-known TiO_2, the bandgaps of the rutile and anatase phase are 3.0 and 3.2 eV, respectively [28]. For ZnO films the optical E_g energy is 3.2 eV [29] and finally, NiO is a p-type semiconductor oxide with a direct E_g of 3.4 eV [30].

3.5 Study of TMOs by Photoelectron Spectroscopy (XPS-UPS)

Photoelectron Spectroscopy is a surface sensitive and element specific technique used for characterizing surfaces and interfaces of materials. The technique is based on the photoelectric effect, which was experimentally observed for the first time in 1887 by Heinrich Rudolf Hertz [31]. The photoelectric effect was explained by Albert Einstein in 1905 [32], for which he was awarded the Nobel Prize in Physics in 1921, and describes how

electrons are emitted from a material when illuminated by photons having an energy exceeding a threshold value, providing the following formula:

$$h\upsilon = E_B + E_K + \varphi, \tag{3.2}$$

where E_K is the kinetic energy, E_B is the binding energy and$\varphi$is the WF (in metals). **Figure 3.6** shows the energy levels diagram of a semiconductor.

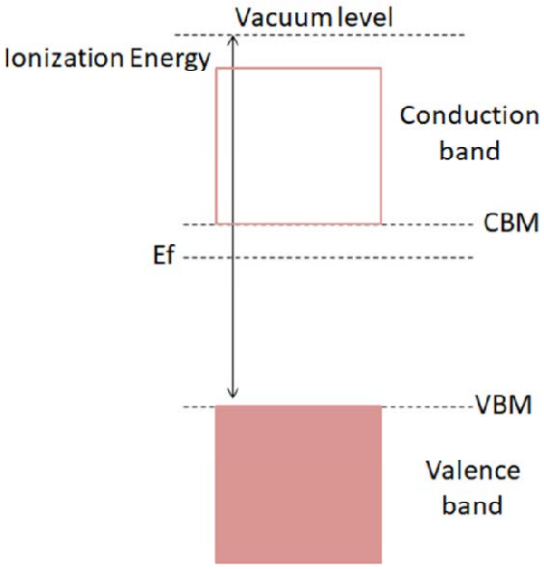

Figure 3.6 Energy levels diagram of a semiconductor.

To obtain a photoelectron spectrum, the number of emitted photoelectrons are measured as a function of the kinetic energy for a given photon energy. Photoelectron spectroscopy is usually divided into core level and valence level, depending on the orbitals involved. Core level refers to localized levels with atomic character, usually at higher binding energies, while valence levels have a delocalized character and are found at lower binding energies.

Here, XPS and UPS were performed in order to investigate the possible changes in chemical composition, E_g and WF, in relation to different sintering temperatures. For the XPS core-shell measurements a monochromatic Al Kα radiation (hυ=1486.6 eV) was employed and a monochromated He I photon source (hυ=21.22 eV) for UPS measurements. For further information of the technique, see Chapter 2. The analysis was performed using the Casa XPS

software and spectra were calibrated in binding energy with C1s peak assumed at 284.8eV, as reported by Moulder *et al.*[33]

The IP is calculated from the expression:

$$IP = \left(\left(21.2 - (SCO - VBM)\right) eV, \right. \tag{3.3}$$

where 21.2 eV corresponds to the excitation energy used, He (I), and the secondary electrons cut off (SCO) is the lowest detected kinetic energy. A bias of -10 V must be applied in order to clear the analyser.

3.5.1 Hole Transport Materials (NiO, MoO_3, CuO and V_2O_5)

This section describes the characterization of the oxides NiO, MoO_3, $CuO_x$and V_2O_5 by photoemission techniques. The use of NiO as an HTL in an inverted planar PSC structure will be described in Chapter 4 of this thesis.

a) NiO

Figure 3.7 (a) shows the XPS spectra of the Ni 2p region and **Figure 3.7 (b)** the O1s lines measured at different preparation temperatures and normalized to the C1s energy reference (284.8 eV). Charging, induced by the insulating character of the material, is in the 0.3-0.6 eV range, as determined from the C1s actual position. This contribution was taken into account in the UPS spectra for each specific temperature.

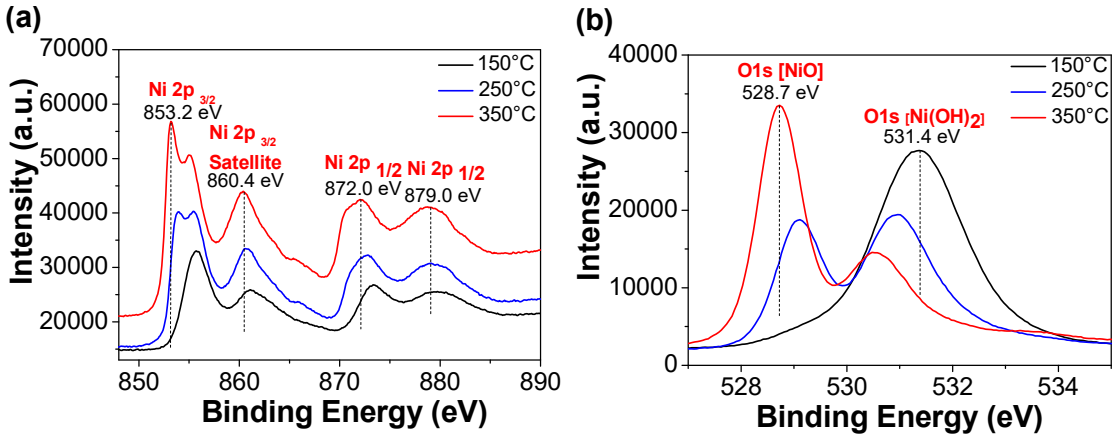

Figure 3.7 (a)XPS Ni 2p $_{3/2}$ and Ni 2p $_{½}$ core level spectra and **(b)**XPS O 1s core level spectra measured for NiO after sintering at 150°C, 250°C and 350 °C.

As shown in **Figure 3.7** a clear evolution as a function of the sintering temperature can be observed. **Figure 3.7 (a)** evidences the presence of $Ni(OH)_2$ and NiO from the characteristic $2p_{3/2}$ 855.6 and 853.6 eV binding energies, respectively [34][35]. At low sintering temperatures the surface is composed essentially of $Ni(OH)_2$and the NiO contribution increases for increasing temperature. Thus, temperatures as high as 350 °C are required for the formation of NiO. In analogy to **Figure 3.7 (a)**, **Figure 3.7 (b)** shows the evolution from $Ni(OH)_2$, with a 531.4 eV binding energy, at 150 ^{o}C to a characteristic of Ni-O bonding, with a peak at 528.7 eV [36].

In order to determine the IP of the samples, the SCO and the VBM have to be determined (see **Eq. 3.3**). This is shown in **Figure 3.8**, where both values are obtained by extrapolation, resulting in VBM=0.6 eV and SCO=16.6 eV for NiO samples prepared at 250 °C.

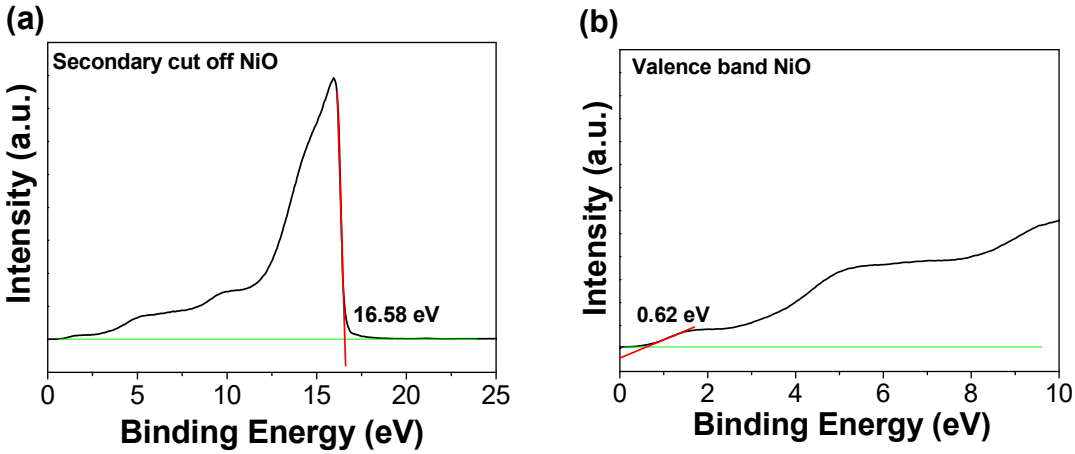

Figure 3.8 Determination of**(a)**SCOand **(b)** VBM for NiO prepared at 250 ^{o}C.

From **Eq.3.3** we obtain IP values of 4.9 and 4.2 eV at 250 ˚C and 350 ˚C, respectively. These experimental values are in good agreement with the data from the literature, for example, Stevanovic*et al.* reported an IP of 4.9 eV for the NiO using computational studies[30].The corresponding VBM values were 0.6eV at 250°C and 0.8eV at 350°C. Taking into account the shifts in the XPS measurements, (0.3 eV shift for the NiO at 250 °C and 0.6 eV shift for the NiO at 350 °C) the corrected real values for the VBM were 0.3 eV at 250 °C and 0.2 eV at 350 °C, respectively. **Figure 3.9** shows the energy levels of the NiO at different preparation temperatures. We can also conclude that NiO is a p-type semiconductor, because the Fermi level lies closer to the VBM.

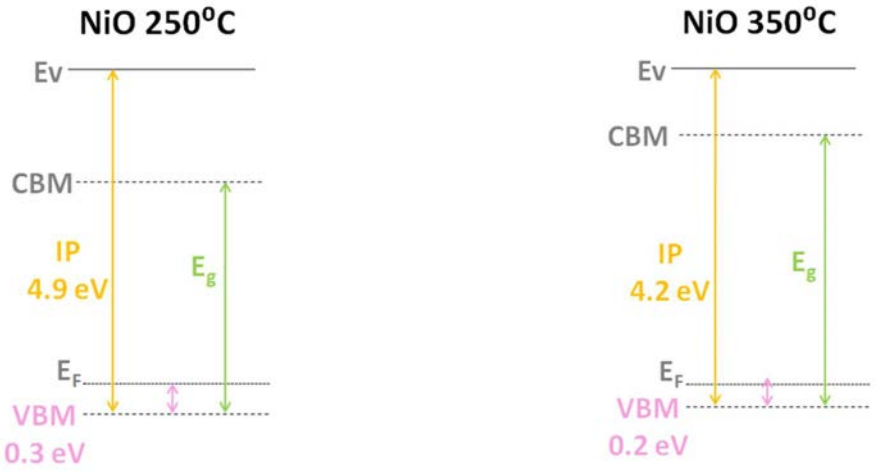

Figure 3.9 Band diagram of NiO thin films at 250 °C (left) and 350 °C (right).

b)MoO_3

Figure 3.10 (a) shows the XPS spectra of the Mo 3d region and **Figure 3.10 (b)** the O1s lines measured at different preparation temperatures and normalized to C1s (284.8 eV). The observed charging is 0.7 eV for 150 °C, while at 300 °C the shift is about 0.1 eV and finally at 450°C there is no significant shift. A main peak at 232.7 eV is attributed to $Mo3d_{5/2}$ corresponding to Mo^{6+} oxidation state [37]. From **Figure 3.10 (b)** we observe that the spectral weight evolves from molybdenum hydroxide (532.8 eV) to Mo-O bonding (530.9 eV).

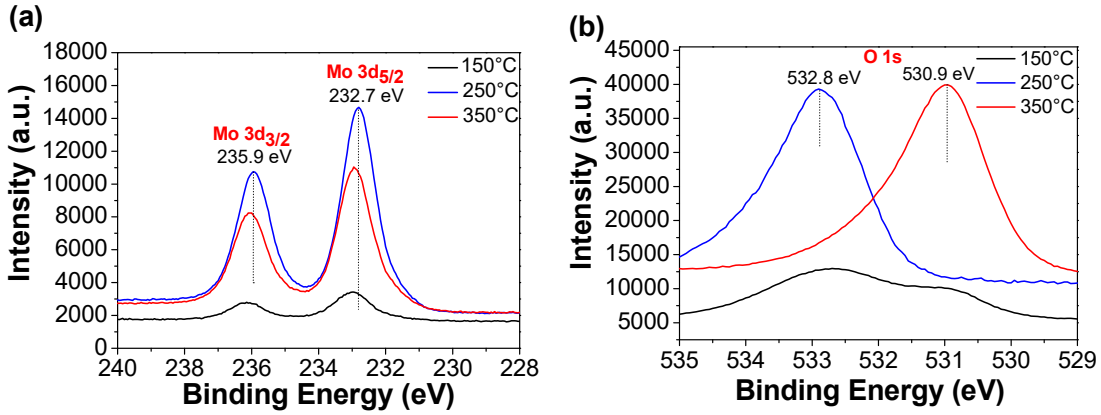

Figure 3.10 XPS spectra of the Mo 3d **(a)** and O1s **(b)** lines of MoO_3 thin films corresponding to different preparation temperatures.

Figure 3.11 shows the energy levels at 250°C and 350°C for the MoO_3 films. The IP lies in the 7.8-7.9eV range and the VBM is 3.2eV at 250°C and 3.4eV at 350°C, following the procedure

previously discussed for Ni. In this case for $MoO_3$the energy correction is not needed since no charging was observed.

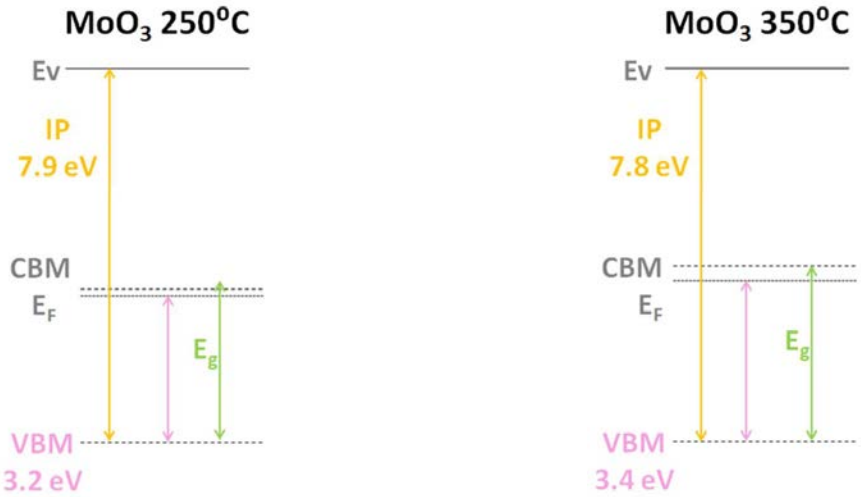

Figure 3.11 Band diagrams of MoO_3 thin films at 250 °C (left) and 350 °C (right) determined by UPS.

b)CuO

Figure 3.12 (a) shows the XPS spectra of the Cu 2p region and **Figure 3.12 (b)** the O1s lines measured at different preparation temperatures and normalized to the adventitious C1s line. For the CuO p-type semiconductor, no significant shift in the XPS spectra was observed (less than 0.1 eV). **Figure 3.12 (a)** shown the characteristic spectra of CuO with a main $Cu2p_{3/2}$peak at 933.9eV and the associated satellites [19][38]. The satellite distribution is characteristic of materials having a d^9 configuration in the ground state [39]. Thus, the spectra reveal a Cu^{2+} oxidation state. The XPS spectra of O1s, as shown in **Figure 3.12 (b)**, are composed of two main components: first, the signal at binding energy located at about 529.7 eV is attributed to the oxygen present in the form of oxide (O^{2-}). Meanwhile, the peak at 530.9 eV is assigned to the surface oxygen, from different species, such as hydroxyl or carbonate groups [40].

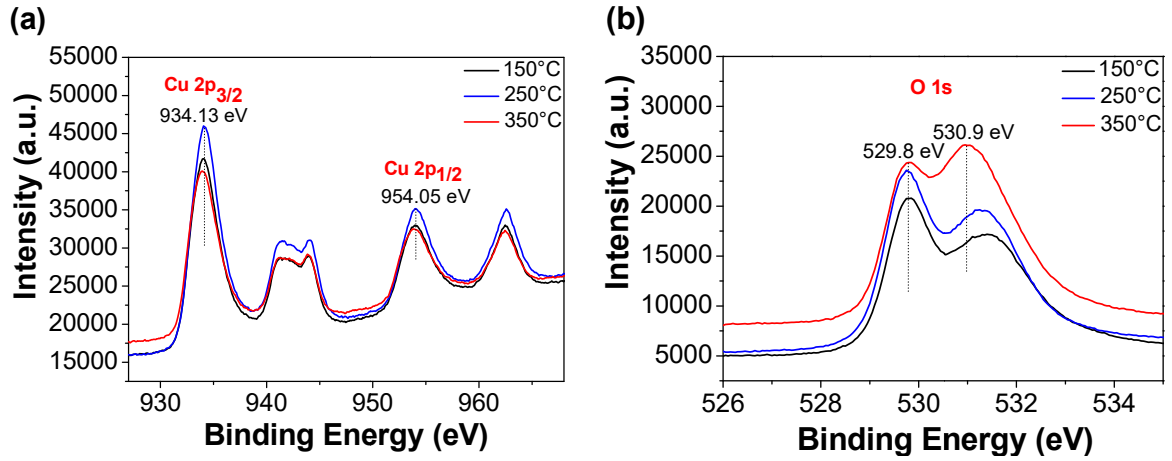

Figure 3.12 XPS spectra corresponding to **(a)** Cu 2p and **(b)** O1s lines of CuO thin films corresponding to different preparation temperatures.

Figure 3.13 shows the energy levels at 250°C and 350°C for CuO. The IP values lies in the 6.7-7.1 eV range and the VBM is located at 2.1 eV at 250°C and at 2.3 eV at 350°C.

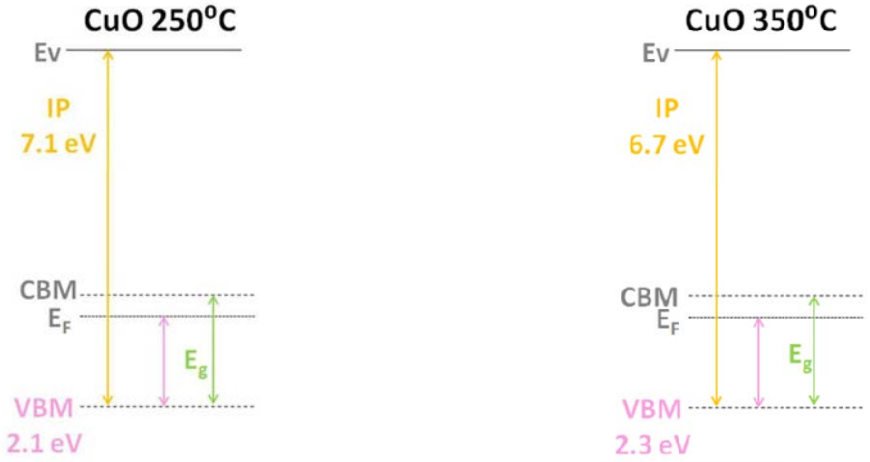

Figure 3.13 Band diagrams of CuO thin films at 250 °C (left) and 350 °C (right) determined by UPS.

d) V_2O_5

Figure 3.14 (a) shows the XPS spectra of the V 2p and O1s regions measured at different preparation temperatures and referred to the 284.8 eV line. No charging effect was detected from XPS spectra. The 517.3 eV peak, corresponding to the$V2p_{3/2}$ line is associated to V^{5+}, while the shoulder at lower binding energy, 516.4 eV, is characteristic of V^{4+} species. The 530.2 eV feature corresponds to O1sand originates from lattice O^{2-}oxygen. Meanwhile, the shoulder which appears at around 532 eV can be attributed to hydroxyl groups [21]. he

energy levels for V_2O_5 are shown in **Figure 3.14 (b)**. The IP and the VBM values show a great similarity between 250 °C and 350 °C.

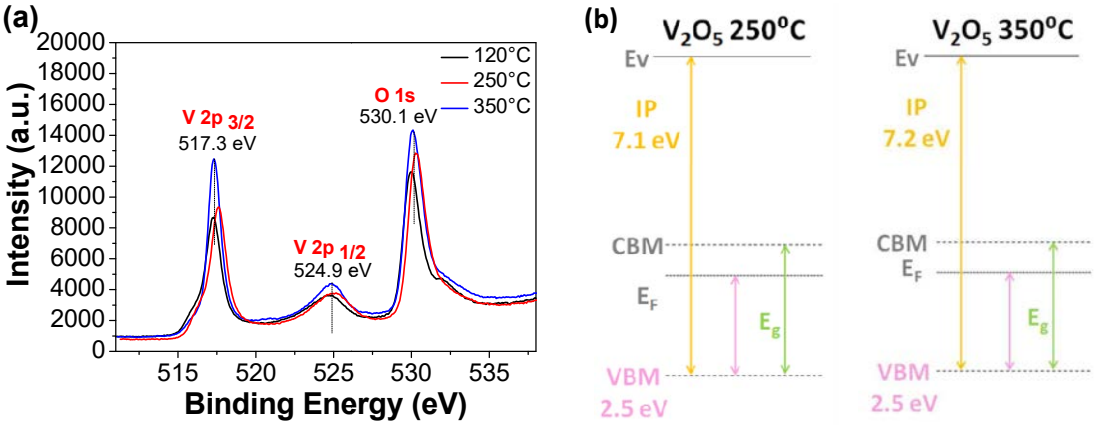

Figure 3.14 (a) V 2p $_{3/2}$, V 2p $_{½}$ and O1s core level of V_2O_5 thin films at different preparation temperatures obtained by XPS and **(b)** band diagram of V_2O_5 thins films at 250 °C (left) and 350 °C (right) determined by UPS.

3.5.2 Electron Transport Materials (TiO_2 and ZnO)

The electronic structure of TiO_2 and ZnO will be discussed next. The application of the well-known n-type semiconductor TiO_2 in fully printable C-based PSC, as a holes blocking and an ETL will be also discussed in Chapter 5 of this thesis. Also, the use of ZnO as an ETL in an inverted planar structure will be described in Chapter 4 of this thesis.

a) TiO_2

Figure 3.15 (a) shows the XPS spectra of the Ti 2p region and **Figure 3.15 (b)** the O1s lines measured at different preparation temperatures. Here, the binding energies are referreed to the well-known 458.5eV of $Ti2p_{3/2}$, characteristic of Ti^{+4}[41].The observed energy shift is about 1eV shift due to sample charging. The XPS spectra exhibit the spin-orbit lines $Ti2p_{3/2}$and $Ti2p_{1/2}$. The XPS O1s line exhibits a main peak at 529.8 eV, as seen in **Figure 3.15 (b)**, characteristic of transition Ti-O bonding[42]. Also, a less intense feature at around 532 eV can be observed which is characteristic surface hydroxides. With an increase of the TiO_2 annealing temperature his signal becomes less intense.

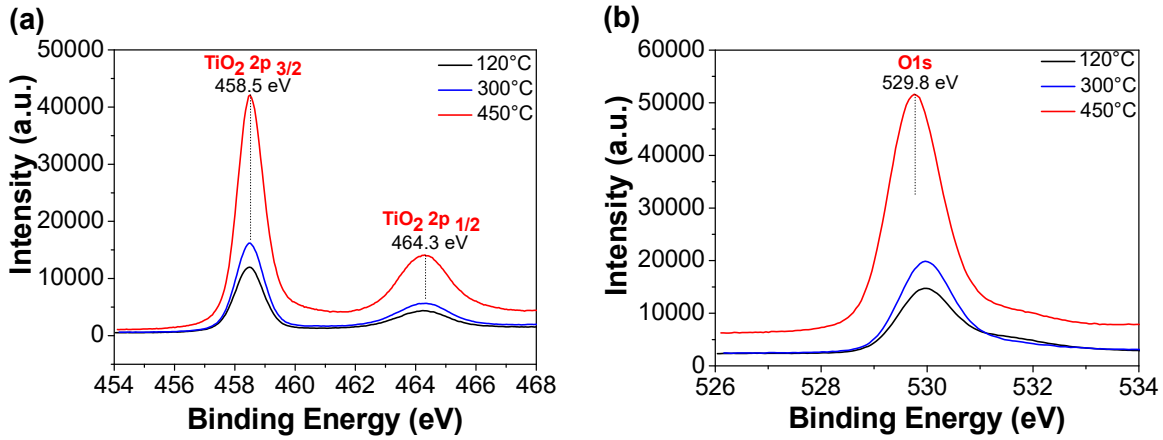

Figure 3.15 (a) Ti 2p $_{3/2}$ and Ti 2p $_{½}$ and**(b)** O1s core level spectra measured for TiO_2 at different preparation temperatures by XPS. Binding energies referred to $Ti2p_{3/2}$ (458.5 eV).

In order to achieve a more precise evaluation of the VBM position, the slopes were calculated from both XPS and UPS spectra [see **Figure 3.16**]. From the XPS spectrum we obtain a VBM value of 3.1 eV, which becomes 2.1 eV after normalization to the 458.5 eV value. Note that the VBM position as calculated from the UPS spectrum is 3.5 eV. This shift between XPS and UPS is due to the differential charging caused from using two different radiation sources, Al Kα and He I, respectively. Thus, for UPS a total charging displacement of 1.4 eV was found. Thus, the VBM value for TiO_2 at 450 °C is 2.1 eV.

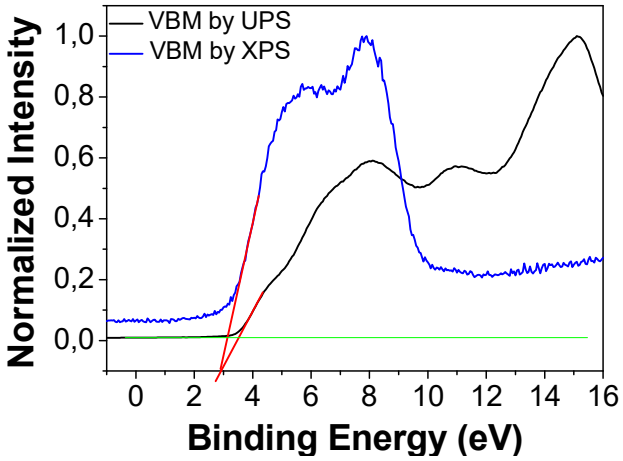

Figure 3.16 Comparative graph between the VBM extracted from the XPS and UPS spectra.

Using **Eq. 3.3** we obtain an IP of value of 7.3 eV at 450 °C. For the TiO_2 at 300 °C, the same procedure was carried out, assuming a total shift of 1.02 eV (taking into account 0.65 eV shift from Ti2p $_{3/2}$ as a reference and 0.37 eV shift between XPS and UPS spectra). For the TiO_2 at 300 °C the VBM was 2.4 eV and the IP value was 7.7 eV. **Figure 3.17** shows the band diagrams at both temperatures.

Figure 3.17 Band diagram of TiO_2 thin films at 300 °C (left) and 450 °C (right) determined by UPS and XPS.

b) ZnO

Figure 3.18 (a) shows the XPS spectra of the Zn2p region and **Figure 3.18 (b)** the O1s lines measured at different preparation temperatures and normalized to the 284.8 eV energy of adventitious carbon. For the ZnO a charging displacement of 0.7 and 0.6 eV was present for the samples in XPS spectra for at 300 °C and 450 °C, respectively. Symmetrical peaks are found in **Figure 3.18 (a)** located at 1021.3 eV for the most intense signal attributed to the $Zn2p_{3/2}$ feature, in agreement with values found by Hosseini *et al.*[43].

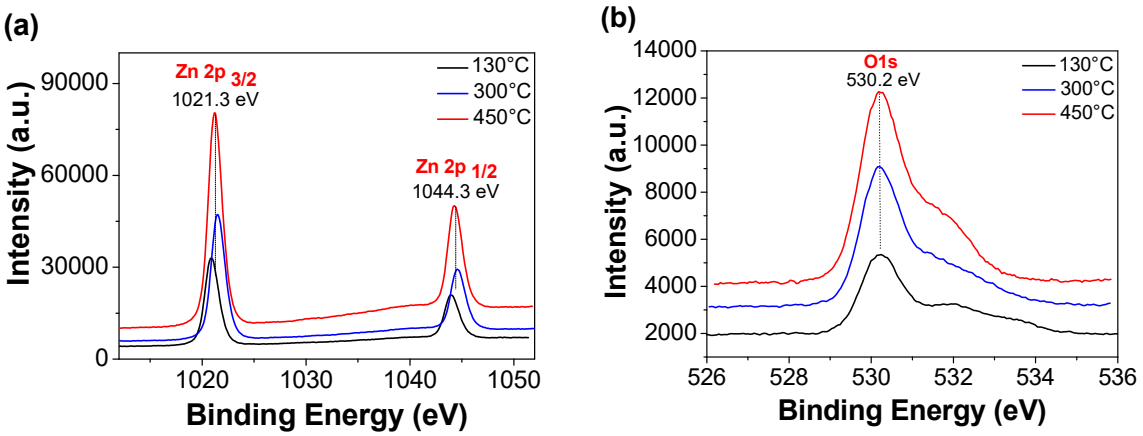

Figure 3.18 XPS**(a)** Zn 2p $_{3/2}$ and Zn 2p $_{½}$ and **(b)** O1s spectra measured for ZnO at different temperatures by XPS. Energies referred to C1s 284.8 eV.

As shown in **Figure 3.18 (b)**, it can be clearly seen that the O1s exhibits two components. The peak at 530.2 eV corresponds to Zn-O bonding while the peak at higher binding energies, around 532 eV, is related to the hydroxyl group [43].

The energy level diagram of ZnO is shown in **Figure 3.19**. The same methodology mentioned before was applied in order to determine the VBM and the SCO for each temperature, taking charging into account. The experimental values remain close to IP (7.3 eV) and VBM (3.5 eV) values found in the literature [44]. ZnO is a n-type semiconductor, because of the Fermi level lies closer to the CBM.

Figure 3.19 Band diagram of ZnO thin films at 300 °C (left) and 450 °C (right) determined by UPS.

3.6. Summary of TMOs properties and selection of the best transport layers

In this chapter several properties of the semiconductors were analysed, from a crystallographic, optical and electronic point of view. **Table 3.2** and **Table 3.3** show a summary of these properties such as the crystal symmetry, E_g value, IP value and VBM value of the oxides related to different preparation temperatures for HTLs and ETLs, respectively.

Table 3.2 Summaryof XPS core level energies from NiO, CuO, V_2O_5, TiO_2 and ZnO.

Oxide	Temperature (˚C)	2p $_{3/2}$(eV)	2p $_{½}$ (eV)	O 1s (eV)
NiO	250	853.9	872.6	529.1
	350	853.2	872.1	528.7
CuO	250	934.1	954.1	531.3
	350	934.1	954.0	530.9
V_2O_5	250	517.3	524.9	530.1
	350	517.6	524.9	530.3
TiO_2	300	458.5	464.3	529.9
	450	458.5	464.3	529.8
ZnO	300	1021.4	1044.6	530.2
	450	1021.3	1044.3	530.2

Table 3.3 Summaryof XPS core level energies from MoO_3.

Oxide	Temperature (˚C)	3d $_{5/2}$(eV)	3d $_{3/2}$(eV)	O1s (eV)
MoO_3	250	232.7	235.9	532.9
	350	232.9	236.1	530.9

Table 3.4 Summaryof oxide, preparation temperature, symmetry, E_g, IP and VBM position for the selected HTLs films.

Oxide	Temperature (˚C)	Symmetry	E_g(eV)	IP (eV)	VBM (eV)
NiO	250	cubic	3.0	4.9	0.3
	350	rhombohedral	3.1	4.2	0.2
MoO_3	250	hexagonal	3.5	7.9	3.2
	350	orthorombic	3.0	7.8	3.4
CuO	250	tetragonal	2.9	7.1	2.1
	350	monoclinic	2.9	6.7	2.3
V_2O_5	250	orthorombic	2.9	7.1	2.5
	350	orthorombic	3.0	7.2	2.5

Table 3.5 Summary of oxide, preparation temperature, symmetry, E_g, IP and VBM position for the selected ETLs films.

Oxide	Temperature (˚C)	Symmetry	E_g(eV)	IP(eV)	VBM(eV)
TiO_2	300	amorphous	3.5	7.7	2.4
	450	tetragonal	3.3	7.3	2.1
ZnO	300	hexagonal	3.2	6.9	3.5
	450	hexagonal	3.1	7.0	3.1

A good energy level alignment is an important requirement for a proper charge transfer between the layers of the PSC. The TMOs guarantees this requirement in order to achieve excellent transfer from the FTO to perovskite absorber and from perovskite absorber to back electrode. **Figure 3.20** shows the energy level alignment of the TMOs used in this thesis such as NiO, TiO_2 and ZnO. **Figure 3.21 (a)** shows the energy level alignment for the inverted perovskite architecture and **Figure 3.21 (b)** shows the energy level alignment for the carbon-based perovskite architecture.

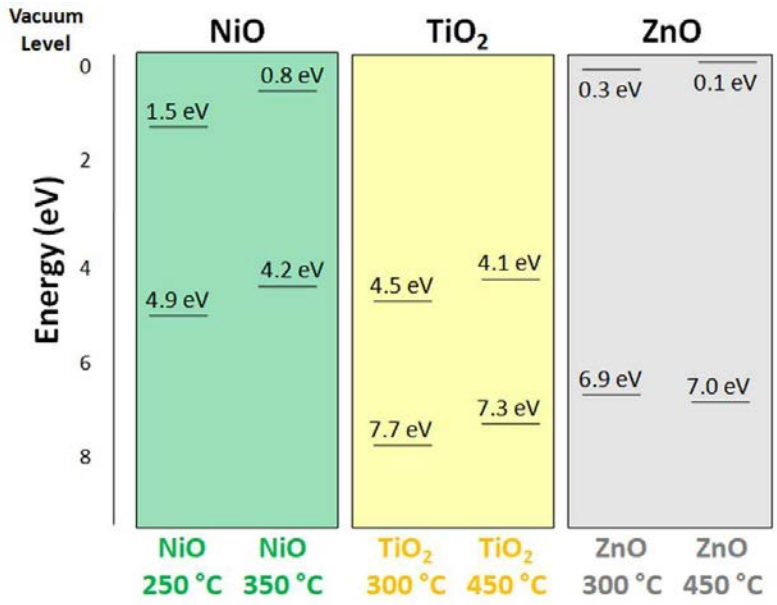

Figure 3.20 Energy level alignment for the TMOs used in this thesis: NiO, TiO_2 and ZnO.

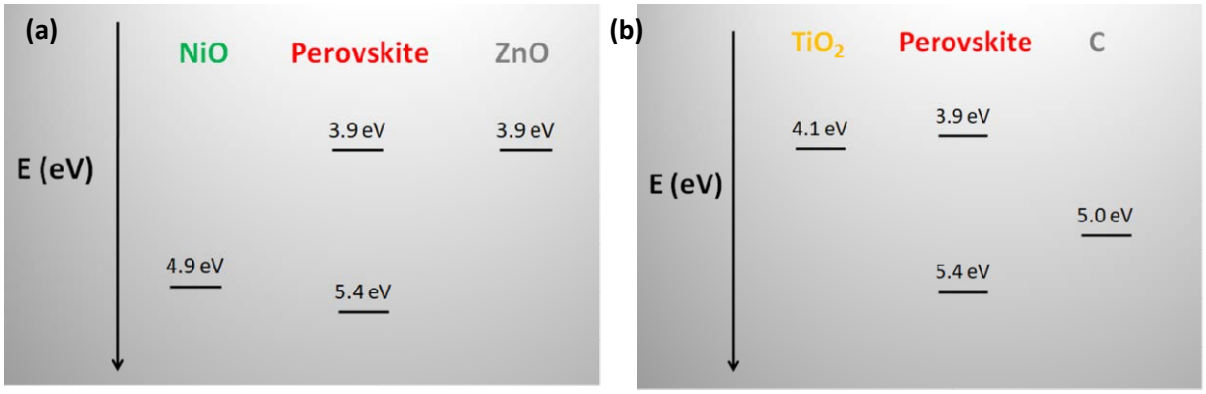

Figure 3.21 Energy level alignments for **(a)** inverted perovskite architecture and **(b)** carbon-based perovskite architecture, using data values of $CH_3NH_3PbI_3$ perovskite.

In summary, semiconductor oxides are promising materials to be applied in PSCs as a transport layer instead of the well-known spiro-OMeTAD or PEDOT:PSS. The spiro-OMeTAD is a widely-used HTL to obtain high-efficiency devices. However, the high costs and the limitation on the long-term stability is a problem for large-scale applications. In addition, additives and dopants must be inserted in order to achieve higher hole-mobility and conductivity [45]. In this sense, PEDOT:PSS presents some drawbacks such as low electrical conductivity. Also, the acidic nature of PEDOT:PSS could cause corrosion in the interface of the device [46]. The main function of the HTL material is to prevent the direct contact between the perovskite and the metal electrode and extract positive charge from perovskite absorber to the electrode. We demonstrate that TMOs are an excellent alternative as a

transport layers because they can be synthesized at low temperatures achieving the desired crystallinity good transparency and a good energy level matching for the complete device [47]. Taking all the above information into account, all these oxides are available to use as a HTL and ETL in PSCs. However, in this thesis we focused our studies only on NiO, ZnO and $TiO_{2,}$ as transport layers in PSCs, because are the most studied as HTL and ETL, respectively.

3.7 Conclusions

In this chapter, we have demonstrated that the study of the optimum sintering temperature, from the electronic, crystallographic and optical point of view, is very important in order to achieve a proper TMO for an interface layer, acting as an HTL or ETL, in PSCs. Several spectroscopic techniques were presented that were used to characterize these oxides as a function of the sintering temperature.

From the XRD studies we conclude that the sintering temperatures directly affects the crystal structure of the oxides where the general trend was that as annealing temperature increased, the cristallinity increased and finally the desired oxide form was achieved.
An ellipsometry study was presented to determine the thicknesses of the corresponding TMOs thin films, which is very useful for the fabrication of inverted PSCs by the spin coating technique. The ranges of the thickness are between 30 and 110 nm.
Regarding the optical properties of the TMOs, no significant differences were observed by UV-visible studies in terms of absorption as a function of annealing temperatures. Generally, all the oxides showed a good transparency in the visible range, a relevant characteristic for PSCs. Furthermore, the experimental values found by applying the Tauc's method for the bandgaps were in accordance with literature values.
Finally, from the XPS studies, we identified the oxidation and reduction of the metals related to the several annealing temperatures and we also determined the oxidation states of the transition metals in TMOs, which fitted properly with literature values. From the XPS analysis, we detected that some spectra had a charging effect because of the insulating behaviour of the semiconductor oxides. These shifts were taken into account for the determination of the energy level diagrams obtained from UPS spectra. Also, the good

energy level matching between the CBM and VBM of the $CH_3NH_3PbI_3$ of the perovskite to the respective TMOs was justified.

We have demonstrated that all these TMOs are suitable to apply in PSCs due to these attractive crystallographic, optical and electronic properties.

3.8 References

[1] Lira-Cantu, M. “The future of semiconductor oxides in next-generation solar cells,” 1st ed, Elsevier, Singapore 2017, *p. 566*

[2] N. Talebian, M. R. Nilforoushan, and R. Ramazan Ghasem, “Enhanced photocatalytic activities of ZnO thin films: a comparative study of hybrid semiconductor nanomaterials,” *J. Sol-Gel Sci. Technol.*, vol. 64, no. 1, pp. 36–46, 2012.

[3] X. Xu *et al.*, “Hole Selective NiO Contact for Efficient Perovskite Solar Cells with Carbon Electrode,” *Nano Lett.*, vol. 15, no. 4, pp. 2402–2408, 2015.

[4] J. You *et al.*, “Improved air stability of perovskite solar cells via solution-processed metal oxide transport layers,” *Nat. Nanotechnol.*, vol. 11, p. 75, 2015.

[5] S. Yang, Y. Wang, P. Liu, Y.-B. Cheng, H. J. Zhao, and H. G. Yang, “Functionalization of perovskite thin films with moisture-tolerant molecules,” *Nat. Energy*, vol. 1, p. 15016, 2016.

[6] Y. Hou *et al.*, “Suppression of Hysteresis Effects in Organohalide Perovskite Solar Cells,” *Adv. Mater. Interfaces*, vol. 4, no. 11, p. 1700007, 2017.

[7] L. Zuo *et al.*, “Tailoring the Interfacial Chemical Interaction for High-Efficiency Perovskite Solar Cells,” *Nano Lett.*, vol. 17, no. 1, pp. 269–275, 2017.

[8] K. Mahmood, S. Sarwar, and M. T. Mehran, “Current status of electron transport layers in perovskite solar cells: materials and properties,” *RSC Adv.*, vol. 7, no. 28, pp. 17044–17062, 2017.

[9] P. Qin, Q. He, D. Ouyang, G. Fang, W. C. H. Choy, and G. Li, “Transition metal oxides as hole-transporting materials in organic semiconductor and hybrid perovskite based solar cells,” *Sci. China Chem.*, vol. 60, no. 4, pp. 472–489, 2017.

[10] J. Choi, S. Song, M. T. Hörantner, H. J. Snaith, and T. Park, “Well-Defined Nanostructured, Single-Crystalline TiO2 Electron Transport Layer for Efficient Planar Perovskite Solar Cells,” *ACS Nano*, vol. 10, no. 6, pp. 6029–6036, Jun. 2016.

[11] K. Lee *et al.*, “Efficient and moisture-resistant hole transport layer for inverted perovskite solar cells using solution-processed polyaniline,” *J. Mater. Chem. C*, vol. 6, no. 23, pp. 6250–6256, 2018.

[12] A. K. Jena, Y. Numata, M. Ikegami, and T. Miyasaka, “Role of spiro-OMeTAD in performance deterioration of perovskite solar cells at high temperature and reuse of the perovskite films to avoid Pb-waste,” *J. Mater. Chem. A*, vol. 6, no. 5, pp. 2219–2230, 2018.

[13] Z. Yuan, “Low-temperature synthesis of ZnO nanoparticles for inverted polymer solar cell application,” *J. Mater. Sci. Mater. Electron.*, vol. 25, no. 3, pp. 1289–1292, 2014.

[14] I. G. Valls, “González Valls, Irene; Lira Cantú, Mónica, dir.; Muñoz Tapia, María, dir. Vertically-aligned ZnO nanostructures for excitonic solar cells. [Barcelona]: Universitat

Autònoma de Barcelona, 2013. 1 recurs electrònic (238 p.). ISBN 9788449037863. Tesi doctora," 2013.

[15] F. Hou *et al.*, "Efficient and stable planar heterojunction perovskite solar cells with an MoO3/PEDOT:PSS hole transporting layer," *Nanoscale*, vol. 7, no. 21, pp. 9427–9432, 2015.

[16] L. Zheng, Y. Xu, D. Jin, and Y. Xie, "Novel Metastable Hexagonal MoO3 Nanobelts: Synthesis, Photochromic, and Electrochromic Properties," *Chem. Mater.*, vol. 21, no. 23, pp. 5681–5690, 2009.

[17] H. Hu, C. Deng, J. Xu, K. Zhang, and M. Sun, "Metastable h-MoO3 and stable α-MoO3 microstructures: controllable synthesis, growth mechanism and their enhanced photocatalytic activity," *J. Exp. Nanosci.*, vol. 10, no. 17, pp. 1336–1346, 2015.

[18] Q. Sun *et al.*, "Efficiency Enhancement of Perovskite Solar Cells via Electrospun CuO Nanowires as Buffer Layers," *ACS Appl. Mater. Interfaces*, vol. 10, no. 13, pp. 11289–11296, 2018.

[19] Y.-F. Lim, C. S. Chua, C. J. J. Lee, and D. Chi, "Sol–gel deposited Cu2O and CuO thin films for photocatalytic water splitting," *Phys. Chem. Chem. Phys.*, vol. 16, no. 47, pp. 25928–25934, 2014.

[20] W. Yan *et al.*, "Hole-Transporting Materials in Inverted Planar Perovskite Solar Cells," *Adv. Energy Mater.*, vol. 6, no. 17, p. 1600474, 2016.

[21] H. Peng *et al.*, "Solution processed inorganic V2Oxas interfacial function materials for inverted planar-heterojunction perovskite solar cells with enhanced efficiency," *Nano Res.*, vol. 9, no. 10, pp. 2960–2971, 2016.

[22] R. Pandiyan, N. Delegan, A. Dirany, P. Drogui, and M. A. El Khakani, "Probing the Electronic Surface Properties and Bandgap Narrowing of in situ N, W, and (W,N) Doped Magnetron-Sputtered TiO2 Films Intended for Electro-Photocatalytic Applications," *J. Phys. Chem. C*, vol. 120, no. 1, pp. 631–638, 2016.

[23] L. M. P. Kovalenko S.A, "Thickness dependences of optical constants for thin layers of some metals and semiconductors," *Semicond. Physics, Quantum Electron. Optoelectron.*, vol. 4, pp 352-357, 2001.

[24] T. K. Pathak, V. Kumar, H. C. Swart, and L. P. Purohit, "Electrical and optical properties of p-type codoped ZnO thin films prepared by spin coating technique," *Phys. E Low-dimensional Syst. Nanostructures*, vol. 77, pp. 1–6, 2016.

[25] N. B. A. Bouzidi H. Tabet-Derraz, C. Mathieu, B. Khelifa, "Effect of substrate temperature on the structural and optical properties of MoO3 thin film prepared by spray pyrolysis technique," *Mater. Sci. Eng. B.*, vol. 97, pp. 5–8, 2003.

[26] B. B. B. A. Asha Radhakrishnan*, "Structural and Optical Absorption Analysis of CuO Nanoparticles ," *Indian J. Adv. Chem. Sci.*, vol. 2, pp. 158–161, 2014.

[27] G. Terán-Escobar, J. Pampel, J. M. Caicedo, and M. Lira-Cantú, "Low-temperature,

solution-processed, layered V2O5 hydrate as the hole-transport layer for stable organic solar cells," *Energy Environ. Sci.*, vol. 6, no. 10, pp. 3088–3098, 2013.

[28] D. O. Scanlon *et al.*, "Band alignment of rutile and anatase TiO2," *Nat. Mater.*, vol. 12, p. 798, 2013.

[29] A. Davoodi, M. Tajally, O. Mirzaee, and A. Eshaghi, "Fabrication and characterization of optical and electrical properties of Al–Ti Co-doped ZnO nano-structured thin film," *J. Alloys Compd.*, vol. 657, pp. 296–301, 2016.

[30] V. Stevanović, S. Lany, D. S. Ginley, W. Tumas, and A. Zunger, "Assessing capability of semiconductors to split water using ionization potentials and electron affinities only," *Phys. Chem. Chem. Phys.*, vol. 16, no. 8, pp. 3706–3714, 2014.

[31] H. Hertz, "Ueber einen Einfluss des ultravioletten Lichtes auf die electrische Entladung," *Ann. Phys.*, vol. 267, no. 8, pp. 983–1000, 1887.

[32] A. Einstein, "Über einen die Erzeugung und Verwandlung des Lichtes betreffenden heuristischen Gesichtspunkt," *Ann. Phys.*, vol. 322, no. 6, pp. 132–148, 1905.

[33] J. F. Moulder, "Handbook of X-ray Photoelectron Spectroscopy: A Reference Book of Standard Spectra for Identification and Interpretation of XPS Data," *Phys. Electron.*, 1995.

[34] "XPSsimplifiedreference."https://xpssimplified.com/periodictable.php

[35] E. Martinez *et al.*, "Properties of innovative resistive memories studied by X-ray and UV photoemission," *Surf. Interface Anal.*, vol. 42, no. 6-7, pp. 783–786, 2010.

[36] D. T. Nguyen *et al.*, "Ellipsometric and XPS characterization of transparent nickel oxide thin films deposited by reactive HiPIMS," *Surf. Coatings Technol.*, vol. 250, pp. 21–25, 2014.

[37] S. Bai *et al.*, "Ultrasonic synthesis of MoO3 nanorods and their gas sensing properties," *Sensors Actuators B Chem.*, vol. 174, pp. 51–58, 2012.

[38] D. S. Murali, S. Kumar, R. J. Choudhary, A. D. Wadikar, M. K. Jain, and A. Subrahmanyam, "Synthesis of Cu2O from CuO thin films: Optical and electrical properties," *AIP Adv.*, vol. 5, no. 4, p. 47143, 2015.

[39] J. Ghijsen *et al.*, "Electronic structure of Cu2O and CuO," *Phys. Rev. B*, vol. 38, no. 16, pp. 11322–11330, 1988.

[40] M. C. Biesinger, B. P. Payne, A. P. Grosvenor, L. W. M. Lau, A. R. Gerson, and R. S. C. Smart, "Resolving surface chemical states in XPS analysis of first row transition metals, oxides and hydroxides: Cr, Mn, Fe, Co and Ni," *Appl. Surf. Sci.*, vol. 257, no. 7, pp. 2717–2730, 2011.

[41] E. Martínez-Ferrero *et al.*, "Nanostructured Titanium Oxynitride Porous Thin Films as Efficient Visible-Active Photocatalysts," *Adv. Funct. Mater.*, vol. 17, no. 16, pp. 3348–3354, 2007.

[42] F. Gracia, F. Yubero, J. P. Espinos, J. P. Holgado, A. R. González-Elipe, and T. Girardeau, “Correlation between optical properties and electronic parameters for mixed oxide thin films,” *Surf. Interface Anal.*, vol. 38, no. 4, pp. 752–756, 2006.

[43] S. M. Hosseini, I. A. Sarsari, P. Kameli, and H. Salamati, “Effect of Ag doping on structural, optical, and photocatalytic properties of ZnO nanoparticles,” *J. Alloys Compd.*, vol. 640, pp. 408–415, 2015.

[44] W. Feng, S. Rangan, Y. Cao, E. Galoppini, R. A. Bartynski, and E. Garfunkel, “Energy level alignment of polythiophene/ZnO hybrid solar cells,” *J. Mater. Chem. A*, vol. 2, no. 19, pp. 7034–7044, 2014.

[45] P. Vivo, J. K. Salunke, and A. Priimagi, “Hole-Transporting Materials for Printable Perovskite Solar Cells,” *Mater. (Basel, Switzerland)*, vol. 10, no. 9, p. 1087, 2017.

[46] B. Xu *et al.*, “Functional solid additive modified PEDOT:PSS as an anode buffer layer for enhanced photovoltaic performance and stability in polymer solar cells,” *Sci. Rep.*, vol. 7, p. 45079, 2017.

[47] J. Müller, B. Rech, J. Springer, and M. Vanecek, “TCO and light trapping in silicon thin film solar cells,” *Sol. Energy*, vol. 77, no. 6, pp. 917–930, 2004.

Chapter 4

Inverted Perovskite Solar Cells

4.1 Introduction

In recent years, PSCs have attracted great attention due to the versatility of properties of the main absorber, the halide perovskite, resulting in highly efficient, low-cost, flexible and semi-transparent photovoltaic devices [1]. In 2009, Miyasaka *et al.* were the first to report the application of $CH_3NH_3PbI_3$ ($MAPbI_3$) and $CH_3NH_3PbBr_3$ ($MAPbBr_3$) as sensitizers in the replacement of the dye reaching 3.8 % and 3.1 % PCEs, respectively [2]. In 2012, M. Grätzel *et al.* fabricated nowadays the well-known normal architecture device, using perovskite films as the photoactive absorber layer, employing the mp-TiO_2 as ETL and spiro-OMeTAD as HTL, achieving 9.7% PCE [3]. This was followed in2013, by M. Z. Liu, M. B. Johnston and H. J. Snaith who fabricated the planar heterojunction PSCs via vapour deposition with a reported efficiency exceeding 15.4 % PCE [4]. The efficiency of the PSCs has improved rapidly until reaching a certified record of 24.2 %positioning itself as a strong competitor for silicon solar cell technology [5].

Organic inorganic halide perovskites are highly interesting materials due to their excellent optoelectrical properties such as their optical absorption coefficient, a direct bandgap, long carrier lifetime and diffusion length [6-8]. One interesting characteristic of organic-inorganic halide perovskite is the tunability of their bandgap which can be built by replacing the cations and anions in their structure. For example, the properties of the halide perovskite $MAPb(I_{1-x}Br_x)_3$can be tuned depending on the halogen concentration to exhibit bandgaps ranging from 1.6 eV to 2.3 eV [9-10].

The term perovskite comes from Gustav Rose which discovered calcium titanate ($CaTiO_3$) in 1839 and named it after the Russian mineralogist Lev Perovski. This material was originally referred to a kind of ceramic oxide with the general molecular formula of ABX_3, where A is an organic cation, (such as $CH_3NH_3^+$, $NH_2CH{=}NH_2^+$, $CH_3CH_2NH_3^+$), B is a metal cation (Pb^{2+},

Sn^{2+}) and X is halogen anion; (such as F^-, Cl^-, Br^-, I^-)[11]. A schematic representation of the perovskite crystal structure can be observed in **Figure 4.1.**

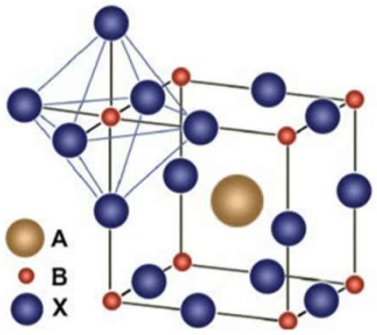

Figure 4.1 Schematic representation of the perovskite crystal structure ABX_3. *Extracted fro*m [12]

One of the simplest and most applied halide perovskite material in photovoltaics is $MAPbI_3$, with formula $CH_3NH_3PbI_3$, also known as MAPI, and with an effective absorption coefficient in the visible range of $1.0x10^5 mol^{-1}$ Lcm^{-1} at 550 nm [13], with a perovskite film thickness in the range of 500-600 nm. However, mixed halide and mixed cation perovskites, triple and quadruple cation, are now being synthesized producing high PCEs and greater stability.

For MAPI different crystal phases occur at different temperatures. At low temperatures, it forms an orthorombic phase (T< - 108 ˚C), corresponding to the space group Pnma. While, at higher temperatures (between - 108 °C and 54 °C), the structure changes to a tetragonal phase, with space group of I4/mcm, where the organic cations are exhibit 2D disorder. Meanwhile, when the temperature increases above 54 ˚C, it corresponds to a cubic phase transition with a space group of Pm3m, leading to a 3D disorder [14-15].

In 2014, Pellet *et al.* studied the mixed cations of MA ($CH_3NH_3^+$) and FA ($NH_2CH{=}NH_2^+$), which at RT crystallizes in the Pm3m space group [16]. The FA cations can build the perovskite structure of $HC(NH_2)_2PbI_3$ (FAPI) with fully vertex connected PbI_6octahedra and FAPI PSCs have reached a maximum conversion efficiency of 20.1 % [17]. The increase of the cation radius from 2.2 Å (MA) to 2.5 Å (FA) further decrease the optical E_g from 1.5 eV to 1.4 eV, extending the absorption into the near-infrared area [18]. However, under 150 ˚C, FA shows a delta-phase perovskite transition, while above 150 °C, the structure exhibits a black perovskite phase of FAPI (α-phase). In order to stabilize these faces mixed cation structures

have been studied. For instance, Yi *et al.* demonstrated the best performance with the addition of 10 % MA, reaching 20.2 % PCE [19]. Inorganic cations such as cesium or rubidium have also been used by several research groups, as the addition of cesium can increase the thermal stability of the device. For example, Seok *et al.* demonstrated that the control of the growth conditions of the perovskite crystal structure can lead to high-efficiency PSCs [20].

4.2 Inverted configuration Halide Perovskite Solar Cell

The inverted PSCs configuration (**Figure 4.2)** emerged as an alternative to the unstable normal configured PSCs. In this configuration, the HTL, like PEDOT:PSS or Spiro-OMeTAD, can be replaced by HTL made of semiconductor oxides such as NiO, V_2O_5 or MoO_3. The HTL layer is an essential part of PSCs as it provides important functions, such as extracting the holes (and blocking electrons) from the perovskite layer, conducting the holes through the HTL layer, and, in the case of semiconductor oxides, isolating the perovskite layer from the oxygen and moisture from the atmosphere.

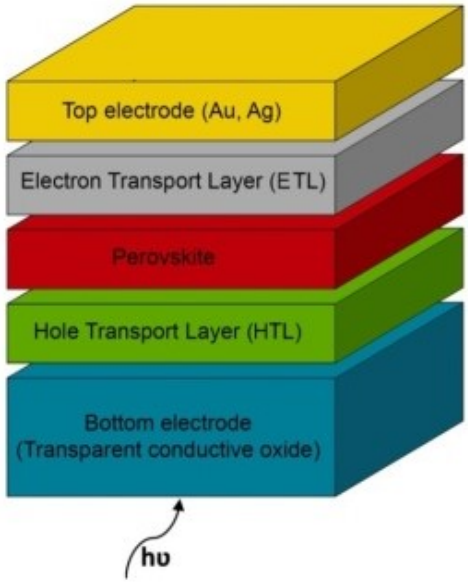

Figure 4.2 Scematic representation of the inverted configuration Halide perovskite solar cell.

A standard used HTL in inverted PSCs is PEDOT:PSS, which is a conducting polymer that possesses high optical transmittance in the visible light wavelength range [21]. However, the acidic nature of PEDOT:PSS is an important drawback for the long-term stability of PSCs devices [22]. As an alternative to PEDOT:PSS, inorganic p-type semiconductors have been

used for the HTL in inverted PSCs with NiO_x being the most common semiconductor oxide used as a replacement. NiO is a well-known p-type semiconductor with superior properties; such as excellent thermal and chemical stability, optical transparency, low cost and it is compatible with simple fabrication process by printing techniques like sol-gel or spray-pyrolisis. Its optoelectronic properties make NiO an excellent candidate to work as HTL in PSCs [27-28]. Docampo *et al.* [26], reported the use of V_2O_5 and NiO as an HTLs, and Guo *et al.* [27] have shown an adjustment of the WF of NiO through doping, improving the final energy level alignment. Doping NiO_x with metal elements, such as Cu or Li, have demonstrated to improve the p-conductivity of NiO_x film and increase device performance and stability [31-32]. Jung *et al.* developed a low-temperature solution processable combustion deposition method for the preparation of high quality Cu:NiO_x film as an efficient HTL in an inverted PSC. As a result, PSCs with efficiencies as high as 17.7 % were obtained [30].

Other alternatives to PEDOT:PSS are CuO or Cu_2O which have shown good energy level alignment with the $CH_3NH_3PbI_3$ and higher V_{oc} [31]. In addition, other inorganic materials, such as PbS, and graphene oxide (GO) have been applied as HTL in inverted architecture PSCs, achieving PCEs of 16.6 %, and for GO, a PCE of 17 %, respectively. In both cases the efficiency was much higher than for the reference PSCs applying PEDOT:PSS [32]. Recently, a PCE of up to 20.4 % was realized in normal configuration through use CuSCN as HTL and TiO_2 as ETL, which is comparable to 20.9 % of the PSC applying spiro-OMeTAD as a HTL [33]. As advantage in front of other organic HTL such as spiro-OMeTAD, PSCs with inorganic HTL showed stability under humid and high temperature condition [34].

It is also important to take into account a good energy level alignment between the absorber layer ($CH_3NH_3PbI_3$) and transport layers (HTL and ETL). **Figure 4.3** shows the energy level alignment for several HTL and ETL used in PSC. In a typical PSC, when the perovskite absorbs light, the electrons in the VBM of the perovskite layer are excited to its CBM creating an electron-hole pair. This electron-hole pair is usually not stable due to the weak exciton binding energy of the halide perovskite [3]. Thus, the HTL plays a critical role in the band energy alignment. Tailoring the energy level of the HTL to match perfectly with the VBM of the perovskite layer can help to better hole extraction and transfer [35].

Besides of its work as the transport of the holes generated in perovskite to the TCO (anode), the HTL in inverted PSCs prevents electrons from leaking to the anode, which can greatly reduce the recombination of electrons and holes at the interface between the perovskite and anode [39-40].

The ETL material (n-type) is in charge of the extraction and transport of electrons (blocking holes) and the reduction/suppression of charge recombination [38]. Also, high electron mobility is mandatory for a proper device performance. The energy alignment between the ETL and the perovskite has to match correctly in order to facilitate the electron extraction and transport, contributing to the increase of J_{sc} and FF. The carefully selection of the ETL is crucial to obtain an uniform, compact and smooth perovskite layer, and directly affects the proper crystallization and nucleation of the halide perovskite thin film [39].

Fullerene and its derivates are widely used as n-type materials. These organic ETLs used in PSCs present an efficient electron extraction, good energy alignment and efficient electron mobility [38]. Liu and co-workers used PCBM in an inverted architecture replacing TiO_2 and they exhibited a PCE of 14.3 % [40]. Another example is the work of Kakavelakis and co-workers; they inserted a reduced graphene oxide (rGO) into PCBM as ETL. Their results demonstrated a hysteresis-free PCE of 14.5 % compared to the only PCBM devices [41].

Moreover, low temperature processed ETLs, such as ZnO, TiO_2, Al_2O_3, are excellent candidates for flexible substrates. Snaith and co-workers reported a low temperature processing route to fabricate mesoscopic Al_2O_3[42]. Kelly *et al.* used a compact ZnO ETL, without any sintering process, to fabricate highly efficient planar PSC with an average efficiency of 13.7 % [43]. Also, amorphous WO_x-TiO_x composites were used as ETL given the highest PCE of 13.5 % [44]. Another example is the use of SnO_2, reported by Ke and co-workers, who applied low-temperature solution-processed SnO_2 reporting an average efficiency of 16.02 %. Also, their procedure is perfectly compatible with large scale roll-to-roll manufacturing of low-cost PSCs on flexible substrates [45]. Other deposition approaches have also been developed for low temperature processed ETLs, e.g, spin-coating, slot-die coating, chemical bath deposition and electrodeposition [38].

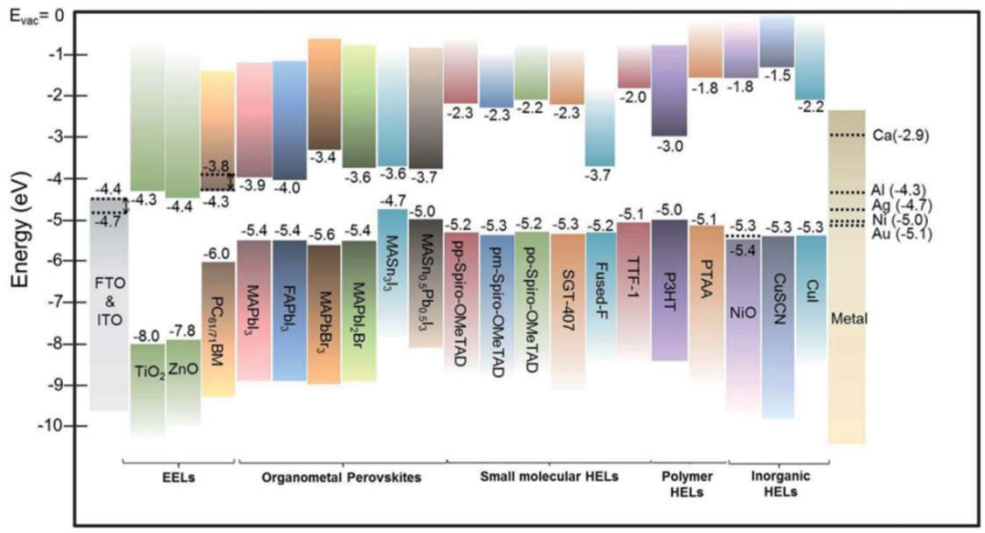

Figure 4.3 Energy level diagram of representative organometal perovskites, HTLs and ETLs, as well as some metal electrodes appliedin PSCs. *Extracted from* [46]

It is known that metal oxides demonstrate much higher carrier mobility and superior stability than the many organic-based transport layers [42-43]. In addition, metal oxides can be processed easily via solution from corresponding precursors and nanoparticles at low temperatures.

In this chapter, NiO was selected as the HTL in PSC. For the fabrication of inverted PSCs, NiO was used as an HTL and four different combinations of $PC_{70}BM$ and ZnO were employed as the ETL. The halide perovskite used was the mixed-ion perovskite $[HC(NH_2)_2]_{0.85}(CH_3NH_3)_{0.15}Pb(I_{0.85}Br_{0.15})_3$. The transparent and back electrodes were FTO and Au, respectively. The PSC was fabricated in a planar and inverted configuration (as in **Figure 4.2**) by the spin-coating technique. This chapter describes the fabrication and optimization of the PSCs parameters to obtain high efficient devices.

4.3 Optimization of the Electron Transport Layer (ETL)

The ETL plays an indispensable role in blocking holes and transporting electrons. It also plays a very important role in separating the perovskite absorber layer from the electrode in order to reduce the direct recombination of photo-induced charge carriers. Accordingly, this section we carried out the optimization of four different combinations of ZnO and PCBM used as ETLs with the aim of finding the best option for a high efficient PSC.

The inverted PSC were fabricated as described in Chapter 2. In all cases, the inverted PSC structure has a configuration: FTO/NiO/PVSK/ETL/Au (where PVSK represents the halide peorvskite). This configuration employs FTO as the bottom electrode, followed by the NiO as the HTL, the absorber layer as mixed-ion PVSK, the ETL layer to be optimized and finally gold as the top electrode. The four configurations used as ETL were **(a)** $PC_{70}BM$, **(b)** ZnO, **(c)** $PC_{70}BM$/ZnO bi-layer (BL), and **(d)** $PC_{70}BM$:ZnO bulk heterojunction (BHJ).

4.3.1 $PC_{70}BM$

PCBM is widely used as an ETL due to its high electron accepting properties and the possibility for the passivation of traps in the perovskite film. The LUMO energy level of PCBM is 3.9 eV matching correctly the band energy level alignment of the perovskite [38-44]. For instance, Nie *et al.* reported $MAPbI_3$/PCBM as an ETL in inverted planar hybrid PSCs and the highest PCE achieved was 17.7 % [50]. Also, Qiu *et al.* used cross-linked PCBM as the interlayer between perovskite and TiO_2 to fabricate planar PSCs with efficiency of 18.4 % [51]. $PC_{70}BM$ is a fullerene electron acceptor and the non-symmetrical C_{70} enables energetic transitions that are forbidden in C_{60}, thereby improving the absorption characteristics over $PC_{60}BM$ for the visible range of the solar spectrum. In our case, we chose to work with $PC_{70}BM$ because it is a commonly used ETL applied in inverted planar heterojunction PSCs displaying high performance as demonstrated by You *et al.*. In their work, they applied the following device structure: substrate/ITO/PEDOT:PSS/$CH_3NH_3PbI_{(3-x)}Cl_{(x)}$/PCBM/Al. All these layers were sintered at low temperature and a resulting PCE of 11.5 % was obtained on rigid substrates (glass/ITO), and a 9.2 % PCE on flexible PET/ITO substrates [52].

In our work, the optimal ETL step process was achieved after exchanging the ETL material from $PC_{60}BM$ to $PC_{70}BM$. The deposition speed of the spin coater to achieve a thin layer of $PC_{70}BM$, was varied from 5000 rpm up to 8000 rpm. Also, the dilution of the $PC_{70}BM$ layer was modified from 0.02 g/ml to the optimized 0.01 g/ml. The deposition of the layer were made with freshly-prepared solutions, flushing the inside of the glovebox with N_2 gas before the experiments to avoid excessive concentration of volatile solvents in the chamber, also the deposition of the $PC_{70}BM$ layer was made once the solution was placed on the FTO substrate before the spinning was initiated (what we call placing the solution “on the

substrate"). The careful application of these steps contributed to the optimum fabrication of the PSC.

Figure 4.4 shows the photovoltaic performance of the inverted configuration PSCs developed in our laboratory applying the optimized $PC_{70}BM$ thin film as the ETL. The figure shows the structure of the $PC_{70}BM$ molecule **(a)**, the IV curves of the as-obtained inverted PSCs **(b)**, the IPCE analyses **(c)** and a table with the photovoltaic parameters **(d)** obtained for the inverted PSC using $PC_{70}BM$ as an ETL and NiO as the HTL. The Figure also shows the IV curves in forward and reverse scans. As observed, the initial efficiencies obtained were not above 2.1 %. The results show poor photovoltaic parameters but quite good reproducibility. The IPCE analysis shows a correct absorption in the whole spectra up to 800 nm, an indication of the absorption and charge injection from the halide perovskite. Nevertheless, the poor FF and low V_{oc} (0.4 V) indicates internal recombination losses, probably due to the problems on the fabrication of smooth thin films without pinholes, or deficiencies at the interfaces with the transport layers. In addition, we observed a difference between forward and reverse scans indicating some level of hysteresis for the PSCs.

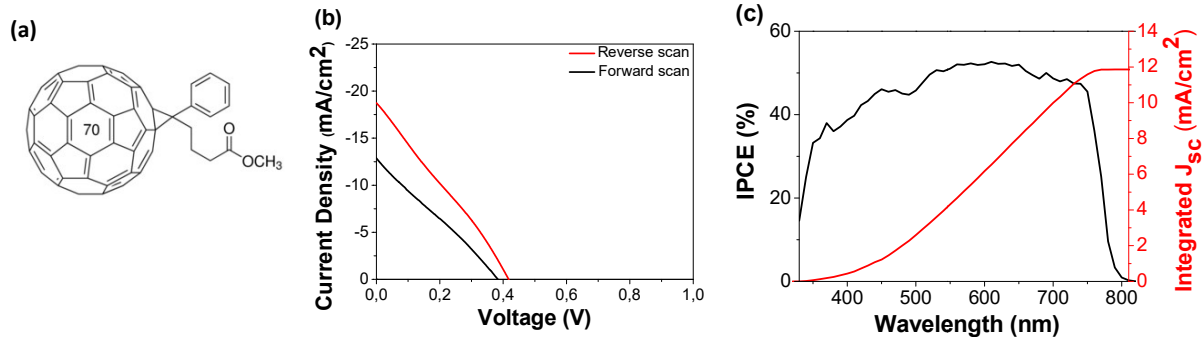

(d)

PSC Sample	PCE (%)		V_{oc} (V)		J_{sc} (mA/cm^2)		FF (%)	
	Forward	*Reverse*	*Forward*	*Reverse*	*Forward*	*Reverse*	*Forward*	*Reverse*
Cell 1	1.2	1.9	0.4	0.4	-15.1	-16.7	21.6	29.2
Cell 2	1.3	1.8	0.4	0.4	-10.9	-16.2	27.2	27.2
Cell 3	1.3	2.1	0.4	0.4	-12.9	-18.7	26.2	26.7

Figure 4.4 (a) $PC_{70}BM$ structure, **(b)** IV curves, **(c)** IPCE and **(d)** table of photovoltaic parameters of inverted PSC using $PC_{70}BM$ as an ETL in forward and reverse IV scans.

4.3.2 ZnO

PCBM is commonly used as an ETL in planar architecture with a high performance; however, this material is associated with high production costs and photochemical instability [53]. As a result, several kinds of n-type metal oxide semiconductors, such as TiO_2, ZnO, SnO_2 have been extensively applied since these solution-processed semiconductor oxides are simple to deposit by spin-coating, are relatively cheap to fabricate, can be synthesized at a low temperature and can produce thin films with good transparency. Among these metal oxide semiconductors, ZnO is a relevant candidate because of its good energy level alignment with the perovskite absorber and high electron mobility [54]. For instance, Bai *et al.* used ZnO nanocrystals to improve the stability of PSCs and demonstrated stable performance up to 140 h for a $MAPbI_{3-x}Cl_x$ perovskite absorber [37]. Also, Zhang *et al.* used a ZnO interlayer and demonstrated up to 60 days of stable efficiency based on PEDOT:PSS as an HTL [55]. Following these studies, You *et al.* developed solution-processed p-type NiO_x and n-type ZnO nanoparticles and used them as the HTL and ETL, respectively, in a PSCs [56].

In this work, to achieve the optimized ZnO layer, several variables in the fabrication process were modified, for example spin coating speed was varied from 5000 rpm to 8000 rpm. After preparation, the thin films were dried in air at 40 °C for 10 min. Finally, the use of fresh solutions, flushing the N_2 gas inside of the glovebox to take out the volatile solvent, and final, the deposition of the ZnO was made by placing the solution on the substrate before spin coating. **Figure 4.5** shows **(a)** the ZnO structure, **(b)** IV curves, **(c)** IPCE and **(d)** a table of photovoltaic parameters corresponding to the inverted PSC using ZnO as an ETL and NiO as the HTL, in forward and reverse IV scans.

The IV curve of the best PSC is depicted in **Figure 4.5 (b).** An improvement in the photovoltaic response in comparison with the PSCs applying only PCBM (**Figure 4.4**) was observed. The best efficiency was observed at 5.8 %, while FF and V_{oc} were around 46 % and 0.6 V respectively, for the best devices. However, the hysteresis is extremely large. The results using only ZnO as an ETL showed higher photovoltaic parameters compared with $PC_{70}BM$, but also presented lower reproducibility between samples. The IPCE analysis of **Figure 4.5 (c),** shows that the absorption region corresponding to the halide perovskite is

slightly lower than what is expected (or what is shown in the PSC applying PCBM), an indication that the use of the ZnO ETL alone is not enough for the correct electron transport in the PSC.

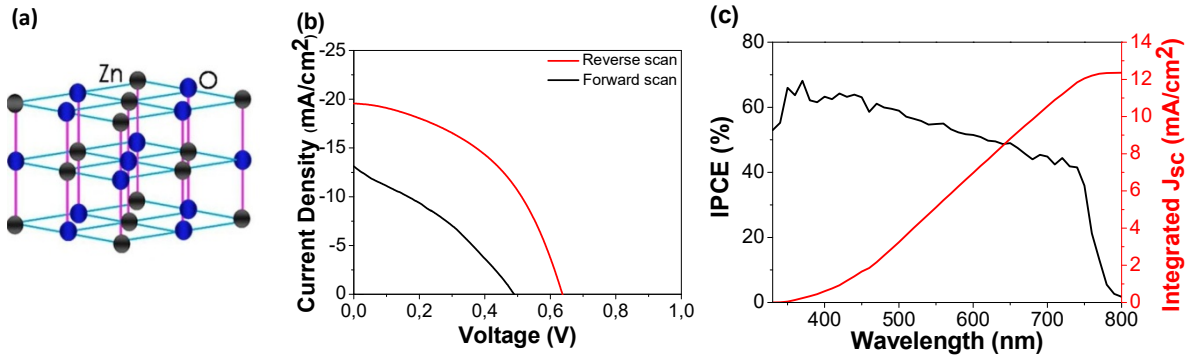

(d)

PSC Sample	PCE (%)		V_{oc} (V)		J_{sc} (mA/cm^2)		FF (%)	
	Forward	*Reverse*	*Forward*	*Reverse*	*Forward*	*Reverse*	*Forward*	*Reverse*
Cell 1	1.4	4.5	0.4	0.6	-14.0	-19.5	27.4	41.1
Cell 2	1.3	3.6	0.3	0.5	-12.4	-19.7	32.5	36.2
Cell 3	2.1	5.8	0.5	0.6	-13.1	-19.6	33.0	46.4

Figure 4.5 (a) ZnO structure, **(b)** IV curves, **(c)** IPCE and **(d)** table of photovoltaic parameters of inverted PSC using ZnO as an ETL in forward and reverse IV scans.

4.3.3 PCBM/ZnO-bilayer (BL)

The application of two electron transport materials, such as PCBM and ZnO, is possible if the band alignment is the adequate. Previous works suggest that these two materials have all the requirements for an optimal ETL. For example, Mali *et al.* employed a ZnO interlayer between PCBM and Ag which avoided unwanted degradation and diffusion between Ag and PCBM as it protected the perovskite layer from air [57]. The best-performing cell exhibited an efficiency exceeding 19 %, providing fast electron transportation and low recombination. Zhang *et al.* consider that the creation of a bilayer structure allows materials that are inherently to be in contact with perovskite active layer. In addition, a sol-gel ZnO layer improved energy level alignment and enhanced charge carrier extraction, and a PCBM layer reduced hysteresis and achieved better thermal stability [58]. Zhang *et al.* inserted a layer of PCBM between ZnO and a perovskite film to passivate the ZnO surface. This helped to avoid thermal decomposition of the perovskite material and reduced the interface barrier alignment between the PCBM and the perovskite layer, the best-performing cell exhibited an efficiency of 19.1 % [59].

In this section we applied a bilayer of PCBM/ZnO as the ETL. To fabricate this bi-layer we first deposited the $PC_{70}BM$ layer by spin coating by applying a solution of 0.01 g/ml of PCBM in chlorobenzene. The deposition of the solution was made at 7000 rpm. After deposition, the film was annealed for 10 min at 40 °C. For the second layer, ZnO, 40 mg/ml of the ZnO in chlorobenzene (procedure described in Chapter 2) was applied by spin coating. The spin coating speed was 7000 rpm and the film was annealed at 40°C for 10 min in air. **Figure 4.6** shows **(a)** the PCBM and ZnO structure, **(b)** the IV curves, **(c)** the IPCE analysis and **(d)** a table of the photovoltaic parameters obtained for the inverted PSC applying the $PC_{70}BM$/ZnO-BL as the ETL and the NiO as the HTL, in forward and reverse IV scans.

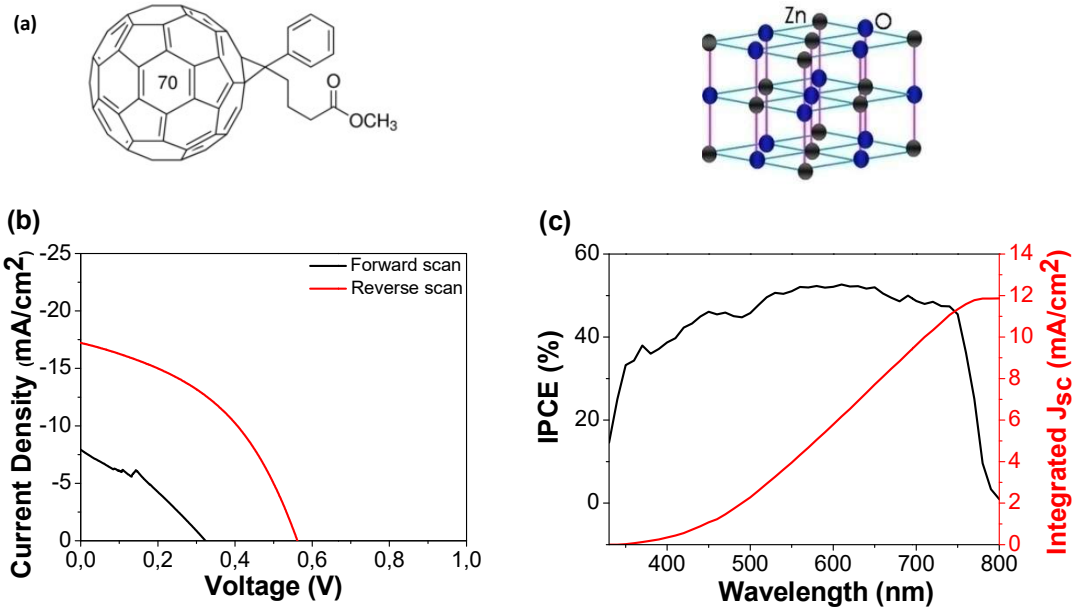

(d)

PSC Sample	PCE (%)		V_{oc} (V)		J_{sc} (mA/cm^2)		FF (%)	
	Forward	*Reverse*	*Forward*	*Reverse*	*Forward*	*Reverse*	*Forward*	*Reverse*
Cell 1	1.5	4.1	0.4	0.6	-11.4	-16.2	31.6	43.5
Cell 2	1.2	3.2	0.3	0.5	-11.1	-19.2	29.9	34.0
Cell 3	0.9	4.2	0.3	0.6	-7.9	-17.2	34.6	43.2

Figure 4.6 (a) PCBM and ZnO structure, **(b)** IV curves, **(c)** IPCE and **(d)** table of photovoltaic parameters of inverted PSC using PCBM/ZnO-BL as an ETL in forward and reverse IV scans.

Figure 4.6 depicts the IV curves of the best PSCs using a bilayer of PCBM/ZnO, the application of bilayer of $PC_{70}BM$/ZnO results in even greater hysteresis than what has been observed with previous ETLs, and the IV curves shows a worse shape compared with the PSC applying only ZnO. We observed that, in general, lower photovoltaic performance was

obtained if compared with PSCs applying only ZnO but better photovoltaic parameters if compared with PSCs applying the $PC_{70}BM$ alone. Moreover, the application of the $PC_{70}BM$ and ZnO as bilayer, presented lower reproducibility between the samples.

4.3.4 $PC_{70}BM$:ZnO bulk heterojunction (BHJ)

Although the bare PCBM and ZnO thin films work well as ETL, as discussed in the previous sections, we analyzed the combination of both materials as part of a bulk heterojunction. We found that the combination of both materials as a mix solution in molar ratio 1:1 with chlorobenzene in our inverted configuration provided the best photovoltaic performance. **Figure 4.7** shows **(a)** PCBM and ZnO structure, **(b)** IV curves, **(c)** IPCE and **(d)** table of photovoltaic parameters of inverted PSC using $PC_{70}BM$:ZnO-BHJ as an ETL in forward and reverse IV scans.

In order to obtain the best results, the process was optimized. Changes in the deposition mode were carried out, after several times we achieved better deposition of the mix PCBM:ZnO by placing the solution on the FTO substrate before spin coating. We made changes in terms of the materials concentration in the solution, we analyzed the PCBM:ZnO molar ratios of 2:1, 1:2 and 1:1 ratios. We also optimized the deposition speed by modifying the spin coating velocity from 5000 rpm to 8000 rpm. The higher the speed the thinner the PCBM:ZnO layer (with a thickness of 70 µm approximately).

The best PSC was obtained with a PCBM:ZnO molar ration of 1:1 and a deposition speed of 7000 rpm. The IV curve of the best cell using $PC_{70}BM$:ZnO solution in chlorobenzene shows an improved FF with values up to 44 %. Moreover, the J_{sc} was observed to be the best one in comparison with the other ETLs analyzed, which improved the efficiency of the solar cell. In addition, the hysteresis observed in the reverse/forward IV curves was observed to be minimal. Thus, the PSCs using a mix solution of $PC_{70}BM$ and ZnO as ETL demonstrated the best photovoltaic response compared with the application of the other ETL materials analyzed in this work.

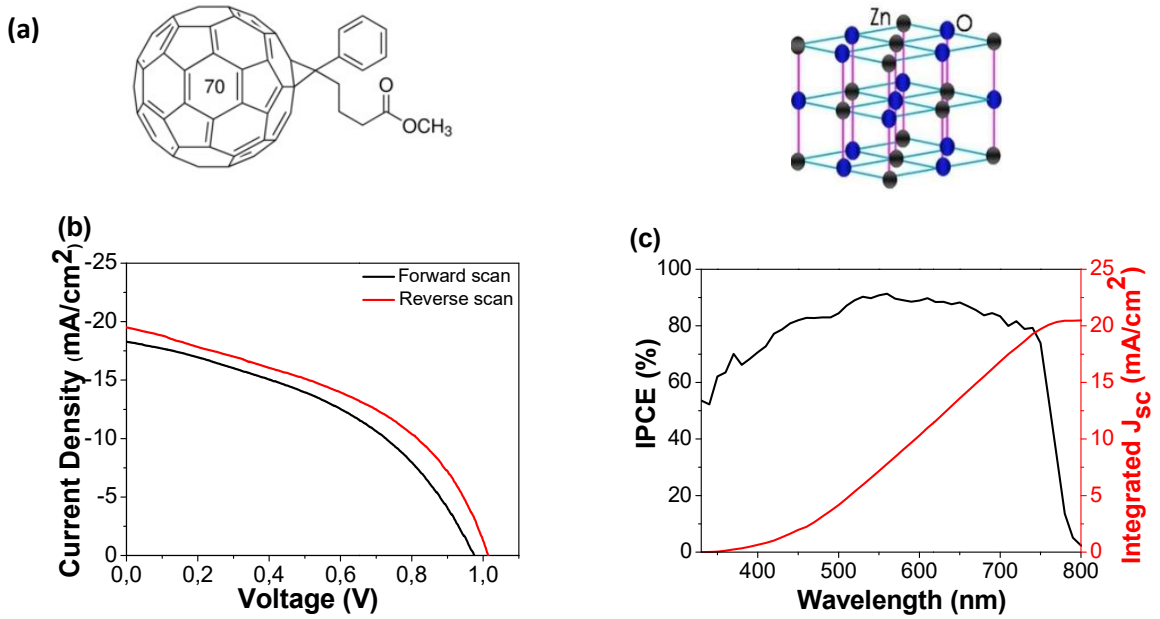

(d)

PSC Sample	PCE (%)		V_{oc} (V)		J_{sc} (mA/cm^2)		FF (%)	
	Forward	*Reverse*	*Forward*	*Reverse*	*Forward*	*Reverse*	*Forward*	*Reverse*
Cell 1	7.6	8.7	0.9	1.0	-18.3	-19.5	42.6	44.2
Cell 2	7.8	8.6	0.8	0.8	-22.9	-24.9	40.7	40.4
Cell 3	6.3	7.3	0.8	0.9	-18.4	-19.4	41.0	39.7

Figure 4.7 (a) PCBM and ZnO structure, **(b)** IV curves, **(c)** IPCE and **(d)** table of photovoltaic parameters of inverted PSC using PCBM:ZnO-BHJ as an ETL in forward and reverse IV scans.

The addition of ZnO facilitates the formation of a highly smooth and uniform ETL layer, which is more effective in preventing undesirable electron-hole recombination between the perovskite layer and the top electrode (Au). As a result, the V_{oc} of the PCBM:ZnO-BHJ based solar cells is increased from 0.4 to 0.9 eV, comparing with only PCBM, which leads to significantly enhanced PCEs of the devices. PCEs as high as 8.7 % were obtained using this ETL. In summary, this study shows that the best photovoltaic performance in terms of all 4 photovoltaic ETLs was achieved using a mix solution of $PC_{70}BM$ and ZnO in molar ratio 1:1 dissolved in chlorobenzene.

4.3.5. Comparisson of the different ETLs applied in inverted PSCs

Table 4.1 shows the comparison of the photovoltaic response of the PSCs applying these four ETLs. The table shows the average values (for $PC_{70}BM$, ZnO, $PC_{70}BM$/ZnO-BL and

$PC_{70}BM$:ZnO-BHJ samples) of the results obtained from the IV curves in forward and reverse scan modes.

Table 4.1 Average of values of photovoltaic parameters of inverted PSCs using different ETLs in forward and reverse scan.

ETL		PCE (%)	V_{oc}(V)	J_{sc}(mA/cm^2)	FF(%)
$PC_{70}BM$	*Forward*	1.25±0.08	0.39±0.04	12.94±2.06	24.99±3.01
	Reverse	1.90±0.17	0.37±0.04	17.21±1.35	27.68±1.34
ZnO	*Forward*	1.60±0.46	0.39±0.09	13.18±0.79	30.94±3.11
	Reverse	4.63±1.09	0.56±0.07	19.59±0.12	41.19±5.12
$PC_{70}BM$/ZnO-BL	*Forward*	1.18±0.31	0.36±0.05	10.13±1.92	32.08±2.38
	Reverse	3.81±0.56	0.54±0.05	17.57±1.53	40.25±5.38
$PC_{70}BM$:ZnO-BHJ	*Forward*	7.27±0.83	0.88±0.07	19.88±2.67	41.42±1.01
	Reverse	8.20±0.79	0.93±0.08	21.26±3.17	41.43±2.43

As **Table 4.1** shows, ETLs with a mix solution of $PC_{70}BM$ and ZnO in chlorobenzene, produced higher V_{oc} and PCE compared with the other materials. In addition, hysteresis behaviour was almost non-existent. Moreover, only $PC_{70}BM$ as an ETL produced very low V_{oc} and FF that impacted directly on the poor efficiency of the inverted PSC.

Figure 4.8 shows the average of photovoltaic parameters PCE, J_{sc}, V_{oc} and FF for the materials studied as an ETL; only $PC_{70}BM$, only ZnO, a bilayer of $PC_{70}BM$/ZnO and a mix solution of $PC_{70}BM$:ZnO-BHJ, at one sun illumination conditions.

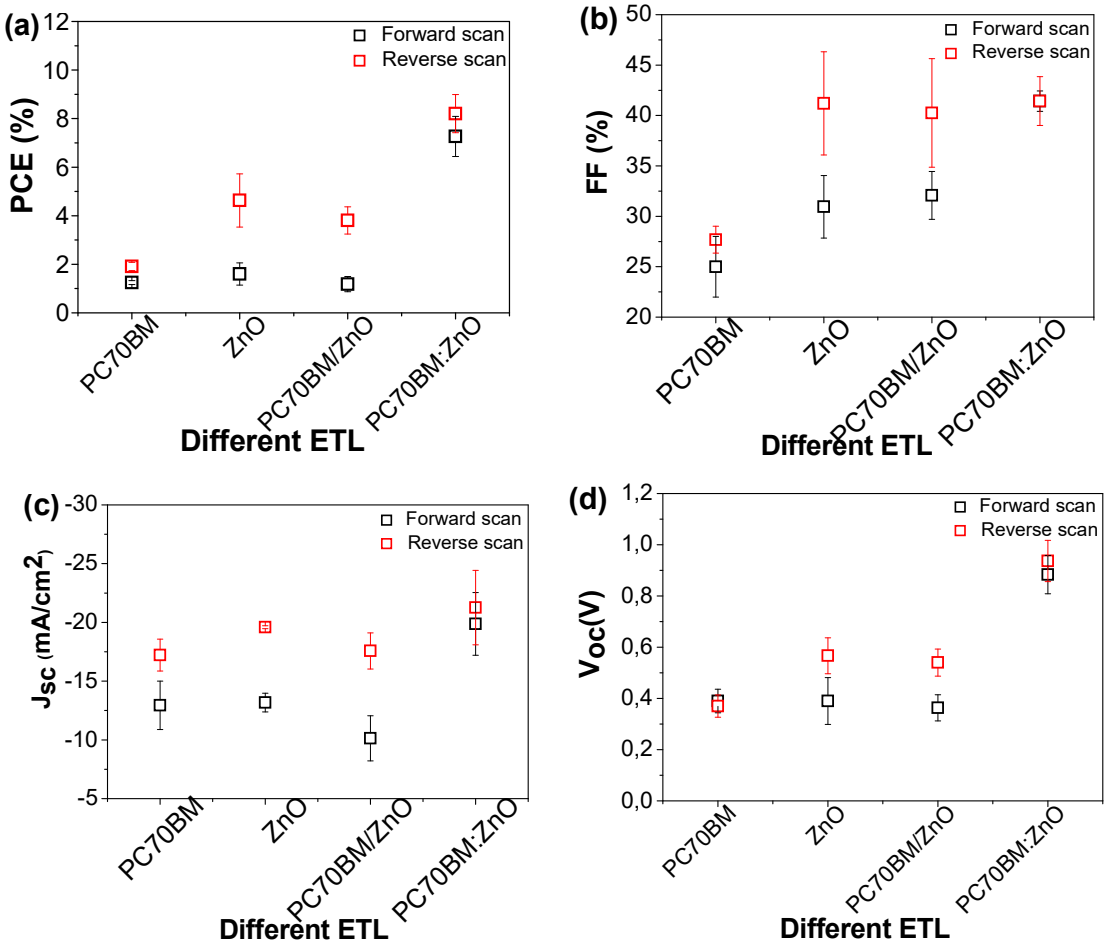

Figure 4.8 PSC photovoltaic parameters (PCE, J_{sc}, V_{oc} and FF) for the four materials used for ETL; **(a)** only $PC_{70}BM$, **(b)** only ZnO, **(c)** a bilayer of $PC_{70}BM$/ZnO and **(d)** a mixed solution of PCBM:ZnO at one sun illumination conditions.

4.4 Optimization of NiO as the Hole Transport Layer (HTL)

The HTL is a very important layer in solar cell devices for efficient charge transport and extraction. An ideal HTL material candidate for high performance PSC should have a good optical transparency, prevent electron leakage, avoid hole-electron recombination as much as possible, and provide a good energy level alignment and support a high-quality and sufficiently thick perovskite film [53]. It is known that p-type semiconductor oxides demonstrate much higher carrier mobility and superior stability than organic materials. Liu *et al.* demonstrated the application of NiO_x nanoparticle as HTL in normal PSC using $MAPbI_{3-x}Cl_x$, reaching a PCE of 9.1 % [60]. Yang *et al.* reported the use of NiO_x in $MAPbI_3$-based normal PSC with a carbon nanotube as an ETL and achieved a PCE of 15.4 %.

This section analyses the effects of 3 different NiO concentrations with the aim of finding the best option for an optimized HTL in an inverted configured PSC. The different solutions used were a 0.06 M, 0.15 M and 0.21 M of NiO dissolved in MeOH. An inverted structure PSC was employed using FTO as the TCO, followed by a NiO in various concentrations to act as the HTL, the absorber layer was mixed-ion perovskite, a mix solution of $PC_{70}BM$ and ZnO in chlorobenzene acted as the ETL, and finally, 80 nm of gold for the top electrode were thermally evaporated. **Figure 4.9** shows the NiO structure. The concentrations analysed are: **a)** 0.06 M NiO, **b)** 0.15 M NiO and **c)** 0.21 M NiO.

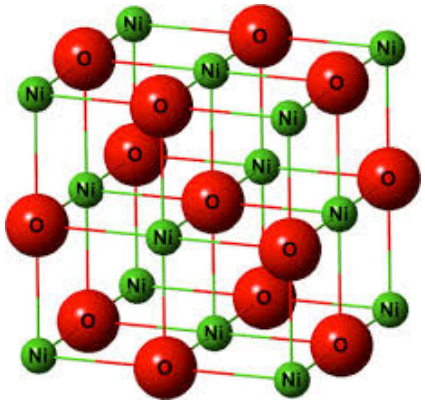

Figure 4.9 The NiO structure.

To achieve the properly NiO solution suitable as a HTL in a perovskite layer, it was modifying, filtered the solution by hydrophobic PTFE synergie filter, non sterile (0.20 µm). Also, after several times of NiO deposition onto FTO substrates, we realize that heating FTO subtrates in a hot plate at 80 °C before the deposition it seems better than at RT. And always, spray air flow to the FTO before the deposition of NiO layer.

4.4.1 0.06 M NiO

Figure 4.10 shows **(a)** IPCE, **(b)** IV curves and **(c)** table of photovoltaic parameters of inverted PSC using NiO 0.06 M as an HTL in forward and reverse IV scans.

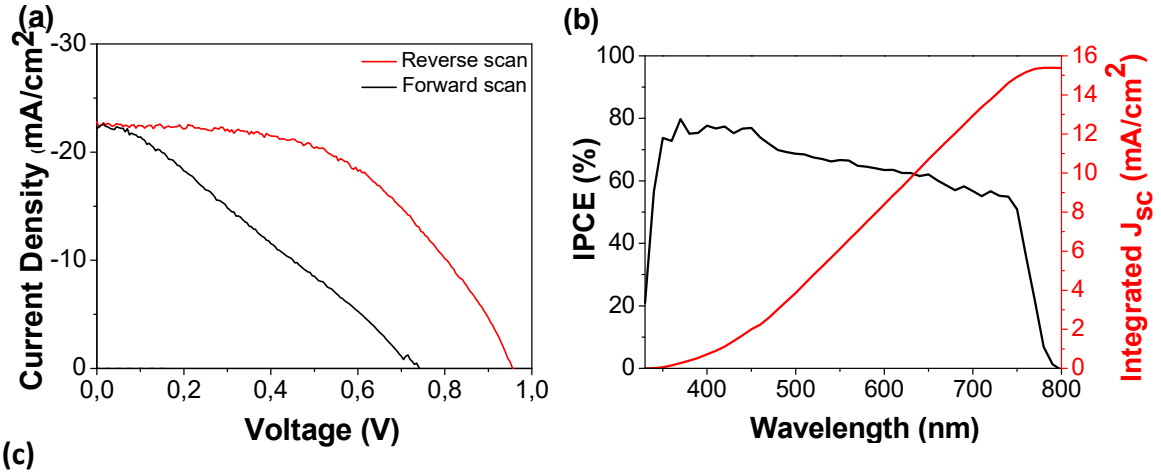

(c)

PSC Sample	PCE (%)		V_{oc} (V)		J_{sc} (mA/cm^2)		FF (%)	
	Forward	*Reverse*	*Forward*	*Reverse*	*Forward*	*Reverse*	*Forward*	*Reverse*
Cell 1	4.7	11.2	0.7	0.9	-22.2	-22.8	28.6	51.2
Cell 2	4.6	11.1	0.8	0.9	-22.8	-22.6	26.1	53.1
Cell 3	5.2	10.6	0.8	0.9	-22.4	-22.4	29.9	52.5

Figure 4.10 (a) IV curves **(b)** IPCE and **(c)** table of photovoltaic parameters of inverted PSC using NiO 0.06 M as an HTL in forward and reverse IV scans.

From the **Figure 4.10** we can conclude that the PSCs using a 0.06 M NiO solution as an HTL showed efficiencies, exceeding 10 % PCE. However, a much higher photovoltaic performance in reverse scan than forward scan was produced, indicating important hysteretical behaviour.

4.4.2 0.15 M NiO

Figure 4.11 shows **(a)** IV curves, **(b)** IPCE and **(c)** table of photovoltaic parameters of inverted PSC using NiO 0.15 M as an HTL in forward and reverse IV scans.

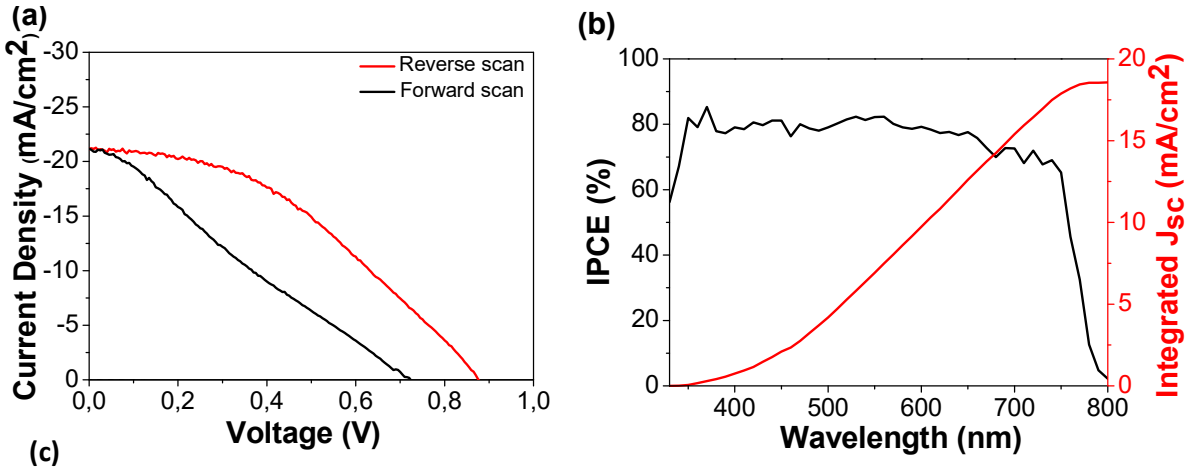

PSC Sample	PCE (%)		V_{oc} (V)		J_{sc} (mA/cm^2)		FF (%)	
	Forwar d	*Reverse*	*Forwar d*	*Reverse*	*Forwar d*	*Reverse*	*Forwar d*	*Reverse*
Cell 1	*6.3*	*11.7*	0.8	0.9	-21.2	-21.3	37.1	57.7
Cell 2	*5.4*	*10.7*	0.8	0.9	-21.3	-21.4	32.3	53.7
Cell 3	*5.8*	*10.6*	0.8	0.9	-20.8	-20.7	35.6	54.3

Figure 4.11 (a) IV curves**(b)** IPCE and **(c)** table of photovoltaic parameters of inverted PSC using NiO 0.15 M as an HTL in forward and reverse IV scans.

From the **Figure 4.11** we observe, that the photovoltaic parameters of the inverted PSC using a 0.15 M of NiO in MeOH as an HTL were marginally better as compared to the PSCs fabricated with the 0.06 M concentration.

4.4.3 0.21 M NiO

Figure 4.12 shows **(a)** IV curves, **(b)** IPCE, and **(c)** table of photovoltaic parameters of inverted PSC using NiO 0.21 M as an HTL in forward and reverse IV scans.

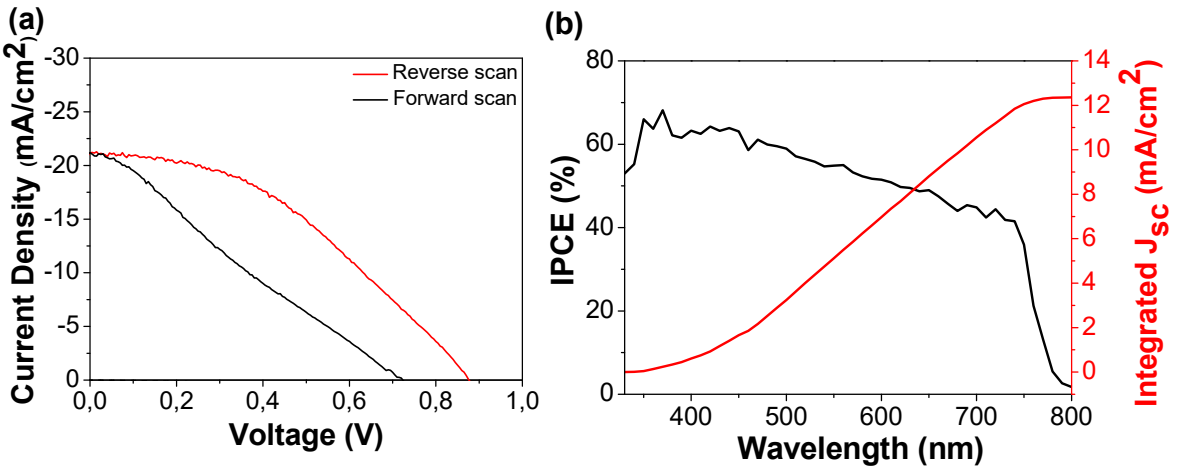

(c)

PSC Sample	PCE (%)		V_{oc} (V)		J_{sc} (mA/cm^2)		FF (%)	
	Forward	*Reverse*	*Forward*	*Reverse*	*Forward*	*Reverse*	*Forward*	*Reverse*
Cell 1	4.7	6.9	0.7	0.8	-20.8	-20.5	32.0	40.3
Cell 2	3.7	6.4	0.7	0.8	-19.9	-19.6	27.6	39.8
Cell 3	3.7	7.5	0.7	0.9	-21.2	-21.2	24.0	40.5

Figure 4.12 (a) IV curves**(b)** IPCE and **(c)** table of photovoltaic parameters of inverted PSC using NiO 0.21 M as an HTL in forward and reverse IV scans.

Table 4.2 shows the average results of the photovoltaic response and **Figure 4.13** the photovoltaic performance obtained for the inverted PSC using a different concentration of NiO as a HTL such as; 0.06 M, 0.15 M and 0.21 M for forward and reverse scan in an inverted architecture. The results indicate that the optimal concentration for this semiconductor oxide applied as an HTL is 0.15 M, also we can conclude that 0.06 M is too diluted and 0.21 M is too concentrated.

Table 4.2 Average of values of photovoltaic parameters of inverted PSCs using different HTLs in forward and reverse scan.

ETL		PCE (%)	V_{oc}(V)	J_{sc}(mA/cm^2)	FF(%)
0.06 M NiO	*Forward*	4.84±0.30	0.76±0.02	22.45±0.32	28.20±1.95
	Reverse	10.94±0.32	0.93±0.03	22.60±0.23	52.28±0.97
0.15 M NiO	*Forward*	5.83±0.43	0.78±0.01	21.10±0.26	35.04±2.44
	Reverse	11.03±0.65	0.94±0.02	21.11±0.33	55.24±2.16
0.21 M NiO	*Forward*	4.00±0.57	0.70±0.03	20.64±0.63	27.89±4.02
	Reverse	6.94±0.55	0.84±0.03	20.44±0.77	40.22±0.33

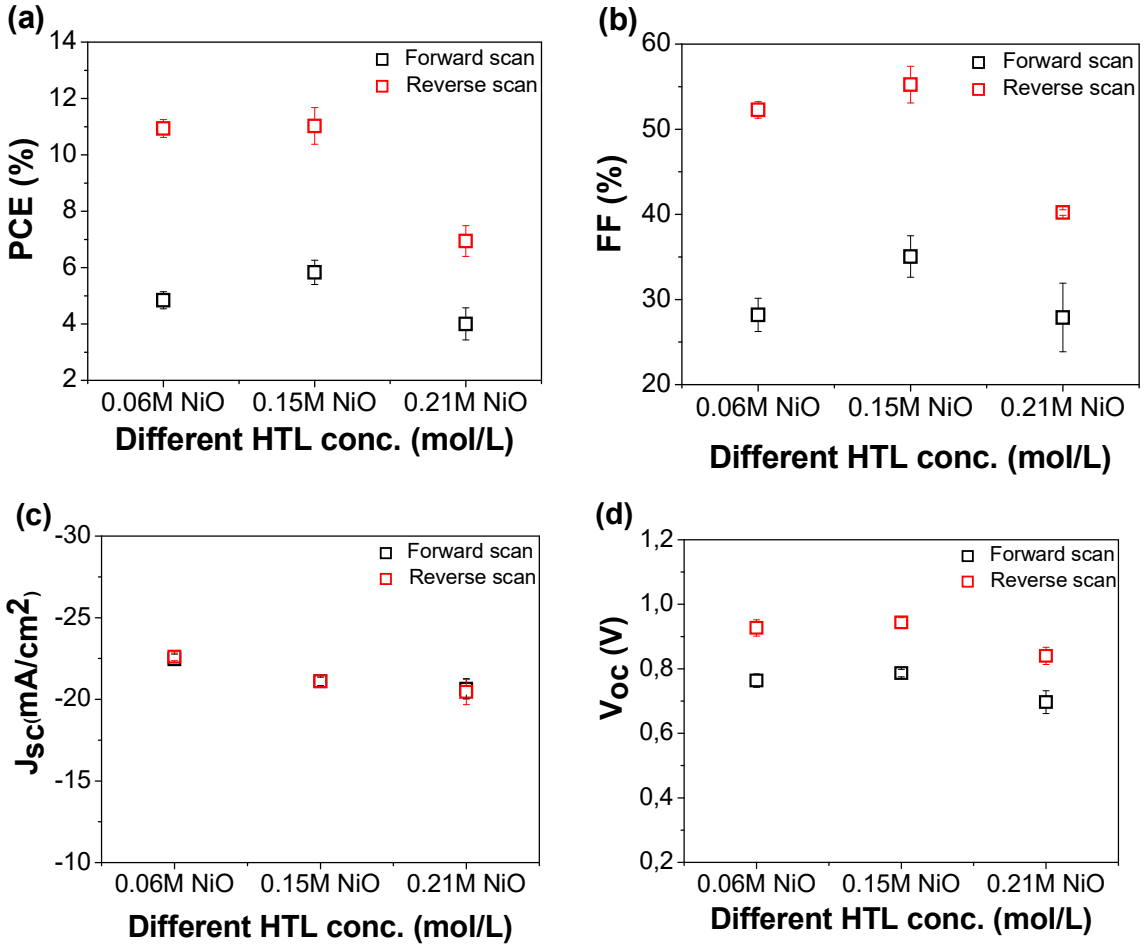

Figure 4.13 Photovoltaic parameters (PCE, J_{sc}, V_{oc} and FF) for the three different concentrations of NiO, used as an HTL in an inverted architecture PSC.

4.5 Additional analyses to enhance PSC efficiency

In this section we analyze the direct relation between the quality of perovskite thin film with the photovoltaic response of the complete PSC, quality that depends on the fabrication conditions (R.H, temperature, etc) which can induce poor thin film formation and poor crystallization of the perovskite absorber and thus low PSC performance. **Figure 4.14** shows the IV curves and IPCE of the cells analysed in this section, *cell A* with a PCE of 4.7 % and *cell B* that exhibits a PCE of 10.7 %.

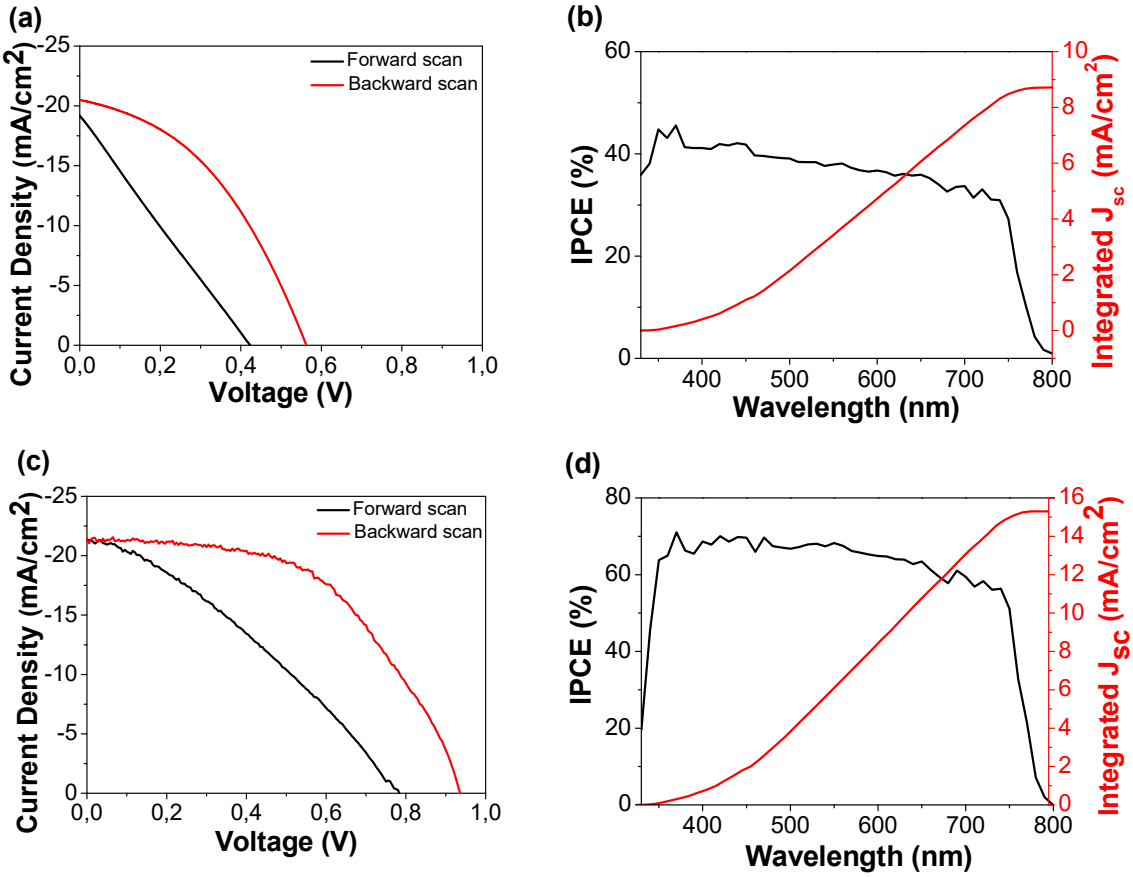

Figure 4.14. Photovoltic performance of PSCs with two dissimilar power conversion efficiencies. **(a)** IV curves and **(b)** IPCE analysis of the perovskite cell with an PCE of 4.7 %, and **(c)** IV curves and **(d)** IPCE analysis of a perovskite solar cell showing 10.7 % efficiency.

In the following sections we characterize these two PSCs showing the two different PCE. Our aim is to understand the reasons behind dissimilar efficiencies through analysing by X-ray diffraction of the perovskite thin film, and by SEM/EDX analysis of complete PSC devices. As mentioned before, the two selected PSCs were fabricated by spin coting applying the two-step method, applying the anti-solvent method with the DMF:DMSO (4:1) solvent mixture. The resulting devices have the configuration glass/FTO/NiO/halide perovskite/PCBM:ZnO-BHJ/Au with 4.7 % and 10.7 % efficiency.

4.5.1 Effect of the purity and crystallinity of the halide perovskite

A study by XRD of the halide perovskite thin film was carried out. We analyze how the purity and crystallization of the halide perovskite can affect the photovoltaic parameters of the PSC. This study is a key point to understand the crystal phase of the mixed-ion perovskite $[HC(NH_2)_2]_{0.85}(CH_3NH_3)_{0.15}Pb(I_{0.85}Br_{0.15})_3$, also called $(MAPbBr_3)_{0.15}(FAPbI_3)_{0.85}$. To carry out

the X-ray analysis the thin films were prepared as described in Chapter 2 (section 2.2.3.1) a complete PSC was analysed, that were kept under N_2 atmosphere until the XRD measurements were carried out.

The $MAPbI_3$ is usually found in a tetragonal phase, however, according to the study by Constantinos *et al.*, it can be transformed to the cubic phase at temperatures around ~54 °C [61]. In the case of the formamidinium lead triiodide ($FAPbI_3$) the preparation of high-quality α-$FAPbI_3$ perovskite is still a challenge. The lack of thermodynamic stability and the further fast formation of the yellow δ-$FAPbI_3$ polymorph phase at RT, are the main obstacles for its application in solar cells [62]. Nevertheless, the advantage that $FAPbI_3$ presents lies in the larger ion size of FA^+ (the ionic radi of FA^+ is 2.79 Å whereas for the MA^+ it is 2.70 Å)[63] which directly affects the optical E_g, which value decrease from 1.54 to 1.47 eV. This change in the ionic radi allows an extension of the absorption into the near-infrared [16]. Solar cells based on $FAPbI_3$ with a maximum PCE of 20.1 % have been recently demonstrated [17]. There are also several studies showing the application of a mix of MA and FA cations. In this case, the formation of the yellow polymorph can be avoided resulting in PSCs with good photovoltaic properties [64]. Thus, the controlled fabrication of high quality halide perovskite films with high crystallinity and smooth (pinhole-free) morphology are highly important for the fabrication of efficient PSCs.

Figure 4.15 shows the XRD patterns of the mixed-ion perovskite applied in an inverted structure PSC with **(a)** low performance, 4.6 % efficiency, and **(b)** high performance, 10.7 % efficiency. Characteristic diffraction peaks in both diffractograms, correspond to the tetragonal perovskite phase (a=8.85 Å, b=8.85 Å and c=12.642 Å) with a space group I4cm of the simple $MAPbI_3$ were found in the mixed-ion perovskite, matching those of the database literature (reference code 250739 from ICSD). However, this mixed-ion perovskite also contains certain amount of $FAPbI_3$ and a hexagonal phase is also present for this structure, with a space group P3m1 and cell parameters of a=8.98 Å, b=8.98 Å and c=11.00 Å, α=90 °, β=90 ° and ɣ=120 °.

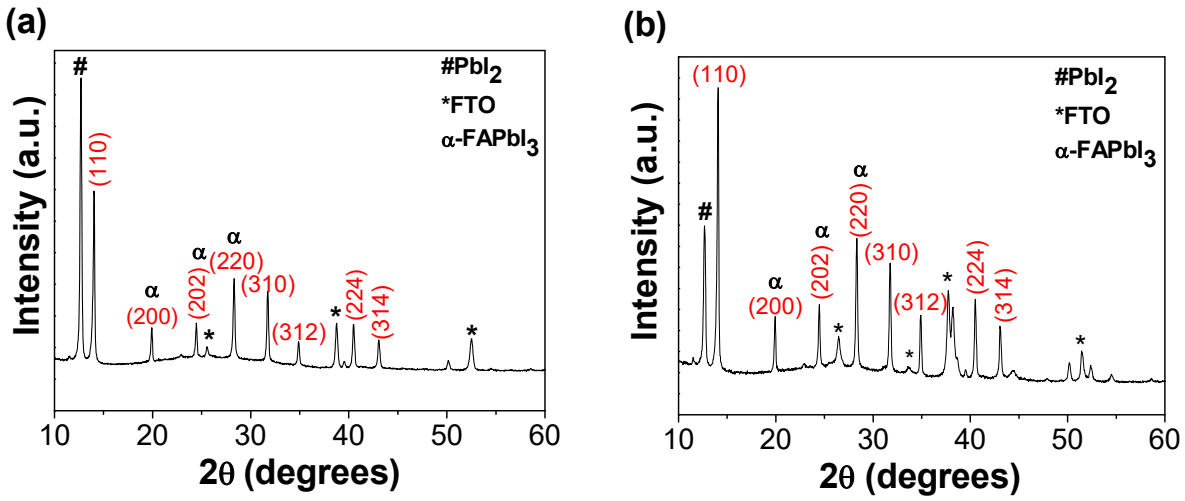

Figure 4.15 Indexed X-ray diffraction analyses of the mixed halide perovskite $(MAPbBr_3)_{0.15}(FAPbI_3)_{0.85}$ applied in an inverted PSC of the type: glass/FTO/NiO/mixed-ion perovskite/PCBM:ZnO/Au. **(a)** solar cell with 4.6 % efficiency and **(b)** solar cell with 10.7 % efficiency.

Following the reported values for the special case of the mixed-ion perovskite $(MAPbBr_3)_{0.15}(FAPbI_3)_{0.85}$, the diffraction peaks were indexed taking into account the α-$FAPbI_3$ phase [65], and the database values (reference code 250736 from ICSD). Furthermore, the peaks assigned to the substrate FTO, are in accordance with those reported in the literature database (reference code 00-046-1088).

The high intensity peak at 12.67°, **Figure 4.15 (a)**, corresponds to the (001) reflection and is attributed to unreacted PbI_2 (labelled as #PbI_2). Although certain excess of PbI_2 has been shown to be beneficial for the high performance PSCs [61-62], its presence in relation to the halide perovskite material should be carefully controlled. The reflection (001) is the strongest peak of the spectra **(a)** which could reflect the unreacted amount of PbI_2 residue and could be one of the reasons behind the low, 4.6 % PCE, of the solar cell. Moreover, the (110) reflection at 14.06° corresponds to the crystal structure of the mixed-ion perovskite which is less intense than the (001) peak of the PbI_2. This has been attributed to the low conversion of the reactants into the $(MAPbBr_3)_{0.15}(FAPbI_3)_{0.85}$, an indication of an incomplete perovskite formation [68].

Figure 4.15 (b) shows the diffraction pattern of the halide perovskite applied in a PSCs with a 10.7 % efficiency. The reflection (001) at 12.63° ascribed to PbI_2 residue exhibits much less intensity in comparison with the same peak in **Figure 4.15 (a)**, an indication that PbI_2 is

present in less amount in this PSC. Moreover, the reflection (110) at 14.04° exhibits a higher intensity compared with the typical PbI_2 peak, which suggests a more efficient conversion into the $(MAPbBr_3)_{0.15}(FAPbI_3)_{0.85}$.

Thus, we have observed that the crystallinity as well as the presence of PbI_2, are key elements that should be carefully controlled in order to fabricate high efficiency PSCs.

4.5.2 Effect of device processing

In order to determine the thickness and quality of the light harvesting halide perovskite thin film, a morphology study was carried out on the inverted PSC.

The thickness of the perovskite layer is a key parameter to take into account for PSC performance. If the perovskite film is very thin, light absorption can be compromised resulting in poor photocurrent. However, if the perovskite film is too thick, the efficiency of the charge carrier extraction will be poor due to an increase in the unwanted charge recombination. Several groups have reported studies of perovskite film thickness for a normal configuration PSC using TiO_2, the optimal thickness is about 650 nm [69]. For a mixed-ion perovskite composed of $CH_3NH_3PbI_{3-x}Cl_x$, a recent study on inverted and normal architectures showed an optimal perovskite film thickness of between 400 and 800 nm for high performance devices [7-65].

Additionally, Liu *et al.* reported an optimum thickness of 330 nm, of an inverted structure ITO/ZnO/$CH_3NH_3PbI_3$/P3HT/Ag, with a PCE of 11.3 % [71]. Following these studies, in this section, we analysed the halide perovskite thin film quality and thickness.

Figure 4.16 and Figure 4.17 show the lateral views of FIB-SEM analysis of PSCs with low (4.6 %) and high (10.7 %) PCE, respectively, which we can relate to the morphology of the perovskite thin film, as follows.

Figure 4.16 (a) shows large voids (pinholes) which are originated in the perovskite absorber layer $(MAPbBr_3)_{0.15}(FAPbI_3)_{0.85}$. These voids indicate a poor thin film quality which results in poor photovoltaic response of the PSC. **Figure 4.16 (b)** shows the thicknesses of each layer of the PSCs: ~650 nm thick perovskite film, ~70 nm for NiO and ~80 nm for the Au electrode. **Figure 4.16 (c)**, shows the EDX analysis of the which confirm that all the expected

elements for the inverted structure PSC FTO/NiO/mixed-ion perovskite/PCBM-ZnO/Au were present in the device in a correct distribution. However, despite these favourable EDX results, the problematic morphology in relation to the absorber layer directly affected the photovoltaic performance of the cell.

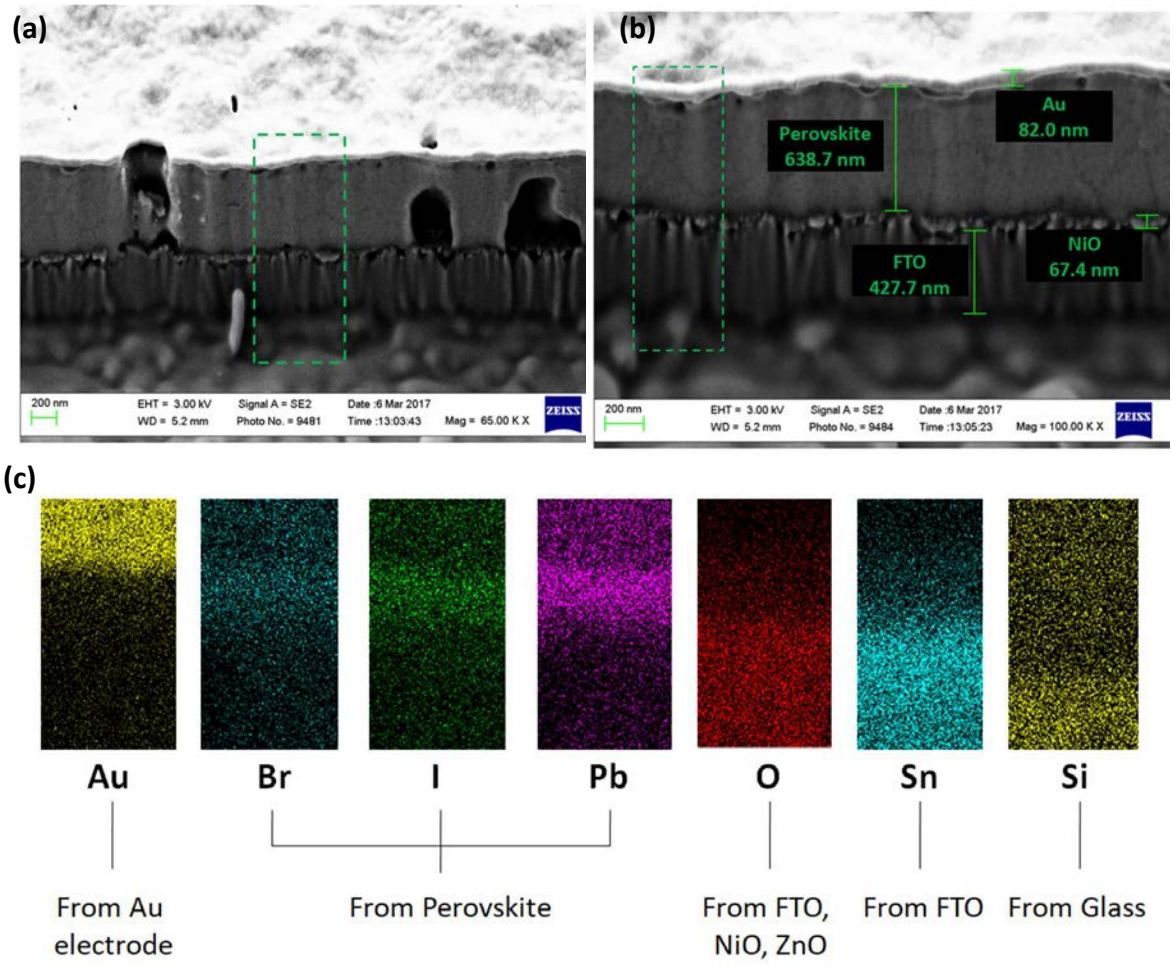

Figure 4.16 (a) Cross-sectional FIB-SEM image of the mixed-ion perovskite cell **(b)** thickness of the mixed-ion perovskite cell and **(c)** individual element distribution in perovskite films.

Figure 4.17 (a) shows the area of the PSC (10.7 % efficiency) milled by FIB. **Figure 4.17 (b)** shows the $(MAPbBr_3)_{0.15}(FAPbI_3)_{0.85}$ perovskite film made of grain-size crystallites of about 450-550 nm. In this case, a ~650 nm thick absorbing halide perovskite layer was observed, which showed homogeneous perovskite grains. The **Figure 4.17 (c)** also shows an homogeneous distribution of the thin films that compose the PSC with the structure of FTO/NiO/perovskite/PCBM:ZnO/Au, as shown by EDX. The concentration distribution signal

in the graph suggests that the adequate thicknesses of the layers provided a good morphology and more stability in the interfaces allowing a good photovoltaic performance.

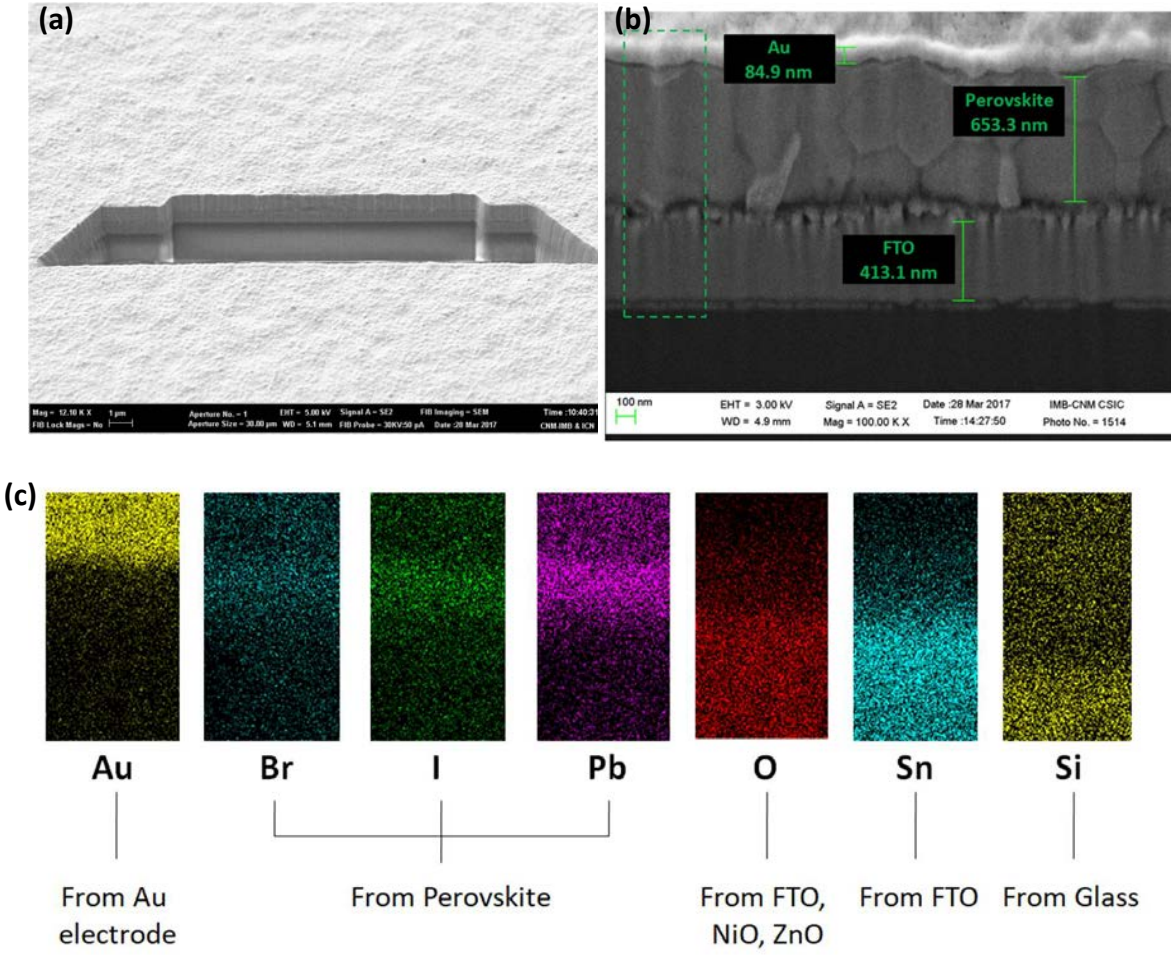

Figure 4.17 (a) Image of section made by FIB milling **(b)** thickness of the mixed-ion perovskite cell in a cross-sectional FIB-SEM image and **(c)** individual element distribution of the thin films of the PSC, analyzed by EDX.

As a summary, we have observed that high amount of PbI_2 in relation to the halide perovskite is detrimental for the photovoltaic performance of the PSCs. The solar cells with higher efficiency show higher crystallinity of the perovskite film and lower PbI_2 content, large and homogeneous perovskite grains and absence of pinholes in the thin films. Our results are in well agreement with reports on the effect of crystallization and morphology of the absorber and the fabrication of high efficient PSCs [72].

4.6 Champion Cell Inverted PSC configuration

In this section we show the optimized inverted configuration PSCs, we considered the optimization parameters carried out for the different transport layers and complete device fabrication described in section 4.5. The optimized device showed a champion solar cell with 11.77 % efficiency. The optimized parameters for its fabrication are: use of 0.15 M of NiO concentration for the fabrication of the HTL layer, where the NiO layer showed a thin film thickness of 70 nm approximately. On the other hand, the best ETL was the $PC_{70}BM$:ZnO-BHJ in a 1:1 molar ratio and with a thin film layer of 60 nm in thickness approximately.

Figure 4.18 shows the **(a)** IV curves and **(b)** IPCE analysis of the champion cell. The corresponding photovoltaic parameters are indicated in the inset of **Figure 4.18 (a)**.

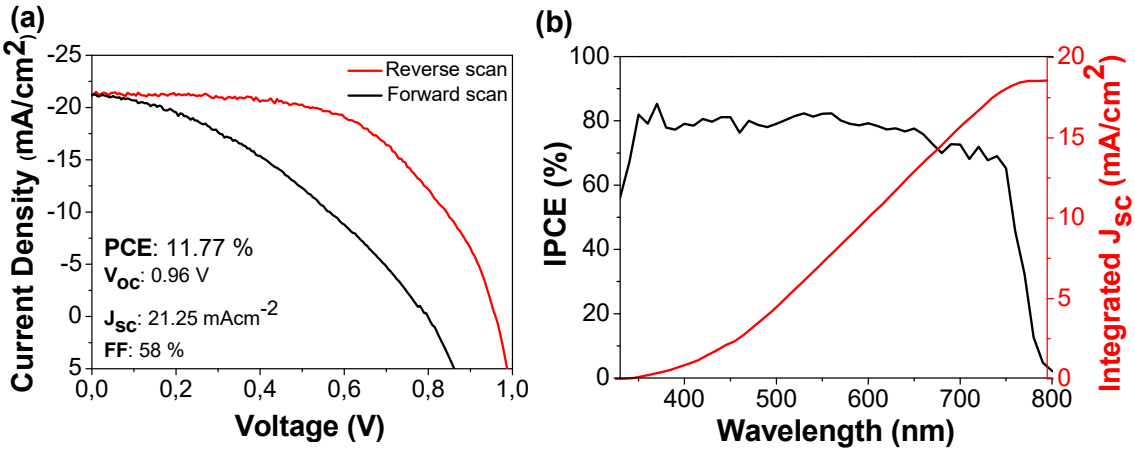

Figure 4.18 (a) IV curves and **(b)** IPCE analysis of the champion PSC with 11.77 % efficiency.

4.7 Conclusions

This chapter describes the fabrication of inverted PSCs applying oxides as transport layers for high efficient and stable solar cells. We have demonstrated the development and optimization of thin film semiconductor oxides, made by solution processing, applied inverted-configuration PSCs. The oxides applied are NiO and ZnO, as the HTL and ETL, respectively, which provided excellent photovoltaic response.

An exhaustive optimization of the transport layers (HTL and ETL), indicated that the best concentration of NiO was 0.15 M as a HTL while for the ETL, four different materials (and mixtures) were analysed. The mixed solution of $PC_{70}BM$:ZnO-BHJ prepared as a bulk

heterojunction configuration demonstrated to be the best option to work as ETL, with champion PSCs with 11.77 % efficiency. Analysis by XRD revealed a direct relation between the halide perovskite peaks intensity and the intensity of the PbI_2 peak: the higher the intensity of the PbI_2 in relation to the halide perovskite the lower the PCE of the solar cell. Thus we have been able to obtain PSC with 10.7 % efficiency for solar cells with low PbI_2 content, in comparison with 4.7 % efficiency observed for the high incomplete crystalized halide perovskite with high content of PbI_2. From the FIB-SEM study, we determined the thickness of the different layers. The perovskite layer exhibited a thickness of 650 nm with large crystals (from 300 nm approximately) for the high performance cell. On the other hand, the layers of the low performance cell showed an adequate thickness and chemical composition, although some voids in the perovskite material were detected leading to poor photovoltaic performance. It is well known that the crystallization and morphology are closely related to light harvesting efficiency and short-circuit photocurrent density. In conclusion, the comparison study between high performance PSC with low performance PSC emphasize the importance and the direct impact of the quality and cristallinity of the perovskite absorber layer on the photovoltaic performance of the device.

4.8 References

[1] D. B. Mitzi, S. Wang, C. A. Feild, C. A. Chess, and A. M. Guloy, "Conducting Layered Organic-inorganic Halides Containing <110>-Oriented Perovskite Sheets," *Science (80-.).*, vol. 267, no. 5203, pp. 1473–1476, 1995.

[2] A. Kojima, K. Teshima, Y. Shirai, and T. Miyasaka, "Organometal Halide Perovskites as Visible-Light Sensitizers for Photovoltaic Cells," *J. Am. Chem. Soc.*, vol. 131, no. 17, pp. 6050–6051, 2009.

[3] H.-S. Kim *et al.*, "Lead Iodide Perovskite Sensitized All-Solid-State Submicron Thin Film Mesoscopic Solar Cell with Efficiency Exceeding 9%," *Sci. Rep.*, vol. 2, p. 591, 2012.

[4] M. Liu, M. B. Johnston, and H. J. Snaith, "Efficient planar heterojunction perovskite solar cells by vapour deposition," *Nature*, vol. 501, p. 395, 2013.

[5] F. Alta and E. S. Asu, "NREL Efficiency Chart," *Www.Nrel.Gov*, p. 2020, 2019.

[6] G. Xing *et al.*, "Long-Range Balanced Electron- and Hole-Transport Lengths in Organic-Inorganic $CH_3NH_3PbI_3$," *Science (80-.).*, vol. 342, no. 6156, pp. 344–347, 2013.

[7] S. D. Stranks *et al.*, "Electron-Hole Diffusion Lengths Exceeding 1 Micrometer in an Organometal Trihalide Perovskite Absorber," *Science (80-.).*, vol. 342, no. 6156, pp. 341–344, 2013.

[8] D. W. de Quilettes *et al.*, "Impact of microstructure on local carrier lifetime in perovskite solar cells," *Science (80-.).*, vol. 348, no. 6235, pp. 683–686, 2015.

[9] J. H. Noh, S. H. Im, J. H. Heo, T. N. Mandal, and S. Il Seok, "Chemical Management for Colorful, Efficient, and Stable Inorganic–Organic Hybrid Nanostructured Solar Cells," *Nano Lett.*, vol. 13, no. 4, pp. 1764–1769, 2013.

[10] S. A. Kulkarni, T. Baikie, P. P. Boix, N. Yantara, N. Mathews, and S. Mhaisalkar, "Band-gap tuning of lead halide perovskites using a sequential deposition process," *J. Mater. Chem. A*, vol. 2, no. 24, pp. 9221–9225, 2014.

[11] H. Tang, S. He, and C. Peng, "A Short Progress Report on High-Efficiency Perovskite Solar Cells," *Nanoscale Res. Lett.*, vol. 12, no. 1, p. 410, 2017.

[12] F. G. Santomauro *et al.*, "Localized holes and delocalized electrons in photoexcited inorganic perovskites: Watching each atomic actor by picosecond X-ray absorption spectroscopy," *Struct. Dyn.*, vol. 4, no. 4, p. 44002, 2017.

[13] S. De Wolf *et al.*, "Organometallic Halide Perovskites: Sharp Optical Absorption Edge and Its Relation to Photovoltaic Performance," *J. Phys. Chem. Lett.*, vol. 5, no. 6, pp. 1035–1039, 2014.

[14] A. P. and D. Weber, "Dynamic disorder in methylammoniumtrihalogenoplumbates (II) observed by millimeter-wave spectroscopy," *J. Chem. Phys.*, vol. 87, no. 11, pp. 6373–6378, 1987.

[15] A. M. Glazer, "Simple ways of determining perovskite structures," *Acta Crystallogr.*

Sect. A, vol. 31, no. 6, pp. 756–762, 1975.

[16] M. T. Weller, O. J. Weber, J. M. Frost, and A. Walsh, "Cubic Perovskite Structure of Black Formamidinium Lead Iodide, α-[HC(NH2)2]PbI3, at 298 K," *J. Phys. Chem. Lett.*, vol. 6, no. 16, pp. 3209–3212, 2015.

[17] W. S. Yang *et al.*, "High-performance photovoltaic perovskite layers fabricated through intramolecular exchange," *Science (80-.).*, vol. 348, no. 6240, pp. 1234–1237, 2015.

[18] A. Amat *et al.*, "Cation-Induced Band-Gap Tuning in Organohalide Perovskites: Interplay of Spin–Orbit Coupling and Octahedra Tilting," *Nano Lett.*, vol. 14, no. 6, pp. 3608–3616, 2014.

[19] Y. Zhang, G. Grancini, Y. Feng, A. M. Asiri, and M. K. Nazeeruddin, "Optimization of Stable Quasi-Cubic FAxMA1–xPbI3 Perovskite Structure for Solar Cells with Efficiency beyond 20%," *ACS Energy Lett.*, vol. 2, no. 4, pp. 802–806, 2017.

[20] W. S. Yang *et al.*, "Iodide management in formamidinium-lead-halide–based perovskite layers for efficient solar cells," *Science (80-.).*, vol. 356, no. 6345, pp. 1376–1379, 2017.

[21] L. Hu *et al.*, "PEDOT:PSS monolayers to enhance the hole extraction and stability of perovskite solar cells," *J. Mater. Chem. A*, vol. 6, no. 34, pp. 16583–16589, 2018.

[22] B. Xu *et al.*, "Functional solid additive modified PEDOT:PSS as an anode buffer layer for enhanced photovoltaic performance and stability in polymer solar cells," *Sci. Rep.*, vol. 7, p. 45079, 2017.

[23] Q. Dong *et al.*, "Encapsulation of Perovskite Solar Cells for High Humidity Conditions," *ChemSusChem*, vol. 9, no. 18, p. 2518, 2016.

[24] P. B. Romita Chouhan Arpana Agrawal, Mukul Gupta, Pranay K. Sen and Pratima Sen, "Effects of oxygen partial pressure and annealing on dispersive optical nonlinearity in NiO thin films," *J. Appl. Phys.*, vol. 122, no. 2, p. 25301, 2017.

[25] J.-H. Y. Ming-Hsien Li Soo-Jin Moon and Peter Chen, "Inorganic p-Type Semiconductors: Their Applications and Progress in Dye-Sensitized Solar Cells and Perovskite Solar Cells," *Energies*, vol. 9, 2016.

[26] P. Docampo, J. M. Ball, M. Darwich, G. E. Eperon, and H. J. Snaith, "Efficient organometal trihalide perovskite planar-heterojunction solar cells on flexible polymer substrates," *Nat. Commun.*, vol. 4, p. 2761, 2013.

[27] J.-Y. Jeng *et al.*, "Nickel Oxide Electrode Interlayer in CH3NH3PbI3 Perovskite/PCBM Planar-Heterojunction Hybrid Solar Cells," *Adv. Mater.*, vol. 26, no. 24, pp. 4107–4113, 2014.

[28] W. Chen *et al.*, "Efficient and stable large-area perovskite solar cells with inorganic charge extraction layers," *Science (80-.).*, vol. 350, no. 6263, pp. 944–948, 2015.

[29] J. H. Kim *et al.*, "High-Performance and Environmentally Stable Planar Heterojunction

Perovskite Solar Cells Based on a Solution-Processed Copper-Doped Nickel Oxide Hole-Transporting Layer," *Adv. Mater.*, vol. 27, no. 4, pp. 695–701, 2015.

[30] J. W. Jung, C.-C. Chueh, and A. K.-Y. Jen, "A Low-Temperature, Solution-Processable, Cu-Doped Nickel Oxide Hole-Transporting Layer via the Combustion Method for High-Performance Thin-Film Perovskite Solar Cells," *Adv. Mater.*, vol. 27, no. 47, pp. 7874–7880, 2015.

[31] C. Zuo and L. Ding, "Solution-Processed Cu2O and CuO as Hole Transport Materials for Efficient Perovskite Solar Cells," *Small*, vol. 11, no. 41, pp. 5528–5532, 2015.

[32] Z. Wu *et al.*, "Efficient planar heterojunction perovskite solar cells employing graphene oxide as hole conductor," *Nanoscale*, vol. 6, no. 18, pp. 10505–10510, 2014.

[33] N. Arora *et al.*, "Perovskite solar cells with CuSCN hole extraction layers yield stabilized efficiencies greater than 20%," *Science (80-.).*, vol. 358, no. 6364, pp. 768–771, 2017.

[34] R. Fan, Y. Huang, L. Wang, L. Li, G. Zheng, and H. Zhou, "The Progress of Interface Design in Perovskite-Based Solar Cells," *Adv. Energy Mater.*, vol. 6, no. 17, p. 1600460, 2016.

[35] W. Ke *et al.*, "Efficient hole-blocking layer-free planar halide perovskite thin-film solar cells," *Nat. Commun.*, vol. 6, p. 6700, 2015.

[36] N. J. Jeon *et al.*, "Compositional engineering of perovskite materials for high-performance solar cells," *Nature*, vol. 517, p. 476, 2015.

[37] Z. W. Sai Bai Xiaojing Wu, Yizheng Jin, Ni Zhao , Zhihui Chen, Qingqing Mei, Xin Wang, Zhizhen Ye, Tao Song, Ruiyuan Liu, Shuit-tong Lee, and Baoquan Sun, "High-performance planar heterojunction perovskite solar cells_Preserving long charge carrier diffusion lengths and interfacial engineering," *Nano Res.*, vol. 7, pp. 1749–1758, 2014.

[38] G. Yang, H. Tao, P. Qin, W. Ke, and G. Fang, "Recent progress in electron transport layers for efficient perovskite solar cells," *J. Mater. Chem. A*, vol. 4, no. 11, pp. 3970–3990, 2016.

[39] K. Mahmood, S. Sarwar, and M. T. Mehran, "Current status of electron transport layers in perovskite solar cells: materials and properties," *RSC Adv.*, vol. 7, no. 28, pp. 17044–17062, 2017.

[40] Z. Liu, X. Xie, G. Liu, and E.-C. Lee, "High-performance metal-oxide-free perovskite solar cells based on organic electron transport layer and cathode," *Org. Electron.*, vol. 64, pp. 195–201, 2019.

[41] G. Kakavelakis *et al.*, "Efficient and Highly Air Stable Planar Inverted Perovskite Solar Cells with Reduced Graphene Oxide Doped PCBM Electron Transporting Layer," *Adv. Energy Mater.*, vol. 7, no. 7, p. 1602120, Apr. 2017.

[42] J. M. Ball, M. M. Lee, A. Hey, and H. J. Snaith, "Low-temperature processed meso-

superstructured to thin-film perovskite solar cells," *Energy Environ. Sci.*, vol. 6, no. 6, pp. 1739–1743, 2013.

[43] D. Liu and T. L. Kelly, "Perovskite solar cells with a planar heterojunction structure prepared using room-temperature solution processing techniques," *Nat. Photonics*, vol. 8, p. 133, 2013.

[44] K. Wang *et al.*, "Amorphous Inorganic Electron-Selective Layers for Efficient Perovskite Solar Cells: Feasible Strategy Towards Room-Temperature Fabrication," *Adv. Mater.*, vol. 28, no. 9, pp. 1891–1897, Mar. 2016.

[45] W. Ke *et al.*, "Low-Temperature Solution-Processed Tin Oxide as an Alternative Electron Transporting Layer for Efficient Perovskite Solar Cells," *J. Am. Chem. Soc.*, vol. 137, no. 21, pp. 6730–6733, Jun. 2015.

[46] C.-C. Chueh, C.-Z. Li, and A. K. Y. Jen, "Recent progress and perspective in solution-processed Interfacial materials for efficient and stable polymer and organometal perovskite solar cells," *Energy Environ. Sci.*, vol. 8, no. 4, pp. 1160–1189, 2015.

[47] H.-L. Y. Steven K. Hau Nam Seob Baek, Jingyu Zou, Kevin O'Malley, and Alex K.-Y. Jen, "Air-stable inverted flexible polymer solar cells using zinc oxide nanoparticles as an electron selective layer," *Appl. Phys. Lett.*, vol. 92, no. 25, p. 253301, 2008.

[48] L. Qian, Y. Zheng, J. Xue, and P. H. Holloway, "Stable and efficient quantum-dot light-emitting diodes based on solution-processed multilayer structures," *Nat. Photonics*, vol. 5, p. 543, 2011.

[49] T. Liu, K. Chen, Q. Hu, R. Zhu, and Q. Gong, "Inverted Perovskite Solar Cells: Progresses and Perspectives," *Adv. Energy Mater.*, vol. 6, no. 17, p. 1600457, 2016.

[50] W. Nie *et al.*, "High-efficiency solution-processed perovskite solar cells with millimeter-scale grains," *Science (80-.).*, vol. 347, no. 6221, pp. 522–525, 2015.

[51] W. Qiu *et al.*, "Highly efficient perovskite solar cells with crosslinked PCBM interlayers," *J. Mater. Chem. A*, vol. 5, no. 6, pp. 2466–2472, 2017.

[52] J. You *et al.*, "Low-Temperature Solution-Processed Perovskite Solar Cells with High Efficiency and Flexibility," *ACS Nano*, vol. 8, no. 2, pp. 1674–1680, 2014.

[53] M. B. Islam, M. Yanagida, Y. Shirai, Y. Nabetani, and K. Miyano, "NiOx Hole Transport Layer for Perovskite Solar Cells with Improved Stability and Reproducibility," *ACS Omega*, vol. 2, no. 5, pp. 2291–2299, 2017.

[54] M. I. Khan, K. A. Bhatti, R. Qindeel, N. Alonizan, and H. S. Althobaiti, "Characterizations of multilayer ZnO thin films deposited by sol-gel spin coating technique," *Results Phys.*, vol. 7, pp. 651–655, 2017.

[55] L. Q. Zhang *et al.*, "Highly efficient and stable planar heterojunction perovskite solar cells via a low temperature solution process," *J. Mater. Chem. A*, vol. 3, no. 23, pp. 12133–12138, 2015.

[56] J. You *et al.*, "Improved air stability of perovskite solar cells via solution-processed

metal oxide transport layers," *Nat. Nanotechnol.*, vol. 11, p. 75, 2015.

[57] S. S. Mali, H. Kim, H. H. Kim, S. E. Shim, and C. K. Hong, "Nanoporous p-type NiOx electrode for p-i-n inverted perovskite solar cell toward air stability," *Mater. Today*, vol. 21, no. 5, pp. 483–500, 2018.

[58] J. Zhang *et al.*, "ZnO-PCBM bilayers as electron transport layers in low-temperature processed perovskite solar cells," *Sci. Bull.*, vol. 63, no. 6, pp. 343–348, 2018.

[59] W. Zhang *et al.*, "Thermal Stability-Enhanced and High-Efficiency Planar Perovskite Solar Cells with Interface Passivation," *ACS Appl. Mater. Interfaces*, vol. 9, no. 44, pp. 38467–38476, 2017.

[60] Z. Liu *et al.*, "Nickel oxide nanoparticles for efficient hole transport in p-i-n and n-i-p perovskite solar cells," *J. Mater. Chem. A*, vol. 5, no. 14, pp. 6597–6605, 2017.

[61] C. C. Stoumpos, C. D. Malliakas, and M. G. Kanatzidis, "Semiconducting Tin and Lead Iodide Perovskites with Organic Cations: Phase Transitions, High Mobilities, and Near-Infrared Photoluminescent Properties," *Inorg. Chem.*, vol. 52, no. 15, pp. 9019–9038, 2013.

[62] Z. Zhou, S. Pang, F. Ji, B. Zhang, and G. Cui, "The fabrication of formamidinium lead iodide perovskite thin films via organic cation exchange," *Chem. Commun.*, vol. 52, no. 19, pp. 3828–3831, 2016.

[63] A. Binek, F. C. Hanusch, P. Docampo, and T. Bein, "Stabilization of the Trigonal High-Temperature Phase of Formamidinium Lead Iodide," *J. Phys. Chem. Lett.*, vol. 6, no. 7, pp. 1249–1253, 2015.

[64] N. Pellet *et al.*, "Mixed-Organic-Cation Perovskite Photovoltaics for Enhanced Solar-Light Harvesting," *Angew. Chemie Int. Ed.*, vol. 53, no. 12, pp. 3151–3157, 2014.

[65] J.-Y. Seo *et al.*, "Ionic Liquid Control Crystal Growth to Enhance Planar Perovskite Solar Cells Efficiency," *Adv. Energy Mater.*, vol. 6, no. 20, p. 1600767, 2016.

[66] B. Park *et al.*, "Understanding how excess lead iodide precursor improves halide perovskite solar cell performance," *Nat. Commun.*, vol. 9, no. 1, p. 3301, 2018.

[67] F. Liu *et al.*, "Is Excess PbI2 Beneficial for Perovskite Solar Cell Performance?," *Adv. Energy Mater.*, vol. 6, no. 7, p. 1502206, Apr. 2016.

[68] J. Ye *et al.*, "High-temperature shaping perovskite film crystallization for solar cell fast preparation," *Sol. Energy Mater. Sol. Cells*, vol. 160, pp. 60–66, 2017.

[69] Y. Zhao and K. Zhu, "Charge Transport and Recombination in Perovskite (CH3NH3)PbI3 Sensitized TiO2 Solar Cells," *J. Phys. Chem. Lett.*, vol. 4, no. 17, pp. 2880–2884, 2013.

[70] G. E. Eperon, V. M. Burlakov, P. Docampo, A. Goriely, and H. J. Snaith, "Morphological Control for High Performance, Solution-Processed Planar Heterojunction Perovskite Solar Cells," *Adv. Funct. Mater.*, vol. 24, no. 1, pp. 151–157, 2014.

[71] D. Liu, M. K. Gangishetty, and T. L. Kelly, “Effect of CH3NH3PbI3 thickness on device efficiency in planar heterojunction perovskite solar cells,” *J. Mater. Chem. A*, vol. 2, no. 46, pp. 19873–19881, 2014.

[72] J. Chen *et al.*, “Solvent effect on the hole-conductor-free fully printable perovskite solar cells,” *Nano Energy*, vol. 27, pp. 130–137, 2016.

Chapter 5

Carbon-based Perovskite Solar Cells

5.1 Introduction

The most employed types of PSCs are the mesoscopic and planar in either the inverted or normal configuration. In all cases, these PSCs apply metal electrodes, like gold, as the back electrode together with expensive hole conductors, such as spiro-OMeTAD. The application of such materials can limit the long-term stability of the device due to their low thermal stability and high reactivity. As a result, the hole-conductor-free perovskite solar cell was initially reported by Etgar *et al*. [1], followed by the Carbon-based PSC (CPSC), which employs carbon as a counter electrode and eliminates also the use of the HTM [2]. CPSCs are currently one of the most stable configurations, partially due to the presence of oxides bi-layers (mesoscopic TiO_2 and ZrO_2), which are able to protect the device from ambient conditions. The CPSC applies also organic modifiers, or organic additives, used as mixtures with the halide perovskite. These additives can passivate trap states found in the halide perovskite material and at the perovskite/oxide interface [3]. Although one of the drawbacks of the CPC is its low PCE, currently at 18 % [4], the elimination of unstable organic hole conductors, the application of double oxides and carbon electrodes, as well as the use of organic additives makes this CPSC configuration one of the most stables up to date.

This device structure consists of tri-layers, two made of mesoporous oxides and a third one of porous carbon (**Figure 5.1**): TiO_2, acting as an ETL, the ZrO_2, as the spacer layer or scaffold, and a layer of a porous carbon film which plays the role of the back electrode. The layers are screen printed, layer by layer, on the FTO substrate followed by the corresponding sintering treatments. This triple thin film layer is called “the shell” in this thesis work, and once is fabricated, its high porosity allows for the halide perovskite solution to be introduced into the structure via infiltration. In the most classic configuration

employing MAPI as the halide perovskite, the organic additive, the 5-aminovaleric acid iodide (5-AVAI), the lead Iodide (PbI_2) and the methylamonnium Iodide (MAI) are dissolved together in a solvent (e.g. ɣ-butyrolactone or GBL) and the resulting solution is used for infiltration. These CPSC structures are highly promising due to their low cost and abundant available materials, such as semiconductor oxides (TiO_2 and ZrO_2) and Carbon [5]. **Figure 5.1** shows a schematic representation of a CPSC **(a)**, the corresponding band energy alignment **(b)** and the possible bonding modes between the organic molecule 5AVAI, the halide perovskite and the oxide layer **(c)**.

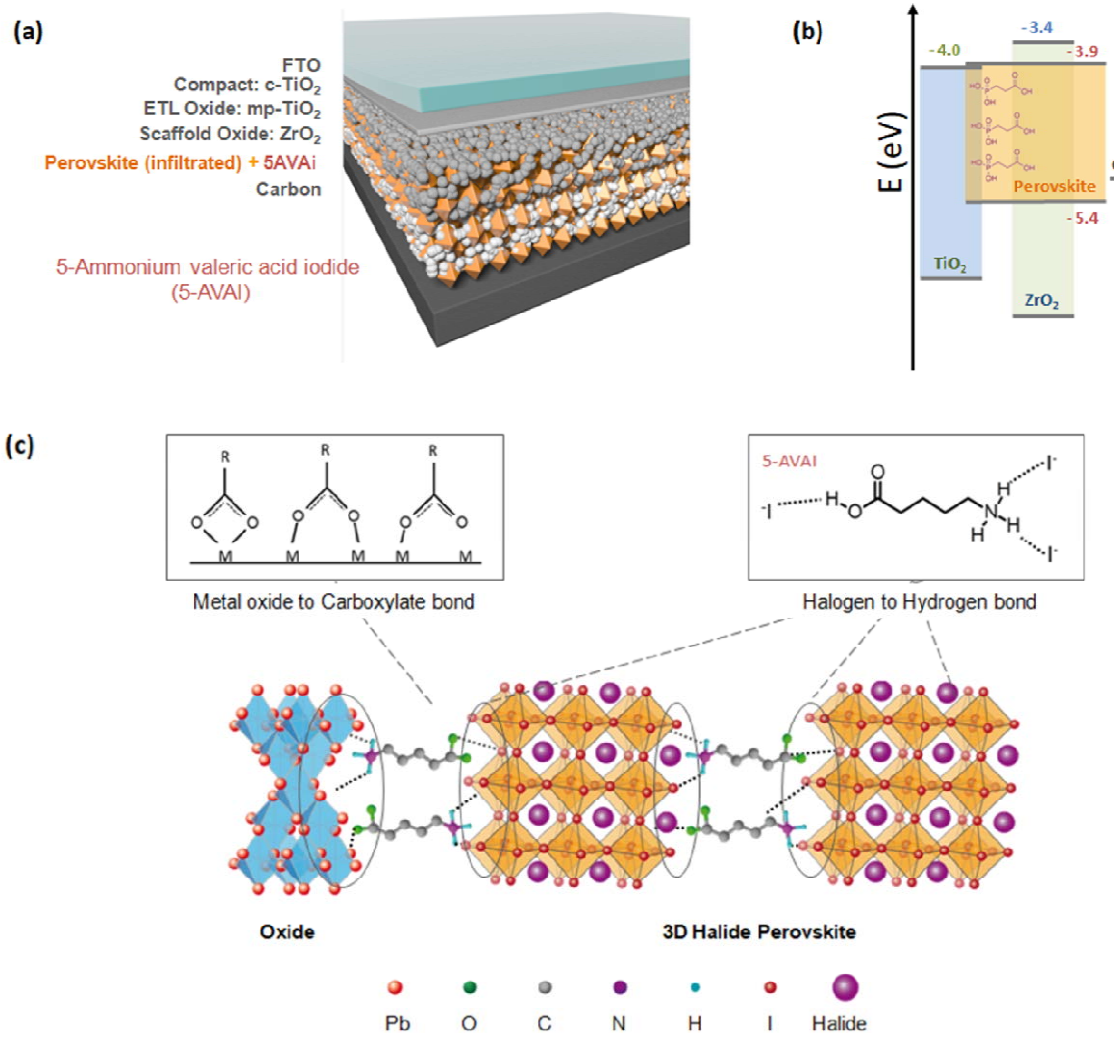

Figure 5.1 Carbon –based Perovskite solar cell (CPSCs). **(a)** Schematic representation of a CPSCs. The halide perovskite absorber is mixed with the organic modifier (or additive) 5AVAI, and introduced in the structure by infiltration, **(b)** Band energy alignment of a CPSC [6], and **(c)** Possible bonding modes between the organic molecule 5AVAI, the halide perovskite and the oxide layer.

Furthermore, the scalable processing methods used for CPSC fabrication (screen printing) and the high stability already reported by several research groups make this technology very attractive for commercialization[6-7].In this regard, Han *et al.* reported a highly efficient, stable and large area printable mesoscopic perovskite module (100 cm^2), exceeding 10 % efficiency. The module showed no sign of degradation under light soaking conditions under constant 1 sun AM1.5 illumination for 1000 h [6].

The energy band alignment of these CPSCs (**Figure 5.1 (b)**) shows that the electron-hole pair generated in the CB and VB of the perovskite absorber layer separates properly after an excitation by light illumination. The photogenerated electrons are injected into the CB of mp-TiO_2 layer, while the holes get extracted and are transported through the carbon counter electrode. For this HTL-free PSC, a spacer layer, such as ZrO_2 is usually employed to separate and prevent direct contact between the TiO_2 and carbon layer. This is because in the absence of the HTL, the direct contact of the TiO_2 and carbon can cause a short circuit negatively affecting the photovoltaic performance. Also, the c-TiO_2 is an important part of the device, acting as an ETL or hole-blocking layer, which prevents the holes generated in the perovskite absorber, reaching the FTO bottom electrode [9]. In this CPSCs structure, the electrons generated in the perovskite absorber are collected by the mp-TiO_2, acting as an ETL, and are transferred to the FTO front electrode via c-TiO_2. At the same time, the holes generated in the perovskite absorber are collected by the carbon counter electrode, as seen in **Figure 5.1 (b).**

In this thesis, we studied two different methods for the infiltration of the halide perovskite into the FTO/TiO_2/ZrO_2/C “shell”, the one-step method and the two-step method, as will be described in the following sections.

5.2 Analysis of the FTO/TiO_2/ZrO_2/C “shell” by SEM and thin film optimization

The optimization of the thickness of each layer that constitutes the“shell” of the CPSCs is one of the most crucial factors affecting cell performance, this directly depends on the structure and thickness of the oxide and carbon layers. The use of thin layers will allow a better infiltration of the perovskite solution, however too thin carbon layer will suffer low

electrical conductivity while a too thin zirconia layer will not provide enough insulation between the TiO_2 and the Carbon [10]. One of the most relevant aspect to achieve good photovoltaic performance is the control of the thickness of the ZrO_2 spacer layer, because it separates the TiO_2 layer and the carbon stack, avoiding any direct contact [11]. Without a ZrO_2 layer, the electrons in TiO_2 layer would find a shortcut to the carbon counter electrode. Many different thicknesses for optimum characteristics have been reported, from 0.5 to 2 µm of mp-TiO_2, from 1 to 3 µm of ZrO_2 and from 9 to 13 µm of carbon layer [4, 11, 12]. Basically, the target thickness is around 1 µm for mp-TiO_2, 2 µm for the ZrO_2 as scaffold layer and 10 µm for the porous carbon layer. One of the aims of this thesis is the optimization of the CPSC fabrication through the optimization of the thickness of each of the layers. Hongwei Han's group, the fathers of the CPSC, reported a PCE exceeding the 10 % efficiency and 1000 h stability through the layer-by-layer optimization [6]. In their ZrO_2 thickness study, the optimal value was found to be 2 µm, which yielded a PCE of 12.4 %, with a V_{oc} of 0.8 V, J_{sc} of 22.9 mA/cm^2 and a FF of 60 %. In addition, the Han group's optimal value of meso-TiO_2 is using a 1 µm of mp-TiO_2 layer achieved a higher PCE of 13.5 %, with a V_{oc} of 938mV, a J_{sc} of 23.3 mA/cm^2 and a FF of 60 %.

In this section we fabricated the different thin film layes of the "shell", this is the mesoporous TiO_2, the mesoporous ZrO_2 and the Carbon layer, by screen printing and analyzed their thickness by SEM/EDX. **Figure 5.2** shows the cross section of the SEM analysis carried out to the "Shell" **(a),** the thickness of each layer **(b)** and the corresponding EDX analysis **(c)**.

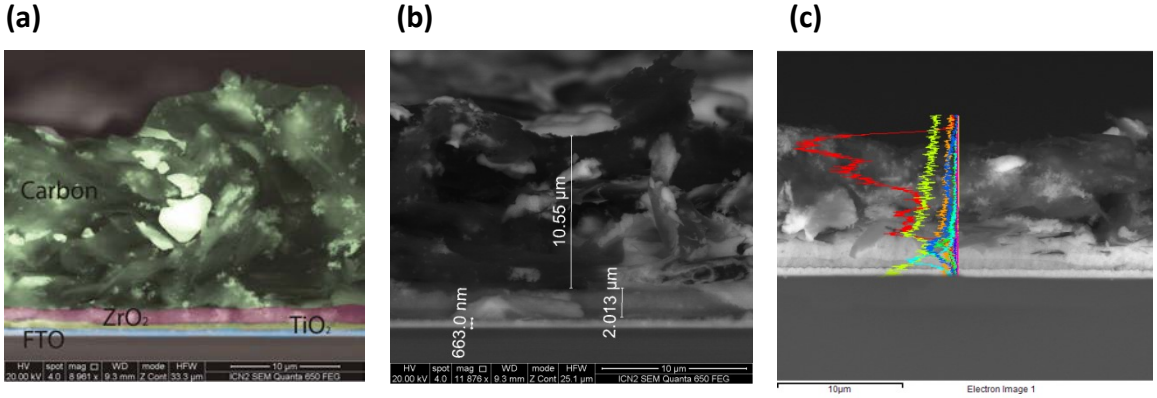

Figure 5.2 SEM and EDX analysis of CPSC. (a) SEM analysis of the different layers that compose the FTO/TiO_2/ZrO_2/C "shell" in a CPSC. **(b)** Thickness of the layers: mp-TiO_2 about 600 nm thickness, mp- ZrO_2 of 2 µm thickness and carbon about 10 µm thickness, and **(c)** EDX image of the cross section $(5\text{-AVA})_x(MA)_{1-x}PbI_3$-based perovskite mesoscopic solar cells obtained by the one-step method (red: carbon, orange: oxygen, green: titanium, light blue: tin, dark blue: lead, yellow: silicon and violet: nitrogen).

The thicknesses of each layer that provided the best overall PCE performance are: 24 nm for c-TiO_2, 490 nm for mp-TiO_2, 1.7 µm for ZrO_2 and 9.8 µm for carbon layer (**Figure 5.3).** The thickness analysis was carried out by profilometry, once the paste was completely dry (after annealing). These values are close to the values obtained by SEM (**Figure 5.2**). These layers were consequently used in this thesis for the fabrication of C-based PSCs in both the two step and one step method.

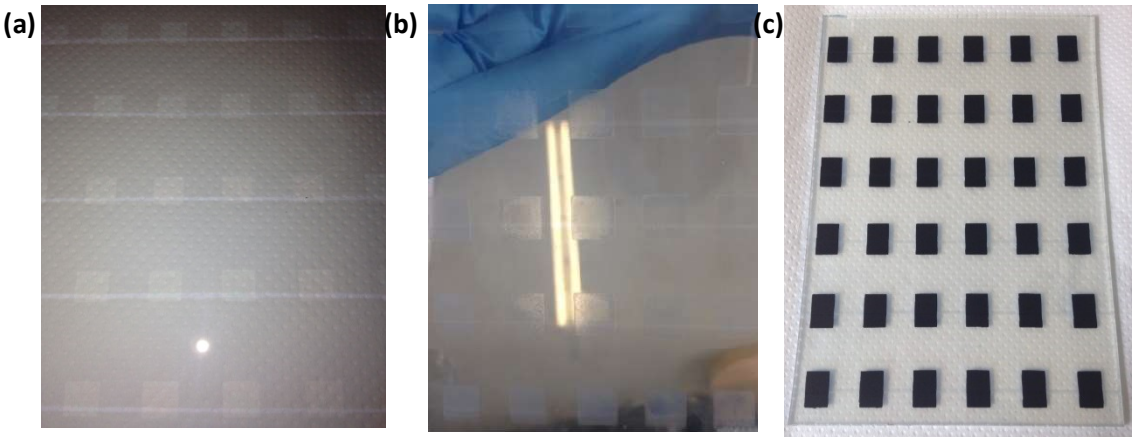

Figure 5.3 Image of **(a)** mesoscopic TiO_2 layer with a 490 nm thickness, **(b)** mesoscopic ZrO_2 layer with a 1.7 µm thickness and **(c)** the carbon layer, 9.8 µm thick. The measurements were carried out by profilometry.

5.3 Application of the two-step infiltration method to fabricate CPSCs

The one-step spin coating method, is the most widely used to prepare PSCs; however, the solvent needs to dissolve both the organic and inorganic parts in the same solution [14]. As a result, Mitzi *et al.* created the two-step deposition technique to prepare hybrid perovskite. Firstly a layer of metal halide (MI_2), was deposited using vacuum evaporation or spin-coating, followed by dipping the film into an organic salt solution, in a two steps procedure [15].

As described in detail in Chapter 2, once the "shell" is made, the halide perovskite absorber can be infiltrated into the FTO/TiO_2/ZrO_2/C applying the one or two-step infiltration methods. For the two-step method, 4 µl of lead Iodide solution was dropped casted through the carbon layer of the shell. The solution was prepared by dissolving 0.46 g lead iodide (PbI_2) in 1 ml of anhydrous DMF and stirred at 70 °C. Then, in the second step a solution of the MAI was provided for the subsequent formation of the perovskite. The MAI solution was prepared with 0.5 g of MAI dissolved in 50 ml of anhydrous IPA inside an N_2 glovebox. The devices are then immersed in this solution for 30 min and rinsed in anhydrous IPA in order to remove the excess material. Finally the devices are sintered in an oven at 70°C for 10 minutes in order to evaporate the solvent.
In this thesis work, the two-step method provided more reproducibility and almost no hysteresis if compared with the one step infiltration method. However, lower efficiencies were obtained. The majority of the PCEs obtained in both, forward and reverse scan were between 3 % and 4 %. It was not possible to achieve more than 5 % efficiency employing this method.

For the mp-TiO_2 we were able to vary the thicknesses from 400 nm to 600 nm, for the mp-ZrO_2 from 1 µm to 2 µm and for the carbon from 7 µm to 12 µm. The thicknesses of the layers were modified by the pressure of the squeeges in the screen printer machine. After the modification, we fabricated complete CPSCs applying the two-step infiltration method. **Figure 5.4** shows the IV curves of the CPSC with different ZrO_2 thicknesses **(Figure 5.4 (a)**) and TiO_2 thicknesses (**Figure 5.4 (b)**) from the study of Hongwei Han and co-workers [6]. The

best performance was observed for CPSC with ZrO_2 thicknesses of 2 µm for ZrO_2 and 1 µm of TiO_2.

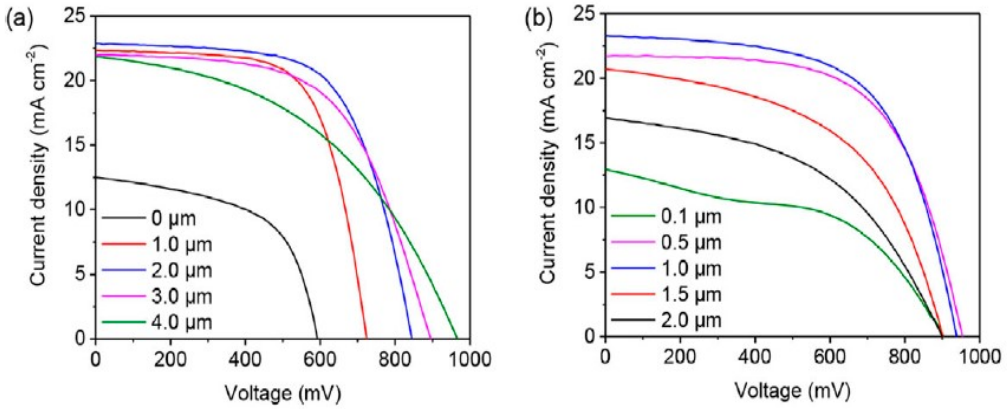

Figure 5.4 Photocurrent-density voltage (I-V curves) of C-based PSC with different thickness of **(a)** ZrO_2 layer and **(b)** TiO_2 layer. *Extracted from* [6].

Figure 5.5 shows the histograms corresponding to the C-based PSCs made by two step method. For the two-step process (already described in Chapter 2), a 4 µl of lead Iodide solution is dropped casted through the carbon layer of the shell, following by the addition of the MAI solution, provided for the subsequent formation of the halide perovskite. Once the devices are immersed in MAI solution for 30 min, they are rinsed in anhydrous IPA in order to remove the excess material. Finally the devices are sintered in an oven at 70 °C for 10 minutes in order to evaporate the solvent. The thickness of the optimized layers used for the shell was 500 nm for mp-TiO_2, 2 µm for ZrO_2 and 10 µm for carbon layer.

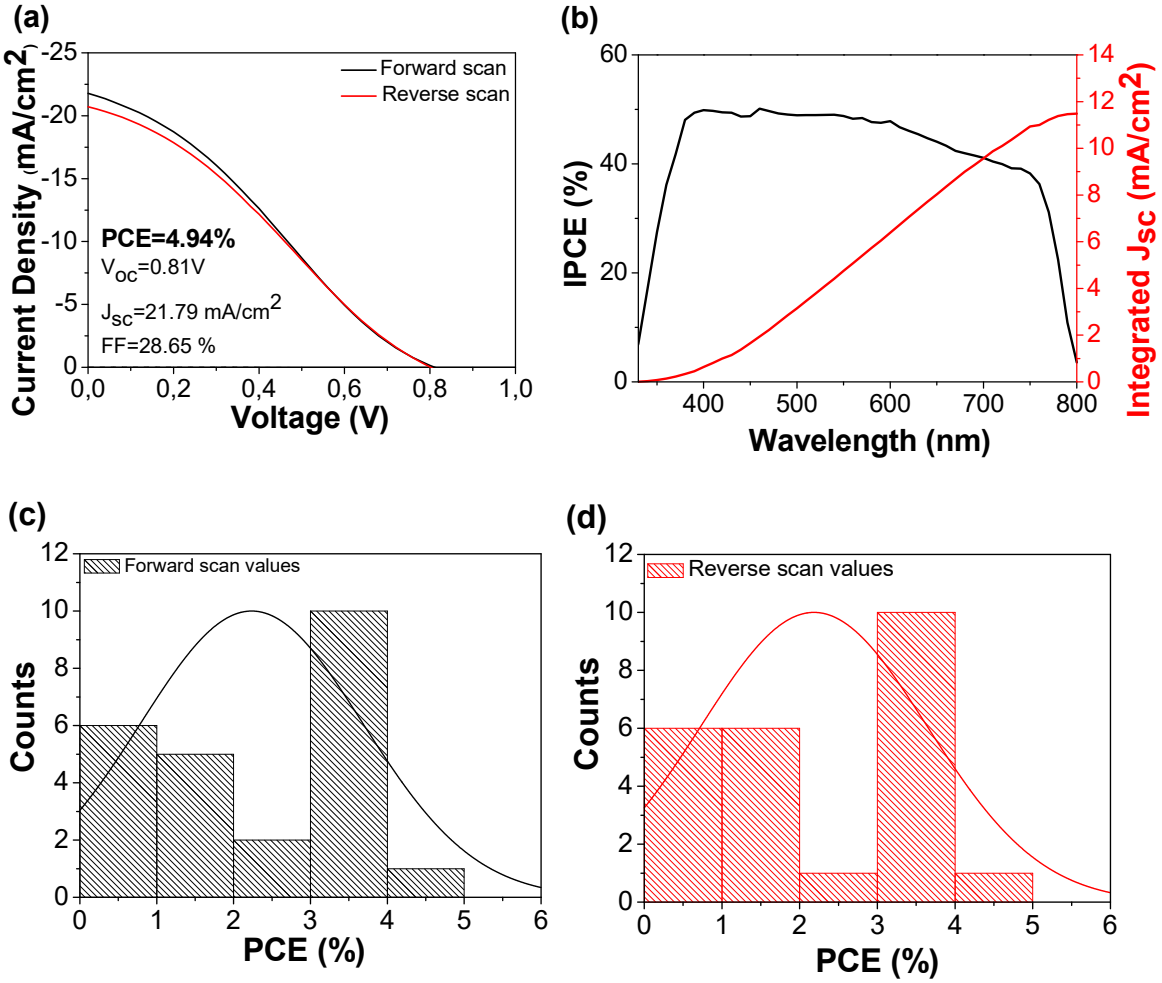

Figure 5.5 (a) I-V curves of C-based PSC and **(b)** IPCE for the best results using two-step method. PCE histogram for **(c)** in forward scan and **(d)** in reverse scan values.

In **Figure 5.5**, the IV curves of a champion cell show a low performance with a PCE of ~5.0 % which is directly affected by the low V_{oc} and FF values. On the one hand, the poor V_{oc} performance can originate from the uneven crystallization of the perovskite material within the shell. On the other hand, a high V_{oc} can be achieve by filling the deep traps in the perovskite material [16]. The identification and suppressing of recombination processes and the effect of grain boundaries in the PSC drives a higher V_{oc} [17].

5.4 Application of the one-step infiltration method applying different organic additives

Organic-inorganic metal halide perovskites can provide a high efficiency and low cost performance within the C-based structure, as previously seen in this thesis. However, many

efforts have been made to obtain high-quality perovskite films. Ion migration has become an important issue in this sense, because the I^- anions from PbI_2 and MAI, can migrate to perovskite grains forming a lot of defects that cause fast degradation of the complete device. One way to improve the crystallinity, grain size and surface coverage can be achieved by the incorporation of additives, which can improve crystal growth and simultaneously lead to higher efficiencies and better stability [18]. To this end, several studies have been carried out. For example, Li *et al.* introduced butylphosphonic acid 4-ammonium chloride into the perovskite grains, which improved the moisture resistance of the PSCs [19]. In addition, 2-aminoethanethiol has been used as a ligand to bridge MAI and PbI_2 which formed compact and stable perovskite film [20]. Many other additives have been incorporated in perovskite films and in this thesis we used 5AVAI, well known in C-based PSCs, as well as other additives, such as 4aminobenzoic acid (PABA), terephtalic acid (TPA) and 3-phosphonopropionic acid (3-Hpp). These additives has some interesting functional groups, such as the hydroxyl group (-OH), carboxyl group (-COOH), and ammonium group ($-NH_2$). The hydrogen bonds of these groups can interact with Pb^{2+} or I^- ions and suppress the ion migration, thereby guaranteeing hysteresis free PSCs with enhanced stability of complete device [21].

In this section we fabricated CPSC by the one-step infiltration method applying the 5-AVAI as the reference organic additive and three other organic additives for comparative purposes. **Figure 5.6 (a)** shows a schematic representation of the interaction between the 5-AVA molecule with the oxide and the perovskite materials. Furthermore, **Figure 5.6** shows the representation of three organic additives under study in this thesis work: **(b)** Terephthalic acid TPA, **(c)** 4 aminobenzoic acid, PABA and **(d)** 3 phosphonopropionic acid, H3pp

As already described, the **5-aminovaleric acid iodide (5AVAI)** is a molecule that has a –COOH group and NH_3^+ group. This molecule is used as an additive for the perovskite precursor. The amino and carboxylic groups interact with halide perovskites resulting in better efficiencies and stability [22]. The **terephthalic acid (TPA)** is one of the most important chemicals in petrochemical industry. An organic compound with formula $C_6H_4(CO_2H)_2$. Hou and co-workers incorporated TPA in the perovskite precursor solution,

with TPA additive their devices exhibited better moisture resistance of $MAPbI_3$ enhancing the crystallization of the perovskite material [23]. The **4aminobenzoic acid (PABA)** is a chemical found in folic acid. PABA is an amino acid commonly used in the cosmetic products as a sunscreen because it can block UV radiation to the skin. This PABA molecule has a carboxylic group and an amino group. In PSCs it has been applied by Li et *al.* in normal architecture by assembling a monolayer of PABA on top of the TiO_2 surface, because of the carboxylic group is easily chemically bonded to TiO_2 and amino group favours large crystal formation [24]. Finally, the **3 phosphonopropionic acid (H3pp)** is a chemical with an amino group and carboxylic group. This small molecule is a beta amino acid used in this thesis work as an organic modifier due to the strong anchoring capability of the phosphonic group. Our group has recently achieved 21 % efficiency applying this additive in normal configuration PSC with 1000 h stability under continuous light irradiation of 1 sun.

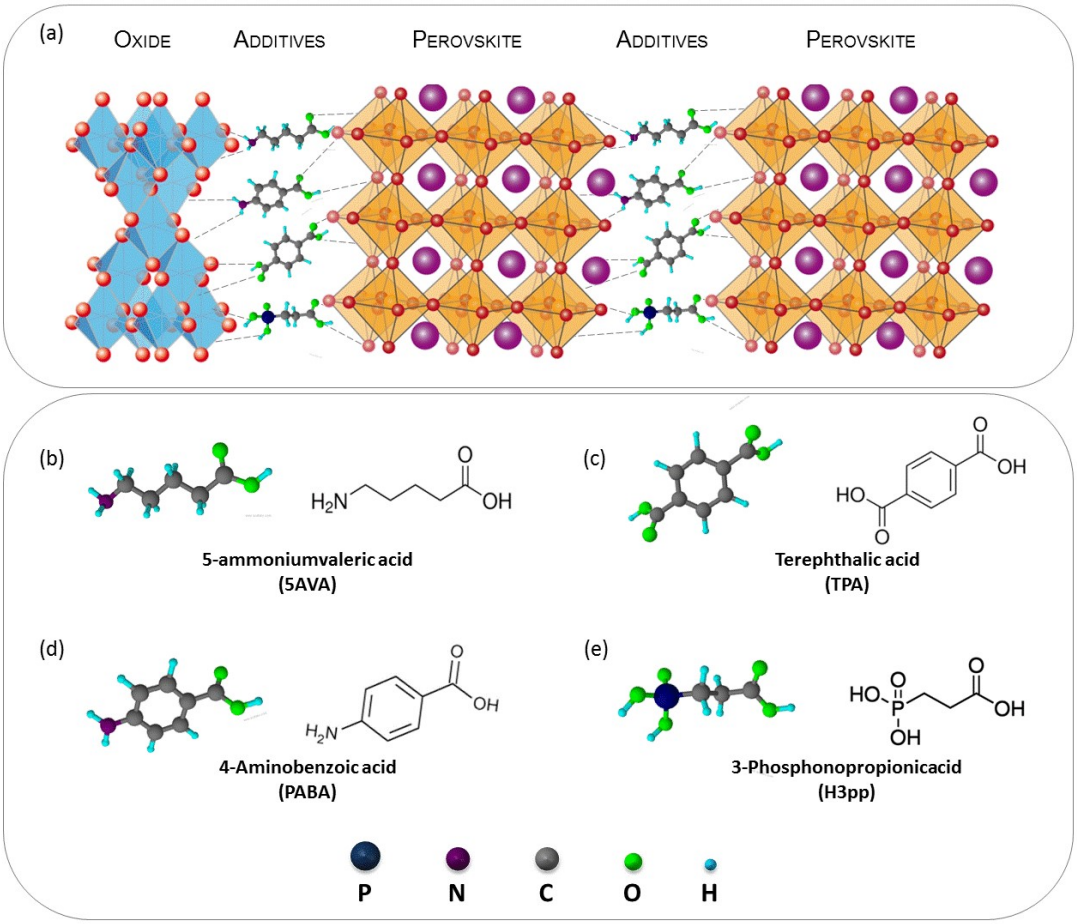

Figure 5.6 Additives applied in CPSCs developed in this work **(a)**. Schematic representation of the interaction between the organic additives and the oxide and perovskite materials. The additives employed are: **(b)** 5AVA, **(c)** TPA, **(d)** PABA and **(e)** H3pp.

In this section, C-based PSCs were fabricated and optimized using the one-step method and applying the different organic molecules as additives as described above.

5.4.1 The 5-Ammoniumvaleric acid iodide (5AVAI)

The application of AVAI mixed with MAPI, results in the formation of (5-AVA)$_x$ (MA)$_{1-x}$PbI$_3$ which provides longer lifetimes and higher quantum yield compared with the use of MAPbI$_3$ alone. A PCE of 12.8 % was achieved with stability of over 1000 h under ambient air. The role of 5AVA cations is to template the formation of perovskite crystals in the mesoporous oxide and induce preferential growth in the normal direction. The (5-AVA)$_x$ (MA)$_{1-x}$PbI$_3$ has better surface contact with the TiO$_2$ surface than the single-cation MAPbI$_3$ form. Furthermore, the orthorhombic perovskite phase formed in the presence of 5AVA resulted in improved PCE compared to the device without the addition of 5AVAI [7]. As reported, the protonated form of the small organic acid (5AVAI) can coordinate, on the one hand, to the semiconductor oxide via the carboxylic acid group, and on the other hand, to the halide perovskite, via the amino groups [25]. As represented in **Figure 5.6**, the interface modification of the interlayers is made through the aminovaleric acid iodide molecule, with carboxyl and amine as anchoring groups.

5.4.1.1 Optimization of the compact TiO$_2$ layer

PSCs suffer from hysteretical behaviour in current-voltage measurements which leads to an inaccurate estimation of device efficiency. From previous studies, the causes of this hysteresis effect have been attributed to the ion migration, charge trapping/detrapping and charge accumulation. However, the origin of hysteresis has not yet been solved. Some studies have found that the hysteresis effect in fully printable mesoscopic CPSC is highly dependent on the interlayer c-TiO$_2$, which can be controlled by the composition of this layer [9]. In fully printable mesoscopic CPSCs, the mp-TiO$_2$ and the c-TiO$_2$ are in charge of collecting and then transferring electrons and the simultaneous transport of electrons and blocking of holes.

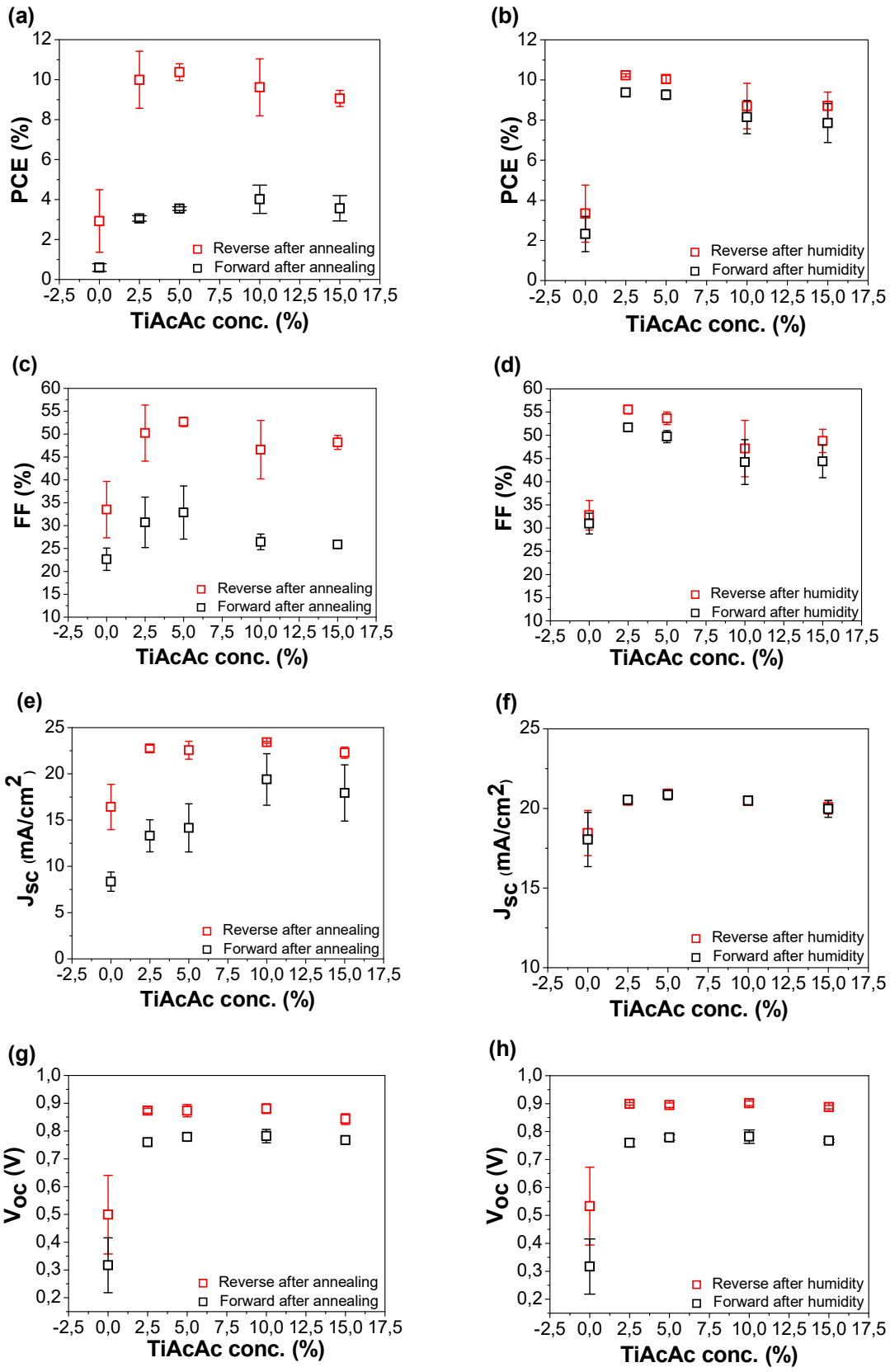

Figure 5.7 CPSCs average output parameters (PCE, FF, J_{sc} and V_{oc}) Vs TiAcAc concentration,in forward and reverse scan modes, after complete PSC device annealing **(a)**, **(c)**, **(e)**, **(g)** and after humidity treatment at 70 % R.H. **(b)**, **(d)**, **(f)**, **(h)**.

In terms of c-TiO_2 solution, we carried out a study on the influence of different concentrations of TiAcAc diluted in IPA. The solutions were then deposited by spray-pyrolisis method using 25 passes in all cases.

Figure 5.7 shows the average photovoltaic values for different TiO_2 solution concentrations: 0 %, 2.5 %, 5.0 %, 10.0 % and 15.0 % in volume of titanium diisopropoxide bis(acetylacetonate) (TiAcAc) with Isopropyl alcohol (IPA). The c-TiO_2 thin film was deposited by spray pyrolysis and sintered at 300 ˚C for 30 min. Finally, the complete devices were finished following the steps described in Chapter 2. All the devices were illuminated for 3 minutes before analysis, commonly known as light soaking, which can minimize the influence of the trap states and obtain a steady state measurement.

As can be seen in **Figure 5.7**, the PSC without the c-TiO_2 (0 % TiAcAC) leads to poor photovoltaic performance in comparison with the PSC devices applying different TiAcAc concentration, indicating that an ETL (hole blocking layer) is extremely necessary for a properly working PSC. Without a c-TiO_2 layer, the perovskite absorber will have direct contact with the FTO bottom electrode causing a charge recombination and a voltage loss of the device [9]. On the other hand, a high concentration solution, such as 15 % of TiAcAc, shows photovoltaic limitations due to the thickness of the c-TiO_2 layer which can provide difficulties in terms of the transport of charge electrons to the electrode. The optimized c-TiO_2 solution was well established between 2.5-5 % TiAcAc, demonstrating that the use of an appropriate c-TiO_2 solution is also necessary for a higher photovoltaic performance with pinhole-free layers.

Figure 5.7 shows the photovoltaic performance corresponding to the same CPSCs after post-humidity treatment overnight at 70 % R.H. After the exposure of this batch under a high humidity environment, it can be seen that hysteresis is clearly reduced in the PCE, FF and J_{sc} parameters although there are no significant, changes in the V_{oc}. With the humidity treatment, the highest efficiency corresponds to the use of 2.5 % TiAcAc, which provided a PCE of 10.3 %, a FF of 56.4 %, a V_{oc} equivalent to 0.8 V and 20.4 $mAcm^{-1}$ of J_{sc} under AM 1.5G illumination at 100 m W/cm^2. These results support the finding that a high humidity

treatment can reduce hysteresis as a result of in-situ degradation to PbI_2 and further recrystallization of the halide perovskite absorber.

Figure 5.8 shows the IPCE analysis of the CPSC with different c-TiO_2 layers before **(a)** and after **(b)** R.H. treatment. The contribution of the TiO_2 can be observed in the wavelength range between 300 to 800 nm. Increasing the concentration of the TiAcAc during the c-TiO_2 thin film formation increases the oxide thin film thickness and the absorption is observed to increase accordingly: up to 45 % before RH treatment and up to 85 % after treatment. The absorption of the halide peorvskite is observed above 500 nm and is very similar for all the samples. The increase in the whole IPCE spectra, which corresponds to a PSC with correct electron injection and transport, is observed for samples applying the c-TiO_2 layer, with the best results observed for the device made with the 2.5 % TiAcAc concentration. The samples analyzed after the humidity treatment (**Figure 5.8 b**) show a clear increase in the IPCE up to ~85 %. Nevertheless this value doesn't correspond to the best device (2.5 % TiAcAc) probably due to a calculation error provoked by a sudden drop observed in the IPCE spectra at around 600 nm. This effect, which we were unable to explain clearly, is probably attribute to changes in the crystal structure of the halide perovskite after exposure to the high humidity treatment.

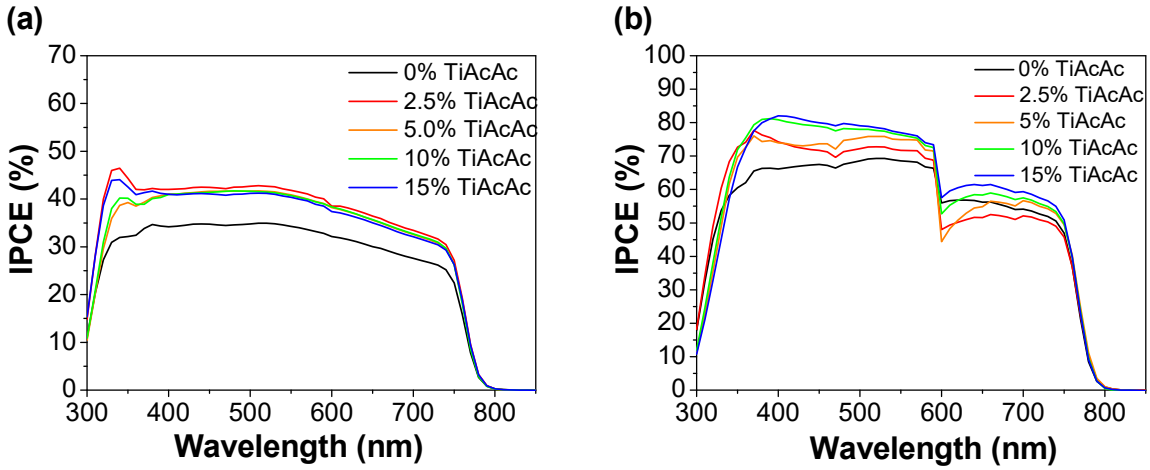

Figure 5.8 IPCE of the corresponding C-based PSCs in different c-TiO_2 solutions **(a)** after annealing and **(b)** after humidity treatment.

Figure 5.9 shows the corresponding IV curves of the PSC applying different concentrations of TiAcAc for the fabrication of the c-TiO_2 layer. The graphs are shown before and after R.H. treatment for 0 % **(a-b)**, 2.5 % **(c-d)**, 5 % **(d-e), 10** % **(e-f) and** 15 %**(g-h)**.

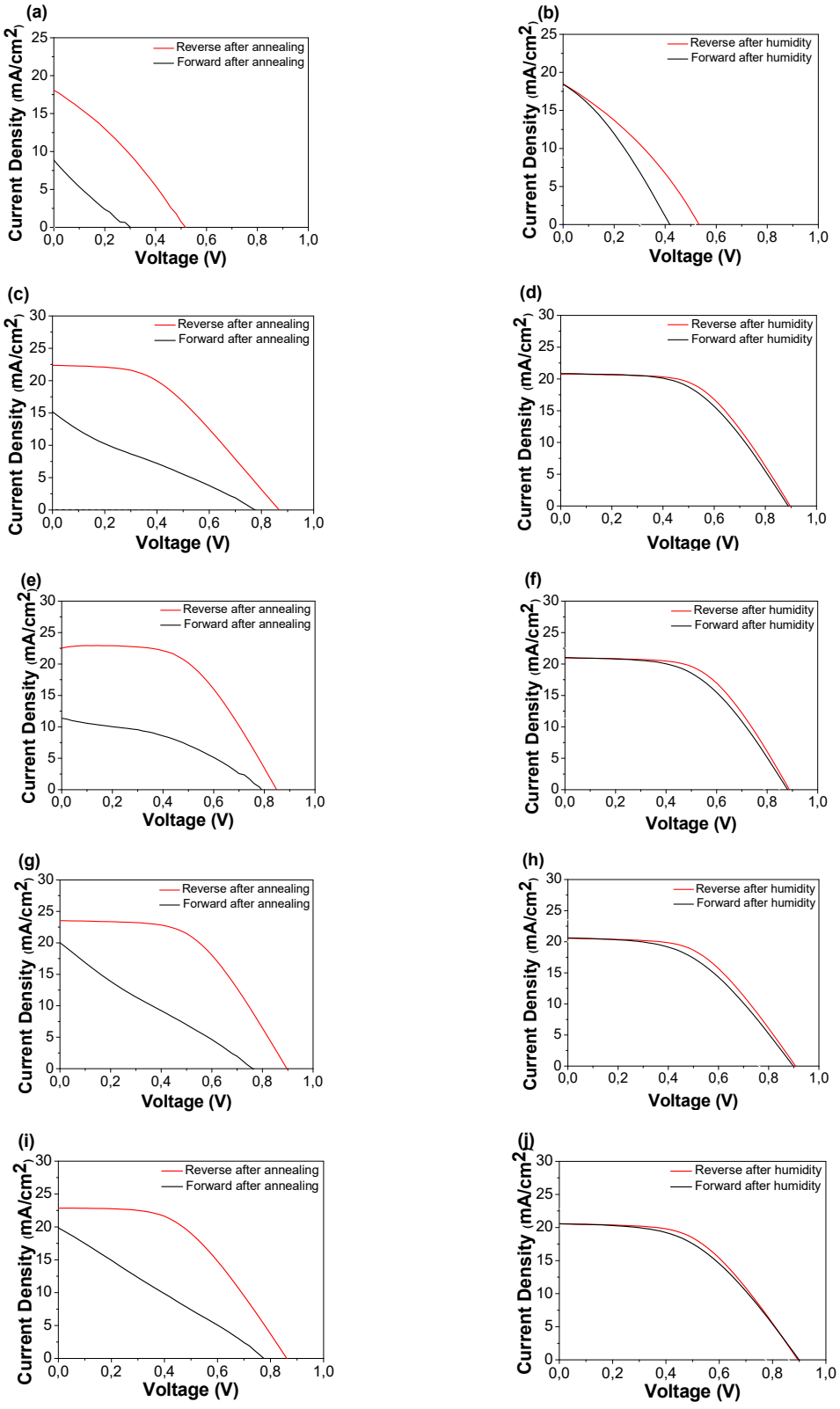

Figure 5.9 IV curves of TiAcAc**(a)** 0% after annealing, **(b)** 0% after humidity, **(c)** 2.5 % after annealing, **(d)** 2.5 % after humidity, **(e)** 5 % after annealing, **(f)** 5 % after humidity, **(g)** 10 % after annealing, **(h)** 10 % after humidity, **(i)** 15 % after annealing, **(j)** 15 % after humidity.

5.4.1.2 Optimization of the 5AVAI concentration

Is well known that the efficiency of a PSC can increase with the incorporation of additives such as 5AVA, GuCl, or NH_4Cl directly related to the enhancement in crystallinity and morphology of the perovskite layer, which result in a perovskite film with fewer defects [26]. The production of high-quality perovskite has received a lot of attention in pursuit of perovskite layers with large grain size, uniform morphology and limited ion migration. An appropriate composition of 5-AVA cations can guarantee all of these characteristics and can also enable hysteresis-free C-based devices [27]. Hongwei Han's group found that $5(AVA)_x(MA)_{1-x}PbI_3$ exhibits much longer crystalline features than only $MAPbI_3$ perovskite. This improvement in perovskite crystal quality originates from the presence of the 5AVA cations resulting from templating action in the perovskite crystal nucleation and growth within the mesoporous oxide [7].

Consequently, it is important to determine the optimum PbI_2:MAI ratio and 5AVAI additive concentration. For this, we carried out experiments to find the optimal $5(AVA)_x(MA)_{1-x}PbI_3$ concentration. A set of different 5AVA concentrations were applied in order to find the optimal value that produce the best photovoltaic performance after annealing treatment at 50 ˚C for 1 h using 1.2 M solution PbI_2:MAI, as shown in **Figure 5.10**. The tendency observed is a clear improvement of the PSC response when applying a low concentration of 5AVAI (in the range between 2 and 3 %).

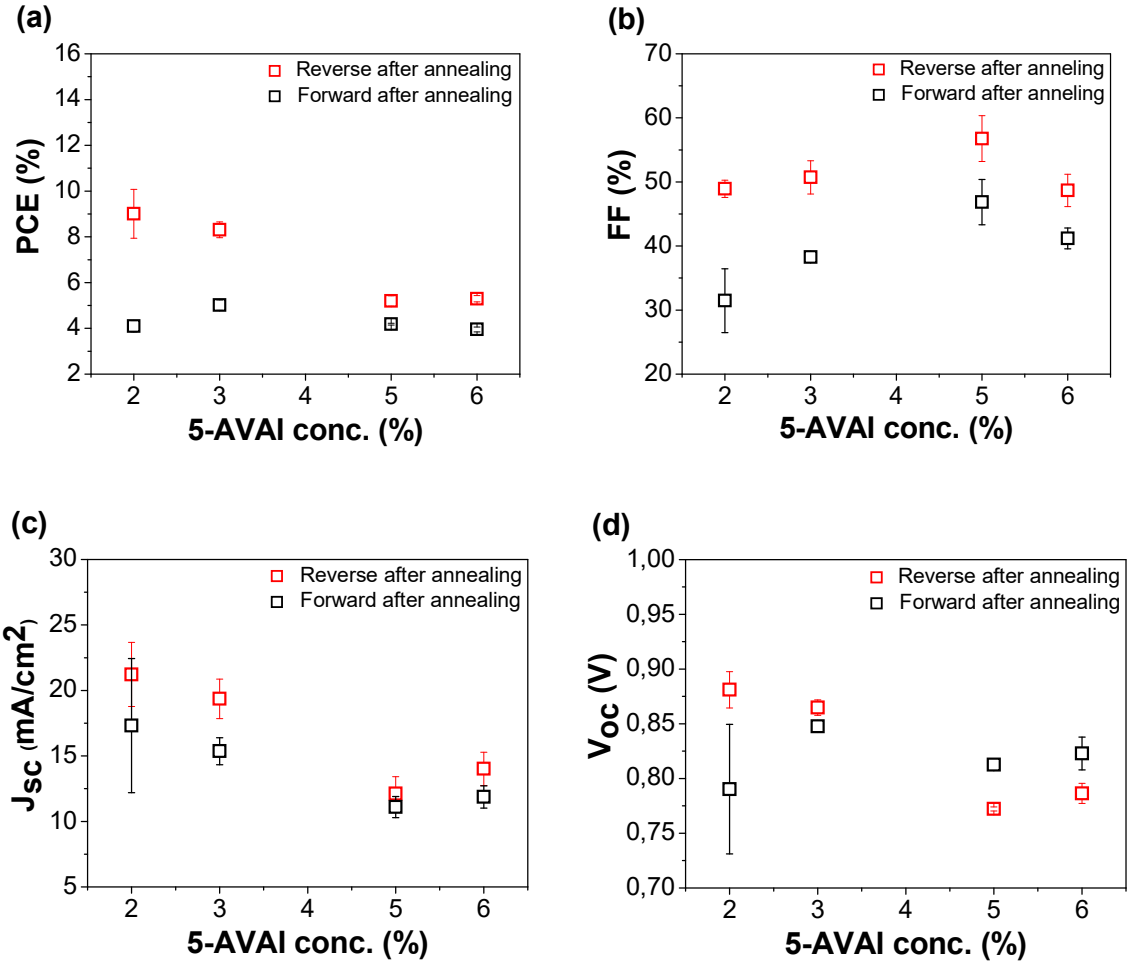

Figure 5.10 Average output parameters (PCE, FF, J_{sc} and V_{oc}) in forward and reverse scan after annealing treatment in C-based PSC using 1.2 M equimolar solution of PbI_2:MAI with different 5AVA concentrations.

A second set of experiments were then performed using a 0.95 M solution of PbI_2:MAI, with the same set of 5AVAI concentrations (from 2 to 6 %), the results are shown in **Figure 5.11**. In this case, the best PCE was observed at 2 % concentration (reverse scan IV curve) and decreased as the concentration increases.

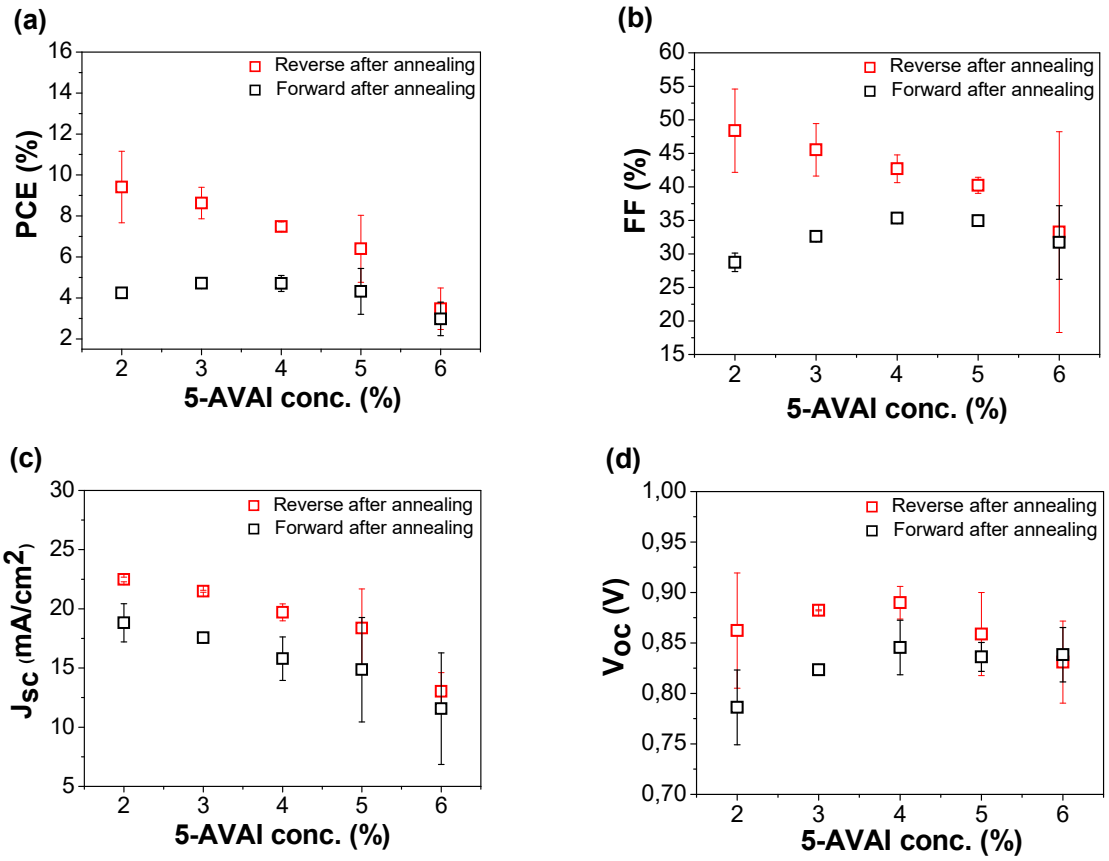

Figure 5.11 Average output parameters (PCE, FF, J_{sc} and V_{oc}) in forward and reverse scan after annealing treatment in C-based PSC using 0.95 M equimolar solution of PbI_2:MAI with different 5AVA concentrations.

Comparison of the results shown in **Figure 5.10** with **Figure 5.11**, after thermal treatment shows an enhancement of the photovoltaic response after annealing treatment of 1 h at 50 ˚C with the use of 0.95 M solution PbI_2:MAI. In this case we applied the 0.95 M PbI_2:MAI solution with the 2 % 5AVA concentration giving the best photovoltaic performance.

5.4.1.3 Humidity treatment to reduce hysteresis

A treatment of the CPSC under high humidity conditions modifies the halide perovskite thin film. It is known that moisture can dissolve the infiltrated halide perovskite located within the mesoscopic oxides and the porous carbon. The halide perovskite can then be recristalized after drying allowing the material to form a more compact and continuous interface. The post-humidity-treatment was carried out in order to obtain a hysteresis-free C-based PSC using the optimized 0.95 M solution. This treatment consisted of exposing the already annealed devices to an elevated degree of moisture, 70 % R.H. at RT overnight. The results after annealing and after the humidity treatment can be seen in **Figure 5.12**.

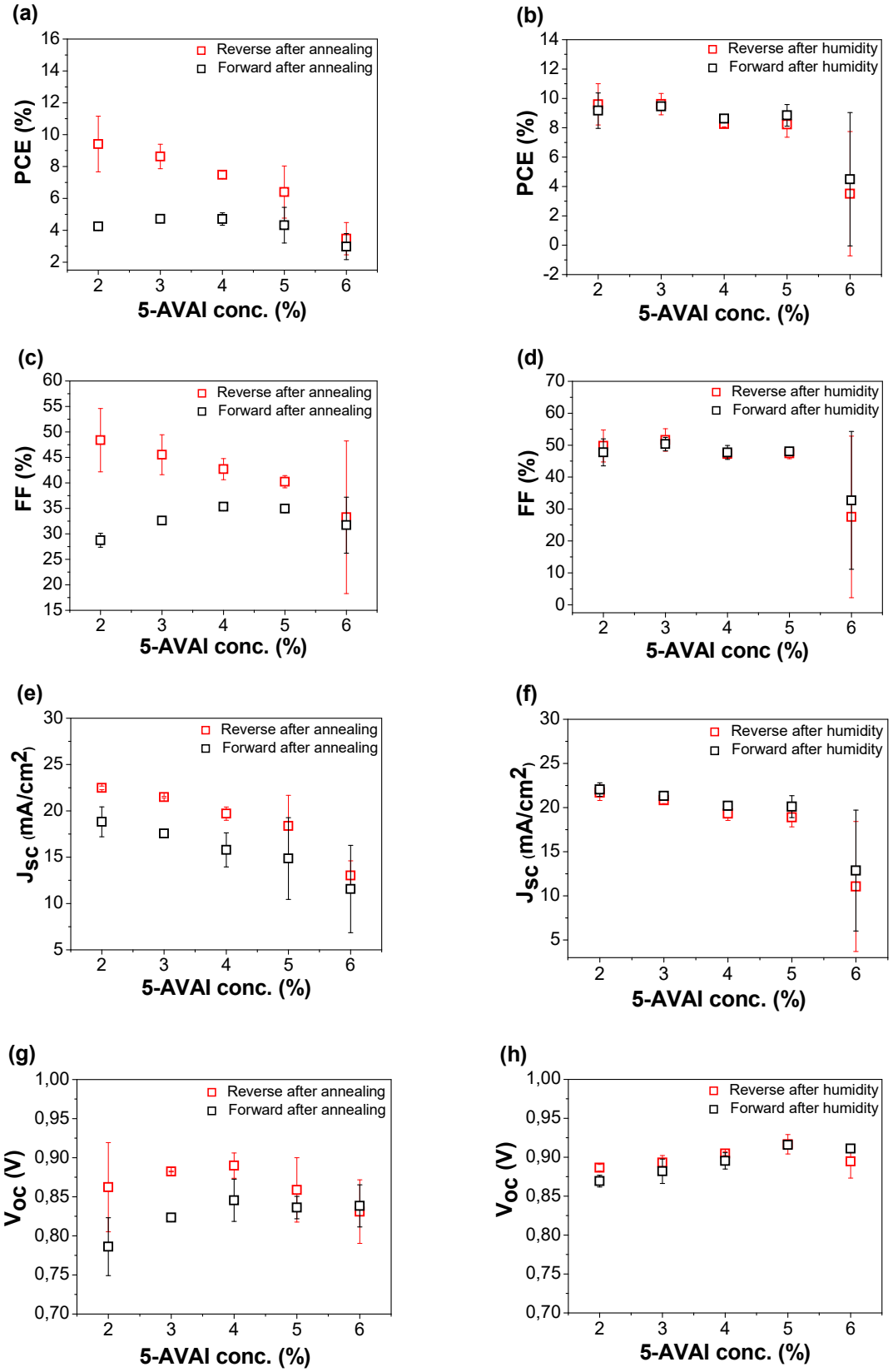

Figure 5.12 Average output parameters (PCE, FF, J_{sc} and V_{oc}) in forward and reverse scan after annealing treatment **(a)**, **(c)**, **(e)** and **(g)** and after humidity treatment **(b)**, **(d)**, **(f)** and **(h)** in C-based PSC using 0.95 M equimolar solution of PbI_2:MAI with different 5AVA concentrations (from 2 % to 6 %).

Figure 5.13 shows the IPCE after annealing and after humidity treatment. The best absorption was given between 2-3 % 5AVA, in which less 5AVA additive led to a higher absorption that matched the photovoltaic response in **Figure 5.12**. A significant difference between after annealing results and after humidity results can be observed. In respect of IPCE, decay was dramatic after the 600 nm wavelength, which may be due to the high humidity treatment causing a change in crystalline structure.

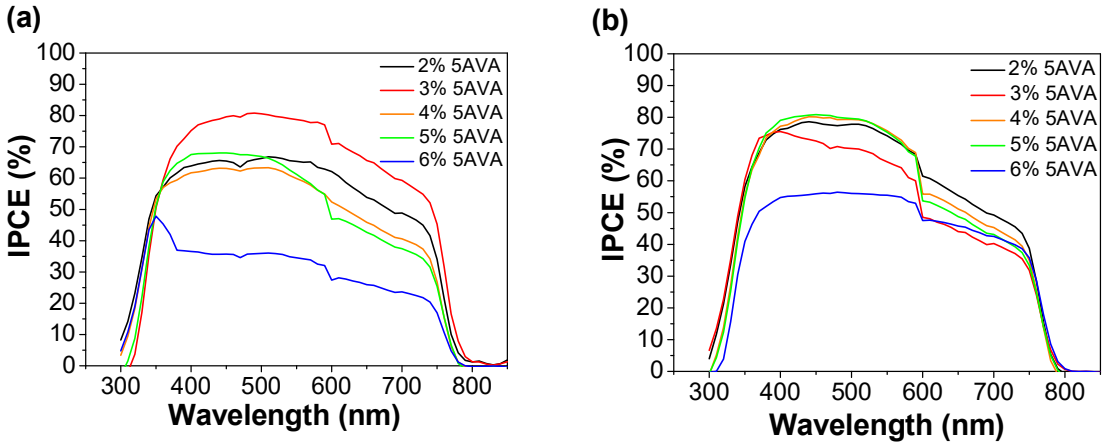

Figure 5.13 IPCE of the corresponding C-based PSC in different 5AVA concentrations for 0.95 M. **(a)** after annealing and **(b)** after humidity treatment.

Figure 5.14 shows the corresponding IV curves of the different concentrations of 5AVA, **(a)** 2 % after annealing, **(b)** 2 % after humidity, **(c)** 3 % after annealing, **(d)** 3 % after humidity, **(e)** 4 % after annealing, **(f)** 4 % after humidity, **(g)** 5 % after annealing, **(h)** 5 % after humidity, **(i)** 6 % after annealing, **(j)** 6 % after humidity.

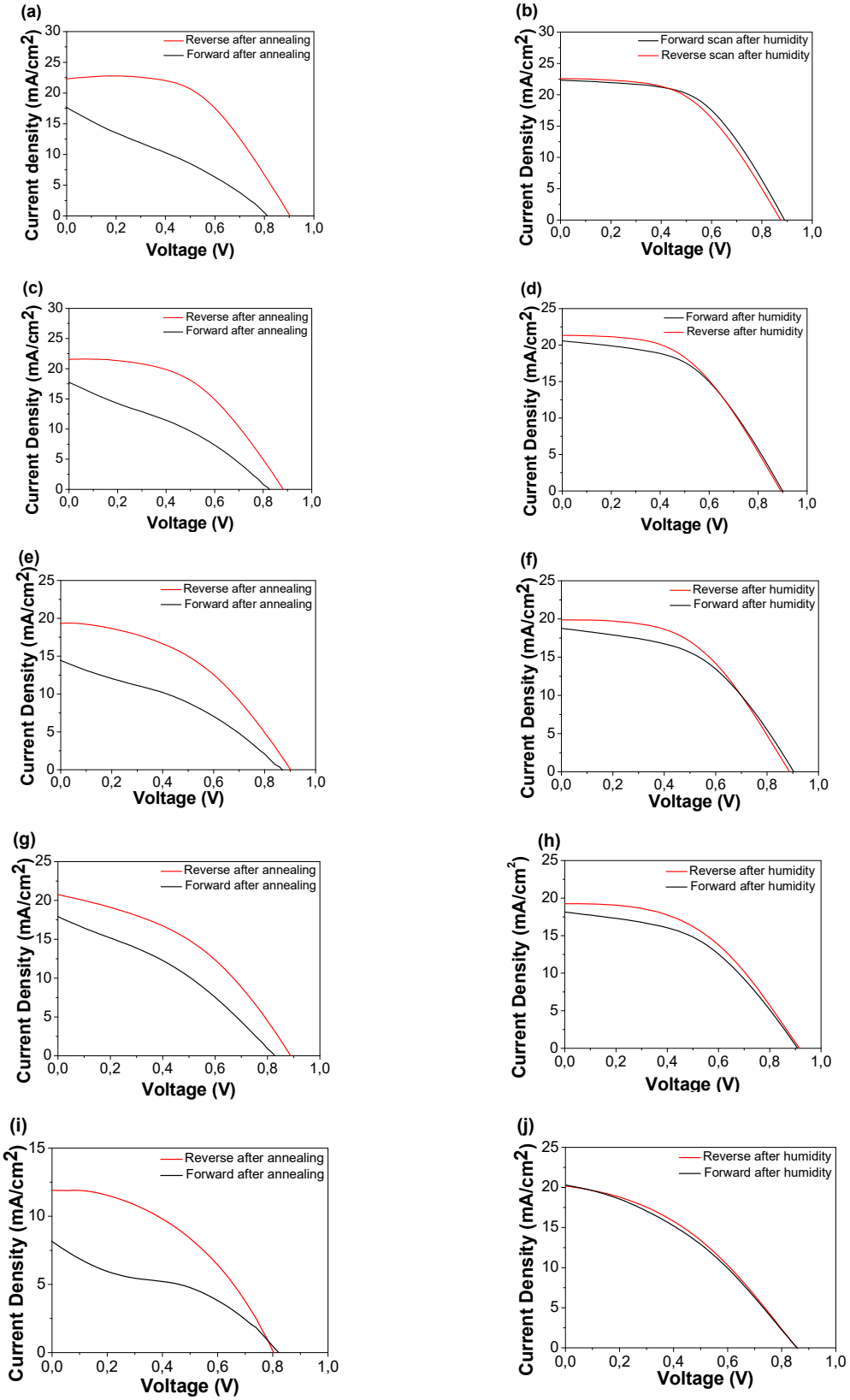

Figure 5.14 IV curves of 5AVA**(a)** 2 % after annealing, **(b)** 2 % after humidity, **(c)** 3 % after annealing, **(d)** 3 % after humidity, **(e)** 4 % after annealing, **(f)** 4 % after humidity, **(g)** 5 % after annealing, **(h)** 5 % after humidity, **(i)** 6 % after annealing, **(j)** 6 % after humidity.

5.4.1.4 Champion cell using one step method

The best PSC using the fully printable mesoscopic carbon-based structure exhibited almost 12 % PCE. **Figure 5.15** shows the **(a)** IV curves and **(b)** IPCE of the champion cell and the corresponding photovoltaic parameters.

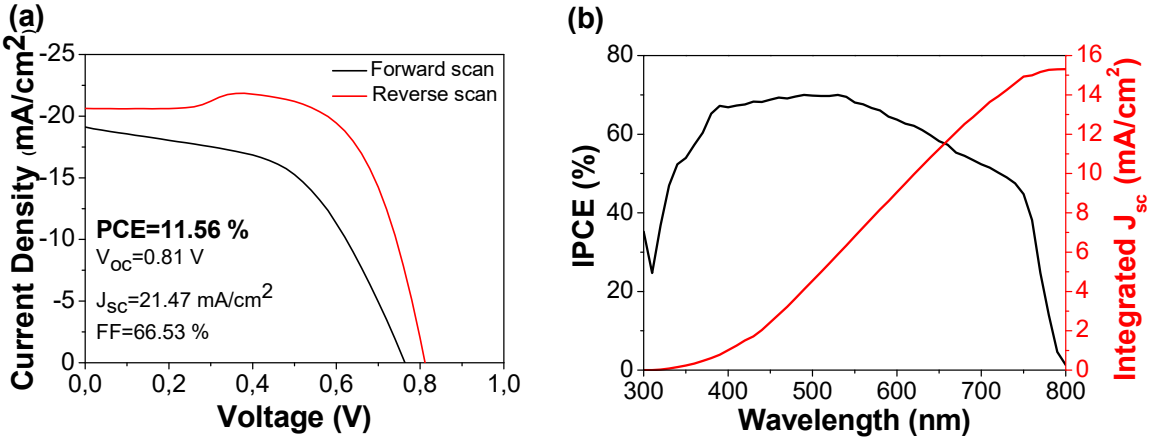

Figure 5.15 Champion cell characteristics. **(a)** J-V curves of C-based PSC. **(b)** IPCE using one-step method.

In this case, the limiting factors are mainly the V_{oc} and the FF. However, an incomplete pore-filling and cristalization of the perovskite absorber,within the mesoporous oxides and the carbon layer, limited its light absorption. This is reflected in the IPCE analysis by the low absorption observed above 550 nm corresponding to the perovskite.

5.4.2 One step infiltration method applying the 4-Aminobenzoic acid (PABA)

The organic additive 4-aminobenzoic acid has been applied by Li *et al.* using a two-step sequential method in normal architecture mesoporous PSC glass/FTO/c-TiO_2/mp-TiO_2/PABA monolayer/$CH_3NH_3PbI_3$/spiro-MeOTAD/Au.

From the results of Li *et al.* [24] it was clear that the introduction of this additive improved the quality of the perovskite crystallinity and reduced the charge trap states due to the interaction between TiO_2 and the perovskite layers, as shown in **Figure 5.16**.

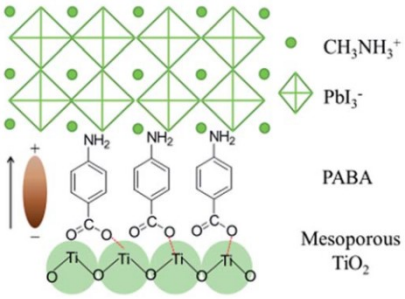

Figure 5.16 The interaction of PABA SAM between mp-TiO_2 and perovskite. *Extracted from* [24].

In their study, the PCE of the perovskite device with the interfacial modification was enhanced from 9.6 % without adding the PABA molecule, up to 10.6 % in the presence of the PABA. In this case the molecule was incorporated as a self assembly monolayer (SAM) by immersion of TiO_2-coated on FTO in 0.2 mM PABA solution dissolved it in ethanol for 24 h [24]. This SAM is a great candidate for passivating defects also in a C-based PSC structure. Considering that the carboxylic group is chemically bonded to TiO_2 and the amino group acts beneficially in a large crystal formation of $CH_3NH_3PbI_3$[31-32]. Furthermore, the phenyl ring has the π-conjugated structure which leads to better electron transport [30].

In this section, these novel SAMs, i.e. PABA and TPA, were applied in the presence of 5AVAI, following a one-step method, directly adding $5(AVA)_x(MA)_{1-x}PbI_3$ solution, dissolved in GBL, as already described in Chapter 2. We expected that the 5AVA would mostly contribute to improve the attachment to the $CH_3NH_3PbI_3$, thereby improving the crystal features, while the PABA, could benefit the electron transport in the device. **Figure 5.17** shows the **(a)** IV curves and **(b)** the IPCE of the best results using PABA as a SAM, and **(c)** the average results from using this SAM in C-based PSCs.

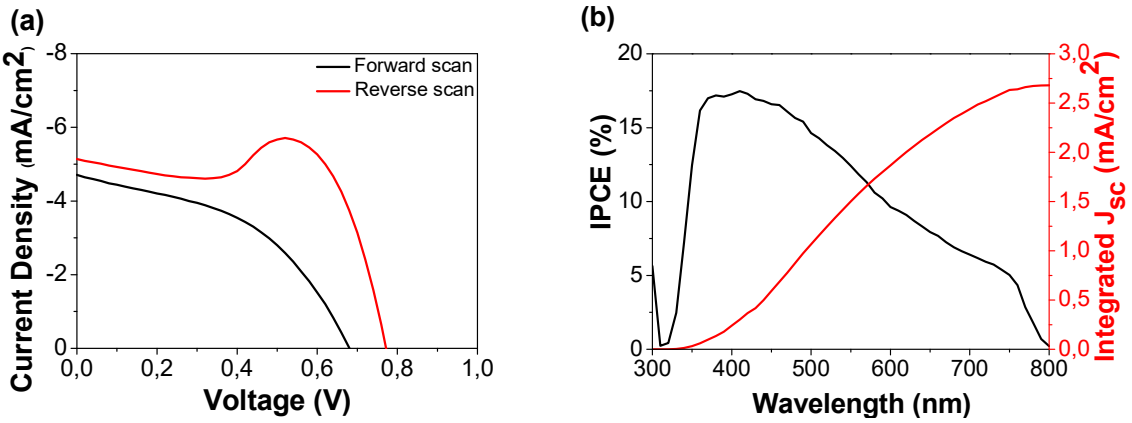

SAM		PCE (%)	V_{oc} (V)	J_{sc}(mA/cm^2)	FF (%)
PABA	*Forward*	1.43±0.12	0.70±0	4.47±0.40	45.8±0.61
	Reverse	2.53±0.65	0.77±0.06	4.70±0.46	69.4±9.60

Figure 5.17(a) JV curves, **(b)** IPCE of the best cell. **(c)** Average values of photovoltaic parameters of C-based PSCs using PABA in forward and reverse scan.

5.4.3 One step infiltration method applying the Terephtalic acid (TPA)

As with previous studies, a high quality perovskite film was obtained by incorporating TPA additive in the perovskite precursor solution employing solvent modified engineering via a one-step spin-coating procedure. The schematic diagram of the PSC device architecture was FTO/c-TiO_2/mp TiO_2/$CH_3NH_3PbI_3$/TPA/spiro-OMeTAD/AgAl. This addition exhibited a PCE of 18.5 % with less hysteresis, much higher than the PCE of 15.5 % from pristine devices. Furthermore the presence of the TPA can improve the moisture resistance and thermal stability of the device [23]. The TPA molecule has two carboxylic acid groups to anchor into the oxide or perovskite part, with a π-conjugated structure.

Figure 5.18 shows the interaction between the SAM and the perovskite reported by Hou *et al.* in their work. The TPA molecules at grain boundaries can act as templates [31] and the TPA can also promote the lateral grow of perovskite grains [32]. At the same time, the strong coordination between I^- and hydrogen bonds of hydroxyl groups in TPA can suppress the ion migration of perovskite.

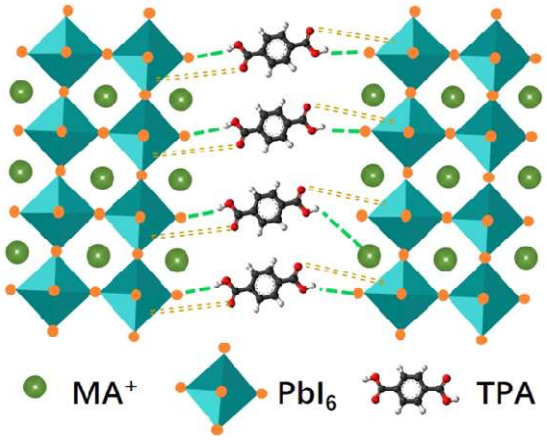

Figure 5.18 Representation of the interaction between perovskite and TPA. *Extracted from* [23]

The TPA used in this thesis was combined with the 5AVA molecule. TPA presents an issue compared to the other additives; TPA requires the use of a different solvent because of the non-solubility in GBL. In order to apply TPA in C-based PSCs, the first step was to find a solvent that could simultaneously work for 5AVA and TPA.

In a previous study, Chen *et al.* carried out a solvent effect study on hole-conductor free fully printable PSCs. The wettability and the stability of intermediate phases were found to be responsible for light harvesting and charge separation of the perovskite layer. A promising 13.9 % was achieved using a mix solvent DMF/DMSO (0.93:0.07 v/v) due to optimized polarity, wettability and coordination of species [33]. Solvent strategy has been found to be a key factor to enhance the morphology and the crystallization of the perovskite [34]. In C-based PSCs, the infiltration of the perovskite solution in the carbon layer is an important step that must be taken into account. This is due to the fact that the hydrophobicity of the carbon and the hydrophilic behaviour of the TiO_2 photoanode require the appropriate polarity and viscosity of perovskite precursor solvents to infiltrate this solution properly. **Figure 5.19** shows the precursor solvents applied in the study of Chen and co-workers. Different solvents have been studied; NMP, DMSO, DMF and GBL and from the results, the coordination ability order of different solvents with PbI_2 is DMSO>DMF>NMP>GBL. Furthermore, Chen *et al.* found the wettability order of different solvents-based perovskite solutions to be DMF>GBL>NMP>DMF/DMSO>DMSO [33].

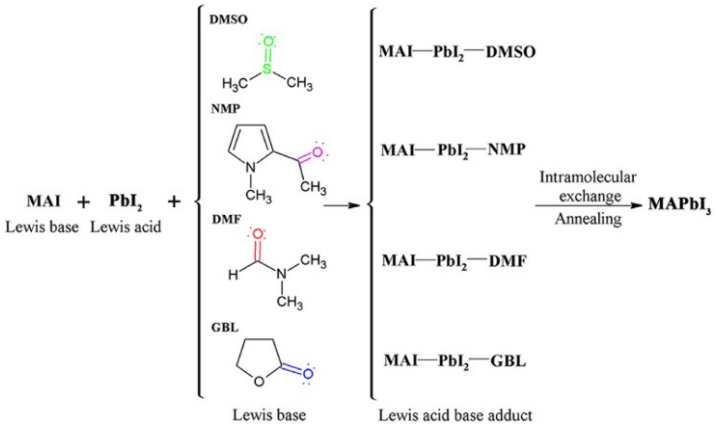

Figure 5.19 The precursor solvents applied with their respective intermediate species to form $MAPbI_3$. *Extracted from* [33].

Consequently, we performed a solvent study to determine the best solvent for the TPA additive. We selected a solvent mixture of GBL/DMSO (3:1), DMF/DMSO (0.93:0.07), and also DMF alone to dissolve TPA in $5(AVA)_x(MA)_{1-x}PbI_3$ solution, as shown in **Figure 5.20**.

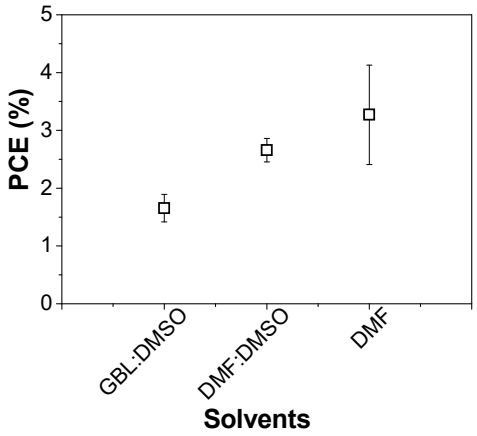

Figure 5.20 The application of several solvents, such as; GBL/DMSO in 3:1 v/v ratio, DMF/DMSO in 0.93:0.07 v/v ratio and only DMF related to PCE.

Once the solvent was selected (DMF), the TPA was then applied in the presence of 5AVA, following a one-step method by drop-casting in $5(AVA)_x(MA)_{1-x}PbI_3$ solution dissolved in anhydrous DMF, as described in Chapter 2. **Figure 5.21** shows the **(a)** JV curves and **(b)** the IPCE of the best results using TPA, and **(c)** the average photovoltaic parameters of the PSC.

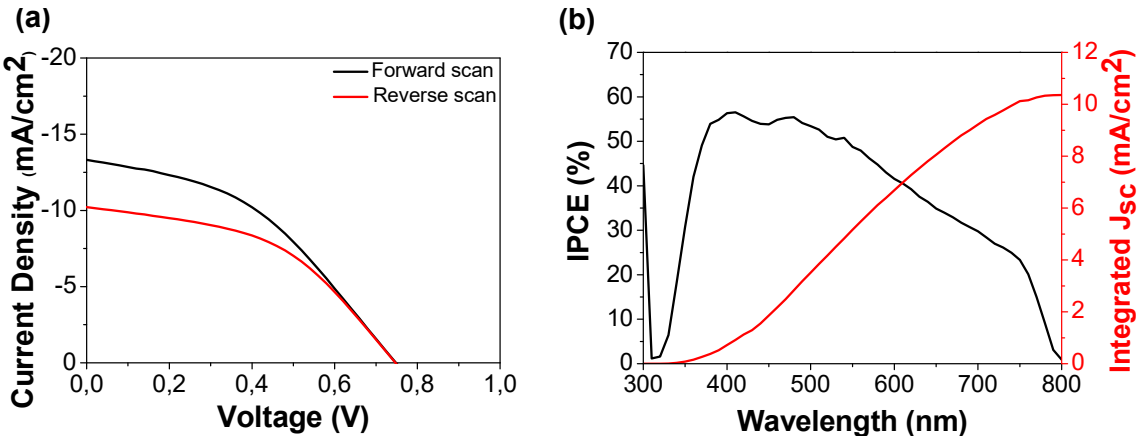

SAM		PCE (%)	V_{oc} (V)	J_{sc}(mA/cm^2)	FF (%)
TPA	*Forward*	3.3±0.85	0.70±0	10.53±2.44	42.33±5.34
	Reverse	2.7±0.85	0.70±0	8.0±2.06	45.97±5.66

Figure 5.21(a) JV curves, **(b)** IPCE of the best cell. **(c)** Average values of photovoltaic parameters of C-based PSCs using TPA as organic modifier in forward and reverse scan.

5.4.4 One step infiltration method applying the 3-Phosphonopropionic acid (3-Hpp)

The 3-phosphonopropionic acid was also applied in the presence of 5AVAI using a one-step sequential method in normal architecture, as described in Chapter 2. In this case, the molecule has two functional groups a phosphonate and a hydroxyl acid group. **Figure 5.22** shows the **(a)** JV curves and **(b)** the IPCE of the best results using 3-Hpp, and **(c)** the average photovoltaic parameters obtained.

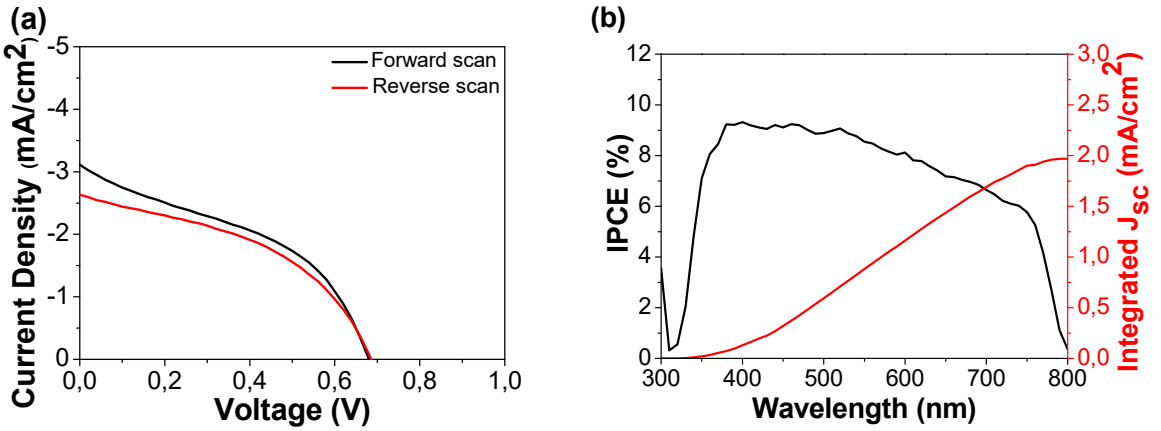

SAM		PCE (%)	V_{oc} (V)	J_{sc}(mA/cm^2)	FF (%)
3-Hpp	*Forward*	0.90±0.10	0.63±0.06	2.83±0.40	50.97±8.69
	Reverse	1.37±0.21	0.70±0	3.57±0.42	54.73±9.24

Figure 5.22 (a) JV curves, **(b)** IPCE of the best cell. **(c)** Average values of photovoltaic parameters of C-based PSCs using 3-Hpp in forward and reverse scan.

5.4.5 Comparison of photovoltaic performance applying different additives

An additive strategy was often used to achieve high-quality perovskite layers. Han and co-workers inserted 5AVAI in the perovskite structure changing from tetragonal to an orthorhombic phase. This 5AVAI molecular addition results in a better surface contact with the TiO_2 and an enhancement of the PCE [7]. Following this strategy in order to decrease charge recombination and improve the efficiency and stability of the devices a set of novel molecules were inserted into perovskite solution. With the reference 5AVAI molecule, we achieved the best results in terms of photovoltaic performance; however, we also analyzed the PABA and TPA additives without the presence of 5AVAI. **Table 5.1** shows a summary of the photovoltaic values from the champion cells using 5AVAI, PABA, TPA or 3-HPP. TPA provides the best results in comparison to the others.

Table 5.1 Summary of the photovoltaic performance values from the champion cells depending on the organic additive used in the perovskite solution.

SAM	solvent	PCE (%)	FF (%)	J_{sc}(mA/cm^2)	V_{oc} (V)
5AVAI	GBL	11.6	66.5	21.5	0.8
PABA	GBL	3.2	79.7	5.1	0.8
TPA	DMF	4.1	46.4	13.3	0.7
3-HPP	GBL	1.6	60.8	3.7	0.7

The application of novel additives into the perovskite solution during infiltration, results in good photovoltaic properties of the device, however, further optimization of the infiltration process is necessary in order to replace the 5AVAI molecule. As observed in **Table 5.1**, the incorporation of this 4-aminobenzoic acid led to a poor photovoltaic response. A possible explanation could be a competition between the PABA additive and the conventional 5AVAI for the sites inside the crystal structure of perovskite, which may have caused an incomplete crystallization process. In addition, the incorporation of the TPA led to a better photovoltaic response in comparison to the 4-aminobenzoic acid. However, the low current densitiy had a direct impact on the poor PCE. Finally, the incorporation of the 3-phosphonopropionic acid resulted in the worst photovoltaic response in comparison with the other organic additives. The FF and the V_{oc} exhibited a standard values, however, the J_{sc} exhibited a low value which

directly impact on the decrease of the PCE value. A further optimization is necessary in order to obtain better results.

Moreover, the above mentioned additives were also applied without the presence of the reference 5AVAI, in a C-based PSC structure. Among the functional groups of these molecules, the amino and the carboxylic acid groups act as anchoring groups similar to the 5AVAI molecule, and no significant difference in photovoltaic performance was noted with or without the addition of 5AVAI. In the case of other additives with different anchoring groups such as TPA and PABA, the PSC showed is about 3.5 %. **Figure 5.23** shows the photovoltaic average values for C-based PSC employing TPA and PABA additives, without the presence of 5AVAI molecule.

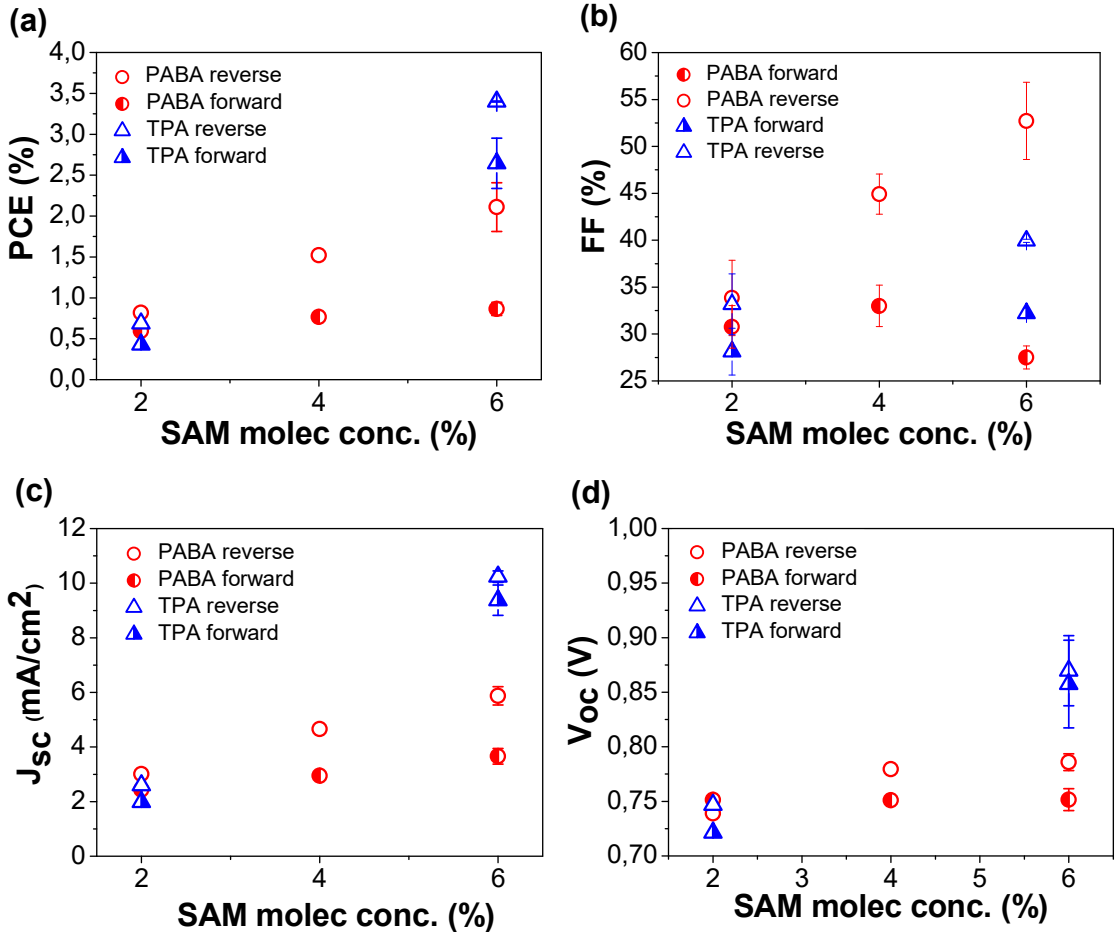

Figure 5.23 Photovoltaic average values for C-based PSC employing TPA and PABA additives, without the presence of 5AVAI molecule.

As seen in **Figure 5.23**, we have demonstrated that the device can work without 5AVAI and when both components are simultaneously in the solution, they compete for the sites in the crystal structure of $CH_3NH_3PbI_3$. As summary, the cell is working slightly better without

5AVAI additive. Without the presence of 5AVAI, the observed trend is that the higher the concentration of the organic additive, the better the photovoltaic performance.

5.5 Conclusions

This chapter deals with screen printed semiconductor oxides, i.e, TiO_2 and ZrO_2, used as ETL and scalffold, respectively, in CPSC. In this chapter, we reported results from the attractive C-based structure, which also provides easy manufacturing and robust devices. We experimentally fabricated a C-based PSC with a PCE as high as 11.5 % under AM 1.5G illumination at 100 mW/cm^2 after several optimization of the complete working device. Firstly we optimized the thicknesses of the oxide layers, in order to achieve an optimal "shell" (c-TiO_2/mp-TiO_2/ZrO_2/C). Other parameters, such as the c-TiO_2 layer thickness and 5AVAI content in perovskite solution, were also optimized. Regarding the optimization of the c-TiO_2, we discovered that the use of 2.5-5 % TiAcAc provided the best photovoltaic performance. We observed that the 5AVAI content in the perovskite infiltrated solution is a relevant parameter in the crystallization of the material as shown with the use of equimolar relation between PbI_2 and MAI at 0.952 M employing 3 % of 5AVAI additive. Furthermore, we demonstrated the effective use of a humidity post-treatment at RT to reduce or avoid the hysteretical behaviour observed in these C-based PSC architectures after annealing. The importance of this C-based PSC lies in 5AVA molecules with anchoring groups that provide fewer defects and prevent charge recombination. Additionally, this structure can be made by screen printing and is therefore very promising technology suitable for large-scale development and future commercialization.

5.6 References

[1] L. Etgar *et al.*, "Mesoscopic CH3NH3PbI3/TiO2 Heterojunction Solar Cells," *J. Am. Chem. Soc.*, vol. 134, no. 42, pp. 17396–17399, 2012.

[2] H. Chen and S. Yang, "Carbon-Based Perovskite Solar Cells without Hole Transport Materials: The Front Runner to the Market?," *Adv. Mater.*, vol. 29, no. 24, p. 1603994, 2017.

[3] M. Lira-Cantu, "The future of semiconductor oxides in next-generation solar cells," *Met. Oxides Ser.*, 2018.

[4] Q.-Q. Chu *et al.*, "Highly stable carbon-based perovskite solar cell with a record efficiency of over 18% via hole transport engineering," *J. Mater. Sci. Technol.*, vol. 35, no. 6, pp. 987–993, 2019.

[5] L. Liu *et al.*, "Fully Printable Mesoscopic Perovskite Solar Cells with Organic Silane Self-Assembled Monolayer," *J. Am. Chem. Soc.*, vol. 137, no. 5, pp. 1790–1793, 2015.

[6] Y. Hu *et al.*, "Stable Large-Area (10 × 10 cm2) Printable Mesoscopic Perovskite Module Exceeding 10% Efficiency," *Sol. RRL*, vol. 1, no. 2, p. 1600019, 2017.

[7] A. Mei *et al.*, "A hole-conductor–free, fully printable mesoscopic perovskite solar cell with high stability," *Science (80-.).*, vol. 345, no. 6194, pp. 295–298, 2014.

[8] S. G. Hashmi *et al.*, "Air Processed Inkjet Infiltrated Carbon Based Printed Perovskite Solar Cells with High Stability and Reproducibility," *Adv. Mater. Technol.*, vol. 2, no. 1, p. 1600183, 2017.

[9] Y. Rong *et al.*, "Tunable hysteresis effect for perovskite solar cells," *Energy Environ. Sci.*, vol. 10, no. 11, pp. 2383–2391, 2017.

[10] C. Raminafshar, V. Dracopoulos, M. R. Mohammadi, and P. Lianos, "Carbon based perovskite solar cells constructed by screen-printed components," *Electrochim. Acta*, vol. 276, pp. 261–267, 2018.

[11] T. Liu *et al.*, "Critical parameters in TiO2/ZrO2/Carbon-based mesoscopic perovskite solar cell," *J. Power Sources*, vol. 293, pp. 533–538, 2015.

[12] X. Jiang *et al.*, "Efficient Compact-Layer-Free, Hole-Conductor-Free, Fully Printable Mesoscopic Perovskite Solar Cell," *J. Phys. Chem. Lett.*, vol. 7, no. 20, pp. 4142–4146, 2016.

[13] Y. Yang *et al.*, "The size effect of TiO2 nanoparticles on a printable mesoscopic perovskite solar cell," *J. Mater. Chem. A*, vol. 3, no. 17, pp. 9103–9107, 2015.

[14] D. Bi *et al.*, "Using a two-step deposition technique to prepare perovskite (CH3NH3PbI3) for thin film solar cells based on ZrO2 and TiO2 mesostructures," *RSC Adv.*, vol. 3, no. 41, pp. 18762–18766, 2013.

[15] K. Liang, D. B. Mitzi, and M. T. Prikas, "Synthesis and Characterization of Organic−Inorganic Perovskite Thin Films Prepared Using a Versatile Two-Step Dipping

Technique," *Chem. Mater.*, vol. 10, no. 1, pp. 403–411, 1998.

[16] Y. Li *et al.*, "Ultra-high open-circuit voltage of perovskite solar cells induced by nucleation thermodynamics on rough substrates," *Sci. Rep.*, vol. 7, p. 46141, 2017.

[17] J.-P. Correa-Baena *et al.*, "Identifying and suppressing interfacial recombination to achieve high open-circuit voltage in perovskite solar cells," *Energy Environ. Sci.*, vol. 10, no. 5, pp. 1207–1212, 2017.

[18] P.-W. Liang *et al.*, "Additive Enhanced Crystallization of Solution-Processed Perovskite for Highly Efficient Planar-Heterojunction Solar Cells," *Adv. Mater.*, vol. 26, no. 22, pp. 3748–3754, 2014.

[19] X. Li *et al.*, "Improved performance and stability of perovskite solar cells by crystal crosslinking with alkylphosphonic acid ω-ammonium chlorides," *Nat. Chem.*, vol. 7, p. 703, 2015.

[20] B. Li *et al.*, "Constructing water-resistant CH3NH3PbI3 perovskite films via coordination interaction," *J. Mater. Chem. A*, vol. 4, no. 43, pp. 17018–17024, 2016.

[21] R. Fu, Y. Zhao, Q. Li, W. Zhou, D. Yu, and Q. Zhao, "Enhanced long-term stability of perovskite solar cells by 3-hydroxypyridine dipping," *Chem. Commun.*, vol. 53, no. 11, pp. 1829–1831, 2017.

[22] N. Santhosh, S. R. Sitaaraman, P. Pounraj, R. Govindaraj, M. S. Pandian, and P. Ramasamy, "Fabrication of hole-transport-free perovskite solar cells using 5-ammonium valeric acid iodide as additive and carbon as counter electrode," *Mater. Lett.*, vol. 236, pp. 706–709, 2019.

[23] X. Hou, S. Huang, W. Ou-Yang, L. Pan, Z. Sun, and X. Chen, "Constructing Efficient and Stable Perovskite Solar Cells via Interconnecting Perovskite Grains," *ACS Appl. Mater. Interfaces*, vol. 9, no. 40, pp. 35200–35208, 2017.

[24] B. Li, Y. Chen, Z. Liang, D. Gao, and W. Huang, "Interfacial engineering by using self-assembled monolayer in mesoporous perovskite solar cell," *RSC Adv.*, vol. 5, no. 114, pp. 94290–94295, 2015.

[25] M. Lira-Cantú, "Perovskite solar cells: Stability lies at interfaces," *Nat. Energy*, vol. 2, p. 17115, 2017.

[26] M. Duan, Y. Hu, A. Mei, Y. Rong, and H. Han, "Printable carbon-based hole-conductor-free mesoscopic perovskite solar cells: From lab to market," *Mater. Today Energy*, vol. 7, pp. 221–231, 2018.

[27] J. H. Heo, H. J. Han, D. Kim, T. K. Ahn, and S. H. Im, "Hysteresis-less inverted CH3NH3PbI3 planar perovskite hybrid solar cells with 18.1% power conversion efficiency," *Energy Environ. Sci.*, vol. 8, no. 5, pp. 1602–1608, 2015.

[28] Y. Ogomi *et al.*, "CH3NH3SnxPb(1–x)I3 Perovskite Solar Cells Covering up to 1060 nm," *J. Phys. Chem. Lett.*, vol. 5, no. 6, pp. 1004–1011, 2014.

[29] L. Zuo *et al.*, "Enhanced Photovoltaic Performance of CH3NH3PbI3 Perovskite Solar

Cells through Interfacial Engineering Using Self-Assembling Monolayer," *J. Am. Chem. Soc.*, vol. 137, no. 7, pp. 2674–2679, 2015.

[30] C. Duan, K. Zhang, C. Zhong, F. Huang, and Y. Cao, "Recent advances in water/alcohol-soluble π-conjugated materials: new materials and growing applications in solar cells," *Chem. Soc. Rev.*, vol. 42, no. 23, pp. 9071–9104, 2013.

[31] L. Steemers, M. J. Wanner, A. W. Ehlers, H. Hiemstra, and J. H. van Maarseveen, "A Short Covalent Synthesis of an All-Carbon-Ring [2]Rotaxane," *Org. Lett.*, vol. 19, no. 9, pp. 2342–2345, 2017.

[32] A. Cacciuto, S. Auer, and D. Frenkel, "Onset of heterogeneous crystal nucleation in colloidal suspensions," *Nature*, vol. 428, p. 404, 2004.

[33] J. Chen *et al.*, "Solvent effect on the hole-conductor-free fully printable perovskite solar cells," *Nano Energy*, vol. 27, pp. 130–137, 2016.

[34] N. Ahn, D.-Y. Son, I.-H. Jang, S. M. Kang, M. Choi, and N.-G. Park, "Highly Reproducible Perovskite Solar Cells with Average Efficiency of 18.3% and Best Efficiency of 19.7% Fabricated via Lewis Base Adduct of Lead(II) Iodide," *J. Am. Chem. Soc.*, vol. 137, no. 27, pp. 8696–8699, 2015.

Chapter 6

Solar Cell Stability following ISOS protocols

6.1 Introduction

As already described in this thesis work, halide PSCs have radically transformed the photovoltaic and energy-conversion arena. Their remarkable and unprecedented improvement of PCEs, currently above 24 %, has occurred in the past few years, and has benefitted from prior developments in other new photovoltaic technologies, e.g. DSSCs and OPVs. This technology has all the ingredients needed to rapidly achieve maturity: (a) inexpensive, abundant light-harvesting perovskite type minerals, (b) the straightforward design and composition of derivatives and homologous substances, and (c) facile solution-based processing methods. Another advantage of PSCs is their ability to be integrated in tandem architectures with silicon-based solar cells. As a result, mechanically flexible and semi-transparent light-harvesting arrays possessing polychromic sensitivity can be attainable. In order to be commercialized, three major barriers must be resolved: (a) the toxicity caused by the use of lead, (b) the degradation due to temperature, humidity and light exposure and (c) the hysteresis phenomena, among others [1]. To be commercially competitive, the long-term stability of halide PSCs must exceed the lifetime of Silicon solar cells: 20 years stability. The understanding of the PSC intrinsic and extrinsic degradation mechanisms can lead to an increase in PSC stability.

Back in 2011, a broad consortium of researchers developed recommendations for stability evaluation of organic photovoltaics. These standardized aging experiments are internationally recognized as the “ISOS protocols”, and were established at the “International Summit on Organic PV Stability” (Roskilde, Denmark). The ISOS protocols outline a consensus between researchers in the OPV field on performing and reporting degradation studies in a controlled and reproducible way. The ISOS protocols have allowed direct comparison of results between different research laboratories working on different

cell designs, thus enabling successful round robin experiments, and an improved understanding of degradation in those devices [2].
These ISOS protocols are currently applied by the Halide perovskite community to report device stability. Nevertheless, the members of the PSC community (among them our research laboratory) have observed a need to upgrade these ISOS protocols to incorporate PSCs special requirements. For this, recent upgrades of these ISOS protocols have been made with the aim to include the requirements observed in PSCs [3].

The ISOS protocols have three different levels depending on laboratory infrastructure. The first level requires basic equipment, while the second and third levels require more specialized equipment. Although the basic level gives less stress control in comparison with levels two and three, this has been designed this way so even those laboratories initiating in the stability research area can carry out stability analysis. The ISOS protocols can be separated in five general types of studies: (a) Dark storage (**ISOS-D**), (b) outdoor (**ISOS-O**), (c) light-soaking (**ISOS-L**), (d) thermal cycling (**ISOS-T**) and (e) light-humidity-thermal cycling (**ISOS-LT**) (See **Table 6.1**).

The Dark storage studies (**ISOS-D**) are characterized to carry out by leaving the samples in the dark with no load. For the ISOS-D-1 the samples are leaving at ambient conditions, for the ISOS-D-2 the samples are keeping at high temperature storage by a hotplate or oven. And finally, for the ISOS-D-3 the samples are keeping under controlled temperature and humidity conditions with an environmental chamber. The Outdoor stability studies (**ISOS-O**) are known to carry out at ambient conditions. For the ISOS-O-1 the devices are kept outside while the testing is inside by a solar simulator. For the samples under ISOS-O-2 testing the measurements are carrying out outside under daylight and the samples are kept also outside. And finally, the ISOS-O-3 the devices are measured inside from time to time and outside for a long time.

Table 6.1 Overview of different categories of ISOS testing protocols [4].

Test ID	Test Type	Light source	Temp. (°C)	R.H. (%)	Characterization light source	Load
ISOS-D-1	Dark	None	Ambient	Ambient	Solar simulator or sunlight	Open circuit
ISOS-D-2	Dark	None	65/85	Ambient	Solar simulator	Open circuit
ISOS-D-3	Outdoor	None	65/85	85	Solar simulator	Open circuit
ISOS-O-1	Outdoor	Sunlight	Ambient	Ambient	Solar simulator	MPP or open circuit
ISOS-O-2	Outdoor	Sunlight	Ambient	Ambient	Sunlight	MPP or open circuit
ISOS-O-3	Outdoor	Sunlight	Ambient	Ambient	Sunlight and solar simulator	MPP
ISOS-L-1	Laboratory weathering testing	Simulator	Ambient	Ambient	Solar simulator	MPP or open circuit
ISOS-L-2	Laboratory weathering testing	Simulator	65/85	Ambient	Solar simulator	MPP or open circuit
ISOS-L-3	Laboratory weathering testing	Simulator	65/85	Near 50	Solar simulator	MPP
ISOS-T-1	Thermal cycling	None	Between RT and 65/85	Ambient	Solar simulator or sunlight	Open Circuit
ISOS-T-2	Thermal cycling	None	Between RT and 65/85	Ambient	Solar simulator	Open Circuit
ISOS-T-3	Thermal cycling	None	-40 to +85	Near 55	Solar simulator	Open Circuit
ISOS-LT-1	Solar thermal humidity cycling	Simulator	Linear or step ramping Between RT and 65	Monitored, uncontrolled	Solar simulator	MPP or open circuit
ISOS-LT-2	Solar thermal humidity cycling	Simulator	Linear ramping between 5 and 65	Monitored, controlled	Solar simulator	MPP or open circuit
ISOS-LT-3	Solar thermal humidity cycling	Simulator	Linear ramping between -25 and 65	Monitored, controlled	Solar simulator	MPP or open circuit

The Light-soaking stability experiments (**ISOS-L**) are carrying out under laboratory weathering testing. For the case of ISOS-L-1 the measurements are taken under uncontrolled conditions of temperature and R.H., while the ISOS-L-2 the temperature is controlled (between 65/85 °C) and for the ISOS-L-3 are controlled both, temperature (between 65/85 °C) and the R.H. (50 %). The Thermal cycling (**ISOS-T**) is usually required for a final product certification; however the samples can be damaged by this type of test. Basically, the sample following the ISOS-T-1 measurements is cycled from a high temperature (65/85 °C) to RT. The ISOS-T-2 is similar than before but with more precisely equipment (environmental chamber with automatically performance). And finally, the ISOS-T-3 requires the advanced equipments with changes in the temperature range from 85 °C to -40 °C. The Light-humidity-thermal cycling (**ISOS-LT**) are solar-thermal-humidity cycling measurements. The ISOS-LT-1 category used a linear or step ramping between RT and 65 °C while the ISOS-LT-2 linear ramping between 5 and 65 °C and ISOS-LT-3 linear ramping between -25 and 65 °C.

In this chapter we carried out stability analysis to our best carbon-based PSCs. We employed two ISOS protocols: ISOS-D and ISOS-L as will be showed in the following section.

6.2 Stability of C-based PSCs

As already mentioned in Chapter 1, the factors affecting the degradation of the devices are moisture and oxygen, thermal and light effect. Among these different factors, moisture has been considered as one of the biggest challenges. Moisture affects the amine group from perovskite layer, the methylamine group is lost via sublimation while PbI_2 is formed, and also oxygen is responsible to degradation of perovskite by hydrolysis reaction [5]:

$$CH_3NH_3PbI_3\ (s) \leftrightarrow PbI_2(s) + CH_3NH_3I\ (aq) \quad (1)$$

$$CH_3NH_3I\ (aq) \leftrightarrow PbI_2(s) + CH_3NH_2(aq) + HI\ (aq) \quad (2)$$

$$4HI\ (aq) + O_2\ (g) \rightarrow 2I_2\ (s) + 2H_2O\ (I) \quad (3)$$

$$2HI\ (aq) \rightarrow H_2\ (g) + I_2(s) \quad (4)$$

Many efforts have been made in order to avoid the degradation cause by water such as controlling the temperature and the R.H conditions during the solar cell fabrication, encapsulation of the devices, the use of additives to protect the perovskite material and the use of 2D perovskite to improve stability [5].

In 2013, Han's group reported carbon-based HTM-free triple-mesoscopic-layer architecture PSC [6]. This kind of architecture, fabricated by the screen printing technique, offers easy and cheap manufacture appropriate for commercialization. One year later, using $(5\text{-AVA})_x(MA)_{(1-x)}PbI_3$ as a light absorber, Mei *et al.* produced a solar cell with a certified PCE of 12.8 %. Also, the cell was stable for over 1000 h in ambient air without any encapsulation under AM 1.5G light soaking [7]. In addition, Han's group fabricated a large-area fully printable module (10 cm x 10 cm), a PCE of 10.4 % has been demonstrated and also their modules show good stability study in outdoor conditions for 1 month [8] .

Furthermore, the advantage of this thick carbon structure (10 µm) can act as water retaining layer which offer an excellent stability of the device even without any encapsulation [9]. And also for the use of semiconductors oxides, such as, TiO_2 and ZrO_2 which act as a electron conductor and spacer layer, respectively, protecting the perovskite material[10]. More recently, a remarkable long-term stability of more than 10,000 h was reported by Grancini *et al.*using the same carbon structure with a 2D/3D mixed perovskite [11]. Furthermore, Baranwal and co-workers proved the thermal stability of these printable CPSCs of over 1500 h at 100 °C [12]. Recently, Chu and co-workers used CPSCs with a P3HT/graphene composite. In their study, the stability was evaluated by testing encapsulated devices under illumination (AM 1.5, 100mW/cm^2). Their results exhibited that the devices retain 89 % of its original PCE after 600 h of testing [13]. Another example, is the work of the Wu *et al.* inserted an inorganic CuSCN between the perovskite and the carbon electrode in order to decrease electron recombination. The addition of CuSCN results in a production of high

stability devices, the best device retains 80 % of its initial PCE value after 1000 h under continuous one sun illumination [14].

These reported results confirmed the advantages of these CPSCs in terms of stability and robustness.

6.2.1 Stability studies of a C-based PSC following ISOS-D-1 protocol

Following the ISOS-D-1 protocol, we conducted stability studies on unencapsulated Carbon-based PSCs. The devices were stored in the dark inside a drybox, under dry conditions, at R.H. 10 % and at RT (25 °C). The PSCs was then analyzed under the sun simulator at 1 sun AM 1.5G at different time intervals.

Figure 6.1 shows the ISOS-D-1 stability test carried out to a PSC under storage conditions in the dark for almost one year. The initial efficiency of the device was 10.6 % and decreased down to 7.2 % after 7800 h.

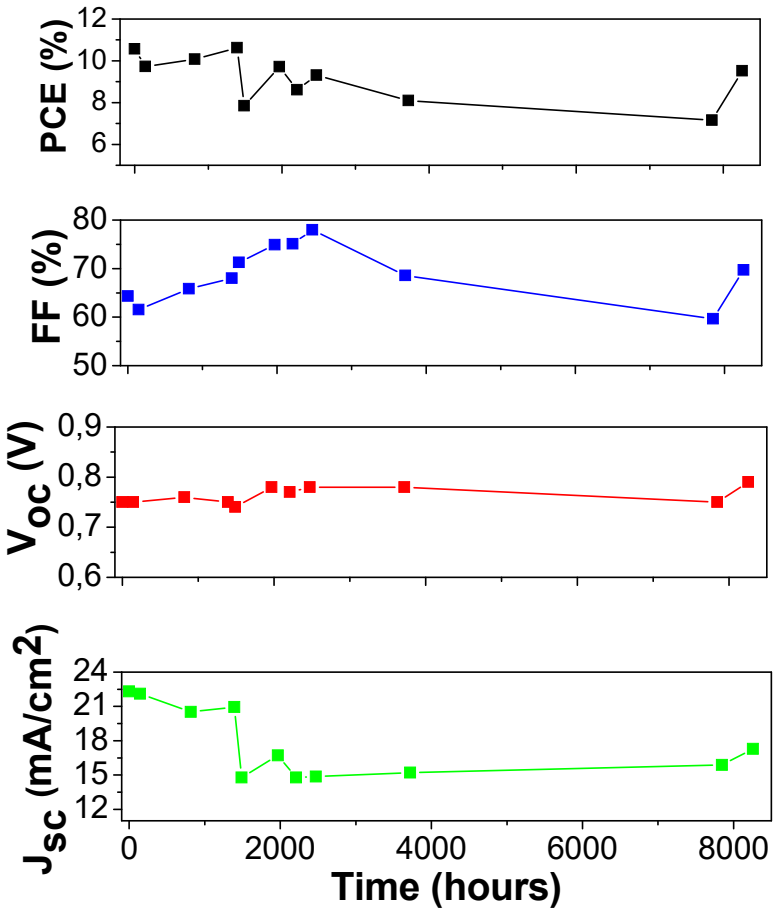

Figure 6.1 Stability test of *cell A* CPSCs under 1 sun AM 1.5G conditions stored in the dark under dry atmosphere for almost 1 year.

From **Figure 6.1**, we can observe that the PCE suffered continuous variations during measurements; however the general trend is decrease slowly during the time. This could be ascribed to the fact that exists some recovery of cells before the next measurement, and is not a dramatically decrease. It can be also observed that the last point is higher in all curves, probably due to a systematic error or also coming from a recovery of the cell.

To provide more examples, **Figure 6.2** shows the stability graphs of two different CPSCs,*cell B* and *cell C*, after almost 6000 h storage in dark conditions under dry air atmosphere from different batches in order to compare the trend even from different days of fabrication. The *cell B* in **Figure 6.2 (a)** shows rapid degradation after the first 25 days, it could be observed that when the initial values are higher, the degradation trend dramatically decreased. However, it can be observed a recovery before 1000 h, following the trend of the *cell A*. In contrast, in **Figure 6.2 (b)** the degradation process is slower when the first values presented low performance, in fact a gradually decay could be observed. This means that the measuring initial values depend directly on the fabrication conditions of the day.

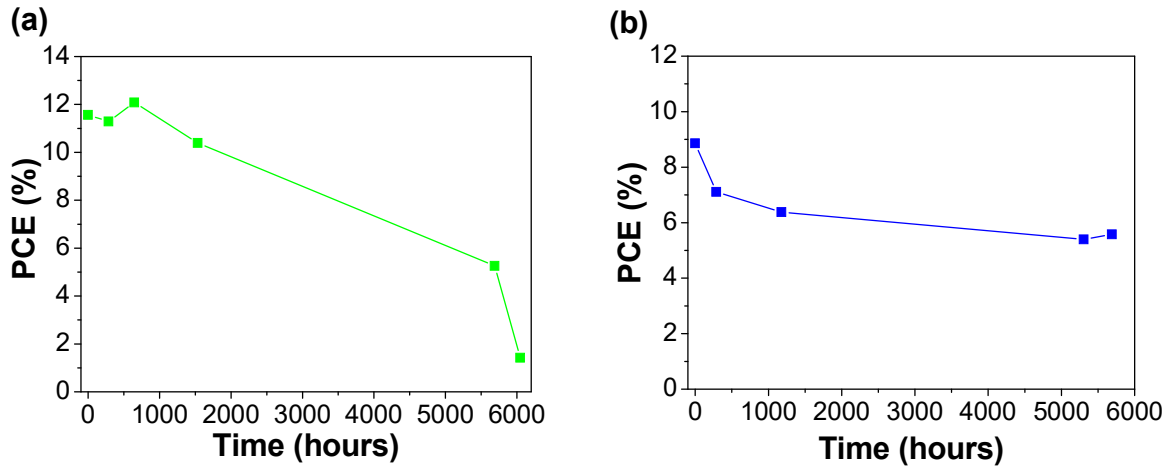

Figure 6.2 Time evolution measurements of non-encapsulated CPSCs during indoor conditions stored in the dark under dry atmosphere. Study from different batches, corresponding to **(a)** *cell B* and **(b)** *cell C*.

We also measured the reproducibility for three different CPSCs in the same batch, as shown in **Figure 6.3.** In this study, the initial PCE for all of them was closer, exceeding 9 %. For all cells, *cell D, E, F*, the PCE dramatically decreased after 800 h, but recovered after 1000 h followed by an almost constant degradation for more than 4000 h. Finally, a remarkable improvement was detected after 5000 h. It can be observed the good reproducibility between these three CPSCs fabricated in the same batch during the time, the first values

show less error between them while at the end of the 6000 h less reproducibility between the values were exhibited.

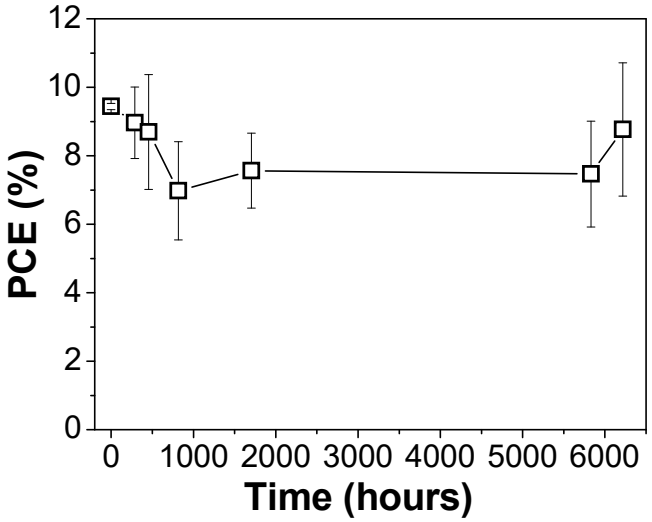

Figure 6.3 Stability test of a triple-layer CPSCs under full AM 1.5 simulated sunlight in ambient air over 6200 hours without encapsulation. The *cells D, E, F* from the same batch, are stored in dark conditions under dry atmosphere.

6.2.2 Stability studies of a C-based PSC following ISOS-L-1 protocol

In order to prove the stability of these CPSCs in more realistic conditions, long-term stability measurements were carried out under a continuous sun simulator illumination at 1000 W/m^2 with a mask of 0.079 cm^2, in ambient conditions (R.H. 50 % and 25 °C temperature) without any encapsulation. These measurements were carried out following the ISOS-L-1 protocols. The time range for the studies was from several minutes to thousands of hours.

Figure 6.4 shows the stability graph for CPSCs, *cell G* analysed for more than 6 hours and *cell H* analysed for more than 40 hours. An unexpected result was obtained as can be clearly seen in the graph because of the improvement in terms of PCE during the time at the beginning of the measurement, as already reported by McGehee *et al.*, who suggested that the pre-conditioning with light-soaking can significantly influence PV performance [15]. As also shown, light-soaking under large positive applied voltage before characterization can dramatically improve the FF, J_{sc}, and PCE of the PSCs [15]. Consequently, the light soaking effect as from continuous illumination must be considered in these kinds of measurements.

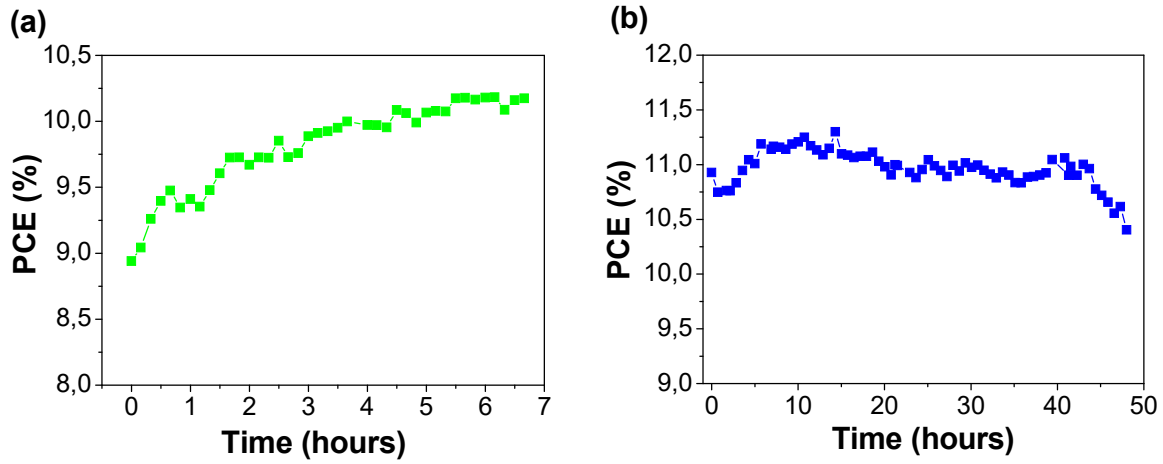

Figure 6.4 Stability test of CPSCs **(a)** *cell G* (over 6 h) and **(b)** *cell H* (over 48 h) under continuous illumination in ambient conditions.

These CPSCs exhibited the same trend between *cell G* and *cell H*, at the beginning of the measure *cell H* exhibited the same trend of *cell G* where the values are keep increasing during the first 7 hours. After almost 10 hours the PCE of *cell H* varied with a general downward trend and finally from 40 hours started to decrease gradually.

The last example presented dessides a long-term stability study carried out by the Polytechnic University of Cartagena (UPCT). This study consisted of the measurement of three CPSCs, *cell I, cell J* and cell *K*, under solar simulator light irradiation (ABET AM1.5 Class AAA, with a mask of 7.1 mm^2), under ambient conditions (25 °C and 50 % R.H.). From the results in **Figure 6.5** three different stages can be clearly seen corresponding to three different slopes. They were considerably stable from the beginning up to 200 hours. The first sign of degradation appears after 300 hours until almost 500 hours where the dramatically stability decreasing occurred from 600 to just over 1000 h.

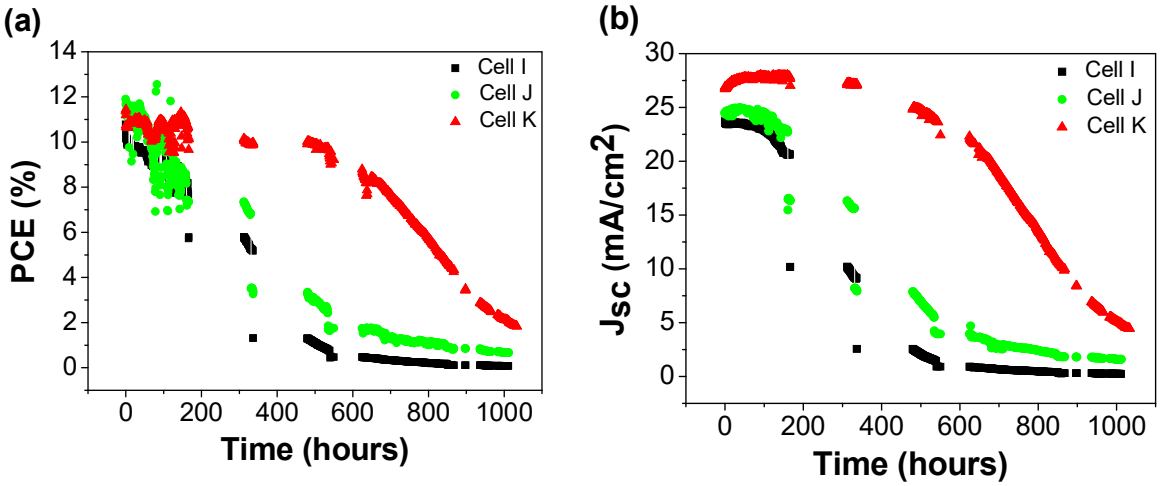

Figure 6.5 Stability test (over 1000 hours) of CPSCs in terms of **(a)** PCE (%) and **(b)** J_{sc} (mA/cm^2) with 5AVA under continuous illumination in ambient conditions. The samples are *Cell I*,*Cell J* and *Cell K*.

The CPSCs analyzed above, applied the AVAI organic modifier, which is the most common organic molecule applied in these type of solar cells. Nevertheless, we also performed ISOS stability test to CPSCs applying two new organic modifiers: the PABA and the TPA molecules. Stability tests were made at RT conditions (25 °C, 50 % R.H.). **Figure 6.6** shows the stability test following the ISOS-L-1 in UPCT installations under continuous illumination of 1 sun, for 150 hours. And **Table 6.2** shows the summary of the description corresponding to the cells which were used for the stability study following the ISOS protocols.

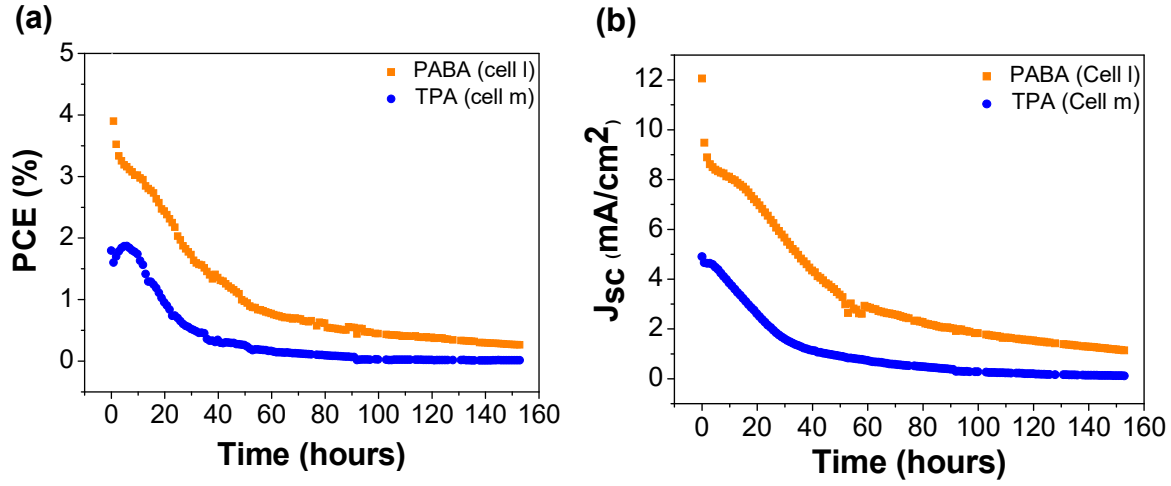

Figure 6.6 Stability test about 150 hours of CPSC with SAMs, in terms of **(a)** PCE (%)and **(b)** J_{sc} (mA/cm^2) under continuous illumination in ambient conditions. The samples are *Cell L* corresponding with PABA and *Cell M* corresponding with TPA.

From the results in **Figure 6.6** we can conclude that PABA provides slightly more stability than TPA, however, 5AVA results in much better stability.

Table 6.2 Summary of the description corresponding to the CPSCs which were used for the stability study following the ISOS protocols.

Sample	Stability Time (hours)	Initial values				Final values				Method	ISOS
		PCE	V_{oc}	J_{sc}	FF	PCE	V_{oc}	J_{sc}	FF		
A	8400	10.6	0.7	22.3	64.3	9.5	0.8	17.3	69.7	Onestep	D1
B	6000	11.6	0.8	21.5	66.5	1.4	0.7	9.3	38.5	One step	D1
C	6000	8.8	0.8	15.7	68.8	5.6	0.7	17.2	46.9	Onestep	D1
D	6000	9.4	0.8	18.6	61.3	9.5	0.7	15.1	82.6	Onestep	D1
E	6000	9.4	0.8	21.3	55.3	6.6	0.7	20.0	45.7	Onestep	D1
F	6000	9.5	0.8	19.2	61.0	10.2	0.7	19.3	71.1	One step	D1
G	7	8.9	0.8	17.4	62.9	10.2	67.8	0,8	18.7	One step	L1
H	50	9.3	0.8	18.6	61.3	9.5	0.7	15.0	82.6	One step	L1
I	1000	10.8	0.7	23.7	-	0.1	0.6	0.2	-	One step	L1
J	1000	11.9	0.7	24.5	-	0.6	0.8	1.6	-	One step	L1
K	1000	11.4	0.7	26.7	-	2.1	0.8	4.9	-	One step	L1
L	150	3.9	0.7	9.5	-	0.3	0.5	1.2	-	One step	L1
M	150	1.6	0.7	4.6	-	0.01	0.4	0.1	-	One step	L1

Further optimization is required in order to achieve more stable devices using these new molecules. However, these results demonstrated the good stability of these carbon-based solar cells, for more than 1000 h of lifetime study.

6.3 Conclusions

In general, we can conclude that C-based PSC show long stability, of almost 1 year under storage conditions in the dark and dry atmosphere without any encapsulation. They also show good long-term stability under irradiation conditions as has been reported for more than 1000 h. Regarding SAMs the 5AVAI exhibited longer lifetime comparing to the others (TPA and PABA).

The understanding of degradation processes and the rejection of the hysteretic behaviour of PSCs is a highly requirement for a proper device characterization and for the fabrication of long term stable devices towards to the market.

6.4 References

[1] S. van Reenen, M. Kemerink, and H. J. Snaith, “Modeling Anomalous Hysteresis in Perovskite Solar Cells,” *J. Phys. Chem. Lett.*, vol. 6, no. 19, pp. 3808–3814, 2015.

[2] M. O. Reese *et al.*, “Consensus stability testing protocols for organic photovoltaic materials and devices,” *Sol. Energy Mater. Sol. Cells*, vol. 95, no. 5, pp. 1253–1267, 2011.

[3] et al. Mark V. Khenkin, Eugene A. Katz, Monica Lira-Cantu, “Consensus on ISOS Protocols for Stability Assessment and Reporting for Perovskite Photovoltaics,” *Nat. Energy*.

[4] M. O. Reese *et al.*, “Consensus stability testing protocols for organic photovoltaic materials and devices,” *Sol. Energy Mater. Sol. Cells*, vol. 95, no. 5, pp. 1253–1267, 2011.

[5] R. Wang, M. Mujahid, Y. Duan, Z.-K. Wang, J. Xue, and Y. Yang, “A Review of Perovskites Solar Cell Stability,” *Adv. Funct. Mater.*, vol. 0, no. 0, p. 1808843, Feb. 2019.

[6] Z. Ku, Y. Rong, M. Xu, T. Liu, and H. Han, “Full Printable Processed Mesoscopic CH3NH3PbI3/TiO2 Heterojunction Solar Cells with Carbon Counter Electrode,” *Sci. Rep.*, vol. 3, p. 3132, 2013.

[7] A. Mei *et al.*, “A hole-conductor–free, fully printable mesoscopic perovskite solar cell with high stability,” vol. 345, no. 6194, pp. 295–298, 2014.

[8] Y. Hu *et al.*, “Stable Large-Area (10 × 10 cm2) Printable Mesoscopic Perovskite Module Exceeding 10% Efficiency,” *Sol. RRL*, vol. 1, no. 2, p. 1600019, 2017.

[9] Y. Rong, L. Liu, A. Mei, X. Li, and H. Han, “Beyond Efficiency: the Challenge of Stability in Mesoscopic Perovskite Solar Cells,” *Adv. Energy Mater.*, vol. 5, no. 20, p. 1501066, 2015.

[10] M. Lira-Cantú, “Perovskite solar cells: Stability lies at interfaces,” *Nat. Energy*, vol. 2, p. 17115, 2017.

[11] G. Grancini *et al.*, “One-Year stable perovskite solar cells by 2D/3D interface engineering,” *Nat. Commun.*, vol. 8, p. 15684, 2017.

[12] A. K. Baranwal *et al.*, “100 °C Thermal Stability of Printable Perovskite Solar Cells Using Porous Carbon Counter Electrodes,” *ChemSusChem*, vol. 9, no. 18, pp. 2604–2608, 2016.

[13] Q.-Q. Chu *et al.*, “Highly stable carbon-based perovskite solar cell with a record efficiency of over 18% via hole transport engineering,” *J. Mater. Sci. Technol.*, vol. 35, no. 6, pp. 987–993, 2019.

[14] X. Wu *et al.*, “Efficient and stable carbon-based perovskite solar cells enabled by the inorganic interface of CuSCN and carbon nanotubes,” *J. Mater. Chem. A*, vol. 7, no.

19, pp. 12236–12243, 2019.

[15] E. L. Unger *et al.*, “Hysteresis and transient behavior in current–voltage measurements of hybrid-perovskite absorber solar cells,” *Energy Environ. Sci.*, vol. 7, no. 11, pp. 3690–3698, 2014.

ANNEX

Surface Functionalization

A.1 Introduction

Despite the rapid progress over the last few years and the impressive properties that characterize halide perovskites, such as high absorption coefficients, widely tunable bandgap, high carrier mobility, versatile and low cost technology, among others [1]; there are still several issues that need to be addressed in order to fully exploit the potential of PSCs. One of the most important issues is the presence of defects. Given that halide perovskites are relatively soft ionic solids, the control and understanding of their defect structures is still limited. Defects in these materials restrict the power conversion efficiency of the solar cells limiting charge carrier transport due to recombination processes taking place in the material. This processes are in detrimental of the photovoltaic performance of the PSCs [2].

In a perfect crystalline solid, every atom is located in its prescribed site. In a real semiconductor defects are found as interruptions in a crystal lattice (crystallographic defects) or as impurities (presence of a foreign atom). Defects can exist as single defects, as array of defects or as series of higher-dimensional defects as schematically represented in **Figure A.1**. In general, single defects or point defects, can be divided in three types: atomic vacancies (atoms missing from the lattice), interstitials (atoms occupying the space between atoms in the lattice), and anti-site substitutions (atoms occupying the wrong site in the lattice) **Figure A.1 (c)**. If they exist in array configuration we have what is known as Frenkel defects and Schottky defects (**Figure A.1 (d)**. Higher-dimensional defects are the result of the combination of point defects and defect arrays, and we know them as dislocations, grain boundaries and precipitates, as illustrated in **Figure A.1** [3].

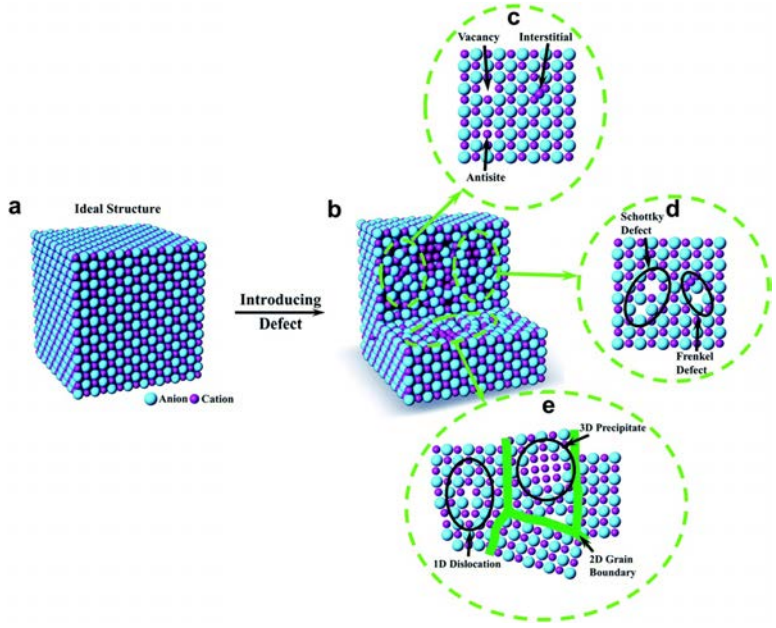

Figure A.1 Defects in semiconductors. Ideal structure **(a)** without defects and **(b)** after introducing defects. **(c)**point defects, **(d)** defect arrays, and **(e)** higher dimensional defects. *Extracted from* [3].

Defects are formed spontaneously during synthesis process of materials. Less defect concentration is observed in single crystals, while solution processed thin films usually contain high amount of defects. When the formation energy of a material is negative the amount of defects is usually large, so the material with the lowest formation energy is in its most stable state. This formation energy depends on the atomic chemical and electronic potential (related to reactants and fermi levels respectively) and thus, defect structure depends on synthesis parameters such as temperature, atmosphere, humidity, concentration of reactants, solvents, doping level, etc [4]. Halide perovskites have shown high defect tolerance. Nevertheless, deep defects in halide perovskites still prevent the enhancement of their power conversion efficiency to reach the Schockley-Queisser limit [2].

Different approaches exist to control and passivate defect in halide PSC materials. Among them is the growth of large grain-size perovskite crystals, defect passivation through the use of organic additives which can be applied at interfaces (surface modification), or within the halide perovskite (as bulk-heterojunction) to form high quality polycrystalline perovskite films [2].

In this thesis work we chose to work with different organic molecules (or additives) in order to passivate defects in Carbon-based PSCs. The organic molecules have been employed in a

bulk-heterojunction configuration (mixed with the halide perovskite) to fabricate complete CPSC as described in Chapter 5. In this Annex, we present the manipulation of these organic molecules to form SAMson different oxide substrates. Our intention is to study and analyse the relation between the organic molecule and the oxide surface with the aim to correlate this interaction to the PCE of the final solar cells. These studies of SAMs were made by Kelvin probe AFM and supported by XPS/UPS analyses. In the following sections we give a brief introduction to SAMs and the possible interactions we can expect between different functional groups present in organic molecules and the components of PSCs. Then we will describe our results on the fabrication and analysis of SAMs on oxide surfaces.

A.2 Self-Assembled Monolayers (SAMs) in PSCs

SAMs are defined as the formation of monolayers by self-assembly of ordered molecules, which interact between them, attached at the solid surface [5]. **Figure A.2 (a)** shows a representation of the different parts that compose a SAM. These consist in a headgroup, which binds to the substrate; the spacer or backbone, in charge of the connection between the headgroup to terminal group and responsible to provide the thickness and the electronic conductivity of the SAM (**Figure A.2 (a)**). And finally, the terminal functional group which consists the outer surface of the film [5]. These functional groups in SAMs can be silanes, phospohonates, carboxylates, amines, and others (**Figure A.2 (b)**). Among the different type of attachment, covalent bonding is the most interesting due to its strong interaction with the surface. The first report of the fabrication SAMs was made in 1946 by Zisman and co-workers who studied the preparation of a monolayer by adsorption onto a metal substrate [6]. In 1996, Ulman *et al.*, studied different kinds of monolayers such as, organosilicon, organosulfur, or alkyl monolayers. Also, they determined the evaluation of intermolecular interactions in SAMs and the surface engineering using SAMs [7].

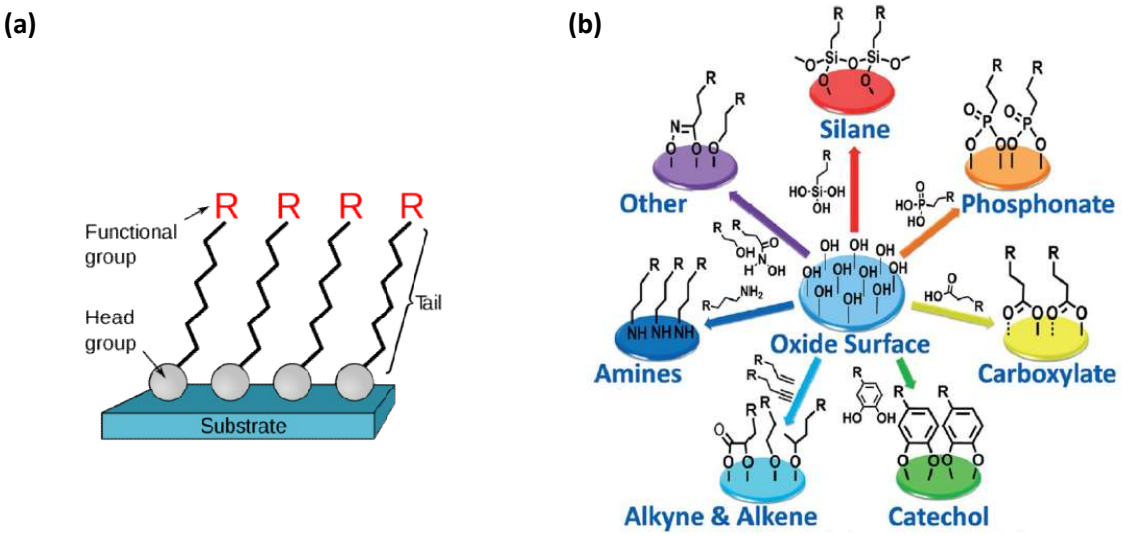

Figure A.2 (a) Representation of the structure of a SAM. *Extracted from* [8]. And**(b)** Different bonding modes of organic molecules on oxide surfaces. *Extracted from* [9].

In PSCs an organic additive can interact in different ways with the materials of the solar cell. Especially important is the interaction with the absorber, the halide perovskite, and, in our case, with the metal oxide applied as transport layer. Organic molecules with functional groups especially selective to bond with oxide surfaces are depicted in **Figure A.2 (b)** [9], where oxide surfaces are prone to different types of attachment and the strength of the attachment is directly dependent on the functional group of the molecule. Among these, there are four types of functional groups more relevant to be applied in solar cells due to the affinity to the PSCs materials: silanes, carboxylates, phosphonates and amines [10].

Silane monolayers exhibit high reactivity and well-ordered monolayers can easily be obtained [11]. Silanes provide high thermal stability and mechanical robustness. Sagiv *et al.* were the first to report the formation mechanism of silanes, consisting on the hydrolysis of the molecules and consequently reaction of the –OH groups with the surfaces [12].

The **phosphonate** family have attracted high interest due to the already reported strong and effective attachment on different metal oxide surfaces, such as Al_2O_3, TiO_2, ZrO_2, TiO_2 and SiO_2. Phosphonic acids have a hydrogen-bond, under heating treatment these phosphonic acid monolayers become phosphonates and bond strongly onto surfaces [13]. A good example of the beneficial effect of phosphonate-linkers is the application of alkylphosphonates that are able to provide well-ordered and dense monolayers. In addition, the stability of these SAMs on titania for more than 14 days of ambient air exposure confirmed the robustness of these monolayer [14]. Consequently, phosphonates are being

use in applications where high stability is required, and can be excellent to enhance the durability of PSCs. **Carboxylates** have a long history in emerging photovoltaics. The attachment of dyes in DSSCs is usually made through the carboxylic functional group of these absorbers [15]. Their importance resides on the easy control of the binding and reactivity of species. In addition, carboxylates can be modify and react with primary amines to form covalent bonding [16]. Also, carboxylic acids are capable of providing robustness and stability on metallic substrates [17].Wang and co-workers, give an example of Br and carboxylic groups attached onto oxide surface, demonstrated effective surface passivation using 4-bromobenzoic acid as a SAM resulting in a clear reduction of charge recombination and enhancement of perovskite crystallization and a PCE exceeding 18%, with the incorporation of this benzoic acid onto an NiO surface [18]. **Amino** self-assembled monolayers [9]can be attached with chemisorptions processes in several types of oxide surfaces, such as alumina, indium tin oxide, quartz, silica, glass, mica or silicon dioxide [19].Amino groups can also be attached to the perovskite absorber. For instance, Hou *et al.* reported the use of Triphenylamine as a SAM onto a perovskite layer following the normal architecture, FTO/c-TiO_2/mp-TiO_2/$CH_3NH_3PbI_3$-TPA/Spiro-OMeTAD/AgAl. The results exhibited a clear improvement in terms of performance and thermal stability of PSCs. The incorporation of triphenylamine allowed a better crystallization process reaching a PCE of 18.5 % [20].

More recently, the application of organic molecules (additives) **with double functional groups** which can both interact with the materials of the PSCs has been reported. For example, Zuo *et al.* demonstrated that the deposition of 3-aminopropanoic acid SAM (C_3-SAM), an example of a SAM with a carboxylic acid and amino group, onto sol-gel ZnO layers induced a significant improvement in the morphology of $CH_3NH_3PbI_3$film due to the enhanced wetting between ZnO and the perovskite film, forming a permanent dipole moment. Also, film crystallinity was increased and the reduction of pin-holes was clearly observed. With the structure of glass/ITO/ZnO/SAM/Perovskite/Spiro-OMeTAD/MoO_3/Ag, a15.7% PCE was reached. According to this study, pinhole-free perovskite film with high crystalline properties is essential for highly efficient PSCs [21]. Li *et al.* introduced a PABA SAM, an example of a SAM with carboxylic and amino groups, on a mp-TiO_2 layer by immersion, resulting in an improvement of the quality of the perovskite, leading to fewer traps, better carrier transport and consequently, a reduction in charge recombination and a

good matching energy level between the TiO_2 layer and the perovskite layer. Using a structure of FTO/c-TiO_2/meso-TiO_2/PABA monolayer/$CH_3NH_3PbI_3$/Spiro-OMeTAD/Au, the best PSCs with SAM modification displayed the highest PCE of 10.6 % [22]. Wang and co-workers inserted 3-Aminopropyl trimethoxysilane (APMS), with an amino and silane group, in the TiO_2/$CH_3NH_3PbI_3$ interface, leading to a passivation effect into surface traps of TiO_2 and better perovskite cristallinity. Their work demonstrates a reduction of recombination processes in this interface that directly affects the performance of the PSCs, reaching a PCE of 15.8 % [23]. In addition, Zuo *et al.*, reported a study applying different SAMs on a SnO_2 surface. Further analysis revealed that proper interfacial interactions can lead to a reduction in trap state density and facilitation of charge transfer. Using 4-pyridinecarboxylic acid (PA) SAM, with the structure of glass/ITO/(SnO_2/SAM)/PVSK/Spiro-OMeTAD/Au, the PSCs exhibited a PCE exceeding 18 %, and an enhancement of 10% compared with those without SAMs[24]. Finally, Liu and co-workers introduced an organic silane self-assembled monolayer in fully printable mesoscopic carbon-based PSC. The shell was inserted in an Aminopropyltrimethoxysilane SAM, which consists an amino and silane groups, for several hours. This surface modification by silane SAM resulted in an enhancement of the energy band alignment, a passivation of defects and reduction of recombination processes. The best cell exhibited a PCE of 12.7 % [25]. All these studies suggest that the application of SAMs in PSCs can improve charge transport, avoid or reduce charge recombination and permits to develop PSCs with excellent efficiency and stability.

Following the use of 5AVAI as an additive employed by Han's group, we inserted the others molecules into CPSCs, in our attempt to assemble them into several surfaces. **Figure A.3** depicts a schematic representation of the idea developed in this thesis work on surface functionalization: **(a)** the different layers of the Carbon-based PSC studied in this thesis work, **(b)** the corresponding band energy level alignment of layers and interfaces and **(c)** the possible interaction between the organic molecules (OM) at the interface between the halide perovskite and the oxide layer**.** The OM under study are (from top to bottom): 5AVA, PABA, TPA and the H3pp**.** These molecules have in common 3 different anchoring groups (amines, carboxylates or phosphates). In this annex we present the characterization of the molecules by different techniques and our attempt to assemble them on different substrates.

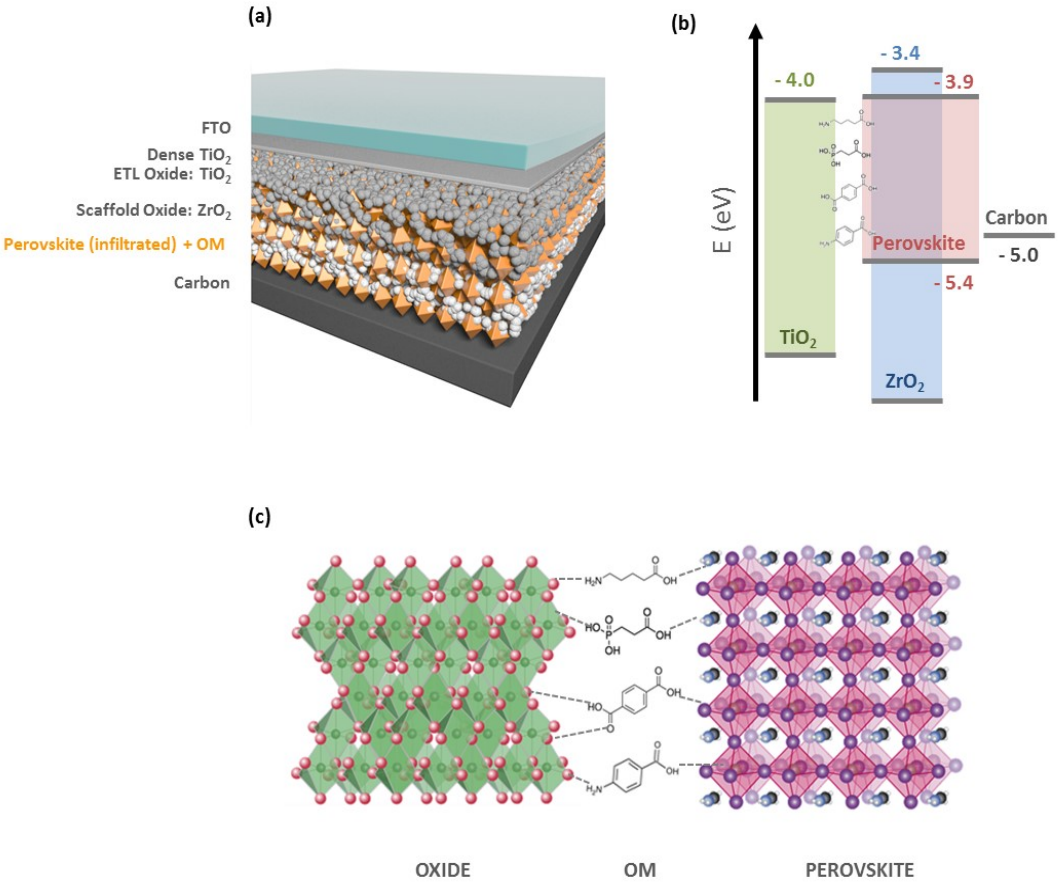

Figure A.3 Schematic representations of **(a)** the different layers of the Carbon-based PSC studied in this thesis work, **(b)** the corresponding band energy level alignment of layers and interfaces and **(c)** the possible interaction between the organic molecules (OM) at the interface between the halide perovskite and the oxide layer.The OM under study are (from top to bottom): 5-ammoniumvaleric acid iodide 5AVA, PABA, TPA and the H3pp.

A.3 Surface and Electronic characterization of SAMs

As already mentioned in Chapter 5, 5-AVAI is the main organic additive applied in C-based PSCs. This moleculeis composed of two terminals groups, an amino group on one side and a carboxylic acid group on the other side. Its main function in the PSC is to act as additive to promote the crystal growth of the perovskite crystalline structure and also to passivate defects through the anchoring of its two functional groups to the oxide and the perovskite materials. It has been shown that the passivation of the oxide defects on surfaces applying a highly ordered organic molecule as SAM, can significantly reduce the density of charge traps at the oxide/molecule interface and thereby provide an enhancement of the device charge-carrier mobility [20-21]. The improvement on these photovoltaic parameters permits to

improve PSC efficiency and reduce performance loss on stability analysis carried out under continuous 1 sun illumination.

In this section, we present the study of the following organic molecules (OM): 5AVAi, PABA and TPA. We made special emphasis on the morphological, electronic, optical and crystallographic properties of the OM and describe the process to fabricate them as SAMs and their study by KPFM and XPS/UPS analysis.

A.3.1 Effect of organic additives on the crystalline structure of perovskite material

A crystallographic analysis was carried out by XRD in order to know the effects on the crystalline structure of $MAPbI_3$when different OM molecules were applied. The crystal structure of the $MAPbI_3$ perovskite has been reported in several studies. $MAPbI_3$ has been shown to have three structural phases; a cubic phase with space groupPm-3m above 330 K, a tetragonal phase with a space groupI4/mcm from 160K to 330K and an orthorhombic phase of space group Pnma below 160 K [26].

Figure A.4 (a) shows a typical pattern diffraction from $MAPbI_3$ at RT which corresponds to a tetragonal phase with cell parameters a=8.49 Å, b=8.49 Å and c=12.64 Å, and α=β=ɣ=90°. Comparing the experimental data with the reported values from Inorganic Crystal Structure Database (ICSD) (reference code 250739) established good agreement between the values. This kind of crystalline structure was used for the two step method of C-based PSCs as mentioned in Chapter 5.

A substantially increase in the b and c lattice parameters is expected when the 5AVA molecule is present in the structure. The pattern fits an orthorhombic perovskite structure with the lattice parameters of a=8.75 Å, b=9.83 Å and c=15.33 Å. The large expansion of the c axis introduced by 5-AVA indicates a dominant orientation during crystal growth due to the contact with lead and iodide ions [27].

Figure A.4 (b) shows the pattern diffraction corresponding to the $5\text{-}(AVA)_x(MA)_{1-x}PbI_3$ used in a one-step method. The peaks at 14.13°, 28.46°, 31.86°, 34.96°, 40.56° and 43.13° corresponding to the reflections of the perovskite (110), (220), (211), (221),(202), (212), respectively, which are in good agreement with the literature reported values from the study of Hongwei Han and co-workers[28].

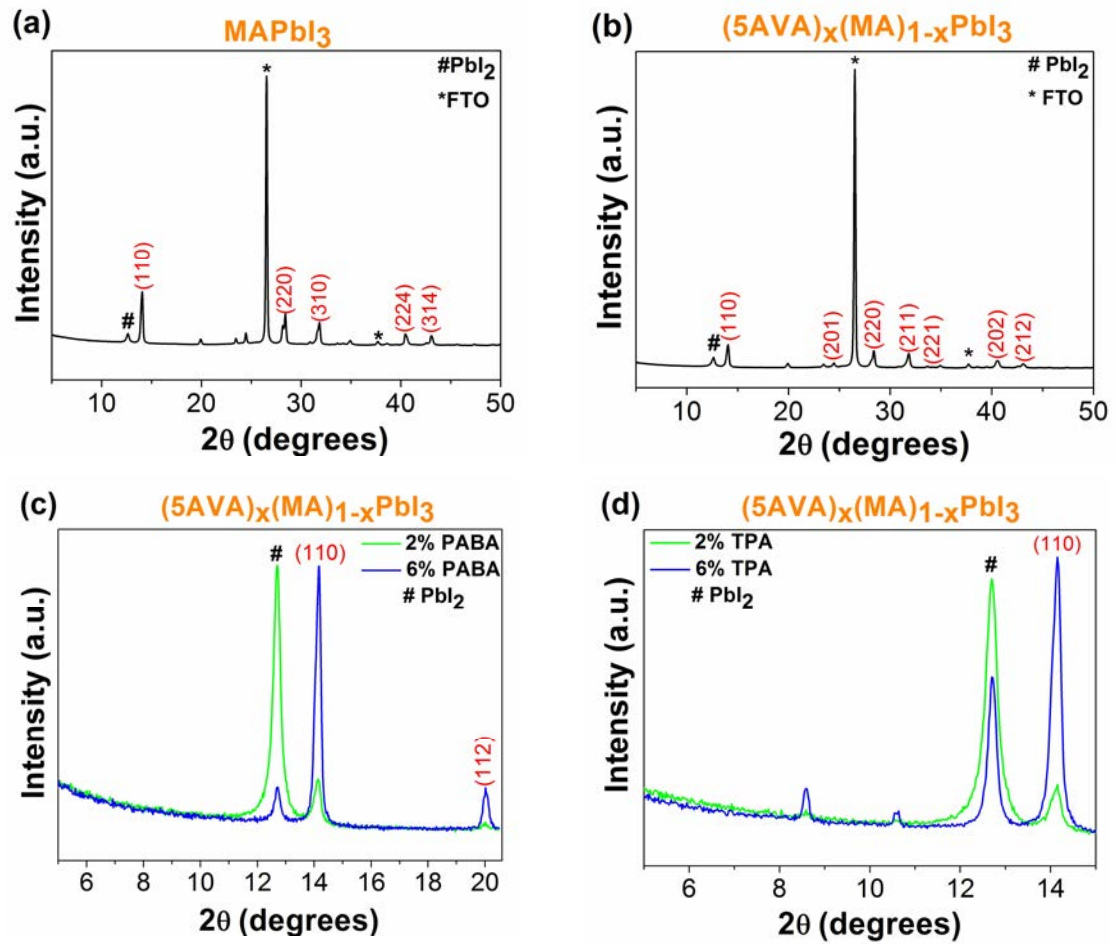

Figure A.4 XRD patterns of mesoscopic $TiO_2/ZrO_2/C$ on FTO glass **(a)** infiltrated $MAPbI_3$ using a two-step method ($MAPbI_3$) and **(b)** infiltrated with 5-$(AVA)_x(MA)_{1-x}PbI_3$ using a one step method. **(c)** a study of the PbI_2 peak in function of PABA concentration infiltrated with 5-$(AVA)_x(MA)_{1-x}PbI_3$**(d)**a study of the PbI_2 peak in function of the TPA concentration infiltrated with 5-$(AVA)_x(MA)_{1-x}PbI_3$.

The addition of the PABA molecule to MAPI at different concentrations should affect two main peaks on the X-Ray diffractogram: the peak at 12.73° ascribed to the (001) reflection of the PbI_2 reagent and the peak at 14.17° ascribed to (110) reflection of the perovskite. This is shown in **Figure A.4 (c)**, where the difference in intensity of these peaks is clearly observed: as the concentration of the PABA molecule increases the intensity of the peak that corresponds to PbI_2 at 12.7° decreases. This response has been attributed to the decrease of the defect content on TiO_2 due to the PABA-oxide interaction. Furthermore, this higher crystallinity employing 6 % of PABA produces an increase in the preferential orientation of the perovskite crystals [22].

Following the same response described for the PABA molecule, changes in the intensity of the peaks of the diffractogram depend on the TPA content as is shown in **Figure A.4 (d).** As

the concentration of TPA solution increased, e.g. at 6 %, the intensity in the reflection (110) at 14.16° increases, whereas at 2 % TPA the peak from PbI_2 dominates. The increase in the TPA concentration suggests an improvement of the perovskite crystallinity and can have an influence on the growth direction of the perovskite crystal [20].

A.3.2 Study of Self-Assembled monolayers (SAMs) by Kelvin Probe Microscopy and Atomic Force Microscopy (KPFM/AFM)

The WF of a metal is defined as the difference in energy between the Fermi level and vacuum level; while, for semiconducting and insulating materials it refers to IP. The WF is extremely sensitive to changes of the state of the surface. AFM and KPFM measurements were performed to understand the surface modification of the WF depending on the terminal groups in SAM molecules. In this section, we used AFM to investigate the morphology of the surfaces, providing information and high resolution topographic maps, and KPFM as a non-invasive method to obtain changes in the electrostatic potential of the surface. Specially, in order to determine the possible interaction between the SAM and the oxide surface (TiO_2), the three SAMs applied in the PSCs were analysed; 5AVA, PABA and TPA. The samples for the measurements were prepared from a different solution of SAM deposited on top of gold and TiO_2 surfaces by spin coating. Within these techniques, a difference in topography and surface potential was detected due to a possible interaction with the SAM molecules.

The functional groups present in the 5AVA, PABA and TPA molecules are amino groups, which are electron donors (activated group) and a carboxylic acid groups, which are electron acceptors (deactivated group). These molecules were selected since they can be attached to a substrate surface through different binding configurations used for the same purpose. Both proposed alternative SAMs, TPA and PABA, are aromatic SAMs used to modify the transport layer interface to achieve preferable barrier alignment and charge carrier injection [30]. Furthermore, the π-conjugated molecular structure can help to increase the charge transfer in aromatic groups with respect to alkyl groups [31].

Analysis of reference surface

For characterizing these samples, it was used a two pass mode. The setpoint of oscillation for the first pass, when topography of the sample is measured, was about 300 mV. During the second pass, when the cantilever is scanned across the surface at a constant height, this height was set around 50 nm. In all the experiments, PPP-EFM tips with stiffness constant of 2 N/m and coated with Ptir were used.

The sample was prepared as follows; the c-TiO_2 was prepared by spray pyrolysis using titaniumiisopropoxidebis(acetylacetonate) 10 % in IPA. The c-TiO_2 was then cooled down to RT and sintered in the oven at 450 ˚C for 2 h with a ramp of 3˚C/min. The gold was thermally evaporated under high vacuum on top of the TiO_2 films. And finally, the 0.01 mM SAMs were deposited on top by spin coating (5000 rpm, 20 s) and further annealed for 5 min at 50˚C.

Before studying the SAM surface molecules, a KPFM characterization was carried out in order to know the background of the device V=200 mV, as a reference. **Figure A.5** shows the different material found in each part of the sample.

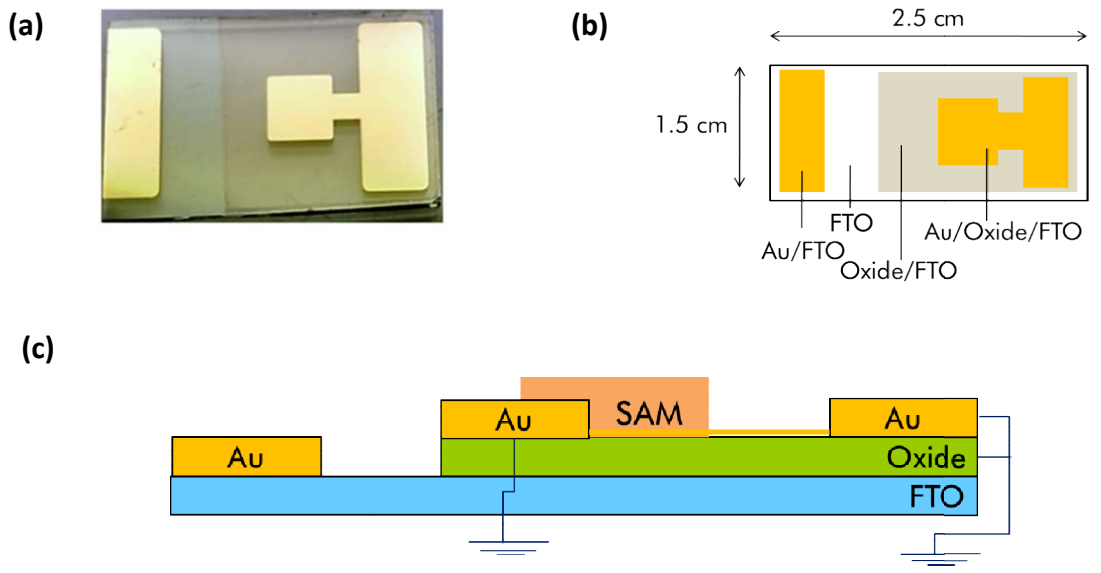

Figure A.5 (a) Image of the sample. **(b)** Schematic representation of the sample**. (c)** Scheme of the layer distribution of the sample.

Figure A.6 shows the Kelvin image of the interface between the Au region and the FTO-TiO_2 area. At the limit between the gold (Au) and the FTO a clear depletion of the electrons was observed indicating an accumulation in this zone, in terms of electronic distribution.

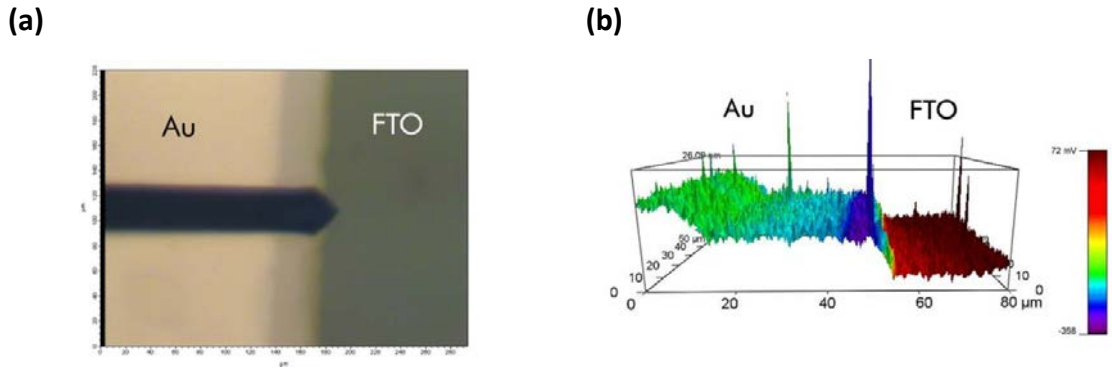

Figure A.6 (a) Optical microscope image of a sample showing the FTO and Au coating regions and **(b)** KPFM map of the same region.

Figure A.7 shows the topographic and Kelvin images taken by AFM-KPFM measurements of the bare FTO/Oxide and Au/Oxide/FTO surfaces. From the topographical point of view no significant difference can be observed, a grain-like topography is predominant in all the area. The surface roughness corresponds to 5.96 nm without the presence of Au and 6.50 nm with the presence of Au. Meanwhile, from the Kelvin mode, slightly more contrast in the TiO_2/FTO surface can be detected providing a difference in surface potential.

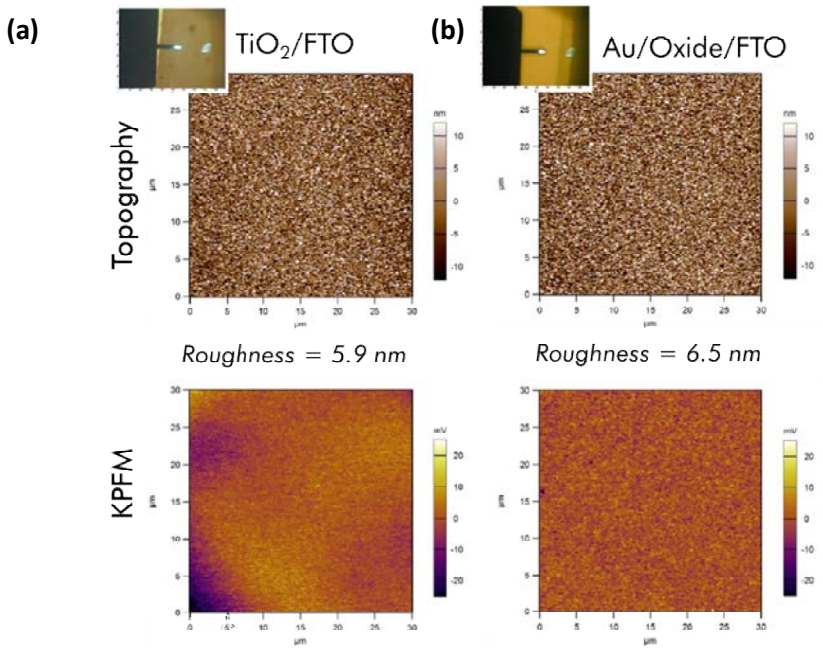

Figure A.7 Image of topography and Kelvin mode in areas without the presence of SAMs, **(a)** TiO_2/FTO and **(b)** Au/TiO_2/FTO.

Surface functionalization with SAMs

After analysis of the bare sample, topographic and Kelvin measurements were carried out in a region with the presence of 5AVA molecules. **Figure A.8** shows images of 5AVA/FTO and 5AVA/Au/FTO surfaces. Areas with the presence of 5AVA can be clearly seen in KPFM (red islands). However, in the topography images it is difficult to distinguish the 5AVA zone, as the images mainly exhibited a grain-like area. In the KPFM image, a contrast in the surface potential can be observed and a large accumulation of molecules can be clearly seen in the red zones. **Figure A.8** also shows the roughness in the presence of the 5AVA SAM. A comparison of the roughness values without the 5AVA deposition suggests that alkyl chains and the anchoring of the amino and carboxylic groups of the molecule provide less roughness (4.5 and 4.3 nm) with respect to the bare surfaces (5.9 and 6.5 nm). From this image, can be confirmed that the accumulation of 5AVA molecules is easier on 5AVA/Au/FTO surfaces than 5AVA/FTO surfaces. However, the trend is not a homogeneous deposition as it can be clearly observed **Figure A.8 (a)**.

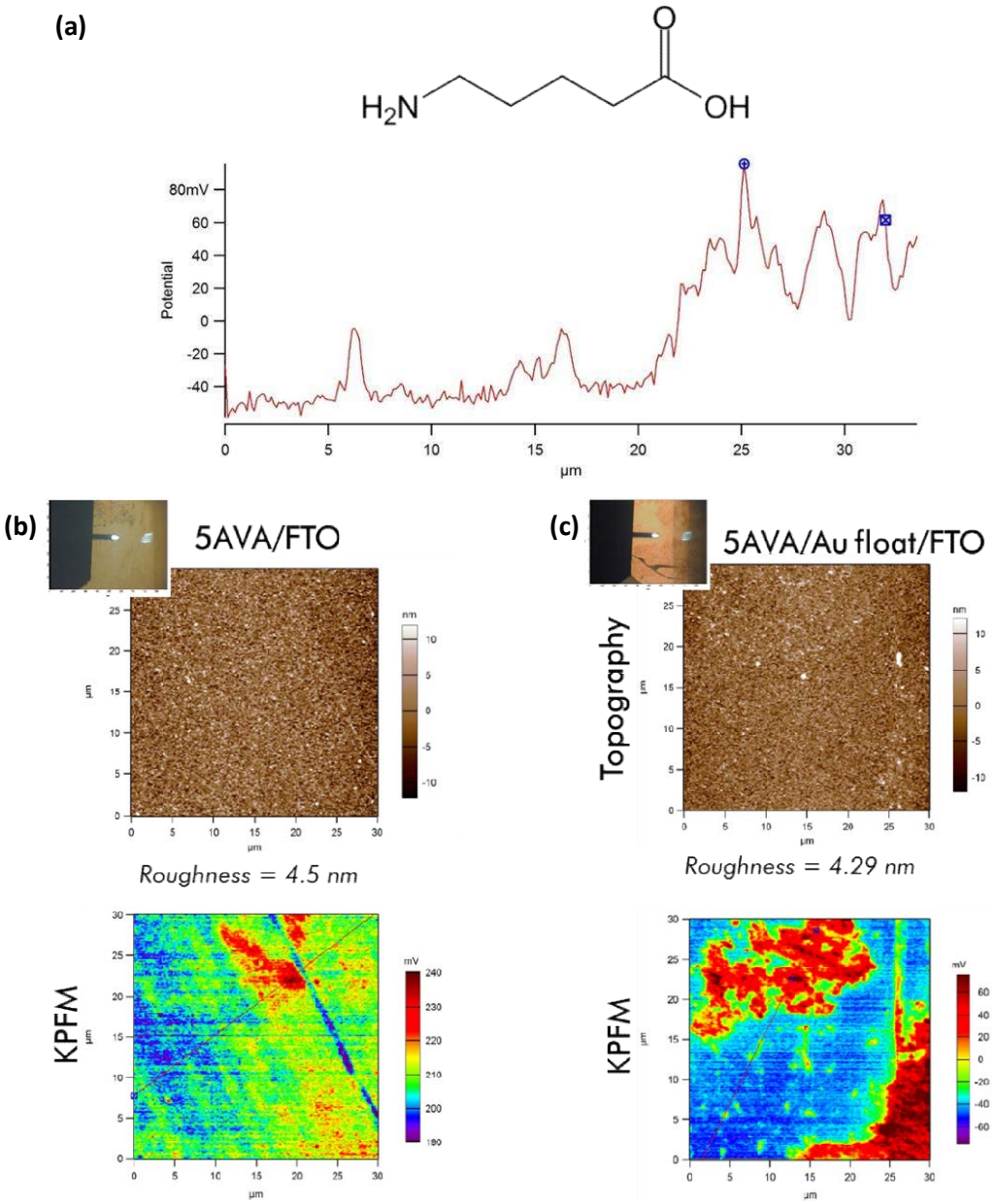

Figure A.8 (a) Image of the molecular structure of 5AVA.Cross section of thesurface potential image of topography and Kelvin mode in areas with the presence of 5AVA. **(b)** 5AVA/FTO and**(c)** 5AVA/Au float/FTO.

Figure A.9 shows the 5AVA images of the topography and Kelvin mode of 5AVA on TiO_2 and Au surface. The two different images in **Figure A.9** correspond to two different regions of accumulation of 5AVA on the Au and TiO_2 surfaces, following the same step building trend. It seems that the organization of molecules presents similarities; every step was determined by 24 mV. Furthermore, a slight difference it can be detected depending on the surface material.

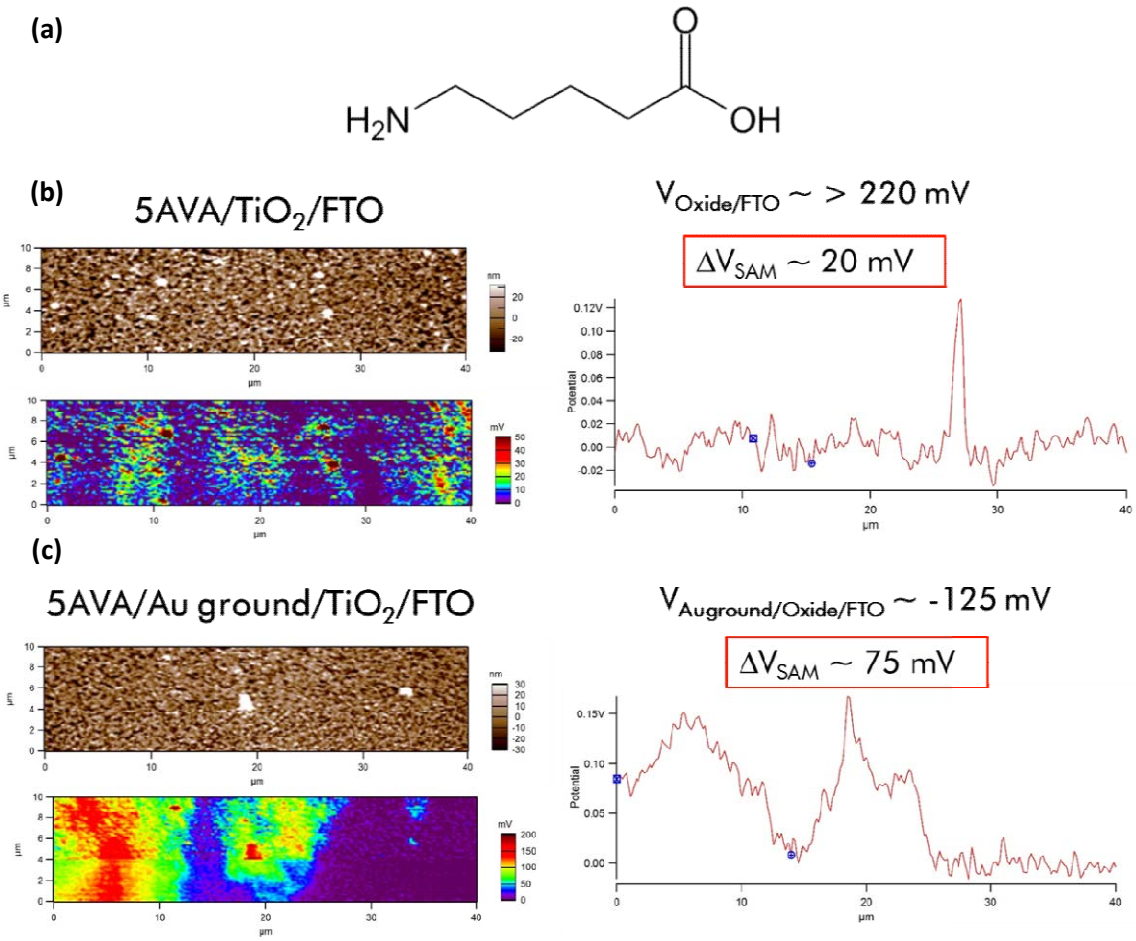

Figure A.9 (a) 5AVA molecule. **(b)** Comparative images of the topography and Kelvin mode of 5AVA on oxide surface and 5AVA on Au surface.

In the case of the 5AVA deposited on the TiO_2, the accumulation of molecules was minimal compared to the big islands that grew on the Au surface. It can be observed that on Au surface the interaction with 5AVA molecules it was improved with more homogeneity and accumulation, as shown in **Figure A9**. In contrast, on top of the TiO_2 less interaction can be seen from the KPFM image due the small areas of accumulated 5AVA and neither the formation of the layers of the material can be noticed.

Thus, the difference in surface potential of about 75mV between the 5AVA and the Au ground could suggest an enhancement of charge density in the device.

Surface analysis measurements of PABA molecules were carried out by AFM and KPFM techniques using a diluted solution in front of the behaviour of PABA molecules in contact with the Au and TiO_2 surfaces. **Figure A.10** shows the Kelvin and topographic analysis of the PABA molecules on top of Au and TiO_2 surfaces. Differences in terms of the distribution of

the material directly depend on surface attachment. A more homogeneous accumulation can be seen when PABA is attached on top of Au, whereas attachment with TiO_2 shows a kind of accumulation in the form of islands. The PABA molecules on Au have a larger difference in surface potential than on top of TiO_2, indicating different electronic interaction.

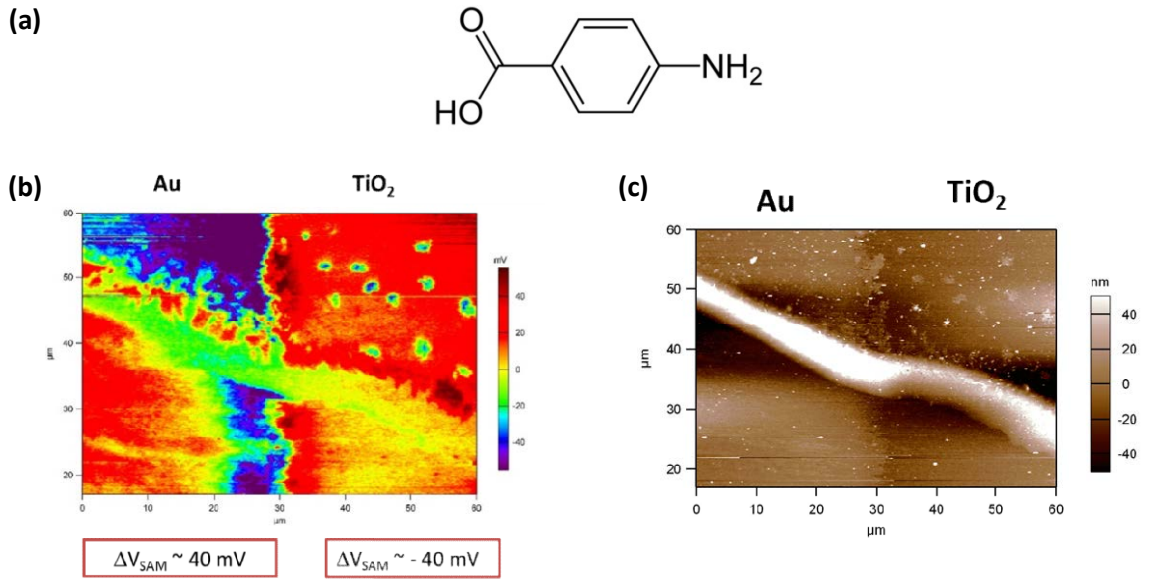

Figure A.10 (a) Image of the molecular PABA structure **(b)** KPFM image and **(c)** topography image of PABA molecules on TiO_2 and Au surfaces.

In this regard, a positive surface potential of +40 mV was measured on the PABA form which we assumed that the positive sign was due to electronic polarization induced in the Au surface by the dipole moment of the PABA molecules [32].

Figure A.11 shows the scheme of surface potential values depending on the PABA molecule zone of the sample. A difference in sign is clearly seen depending on the surface interaction. As Yagmurcukardes *et al.* proposed with n-Si surfaces in the presence of SAM molecules, an increase in surface potential is directly related to an enhancement of the charge density on the surface [30].

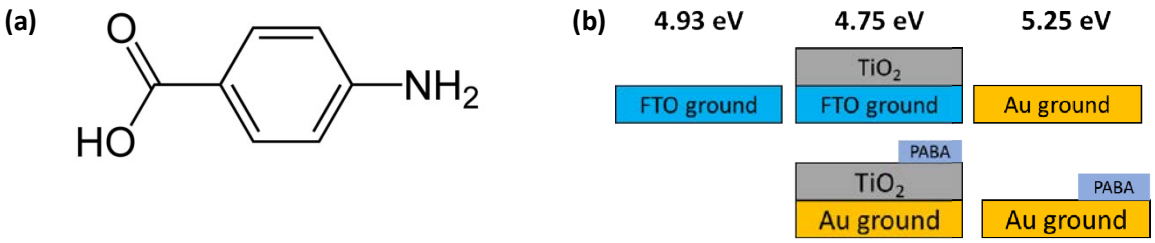

Figure A.11 Different values of absolute WF values depending on the region of the device, with the presence of PABA molecules.

Surface analysis measurements of TPA molecules were carried out by AFM and KPFM techniques using a diluted solution regarding the behaviour of TPA molecules in contact with Au and TiO_2 surfaces. **Figure A.12** shows the Kelvin and topographic analysis of the TPA molecules on top of Au and TiO_2 surfaces and **Figure A.13** shows the scheme of surface potential values depending on the TPA molecule zone of the sample.

In contrast of the interaction of PABA discussed above, with these surfaces, no significant difference using the TPA molecules were exhibited, neither in the WF or the surface coverage. A possible explanation could be that TPA molecules consist of the same anchoring groups, such as two carboxylic groups.

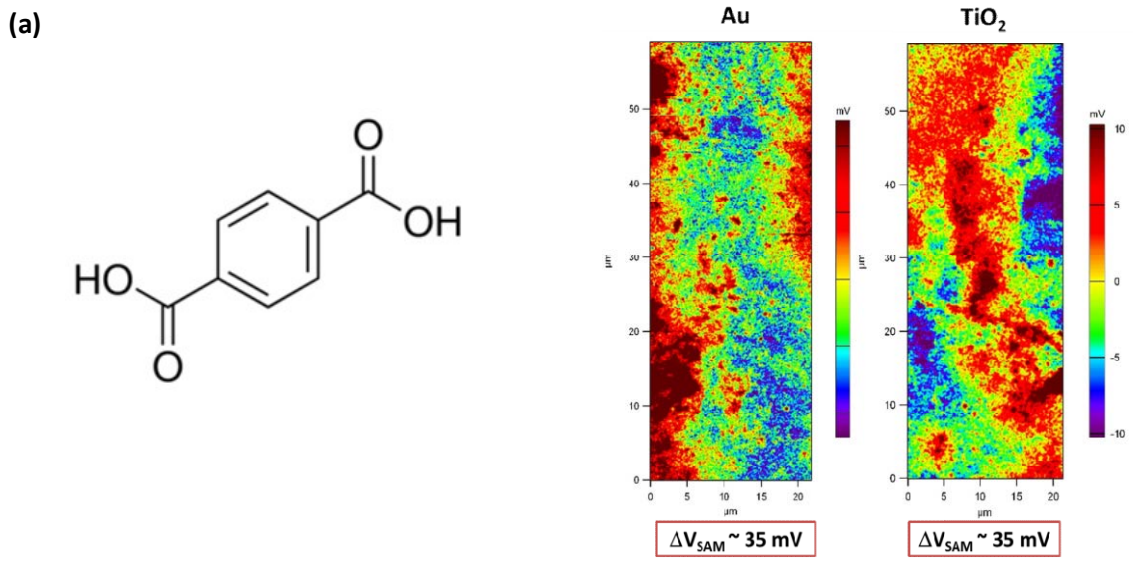

Figure A.12 (a) TPA molecule.**(b)** KPFM images of the TPA molecules on top of TiO_2 and Au surfaces.

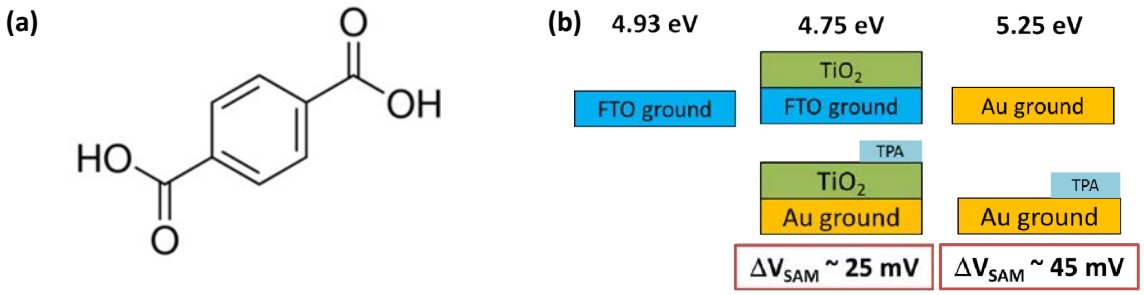

Figure A.13 (a) TPA molecule.**(b)** Different values of absolute WF values depending on the zone of the device, with the presence of TPA molecules.

As a conclusion of the AFM/KPFM measurements it have been seen more contrast in the TiO_2/FTO surface, providing a clear difference in surface potential. The accumulation of the deposited SAM grew with the same step building trend. Also, it has been observed that the interaction of the SAMs into Au surface it was enhance with more homogeneity and accumulation while in the case of the interaction with the oxide the accumulation results in form of islands.

A.3.3 Electronic study of SAMs by Photoemission (XPS/UPS)

We used photoelectron spectroscopy (XPS and UPS) in order to study the electronic properties and the IP of the different SAMs and also to obtain more information about the chemical bonding of these SAMs inserted in the PSCs devices. **Figure A.14** shows a scheme of the difference between IP and Eg in a semiconductor material.

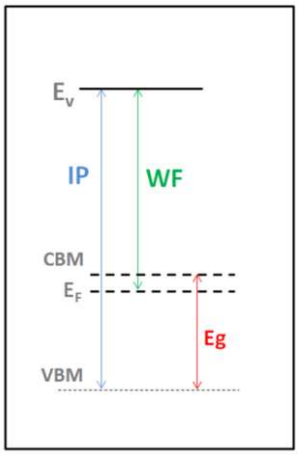

Figure A.14 Scheme of the difference between IP and WF values in a semiconductor material.

Several samples were prepared on top of TiO_2/FTO substrates with 0.1 mM and 0.01 mM concentrations. The photoemission is a surface sensitive technique and the probing depth is about 2 nm of surface analysis and the analysed peaks were C1s, N1s, O1s and $Ti2p_{3/2}$.

Firstly, the XPS-UPS analysis was carried out for the 5AVAI molecules. The binding energies are referred to the well-known $Ti2p_{3/2}$ line (458.5 eV) [33]. **Figure A.15 (a)** shows the XPS spectra of the N1s line for the 0.1 mM, 0.01 mM and without 5AVA samples. From the Figure it can be observed, that there is a direct relation between the concentration of the SAM molecules and the intensity of the nitrogen peak. When 5AVA is not present a main peak at 400 and a shoulder at 402 eV are found, both components correspond to molecularly chemisorbed nitrogen [33]. Regarding the diluted concentration of 5AVA (0.01 mM) no significant difference could be detected. As the concentration of 5AVA solution increased, the peaks become more intense. For the highest 5AVA concentration two predominant peaks were shown, one peak at 399.8 eV assigned to a primary amine and a feature at 401.6 eV assigned to protonated amine species [34].

Figure A.15 (b) shows the TiO_2 spectra as a function of 5AVA concentration. Even at 5AVA concentration of 0.1 mM the signal corresponding of the substrate TiO_2 was present, indicating a non uniform layer of 5AVA molecules.

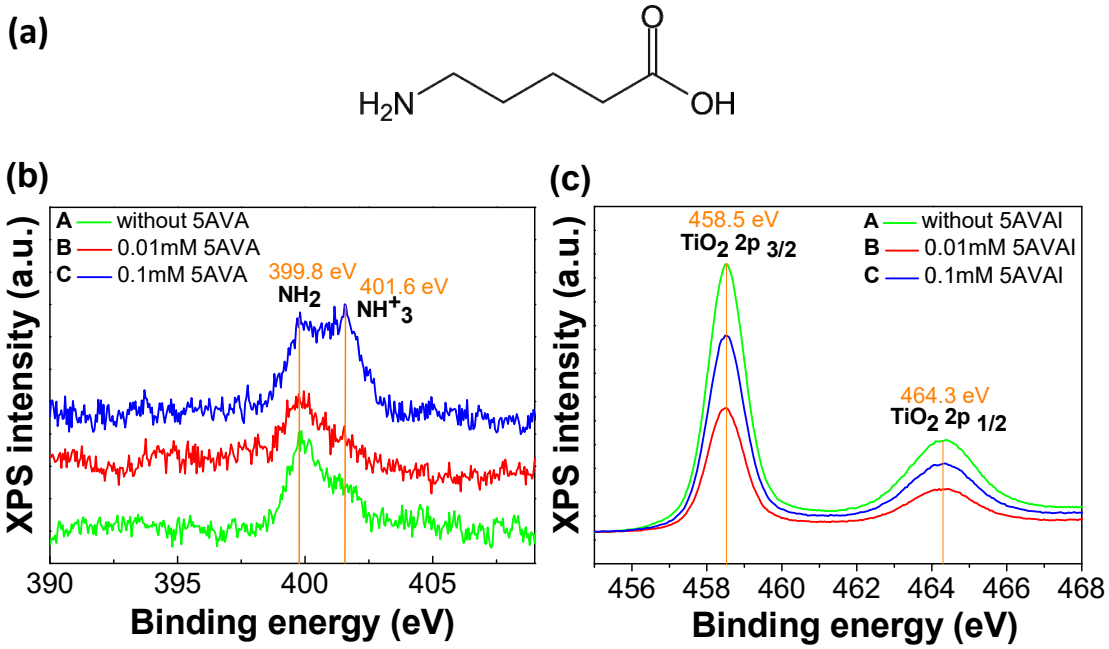

Figure A.15 (a) 5AVA molecule **(b)** N1s spectra measured by XPS corresponding to TiO_2 films covered with 5AVAI at different concentrations (0 mM 5AVA, 0.01 mM 5AVA and 0.1 mM 5AVA) and **(c)** Ti 2p $_{3/2}$ and Ti 2p $_{½}$ core level spectra measured for TiO_2 surfaces at different concentrations (0 mM 5AVA, 0.01 mM 5AVA and 0.1 mM 5AVA) by XPS.

UPS measurements were also carried out in order to determine the IP values following the methodology described in Chapter 3. **Table A.1** shows the different IP values according to 5AVA concentration. A clear increase of about 1 eV can be observed when the 5AVA was deposited on the TiO_2 surface for both concentrations: 0.1 mM and 0.01 mM.

Table A.1 IP values of 5AVAI/TiO_2/FTO as a function of 5AVAI solution concentration measured by UPS.

Substrate	5AVAI conc. (mM)	IP (eV)
FTO/TiO_2	0mM	7.3
FTO/TiO_2	0.1mM	8.3
FTO/TiO_2	0.01mM	8.2

The same analysis was carried out for the other SAMs. PABA was measured on top of the TiO_2 surface for two different concentrations: 0.1 mM and 0.01 mM. **Figure A.16 (a)** shows the N1s spectra where it can be observed that the protonated signal (NH_3^+) is less intense. Also, it could be notice that an increase in PABA concentration is directly related with an increase in the nitrogen signal. **Figure A.16 (b)** shows a typical TiO_2 peak with the same intensity even on top of the PABA molecules.

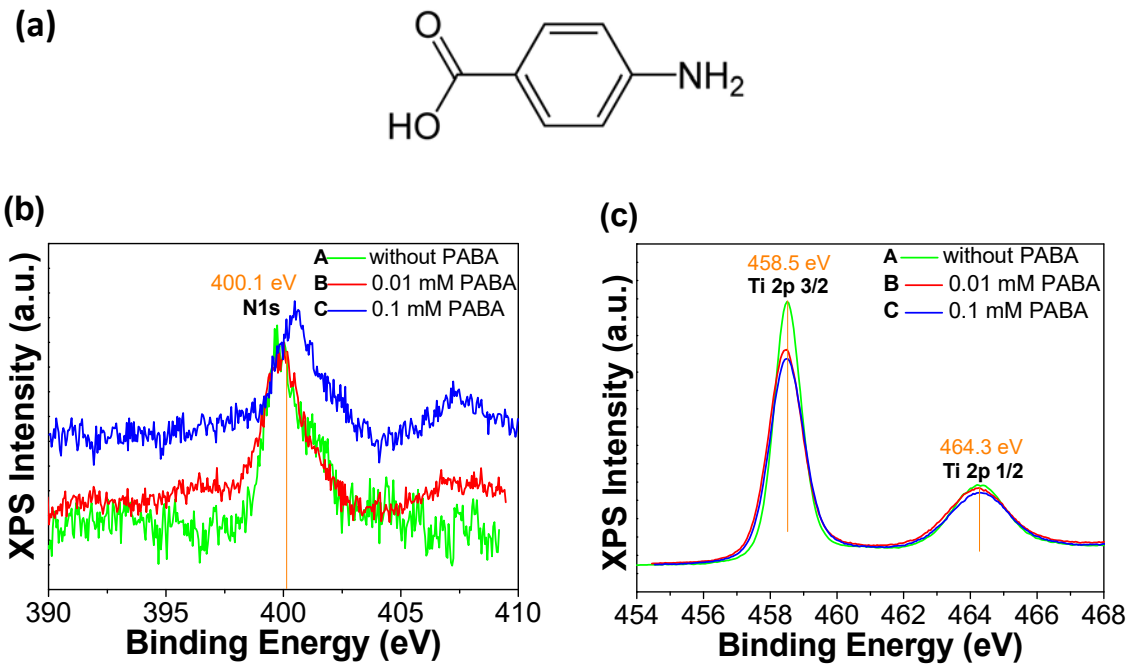

Figure A.16 (a) N1s spectra measured by XPS for PABA molecules at different concentrations and **(b)** Ti 2p $_{3/2}$ and Ti 2p $_{½}$ core level spectra measured for TiO_2 surface at different concentrations by XPS.

Table A.2 shows the IP values as a function of PABA concentration. In this case, a small difference of about 0.2-0.3 eV can be observed.

Table A.2 IP values of PABA/TiO_2/FTO as a function of PABA concentration solution measured by UPS.

Substrate	PABA conc. (mM)	IP (eV)
FTO/TiO_2	0 mM	7.3
FTO/TiO_2	0.1mM	7.0
FTO/TiO_2	0.01mM	7.5

TPA was also measured on top of the TiO_2 surface comparing two different concentrations: 0.1 mM and 0.01 mM. **Figure A.17 (a)** shows the TPA molecular structure, **Figure A.17 (b)** shows the C1s spectra of TPA at 0.1 mM and 0.01 mM, **Figure A.17 (c)** shows the Ti 2p $_{3/2}$ and Ti 2p $_{½}$ core level spectra for TPA molecules and **Figure A.17 (d)** shows the O1s spectra of TPA molecules. In this case, the predominant peak is due to contribution of oxygen in the oxide in the FTO/TiO_2 sample and also the contribution of the carboxyl group in the TPA molecules at 532 eV.

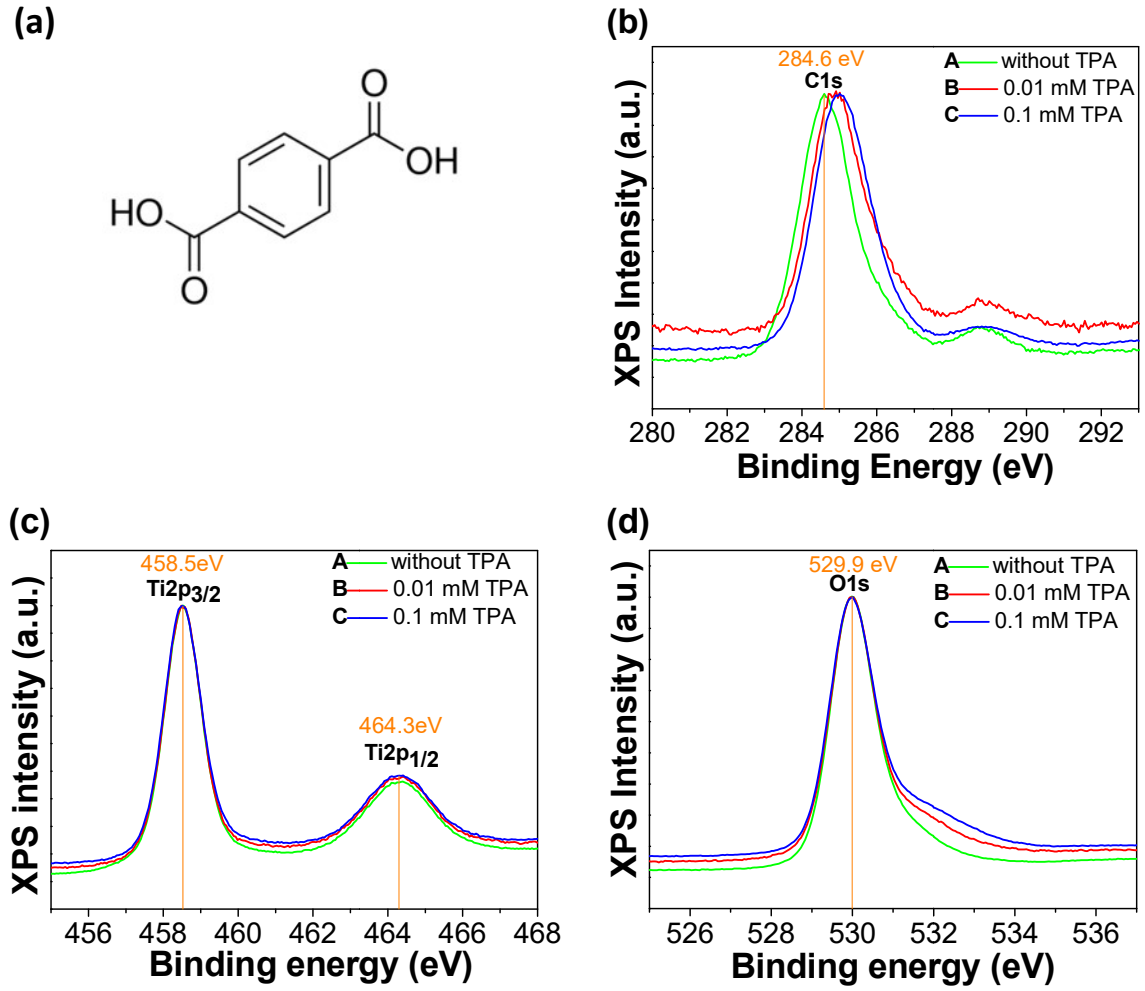

Figure A.17 (a) C1s line spectra, **(b)** O1s line spectra and **(c)** Ti 2p $_{3/2}$ and Ti 2p $_{½}$ core level spectra measured for TPA molecules at different concentrations by XPS.

Table A.3 shows the difference between IP values depending on TPA concentration. In this case, there is no significant difference for all concentrations.

Table A.3 IP values of TPA/TiO_2/FTO as a function of TPA concentration solution measured by UPS.

Substrate	TPA conc. (mM)	IP (eV)
FTO/TiO_2	0 mM	7.3
FTO/TiO_2	0.1mM	7.2
FTO/TiO_2	0.01mM	7.2

Comparing the three different SAMs applied in this thesis; we could notice a significant difference in terms of IP between 5AVA in front of PABA and TPA. When 5AVA is not present into FTO/TiO_2 surface we obtained an IP of 7.3 eV, however, when 5AVA is deposited on top of the oxide the IP value increase 1 eV. The highest interaction between the surface and the

SAMs could be achieved using 5AVA. In addition, this value could be directly related to the highest photovoltaic performance obtained using 5AVA as compared to the other SAMs (PABA and TPA) as was already discussed in Chapter 5 of this present work.

It is important to note that both AFM and KPFM techniques showed that the prepared samples exhibited a heterogeneous surface morphology with an accumulation of material in layers or steps. However there were some differences as KPFM provides information at local level and allows a more accurate and deep analysis whereas the XPS-UPS technique presents a not a local analysis.

If SAMs with negative dipole moment are used to modify the surface, the WF value can decrease compared to the bare substrate. In a contrast, the use of SAMs with a positive dipole can lead to an increase in WF, compared to the bare substrate. This implies that SAMs with positive dipole moment can increase the WF of the functionalized films [18]. The experimental dipole moment values of the SAMs applied in this present work were as found in the literature, for PABA a dipole moment +3.10 D and for the TPA +2.60 D, leading to an enlargement of the WF values [35].

In the case of PABA, better interaction was achieved with gold substrate. By theoretical calculations and vibrational photoelectron spectra Liu *et al.* suggest that the Au-C bonding is extremely strong, indicating a covalent bonding between the Au surface and the carboxylic functional group [36]. However, with carboxylate-metal bonds, an attachment between the carboxylic group and the TiO_2 could be possible via bonding between the carboxylate anion and a surface metal cation, where this type of bonding is typically weaker.

A.4 Conclusions

This Annex section included the previous results of the SAMs from an electronic point of view.

At the limit between gold and FTO a grain-like area was observed with a clear depletion of electrons indicating electronic accumulation in this zone. When SAMs were applied, a

heterogeneous step-like accumulation was observed, whereas in kelvin mode, SAMs were found in form of islands. In the case of 5AVA on gold substrates, the 5AVA molecules exhibited more accumulation than on top of TiO_2, confirmed by the difference in surface potential, 20 mV for TiO_2/5AVA and 75 mV for Au/5AVA. Different electronic interaction was found for PABA depending on the attachment surface, +40 mV for Au and -40 mV for TiO_2. Furthermore, the surface potential increased with respect to the bare surface. Similar results were obtained for the TPA molecules, as are composed of the same carboxyl functional group; a difference in surface potential of 35 mV was obtained for both cases of attachment (Au and TiO_2). From XPS/UPS analysis a change in surface potential for all SAM samples was clearly seen which we proposed was due to molecular interaction.

A.5 References

[1] C. Zuo, H. J. Bolink, H. Han, J. Huang, D. Cahen, and L. Ding, "Advances in Perovskite Solar Cells," *Adv. Sci.*, vol. 3, no. 7, p. 1500324, 2016.

[2] F. Wang, S. Bai, W. Tress, A. Hagfeldt, and F. Gao, "Defects engineering for high-performance perovskite solar cells," *npj Flex. Electron.*, vol. 2, no. 1, p. 22, 2018.

[3] C. Ran, J. Xu, W. Gao, C. Huang, and S. Dou, "Defects in metal triiodide perovskite materials towards high-performance solar cells: origin, impact, characterization, and engineering," *Chem. Soc. Rev.*, vol. 47, no. 12, pp. 4581–4610, 2018.

[4] J. M. Ball and A. Petrozza, "Defects in perovskite-halides and their effects in solar cells," *Nat. Energy*, vol. 1, p. 16149, Oct. 2016.

[5] R. Qiao and L. Zuo, "Self-assembly monolayers boosting organic–inorganic halide perovskite solar cell performance," *J. Mater. Res.*, vol. 33, no. 4, pp. 387–400, 2018.

[6] W. C. Bigelow, D. L. Pickett, and W. A. Zisman, "Oleophobic monolayers: I. Films adsorbed from solution in non-polar liquids," *J. Colloid Sci.*, vol. 1, no. 6, pp. 513–538, 1946.

[7] A. Ulman, "Formation and Structure of Self-Assembled Monolayers," *Chem. Rev.*, vol. 96, no. 4, pp. 1533–1554, 1996.

[8] "https://en.wikipedia.org/wiki/Self-assembled_monolayer."

[9] S. P. Pujari, L. Scheres, A. T. M. Marcelis, and H. Zuilhof, "Covalent Surface Modification of Oxide Surfaces," *Angew. Chemie Int. Ed.*, vol. 53, no. 25, pp. 6322–6356, 2014.

[10] M. Lessel *et al.*, "Self-assembled silane monolayers: an efficient step-by-step recipe for high-quality, low energy surfaces," *Surf. Interface Anal.*, vol. 47, no. 5, pp. 557–564, 2015.

[11] C. Haensch, S. Hoeppener, and U. S. Schubert, "Chemical modification of self-assembled silane based monolayers by surface reactions," *Chem. Soc. Rev.*, vol. 39, no. 6, pp. 2323–2334, 2010.

[12] J. Sagiv, "Organized monolayers by adsorption. 1. Formation and structure of oleophobic mixed monolayers on solid surfaces," *J. Am. Chem. Soc.*, vol. 102, no. 1, pp. 92–98, 1980.

[13] I. Gouzman, M. Dubey, M. D. Carolus, J. Schwartz, and S. L. Bernasek, "Monolayer vs. multilayer self-assembled alkylphosphonate films: X-ray photoelectron spectroscopy studies," *Surf. Sci.*, vol. 600, no. 4, pp. 773–781, 2006.

[14] G. Mani *et al.*, "Stability of Self-Assembled Monolayers on Titanium and Gold," *Langmuir*, vol. 24, no. 13, pp. 6774–6784, 2008.

[15] L. Zhang and J. M. Cole, "Anchoring Groups for Dye-Sensitized Solar Cells," *ACS Appl. Mater. Interfaces*, vol. 7, no. 6, pp. 3427–3455, 2015.

[16] A. Myrskog, H. Anderson, T. Aastrup, B. Ingemarsson, and B. Liedberg, “Esterification of Self-Assembled Carboxylic-Acid-Terminated Thiol Monolayers in Acid Environment: A Time-Dependent Study,” *Langmuir*, vol. 26, no. 2, pp. 821–829, 2010.

[17] S. A. Jadhav, “Self-assembled monolayers (SAMs) of carboxylic acids: an overview,” *Cent. Eur. J. Chem.*, vol. 9, no. 3, pp. 369–378, 2011.

[18] Q. Wang *et al.*, “Effects of Self-Assembled Monolayer Modification of Nickel Oxide Nanoparticles Layer on the Performance and Application of Inverted Perovskite Solar Cells,” *ChemSusChem*, vol. 10, no. 19, pp. 3794–3803, 2017.

[19] Y. Ofir, N. Zenou, I. Goykhman, and S. Yitzchaik, “Controlled Amine Functionality in Self-Assembled Monolayers via the Hidden Amine Route: Chemical and Electronic Tunability,” *J. Phys. Chem. B*, vol. 110, no. 15, pp. 8002–8009, 2006.

[20] X. Hou, S. Huang, W. Ou-Yang, L. Pan, Z. Sun, and X. Chen, “Constructing Efficient and Stable Perovskite Solar Cells via Interconnecting Perovskite Grains,” *ACS Appl. Mater. Interfaces*, vol. 9, no. 40, pp. 35200–35208, 2017.

[21] L. Zuo *et al.*, “Enhanced Photovoltaic Performance of CH3NH3PbI3 Perovskite Solar Cells through Interfacial Engineering Using Self-Assembling Monolayer,” *J. Am. Chem. Soc.*, vol. 137, no. 7, pp. 2674–2679, 2015.

[22] B. Li, Y. Chen, Z. Liang, D. Gao, and W. Huang, “Interfacial engineering by using self-assembled monolayer in mesoporous perovskite solar cell,” *RSC Adv.*, vol. 5, no. 114, pp. 94290–94295, 2015.

[23] Y.-Q. Wang, S.-B. Xu, J.-G. Deng, and L.-Z. Gao, “Enhancing the efficiency of planar heterojunction perovskite solar cells via interfacial engineering with 3-aminopropyl trimethoxy silane hydrolysate,” *R. Soc. Open Sci.*, vol. 4, no. 12, 2017.

[24] L. Zuo *et al.*, “Tailoring the Interfacial Chemical Interaction for High-Efficiency Perovskite Solar Cells,” *Nano Lett.*, vol. 17, no. 1, pp. 269–275, 2017.

[25] L. Liu *et al.*, “Fully Printable Mesoscopic Perovskite Solar Cells with Organic Silane Self-Assembled Monolayer,” *J. Am. Chem. Soc.*, vol. 137, no. 5, pp. 1790–1793, 2015.

[26] P. S. Whitfield *et al.*, “Structures, Phase Transitions and Tricritical Behavior of the Hybrid Perovskite Methyl Ammonium Lead Iodide,” *Sci. Rep.*, vol. 6, p. 35685, 2016.

[27] A. Mei *et al.*, “A hole-conductor–free, fully printable mesoscopic perovskite solar cell with high stability,” vol. 345, no. 6194, pp. 295–298, 2014.

[28] X. Jiang *et al.*, “Efficient Compact-Layer-Free, Hole-Conductor-Free, Fully Printable Mesoscopic Perovskite Solar Cell,” *J. Phys. Chem. Lett.*, vol. 7, no. 20, pp. 4142–4146, 2016.

[29] Y. Hu *et al.*, “Improved Performance of Printable Perovskite Solar Cells with Bifunctional Conjugated Organic Molecule,” *Adv. Mater.*, vol. 30, no. 11, p. 1705786, Mar. 2018.

[30] H. A. N. Yagmurcukardes M. Can,A. Yanılmaz,O. Mermer,S. Okur,and Y. Selameta,

"Effect of Aromatic SAMs Molecules on Graphene/Silicon Schottky Diode Performance," *ECS J. Solid State Sci. Technol.*, vol. 5, 2016.

[31] M. Can *et al.*, "Electrical properties of SAM-modified ITO surface using aromatic small molecules with double bond carboxylic acid groups for OLED applications," *Appl. Surf. Sci.*, vol. 314, pp. 1082–1086, 2014.

[32] Y. Wu, G. Haugstad, and C. D. Frisbie, "Electronic Polarization at Pentacene/Polymer Dielectric Interfaces: Imaging Surface Potentials and Contact Potential Differences as a Function of Substrate Type, Growth Temperature, and Pentacene Microstructure," *J. Phys. Chem. C*, vol. 118, no. 5, pp. 2487–2497, 2014.

[33] E. Martínez-Ferrero *et al.*, "Nanostructured Titanium Oxynitride Porous Thin Films as Efficient Visible-Active Photocatalysts," *Adv. Funct. Mater.*, vol. 17, no. 16, pp. 3348–3354, 2007.

[34] X. Song, Y. Ma, C. Wang, P. M. Dietrich, W. E. S. Unger, and Y. Luo, "Effects of Protonation, Hydrogen Bonding, and Photodamaging on X-ray Spectroscopy of the Amine Terminal Group in Aminothiolate Monolayers," *J. Phys. Chem. C*, vol. 116, no. 23, pp. 12649–12654, 2012.

[35] "Tables of Experimental Dipole Moments. ," 1963.

[36] H.-T. Liu *et al.*, "Probing the nature of gold–carbon bonding in gold–alkynyl complexes," *Nat. Commun.*, vol. 4, p. 2223, 2013.

Conclusions and Outlook

One of the aims of this thesis is to study the synthesis of semiconductor oxides. We chose these TMOs for transport layer materials of PSCs as they can be obtained by a low-temperature sintering, water-based and solution processable methods using low cost materials. We found that the optimal sintering temperature is in terms of optimal crystallization, electronic and optical properties. Information about the oxidation states and the energy level alignment was also obtained. In summary, NiO was demonstrated as a good HTM, and ZnO and TiO_2 were shown to be good electron transport materials that perfectly matched the other device components comprising perovskite material, FTO and the metal electrodes, used in inverted and carbon-based PSCs.

We have also demonstrated the feasible application of semiconductor oxides in an inverted and C-based structure and the use of low cost and easy-fabrication techniques, such as spin coating and screen printing, for large scale commercial PSC production. We optimized the methodology of the processes in terms of material, concentration, additives, thicknesses, and hysteresis behaviour. Furthermore, we achieved up to 11 % PCE champion cells in an inverted structure, FTO/NiO/mixed-ion perovskite/PCBM:ZnO/Au and also for the C-based structure, FTO/c-TiO_2/mp-TiO_2/mp-ZrO_2/Carbon/Ag. We also demonstrated that the replacement of 5AVA by other SAMs, such as PABA and TPA is possible but further optimization is required for highly efficient PSCs.

We applied novel SAMs, PABA and TPA in the oxide surfaces, and demonstrated an improvement of the crystallization by employing a more concentrated solution. In terms of morphology, no significant difference could be detected by AFM/KPFM analysis. However, SEM/EDX indicated a grain-like area without full coverage, which was predominant in the presence of the additives. The thickness of the shell layers was almost constant for the PSCs devices. Furthermore, from the AFM results we confirmed a step-like accumulation of the SAM molecules in a heterogeneous mode. We also demonstrated a change in surface potential from KPFM results, in agreement with UPS experimental IP data. This suggests a

strong interaction between SAMs and Au, such as covalent bonding, and a weaker interaction between SAMs and the oxide surface.

From the stability results, we demonstrated that no significant degradation was exhibited after almost one year under dark storage conditions and more than 1000 h for continuous illumination.

In conclusion, this thesis confirmed the suitability of the use of semiconductor oxides for excellent photovoltaic performance and highly stable PSCs.

We suggest that future research should focus on more characterization of PSC devices from a physical point of view, for example, impedance and electron lifetime measurements, etc. Also, an optimization of the novel SAMs added to the PSC will be required as well as further computational studies to understand their behaviour and to confirm our preliminary studies. At the same time, thorough long-term stability tests should be carried out to understand how to avoid fast degradation in presence of novel SAMs. Furthermore, the use of TMOs and additives could be applied in plastic substrates to obtain flexible PSCs with, for example, the use of the R2R technique. The concern about lead toxicity is also important and protective measures and protocols have to be determined for large-scale manufacture. Finally, recycling strategies must be established for the degraded perovskite material.

List of Publications

1. Gevorgyan, S. A.; Espinosa, N.; Ciammaruchi, L.; Roth, B.; Livi, F.; Tsopanidis, S.; Züfle, S.; Queirós, S.; Gregori, A.; Benatto, G. A. D. R.; Corazza, M.; Madsen, M. V.; Hösel, M.; Beliatis, M. J.; Larsen-Olsen, T. T.; Pastorelli, F.; Castro, A.; **Mingorance, A.**; Lenzi, V.; Fluhr, D.; Roesch, R.; Maria Duarte Ramos, M.; Savva, A.; Hoppe, H.; Marques, L. S. A.; Burgués, I.; Georgiou, E.; Serrano-Luján, L.; Krebs, F. C., Baselines for Lifetime of Organic Solar Cells. *Advanced Energy Materials* **2016,** *6* (22).
2. Perez-Tomas, A.; **Mingorance,A.;** Reyna, Y.; Lira-Cantu, M., Metal Oxides in Photovoltaics: All-Oxide, Ferroic, and Perovskite Solar Cells. In *The Future of Semiconductor Oxides in Next Generation Solar Cells*, 1st ed.; Lira-Cantu, M., Ed. Elsevier Singapur: 2017; p 566.
3. Zhang, J.; Xu, B.; Yang, L.; **Mingorance, A.;** Ruan, C.; Hua, Y.; Wang, L.; Vlachopoulos, N.; Lira-Cantú, M.; Boschloo, G.; Hagfeldt, A.; Sun, L.; Johansson, E. M. J., Incorporation of Counter Ions in Organic Molecules: New Strategy in Developing Dopant-Free Hole Transport Materials for Efficient Mixed-Ion Perovskite Solar Cells. *Advanced Energy Materials* **2017,** *7* (14), 1602736.
4. **Mingorance, A.;** Xie, H.; Kim, H.-S.; Wang, Z.; Balsells, M.; Morales-Melgares, A.; Domingo, N.; Kazuteru, N.; Tress, W.; Fraxedas, J.; Vlachopoulos, N.; Hagfeldt, A.; Lira-Cantu, M., Interfacial Engineering of Metal Oxides for Highly Stable Halide Perovskite Solar Cells. *Advanced Materials Interfaces* **2018,** 5, 1800367.
5. Reyna, Y.; Perez-Tomas, A.; **Mingorance, A.;** Lira-Cantu, M., Stability of Molecular Devices: Halide Perovskite Solar Cells. In *Molecular Devices for Solar Energy Conversion and Storage*, Tian, H.; Boschloo, G.; Hagfeldt, A., Eds. Springer-Verlag Berlin: Berlin, 2018; pp 477-531.
6. Xie, H.; Wang, Z.; Tang, P.; Józef, K. D.; Anand, A.; Kim, H.-S.; Daniel, P.; **Mingorance, A.;** Domingo, N.; Zakeeruddin, S. M.; Arbiol, J.; Grätzel, M.; Hagfeldt, A.; Lira-Cantu, M., **2019 Submitted**.

Acknowledgments

To my supervisors Prof. Mónica Lira-Cantu and Prof. Jordi Fraxedas, to give me the chance to be PhD student in UAB University and be part of their research groups in ICN2. Thank you to all that I learn in science and as a person during these years. Thank you to introduce in the solar cells and photoemission field. I think that I grew professionally during this PhD path. Thank you to take out the best of me. Thank you to project manager Marta Fonrodona, and all to my colleagues during this years; Yegraf, Irene, Andressa, Anderson, Gerard, Javi, Fernando, Marc, Ian, Oscar, Anna, Dr. Haibing, Jose Carlos, Janette, Rico, Elia, Laia, Pierre and Vanessa. I learning during this time from all of you, you know the effort to work in this competitive field and the achievement of good devices and we were always supporting each other, I am also proud of you guys. It was a pleasure to work with you.

Thanks also to the tutor of this thesis, Dr. Jordi García-Antón Aviñó.

Special acknowledgment to the Spanish MINECO through the Severo Ochoa Centers of Excellence Program under Grant Nos.SEV-2013-0295 and ENE-2013-48816-C5-4-R. Thanks goes to Agencia de Gestió d'Ajuts Universitaris i de Recerca for the support thorugh the Xarxa de Referencia de Materials Avançats per a l'Energia (XaRMAE) and the consolidated research group No. 2014SGR-1212. Thanks to the COST Action StableNextSol Project No. MP1307. This work is being carried out under the Materials Science Ph.D. degree for A.M of the Universitat Autònoma de Barcelona. Thanks to the following sources for research travel grants, COST MP 1370 and Severo Ochoa Mobility program.

Then thanks to, Dr. Jinbao Zhang, Professor David Tanenbaum and Mr. Marc Balsells. I am really grateful because they also contributed to make me who I am today in my career. Firstly, this thesis could not be possible without the mentoring of my dear colleague and friend Dr. Jinbao Zhang, an excellent person and better professional. I don't know anybody like you; you are the perfectionism of working. You introduce me in how to achieve nice results in PSCs field. You were like a professor for me; you teach me how to work towards to the excellence. Also, thank you for your constant assistance and really nice hosting in

Sweden, with your wife Li also. Secondly, thanks to Prof. David Tanembaum. He was born for teaching, thank you for your inexhaustible kindness and patience. Thank you to transfer worthy knowledge about science and transfer your enthusiasm and curiosity for the world. You are excellent as a person and professor as well. Also, thank you to provide light and fresh ideas for our group, we spent nice days all together. And finally, also thanks to my colleague Mr. Marc Balsells. Thank you to introduce me in the screen printing world with the mentoring of Prof. David. Thank you for your brilliant ideas, research discussions from different point of views, and for your help and support.

I would also like to thank all my collaborators for doing wonderful research together and give me the opportunity to stay in their respective research groups. In one hand, all the team from Uppsala University (Sweden) led by Prof. Gerrit Boschloo and all his group members. Thank you for your kind hosting, the shared knowledge, in special to Dr. Jinbao Zhang as mentioned before, also thanks to Dr. Erik Johansson, Dr. Kerttu Aitola, Dr. Malin B. Johansson, Dr. Xiaoliang Zhang, Dr. Yan Hao, Dr. Marina Freitag, Dr. Haining Tian, Huimin, Leif, Viktor, among others. And on the other hand, thank you all the team from SPECIFIC (United Kingdom) led by Prof. Trystan Watson. Thank you for your warm hosting, your excellent installations, and the knowledge shared. Special thanks to Dr. Francesca de Rossi, it was a *piacere* to work with you. Thanks for your advice, thanks for your time, thanks for the planning that we reach perfectly. Definitely, thanks to be so nice with me, I was learning a lot from an expertise like you of screen printing technique, thanks for your enthusiasm and your time always. I am really grateful for your dedication. Also thanks to Dr. Jenny Baker, Dr. Jérémy Barbé, Dr. Youmna Mouhamad, Dr. Jain Sagar, Dr. Adam Pocket, Simone, Anthony, Giovanni, among others.

Thanks to Prof. Antonito Urbina and all his team from Polythecnic University of Cartagena. Thanks for your long-term stability measurements, your hardworking and your kindness. Thanks to Dr. Neus Domingo and Ms. Christina Stefani for your AFM-KPFM measurements in your lab, your time and your hardwork also. Thanks to Dr. Xavier Borrisé and his team in CNM facilities, thanks for your FIB-SEM measurements.

Thanks to Dr. Anna Crespi and her team in X-ray diffraction lab in ICMAB facilities for your XRD measurements. Thanks to Dr. Mariano Campoy and all his team for your ellipsometry measurements in ICMAB facilities and your kindness as well.

I am really grateful of all the expertise in charge of the characterization equipment in ICN2.